

A Practical Circuit-based Model for State of Health Estimation of Li-ion Battery Cells in Electric Vehicles

*Long Lam
Delft, 23 August 2011*

Master of Science Thesis

University of Technology Delft
Faculty of Electrical Engineering, Mathematics and Computer Science
Department of Electrical Sustainable Energy

Supervisor: Prof.dr.ir. P. Bauer

Exam committee: Prof.dr. J.A. Ferreira
Prof.dr.ir. P. Bauer
Dr. E.M. Kelder



Abstract

In this thesis the development of the state of health of Li-ion battery cells under possible real-life operating conditions in electric cars has been characterised. Furthermore, a practical circuit-based model for Li-ion cells has been developed that is capable of modelling the cell voltage behaviour under various operating conditions. The Li-ion cell model can be implemented in simulation programs and be directly connected to a model of the rest of the electronic system in electric vehicles.

Most existing battery models are impractical for electric vehicle system designers and require extensive background knowledge of electrochemistry to be implemented. Furthermore, many models do not take the effect of regenerative braking into account and are obtained from testing fully charged cells. However, in real-life applications electric vehicles are not always fully charged and utilise regenerative braking to save energy. To obtain a practical circuit model based on real operating conditions and to model the state of health of electric vehicle cells, numerous 18650 size LiFePO₄ cells have been tested under possible operating conditions.

Capacity fading was chosen as the state of health parameter, and the capacity fading of different cells was compared with the charge processed instead of cycles. Tests have shown that the capacity fading rate is dependent on temperature, charging C-rate, state of charge and depth of discharge.

The obtained circuit model is capable of simulating the voltage behaviour under various temperatures and C-rates with a maximum error of 14mV. However, modelling the effect of different temperatures and C-rates increases the complexity of the model. The model is easily adjustable and the choice is given to the electric vehicle system designer to decide which operating conditions to take into account. By combining the test results for the capacity fading and the proposed circuit model, recommendations to optimise the battery lifetime are proposed.

Preface

This thesis is part of the High Tech Automotive Systems (HTAS) project HSH10001, project name Databox. In project Databox the development of the battery health in electric cars is estimated by logging the driving behaviour and battery parameters on a data box installed in electric vehicles, which are driving around in the area of Amsterdam. Project Databox initiated by MisterGreen, an E-mobility provider, in cooperation with Technolusion, M2Power, TU Delft, Miton and Wetac, and is subsidised by the Dutch Ministry of Economic Affairs. The electric vehicle used in the project is the Tazzari Zero, an Italian lightweight battery electric city vehicle. The role of TU Delft was to investigate methods to estimate the state of health of the battery based on the measured driving data, so that lease companies can charge clients of according to their driving behaviour.

My role as a MSc. student of TU Delft was to approach the battery modelling with electrical circuits based on literature and experiments. The biggest hurdle as an electrical engineer was the understanding of lithium ion (Li-ion) batteries and the associated degradation. Battery modelling is a field where electrochemistry, electrical engineering and control engineering are intertwined. This thesis is written from an electrical engineer's point of view and a user's perspective. Nevertheless, to be able to understand the published results and interpret my own results, a feeling for the electrochemical processes in the cells has to be developed. This is a lengthy process of collecting and reading different literature sources. With this thesis I would like to save future electrical engineering researchers in battery modelling the time and effort in collecting and understanding Li-ion batteries, which is why I have conducted such an extensive literature review in this thesis. In chapter 3 the operation of Li-ion cells and possible degradation mechanisms are explained. Chapter 4 is an extensive literature review on capacity fading models and state of health determination. Chapter 5 explains various electrical circuit models and tries to connect circuit models used by electrochemical engineers with the circuit models used by electrical engineers.

First of all I would like to thank my family, my girlfriend and friends for their continuous support. I would also like to thank my supervisor Prof. Pavol Bauer for his guidance throughout my thesis. Many thanks go out to Dr. Erik Kelder and his Li-ion battery group for providing me with the test equipment, and in particular Corrado Locati for helping me with the experimental setup. I would also like to thank Maarten Dieleman and the rest of MisterGreen for their guidance during my internship at MisterGreen and their continuous support in this project. Additionally, I would like to thank the other project partners Technolusion, M2Power, Miton, Wetac, and Dr. Matteo Corno and Dr. Stephan van Dijk from TU Delft for their support. Finally, special thanks go out to Subhadeep Bhattacharya for thoroughly proofreading my thesis and my other colleagues at TU Delft for their fruitful discussions and support.

Long Lam
Delft, August 2011

Table of Contents

Abstract	ii
Preface	iii
Glossary	vii
List of abbreviations	viii
List of symbols.....	ix
1 Introduction.....	1
2 Problem definition and research goals	2
2.1 Research problem definition	2
2.2 Research goals and requirements	4
2.3 EV battery types.....	5
2.4 Battery definitions.....	6
2.4.1 State of health (SoH).....	6
2.4.2 State of charge (SoC)	6
2.4.3 Cell capacity	7
2.4.4 Depth of discharge (Δ DoD).....	7
2.4.5 Cycle	7
2.4.6 C-rate	8
2.4.7 Internal resistance	8
2.5 Thesis scope	8
2.6 Thesis outline.....	9
3 Degradation mechanisms of Li-ion cells.....	11
3.1 Operation of a Li-ion cell.....	11
3.2 Li-ion battery types	12
3.3 Normal degradation of Li-ion cells due to cycling	14
3.4 Accelerated degradation of Li-ion cells due to cycling	16
3.4.1 Temperature.....	17
3.4.2 C-rate	20
3.4.3 State of charge (SoC)	22
3.4.4 Depth of discharge (DoD).....	23
3.5 Degradation of Li-ion cells due to storage	24
4 Capacity fading model for state of health determination.....	26
4.1 Capacity fading models: a literature review	27
4.2 SoH models on capacity fading.....	30

4.2.1	Palmgren-Miner rule model.....	31
4.2.2	Damage accumulation model.....	31
4.2.3	Choice of SoH model.....	32
4.3	Capacity fading rate model.....	33
4.3.1	Calendar loss rate	33
4.3.2	Cycling loss rate.....	33
4.4	Modelling stress factors of capacity fading	35
4.4.1	Stress factor: temperature.....	35
4.4.2	Stress factor: ΔDoD	36
4.4.3	Stress factor: overcharge/SoC.....	38
4.4.4	Stress factor: C-rate	39
4.4.5	Modelling choice of stress factors.....	40
4.5	Chosen literature-based capacity fading model for SoH determination.....	41
4.5.1	Chosen capacity fading model.....	41
4.5.2	SoH determination with capacity fading.....	42
5	Practical circuit-based model including ageing effects.....	44
5.1	Lithium ion cell models including ageing effects: a literature review.....	44
5.1.1	Electrochemical and analytical models with ageing	45
5.1.2	Impedance-based models with ageing.....	46
5.1.3	Equivalent circuit-based models	46
5.1.4	Analysis literature review Li-ion cell models	48
5.2	A practical circuit-based model.....	48
5.2.1	Thevenin-based circuit models.....	48
5.2.2	Impedance-based circuit models	49
5.2.3	Runtime-based circuit models	50
5.2.4	Compatibility of electrical circuit-based models.....	50
5.2.5	Combined electrical circuit-based model for practical applications	52
5.3	Determination of the nonlinear circuit components	53
5.3.1	Energy balance circuit components.....	53
5.3.2	Voltage response circuit components	55
5.3.3	Chosen non-linear circuit component models.....	66
5.4	Chosen literature-based practical circuit model including ageing	67
6	Empirical development of an improved practical circuit-based model.....	70
6.1	Experimental setup	70
6.2	Test procedure	71
6.2.1	Proposed cycling current profile.....	72
6.2.2	Capacity and parameter test cycle.....	73
6.2.3	Test conditions	74
6.3	Measurement method	76

6.4	Measurement and modelling results.....	77
6.4.1	Capacity fading.....	78
6.4.2	Useable cell capacity.....	91
6.4.3	Open-circuit voltage	92
6.4.4	Internal cell impedance.....	95
6.4.5	Coulombic and energy efficiency	120
6.5	The improved practical circuit-based model including ageing effects	121
7	Lifetime optimisation of EV batteries – A case study	126
7.1	Upscaling to an EV battery pack.....	126
7.1.1	From small cylindrical to large prismatic cells	126
7.1.2	From battery cell to battery pack.....	127
7.2	SoH simulation of real-life EV batteries	127
7.2.1	EV cell Simulink model.....	128
7.2.2	SoH simulation with the New European Driving Cycle.....	130
7.2.3	SoH simulation with the United States Federal Test Procedure 75.....	135
7.2.4	SoH simulation with real driving data	137
7.3	Recommendations	139
8	Conclusion.....	140
8.1	Recommendations for EV battery cell life optimisation	142
8.2	Future work.....	143
References	144	
Appendices:	152	
Appendix A.1:	Overview of the Literature-based model	152
Appendix A.2:	Overview of the Proposed model	153
Appendix B:	Model parameters	154
Appendix C	A Practical Circuit-based Model for Li-ion battery cells in electric vehicle applications.....	156

Glossary

Battery management system	The control system behind the battery to ensure the battery stays within its specified operating region.
Calendar loss	Capacity fading as a result of cell storage.
Cycle life	The lifetime of a cell expressed in cycles as a function of the depth of discharge.
Cycling loss	Capacity fading as a result of cell operation.
Intercalation	A reversible chemical process of binding a molecule between other molecules. Deintercalation is the reverse process.
Overcharge/overdischarge	Charging/discharging beyond the maximum/minimum voltage of the cell according to the specifications by the manufacturer.
Overpotential	Voltage drop.
Polarisation resistance	The internal cell resistance caused by the electrochemical processes unable to accommodate the required electrochemical process rate for a given current.
Rate capability loss	The current dependent capacity fading at reference temperature caused by an increase in voltage drop over the internal cell impedance, so that the minimum cell voltage is reached at a higher state of charge.
Round trip efficiency	The ratio between the charge or energy discharged from the cell and the charge or energy charged in the cell.
Thermal runaway	Temperature rise causes chemical reactions, which induces more temperature rise and lead to a destructive result. A form of positive feedback with temperature.
True capacity fading	Capacity fading of the useable capacity at reference temperature.
Useable capacity	The theoretically possible amount of charge that can be discharged from a fully charged cell with an infinitely small current for a given minimum cell voltage, so that the voltage drop over the internal resistance becomes close to zero.

List of abbreviations

Ah	Ampere-hour
BEV	Battery electric vehicle
BMS	Battery management system
CCCV	Constant voltage constant current
EIS	Electrochemical Impedance Spectroscopy
EoD	End of discharge
EoL	End of life
EUDC	European Urban Driving Cycle
EV	Electric vehicle
FTP-75	Federal Test Procedure 75
HEV	Hybrid electric vehicle
LiFePO ₄	Lithium iron phosphate
Li-ion	Lithium ion
NEDC	New European Driving Cycle
OCV	Open-circuit voltage
PHEV	Plug-in hybrid electric vehicle
PM	Palmgren-Miner
SEI	Solid electrolyte interphase
SoC	State of charge
SoH	State of health
SPI	Solid permeable interphase
VTF	Vogel-Tamman-Fulcher
Wh	Watt hour
ΔDoD	(Incremental) Depth of discharge

List of symbols

ΔT	Temperature deviation from reference temperature T_{ref} (25°C)
Ah	Amp-hours processed (Ah)
C_{dl}	Double layer capacitance (F)
cf	Correction factor for dynamic profile
C_l	Long time transient capacitance (F), subscript d for discharging, c for charging
C_s	Short time transient capacitance (F), subscript d for discharging, c for charging
C_{use}/Q_{use}	Useable capacity (Ah)
E	Total events
E_a	Activation energy (Jmol ⁻¹)
i	An event
I	Instantaneous cell current (A)
L	Life parameter
n	Cycle number
N	Total number of cycles
Q_{cal}	Calendar loss (Ah)
R	Gas constant (J(molK) ⁻¹)
R_b	Bulk resistance (Ω)
R_{ct}	Charge transfer resistance (Ω)
R_l	Long time transient resistance (Ω), subscript d for discharging, c for charging
R_o	Ohmic resistance (Ω), subscript d for discharging, c for charging
R_s	Short time transient resistance (Ω), subscript d for discharging, c for charging
R_{sdis}	Self-discharge resistance (Ω)
R_{SEI}	Surface layer resistance (Ω)
R_{tot}	Total internal resistance (Ω), subscript d for discharging, c for charging
SoC_{avg}	Average state of charge
SoC_{dev}	State of charge deviation
t	time (s)
T	Temperature (K)
T_{env}	Environmental temperature (K)
t_{life}	Time until the end of life capacity is reached due to calendar losses (s)
T_{ref}	Reference temperature (K)
V_i	Terminal voltage minus ohmic voltage drop (V)
V_{min}	Minimum cut-off voltage (V)
V_o	Ohmic voltage drop (V)
V_{oc}	Open-circuit voltage (V)
V_{trans}	Total time dependent voltage drop over the transient impedance (V)
Z_{ref}	Total cell impedance at reference temperature (Ω)
Z_W	Warburg impedance (Ω)
ξ	Capacity faded (Ah)
σ	Capacity fading stress factor
φ	Capacity fading rate (Ah/unit)

1 Introduction

The most crucial component and the weakest link in the modern electrification of transportation is the energy storage component i.e. the battery. With the conversion of fossil fuel based vehicles to hybrid electric vehicles and electric vehicles (EVs), the heart of the vehicle has moved from the engine to the battery. This conversion wave is the strongest in the automotive industry, where rising oil prices and environmental concerns have caused an emersion of electric and hybrid electric cars [1]. However, the introduction of electric cars is not going smoothly due to range anxiety, a lacking charging infrastructure, long charging times and the high purchase price. Most importantly, it is unknown how electric cars and their battery behave in the long run and what their rest value will be. This also causes an unnecessary high lease price for electric cars.

Many different models have been developed to characterise the ageing and long term behaviour of batteries, but not all models are practically applicable for electric vehicles. The battery models can be divided into analytical, electrochemical and electrical circuit models or a combination of the model types. Analytical models do not give a good view of the electrochemical processes occurring in the cell. Electrochemical models require a large amount of computational power to solve the time-varying spatial partial differential equations and cannot be directly connected to the rest of the system. Combined analytical and electrochemical models also suffer from high complexity and poor system modelling compatibility. On the other hand, electrical circuit models can easily be connected to the rest of the electronic systems, but suffer from lower accuracy. A trade-off must therefore be made between complexity and accuracy to obtain the most optimal model.

In this thesis a practical circuit-based model for state of health (SoH) estimation of lithium ion (Li-ion) battery cells in electric vehicles is proposed. Due to their superiority in energy density, power density, low self-discharge and high cycle life, Li-ion batteries are applied in EVs. Based on real operating conditions, the different stress factors on the SoH of Li-ion cells are identified from testing numerous Li-ion cells of the type LiFePO₄ and an attempt is made to empirically quantify the stress factors. The SoH model is then expanded to a complete electrical circuit model describing the voltage behaviour of Li-ion cells under various real operating conditions.

The practical circuit-based model is developed from a perspective of an electrical engineer and user instead of from a perspective of a chemical engineer and manufacturer. Trade-offs and simplifications in the model are made based on practical considerations. The proposed model can be directly connected to the rest of the electronic system in an EV and offers EV system designers the choice of including various operating conditions in exchange for higher complexity. With the proposed model more insight is gained in the SoH development of Li-ion cells for different driving behaviours, and suggestions for battery lifetime optimisation can be made.

This thesis is organised as follows. In chapter 2 the research problem and goals are explained in more detail, and various ambiguous terms in battery modelling are discussed and defined. Chapter 3 explains the operation of Li-ion cells and possible degradation mechanisms affecting the SoH, focussing on capacity fading. Based on extensive literature review on capacity fading modelling, a literature-based SoH model is proposed in chapter 4. In chapter 5 the SoH model is expanded to a literature-based circuit model. However, the literature-based models have several shortcomings and inconsistencies. A practical circuit-based model with empirical equations will therefore be developed in chapter 6. Chapter 7 demonstrates a possible application of the developed model for battery lifetime optimisation and chapter 8 concludes this thesis.

2 Problem definition and research goals

The greatest limiting factor for the breakthrough of electric vehicles (EV), especially battery electric vehicles (BEV), as transportation is currently the battery of the vehicle. The battery makes a BEV more expensive than conventional vehicles, increasing the vehicle cost by 30 to 50 percent [2]. For this reason the BEV has been first introduced in the lease market to let the consumer familiarise themselves with BEVs. Currently BEVs use Li-ion batteries due to its many advantages. However, since BEVs with Li-ion batteries have not been actively on the market for a long time, it is unknown what the depreciation of the batteries will be. To minimize their financial risk BEVs are depreciated with the ‘worst case scenario’ by lease companies, making leasing an EV more expensive than necessary.

This thesis is part of a project to make leasing EVs cheaper and to gain knowledge in the degradation of EV batteries. If more knowledge is gained about batteries and their behaviour, then batteries do not have to be depreciated according to the ‘worst case scenario’. Leasing a BEV will become more affordable and many consumers will realise the advantages of electric driving. With a battery model the behaviour of the battery can be predicted and the rest value of the battery can be determined more accurately. To obtain practical battery model, more knowledge is required about the short and long term behaviour of batteries. In the project numerous BEVs of the same type are driving around and logging their battery data. With the data realistic situations can be simulated and the model can be validated. In this thesis the BEVs will be referred to as the EVs in the project.

First the research problems will be identified and defined. To tackle the research problems for the specified applications, the goals and requirements of the research will be given. As different battery types result in different models, a short overview of existing battery types will be given next and the question why lithium-ion (Li-ion) batteries are used in BEVs will be answered. Since in battery research many ambiguous terms exist, the terms used in this thesis will be defined. Then the scope of the thesis will be defined, as battery modelling is a very extensive field. This chapter will conclude with an outline of this thesis.

2.1 Research problem definition

In the field of battery modelling many different battery models exist for both the short and long term behaviour of battery cells. The short term behaviour of a cell consists of the voltage response, the useable capacity and state of charge determination; in other words how a cell behaves over one cycle. The long term behaviour is mainly described by capacity and power fading of a cell, i.e. the development of the capacity and internal cell impedance over the lifetime of a cell. The development of the cell efficiency is correlated to the capacity and power fading.

For determination of the rest value, only the long term behaviour of the cell seems of importance. However, the short term behaviour of a cell can be used to optimise the energy efficiency of the system and reduce heating of the cells; the long term behaviour of battery cells is greatly influenced by temperature. To model either the short or long term behaviour of battery cells many different types of models have been developed, each with its own advantages and disadvantages:

- **Electrochemical models:** electrochemical models are very accurate, but complex and require a good understanding of the electrochemical processes in the cell. Each electrochemical process is modelled with an own set of equations consisting of time variant spatial partial differential equations.
- **Mathematical, analytical and stochastic models:** these models can represent the behaviour of each battery cell accurately, but the models are often not applicable for other battery cells. Additionally, these models are abstract and do not give an insight of the electrochemical processes in the cell.
- **Impedance-based models:** Impedance-based models are a form of electrical models. The impedance elements in impedance-based models are determined from Electrochemical Impedance Spectroscopy (EIS) measurements. The models represent each electrochemical process in the cell by impedance elements in an electrical circuit. However, EIS measurements require additional high frequency equipment and impedance-based models can only model the voltage response of a cell.
- **Electrical circuit models:** in electrical circuit models the circuit components model the behaviour of the cell rather than the electrochemical processes in the cell. Electrical circuit models are easy to understand, as simplicity is offered in exchange for accuracy. Furthermore, most existing electrical circuit models are limited to modelling the voltage response and runtime of a cell.

Depending on the application and specifications, a choice between the models can be made. Electrochemical models are capable of modelling each influence on behaviour of a cell, but a complete model has rarely been constructed due to the high complexity. Moreover, from an electrochemical point of view different cell chemistries will result in different models; to the author's knowledge, for the Li-ion cell chemistries used in EV applications not all electrochemical processes are modelled yet.

Empirical and semi-empirical models are the alternative to electrochemical models. Since empirical and semi-empirical models are based on measurements of experiments, many factors concerning short and long term behaviour of battery cell are still unclear or not modelled. The voltage response has mainly been modelled for discharge. Furthermore, modelling of the voltage response under different temperatures has only been done for impedance-based models.

Cycling experiments are always performed with fully charged cell and often with constant current discharge and temperature. In real-life EV applications the battery cells do not operate at a constant temperature and are not always fully charged, especially if EVs are integrated in the grid. The EV will experience different depths of discharge (Δ DoDs) from different states of charge (SoCs). Moreover, the battery cells experience regenerative braking during operation. To model real-life situations, cells are cycled profiles representing real EV operations. Real-life profiles contain different C-rates for both charging and discharging, and it is simply assumed that different C-rates do not have a direct influence on the ageing of the cell [3][4].

The largest problem is, however, the lack in quantification and modelling of results. Especially cell ageing results are often presented by a simple model without quantification of the different stress factors. The published data is also often insufficient for other researchers to create a model. This makes it difficult to predict and optimise the battery life time by battery monitoring and control. Hence, a demand is present for a quantified model capable of modelling both the short and long term behaviour of EV battery cells.

2.2 Research goals and requirements

The desired result of the research is to find a way to determine and predict the state of health (SoH) of EVs, and especially BEVs, so a rest value of the battery can be determined from the SoH. However, several research steps need to be taken to reach the desired result. The research goal of this thesis is to take the first step towards the rest value determination, and is summarised by the title of this thesis:

'A practical circuit-based model for state of health estimation of Li-ion battery cells in electric vehicles.'

The title summarises several research goals. The emphasis of the goals lies on 'practical', as not every type of battery model is practical applicable in actual EV applications. The focus will therefore be on the Li-ion cell type lithium iron phosphate (LiFePO_4) cells, which is expected to be widely used in EVs due to advantages which will be explained in paragraph 3.2. Different Li-ion types have different stress factors, which influence the SoH of the cell. Consequently, stress factors which have a noticeable influence on the SoH will be identified and modelled.

Moreover, this thesis is written from the point of view of a battery user and electrical engineer. This means that the battery is seen as a part of a larger electrical and electronic system. An equivalent circuit-based model is then highly desirable; the terminals of the model can be directly connected to the rest of the system. In the system the resulting short and long term behaviour of the battery cells are of more interest rather than which electrochemical processes caused the behaviour. It is, however, undesirable to see the battery as a black box and decouple the model from the electrochemical processes. An attempt will therefore be made to couple the electrochemical processes to circuit elements and to explain the cell behaviour, so that an intuition for the processes in the battery is developed.

To ensure the applicability and practicality of the model several restrictions will be imposed on the model. In return the model will have more freedom in accuracy. The restrictions lead to the following requirements for the model:

- The influence of regenerative braking must be taken into account in the model.
- The battery cell will be modelled according to realistic conditions for EVs, and in particular BEVs.
- The model must be able to simulate the noticeable influences on the short and long term behaviour of the cell with the least complexity.
- The model must be comprehensible for electrical engineers with little background knowledge of the electrochemical processes in the cell.
- The model must have the capability to connect to the rest of an electrical or electronic system in simulations.
- It must be possible to integrate the model in EV applications to predict the short and long term behaviour of the cell without additional equipment.
- It must be possible to determine the parameters in the model from measurements in real-life EV applications.

Furthermore, an attempt will be made to connect the equivalent circuit components and SoH development to electrochemical processes. With the requirements above in mind, a practical equivalent-circuit based model will be developed which is capable of predicting the SoH development of a LiFePO_4 cell for a given driving profile and conditions.

2.3 EV battery types

From the beginning of the development of EVs many different battery types were used. Figure 2.1 gives the Ragone plot for possible battery types in EVs. The first EVs developed since the revival of EVs in the nineties used lead-acid batteries [5]. The range was around 100 kilometres, but since lead-acid batteries have a low energy density, the weight of the vehicle was large. To improve the weight of the batteries, other battery chemistries were used in the years after.

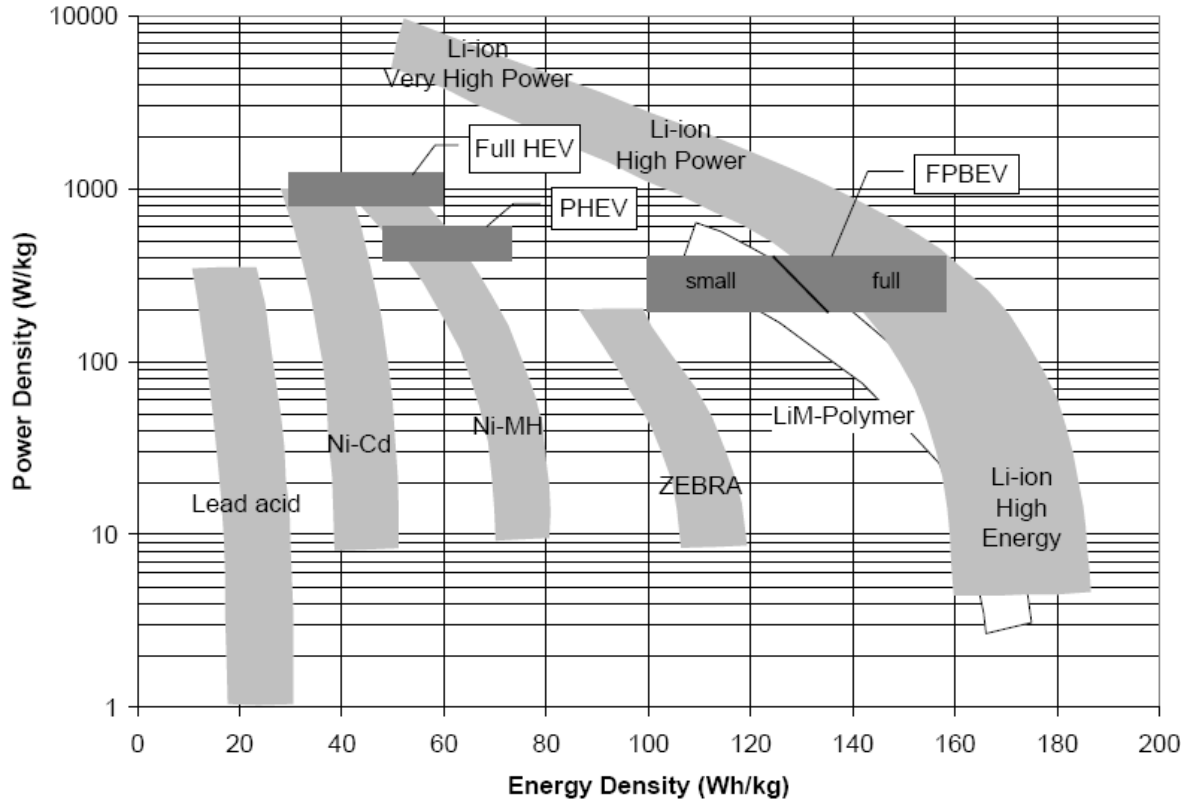


Figure 2.1: The Ragone plot of various cell types capable meeting the requirements for EV applications [6]. Possible EV applications have been indicated in the plot.

Skipping the environmental harmful nickel cadmium (NiCd) batteries, EVs started to use nickel metal hydrate (NiMH). NiMH batteries did not only have a higher power and energy density as shown in figure 2.1, but also improved in cycle life and robustness. Today NiMH batteries are still used in hybrid electric vehicles (HEV) and plug-in hybrid electric vehicles (PHEV) for their low cost per Watt. NiMH batteries have, however, a high self-discharge, limited SoC operation range and low energy density, making them unsuitable for BEVs.

ZEBRA or molten salt batteries are also used in EVs. These batteries have the advantages of low cost and high safety. Nevertheless, ZEBRA batteries are not popular in EV manufacturers, because of their high operating temperature ($270\text{--}350^{\circ}\text{C}$) and low power density [6]. The batteries have to be kept at a high temperature, since it will take one to two days to reheat the batteries to operating temperature. To prevent cooling down, ZEBRA batteries use their own energy to maintain the temperature or continuously consume energy while connected to the grid, making them very energy inefficient.

Most EVs produced today use Li-ion batteries; they are superior in energy density, power density, low self-discharge and high cycle life. The disadvantages of Li-ion batteries are the high cost and safety issues. There are, however, different types of Li-ion batteries, each with their

2 Problem definition and research goals

own advantages and disadvantages; the Li-ion type is chosen based on the requirements of the application. The different Li-ion battery types will be discussed in paragraph 3.2. Finally several characteristics of the different battery types is summarised in table 2.1. Li-ion batteries include every type of Li-ion cell, so the characteristics are given by a range including each type.

	Lead Acid	NiMH	ZEBRA	Li-ion
Nominal cell voltage	2V	1.2V	2.58V	2.5V/3.3V/3.6-3.7V
Specific energy	30-45 Wh/kg	30-80 Wh/kg	90-100 Wh/kg	90-220 Wh/kg
Energy density	60-75 Wh/L	140-300 Wh/L	160 Wh/L	280-400 Wh/L
Specific power	180 W/kg	250-1000 W/kg	150 W/kg	600-3400 W/kg
Cycle life	500-800	500-1000	1000	1000-8000
Self-discharge	2-4%/month	20-30%/month	0%/month	2-5%/month
Temperature range	-20-60°C	-20-60°C	270-350°C	-20-60°C
Relative costs	Low	Moderate	Low	High

Table 2.1: The characteristics of battery types used in EVs [6][7][8][9]. Different types of Li-ion cells are included in **Li-ion**.

2.4 Battery definitions

There are many ambiguous terms to describe the state and properties of battery cells. This can lead to misinterpretation of the results or comparing results with different properties. In this paragraph the terms used in this thesis will be defined.

2.4.1 State of health (SoH)

The state of health (SoH) of a battery is a subjective term and mainly depends on the application. The SoH indicates the state of the battery between the beginning of life (BoL) and end of life (EoL) in percentages. The EoL of a battery is reached when the battery cannot perform according to the minimum requirements. For EV applications this is defined by the battery manufacturers when one of the following conditions has been fulfilled [10]:

- The capacity of a battery under reference conditions has dropped to 80% compared to the rated capacity under reference conditions. This is known as capacity fading.
- The maximum power delivered by the battery under reference conditions has dropped to 80% compared to the rated power under reference conditions. This is known as power fading.

For BEVs generally the capacity fading criteria is taken as the SoH indicator; batteries in BEVs are normally oversized to have sufficient driving range, so the maximum power drawn from the BEV is much lower than the maximum power rating of the battery. This is also the definition used in this thesis. It is, however, not defined whether the amount of capacity faded or remaining energy/charge throughput (driving kilometres) is used as the SoH parameter. This will be explained in more detail in paragraph 4.2.

2.4.2 State of charge (SoC)

The state of charge (SoC) indicates the amount of charge in Amp-hours left in the battery. The SoC can be divided into two types: engineering-SoC (e-SoC) and thermodynamic-SoC (t-SoC) [11]. The e-SoC is the SoC apparent to the user of the battery and is rate dependent; it is the state of the capacity at a certain discharge rate, so different discharge rates will result in a different e-SoC at the same amount of charge in the battery. The t-SoC is the SoC of a battery

defined by the thermodynamic properties in the cell and can be determined by the open-circuit voltage of the battery; it is the state of the useable capacity in the cell. In this thesis the SoC is the t-SoC unless stated otherwise. Every model element will therefore be dependent on the t-SoC.

2.4.3 Cell capacity

In this thesis several different cell capacities are used. The apparent capacity of the cell is the rate dependent capacity experienced by the user. This capacity is strongly dependent on the internal impedance of the cell and varies extensively depending on the operating conditions. On the other hand, the useable capacity is the amount of charge the battery contains and is not rate dependent. It is the theoretically possible amount of charge that can be discharged from a fully charged cell with an infinitely small current for a given minimum cell voltage, so that the voltage drop over the internal resistance becomes close to zero. Both definitions of capacity are dependent on the temperature. Since the internal resistance voltage drop causes the battery to reach the minimum voltage before 0% SoC, it will not be possible to use the complete useable capacity.

To determine the capacity fading, the terms true capacity and 1C capacity are introduced. The true capacity is the useable capacity under reference temperature and is used as a measure for the capacity fading determination. The 1C capacity is the determined with a C-rate of 1C under reference conditions and is generally used to measure the capacity fading [12]. For modelling purposes the true capacity will determine the capacity fading as the 1C capacity is dependent on the cell impedance. For the same modelling purposes the useable capacity will be considered the cell capacity unless stated otherwise.

2.4.4 Depth of discharge (Δ DoD)

The depth of discharge (DoD) of the battery is generally defined as the amount of charge removed from a fully charged cell in percentages [12]. Based on the DoD, the number of possible cycles before the EoL of a cell is estimated. However, in real-life EV applications the battery is not always fully charged, and in possible future applications as storage in the grid even rarely fully charged. According to the standing definition, discharging from 90% to 40% SoC will have an equal influence on the cycle life as discharging from 50% to 40% SoC. This would mean that the possible cycle life estimate for the battery cell would be overly pessimistic and incorrect.

Therefore, the term incremental depth of discharge (Δ DoD) is introduced. The Δ DoD is the change in SoC for a certain period or cycle, so a change from 50% to 40% SoC would result in a Δ DoD of 10%. For convenience Δ DoD will be named the depth of discharge in the rest of the thesis.

2.4.5 Cycle

Before batteries were used for EV applications, a cycle could be defined as a period of discharge followed by a full recharge. EVs, however, experience regenerative braking during operation, which required a change in cycle definition. Some defined a cycle as one event of discharge followed by recharge [13], which leads to an overly pessimistic estimate of the SoH with the standing DoD definition. Others define a cycle as a period of discharge with regenerative braking followed by a full recharge [14] or an amount of energy discharged with regenerative braking followed by the equal amount recharged [12].

Depending on the cycle definition, the operating conditions during a cycle can vary extensively during. Furthermore, a fixed definition of a cycle prevents flexibility of the SoH prediction

2 Problem definition and research goals

system in regards of sampling time. A better alternative to measure the usage of a battery is the charge or energy processed in the battery. The ambiguous definition of a cycle is hereby also avoided. In this thesis the charge processed in the battery is chosen to determine the battery usage. Cycling will, however, still be used as a verb to describe continuous operation of the battery.

2.4.6 C-rate

The C-rate is a measure for the current of a battery cell and is scaled to the nominal capacity of a cell stated by the manufacturer at reference conditions. The current level that a battery cell can discharge at depends on the capacity of the battery. A current of 1C means that the battery cell is ideally charged or discharged in one hour, C/2 in two hours and 2C in half an hour. So a current of 1C for a cell with nominal capacity of 160Ah is 160A and 1C for a 10Ah cell is 10A.

2.4.7 Internal resistance

The internal resistance of a battery cell depends on many factors and cannot be considered as a constant, even though manufacturers tend to give a single value. The internal resistance is dependent on temperature, SoC and C-rate. The internal resistance is sometimes considered as the ohmic resistance of the cell, which is the direct voltage change after application of a current step on a cell in equilibrium [15]. Another definition for the internal resistance is the sum of the ohmic, activation and diffusion polarisation resistances [16], which is the largest possible voltage drop in the cell. Nevertheless, the complete voltage drop will result in power dissipation in the form of heat.

Depending on the measurement method, different values for the internal resistance can be found [17]. This is caused by the time constants associated with the activation and diffusion polarisation resistances; whether the battery electrodes are in equilibrium or not is also important in determining the value of the internal resistance. The internal resistance of a battery cell is used to model the voltage drop over the cell and the power dissipation associated with the voltage drop with the well known equation $I_i^2 R_i$ where R_i is the internal resistance and I_i the current through the internal resistance. In this work the internal resistance will be the sum of all resistive components in the model, as the battery cell will mostly not be in equilibrium. The power dissipation will, however, not be modelled with the internal resistance, since the activation and diffusion polarisation voltage drop are variant with a certain time constant. The power dissipation will be a summation of the individual power dissipation in each of the resistances.

2.5 Thesis scope

Battery modelling is a very extensive field with many research topics, so a scope must be defined to limit the topics in this thesis. In this thesis a practical circuit-based model will be developed focussing on single Li-ion cells. LiFePO₄ is chosen as the Li-ion chemistry in this thesis; the results will only be verified for LiFePO₄ cells, although other Li-ion chemistries may have similar results. The model will be based on empirical equations obtained from measurements, so it will not represent the exact electrochemical processes in the cell. An attempt will, however, be made to link the circuit components in the model the electrochemical processes for illustrative purposes.

In the SoH modelling only capacity fading losses as a result of cycling are tested. The calendar losses, capacity fading when the cell is not in use, are not taken into account. With the SoH

modelling it is also assumed that the battery management system (BMS) will keep the cell voltage within the specifications. Any form of abuse of the cells is not taken into account.

In this thesis the determination of the SoC apparent to the user i.e. the e-SoC, and thermal modelling of a cell are not modelled. The determination of the e-SoC is a subject on its own, as it depends on many different operating conditions. Many different methods have been developed to determine the e-SoC for the user [18]. Thermal modelling of a cell is also a very extensive subject, as the temperature in cells is not uniform and different cell constructions require different thermal models.

EVs do not have a single cell as their battery pack, but the battery pack contains multiple cells in series or parallel. Modelling of multiple cell configurations introduces additional complications such as cell imbalance, cell connections, cell voltage control and battery pack heat flow modelling.

The model will be constructed based on real-life operating conditions and practical considerations for BEVs. The C-rates of the cells will therefore be much lower than the maximum rated C-rate, but also lower than C-rates found in HEV and PHEVs. Nevertheless, the model will be valid for all types of EVs with LiFePO₄ cells operating within the cell specifications. Therefore no differentiation between the different EVs is made in the rest of the thesis. Excessively high temperatures will also not be tested, as it is assumed that the BEVs will have cooling systems to prevent the temperature of the battery pack to rise too high.

2.6 Thesis outline

Several steps have to be taken to obtain a practical circuit-based model for SoH estimation for Li-ion cells in EVs. The first part of the thesis is based on models found in literature, whereas the second part describes the experimental results and the similarities with literature. A literature review will be done in the beginning of the two modelling chapters, as the literature review is different for both modelling chapters.

In chapter 3 an overview of the possible electrochemical degradation processes in the cell is given. First the operation of a Li-ion cell is explained, followed by an overview of different types of Li-ion cells and why LiFePO₄ cells are chosen in this thesis. Then the normal degradation mechanisms in Li-ion cells are described. The chapter is concluded with a description of possible stress factors and their associated degradation processes that accelerate ageing of the cell.

Chapter 4 is focused on the SoH determination of a cell. The EoL of a cell is determined by capacity fading, but different variables can be used to define the SoH. An overview of existing capacity fading models will be given first in the form of a literature review. Then two different SoH models will be explained. Several equations for capacity fading rates of Li-ion cells were found in literature, but all for different Li-ion chemistries. This was the same case for capacity fading stress factors. From the different equations a literature-based capacity fading model was constructed and the variables for the SoH determination chosen.

In chapter 5 the capacity fading is incorporated into a complete cell model capable of modelling the short and long term behaviour. First a literature review on all types of different Li-ion cell models including ageing effects is done. An attempt is then made to connect the electrical models to the electrochemical processes and construct a practical equivalent circuit-based model. Each circuit component in the equivalent circuit-based model is non-linear and dependent on many

2 Problem definition and research goals

factors. An overview of different models for each non-linear circuit component with the different factors is given and a literature-based equivalent circuit model including ageing effects is constructed.

The experimental results are given in chapter 6. First the experimental setup and test procedure for the tests with LiFePO₄ cells is described, followed by an explanation of the measurement method used to obtain the data for equivalent circuit-based model. Then in the most important paragraph of this thesis the measurement results are presented and a model based on empirical equations is created. The model is compared to the literature-based model and final conclusions are drawn in regards of Li-ion cell modelling.

In chapter 7 an application of the proposed model is demonstrated and a case study on the battery pack in BEVs under different operating conditions is conducted based on standard and real-life driving profiles. The case study is based on the model developed in chapter 6 and assumptions in regards of upscaling the cell model to a pack model are made. Finally advice about the battery usage for an optimal lifetime of the battery is given.

This thesis is concluded in chapter 8. The findings in respect to battery cell modelling and SoH determination are summarised and recommendations on optimising the battery lifetime are reviewed. Finally future works on battery modelling is suggested.

3 Degradation mechanisms of Li-ion cells

With increasing cycling or storage time, the maximum capacity and power of the lithium ion (Li-ion) cells will slowly decrease to the point at which the low capacity or power is not acceptable anymore. The state-of-health (SoH) of the battery cell reaches 0%. A Li-ion cell operating within specifications will, however, not undergo sudden death, but gradually experience performance degradation. This degradation does not only occur due to continuous use of the battery cell, but also during storage of the battery. The performance degradation during cycling occurs, however, much faster than storage under the same conditions.

To be able to understand the degradation of a Li-ion cell, first the operation of a Li-ion cell is explained. Then an overview and comparison of Li-ion cell types that are suitable for electric vehicles (EV) are given. One of the Li-ion cell types will be chosen as the focus of this thesis. Finally the normal and possible accelerated degradation mechanisms will be described for cycling and storage. As mentioned in the research goals the main focus of performance degradation lies in capacity fading. Therefore, the degradation mechanisms will be described from the point of view of capacity fading, although power fading will be briefly mentioned.

3.1 Operation of a Li-ion cell

Li-ion battery cell is a collective term for battery cells that utilise lithium ions to store and provide energy. A Li-ion battery cell consists of two electrodes, cathode and anode, with a separator in between, and current collectors on each side of the electrodes. In the case of a liquid electrolyte, the electrodes and the separator are soaked in the electrolyte as shown in figure 3.1. The copper current collector on the negative electrode and the aluminium current collector on the positive electrode side connect the Li-ion cell to an external circuit.

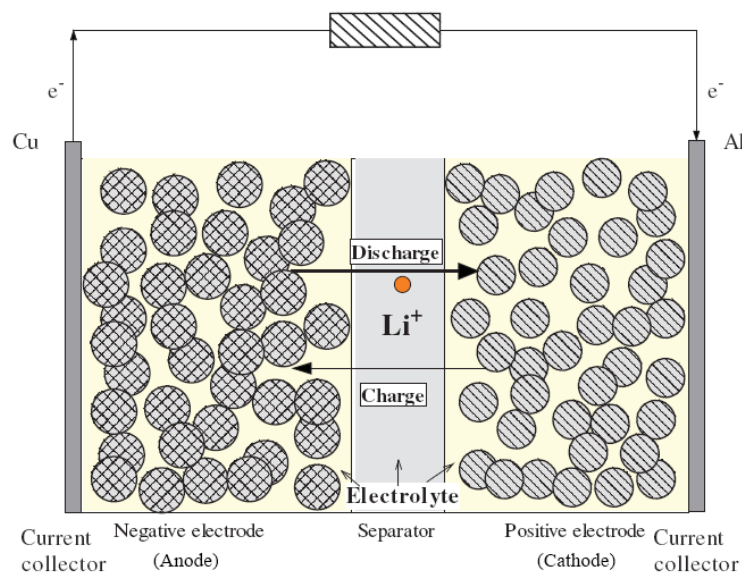


Figure 3.1: A schematic representation of a Li-ion battery cell [19].

The cathode is made of a composite material and defines the name of the Li-ion battery cell. The electrolyte can be liquid, polymer or solid. In case of a polymer or solid electrolyte, the electrolyte will act as a separator as well. The separator is porous to enable the transport of lithium ions. It prevents the cell from short-circuiting and protects the cell from thermal runaway [20]. The anode is usually made out of graphite or a metal oxide.

During discharge the lithium ions diffuse from the anode to the cathode through the electrolyte. The lithium ions will intercalate into the cathode, causing the cathode to become more positive. Due to the potential difference between the cathode and anode, an electric current will flow through the external circuit, supplying power to the load. During charging the opposite effect occurs. The current will cause the lithium ions to deintercalate from cathode and diffuse to the anode. At the anode intercalation of the lithium ions occur, charging the battery. In theory this could go on infinitely. Unfortunately, due to degradation of the cell material and other chemical reactions in the cell, the cell capacity and power capability degrade as the cell is used more often or ages.

3.2 Li-ion battery types

Nowadays there are many Li-ion battery types suitable for EV applications. Each type of Li-ion battery has its own advantages and disadvantages. Different types of Li-ion batteries are used in EVs that are currently sold on the market, and new Li-ion batteries are continuously being developed; there is no superior Li-ion battery type yet. Li-ion types can be compared in many dimensions and the choice of Li-ion type is mainly based on the criteria of the EV application and preference of the manufacturer. In figure 3.2 a comparison is made between the most important EV suitable Li-ion types. The Li-ion types are compared in specific energy, specific power, safety, performance, life span and costs.

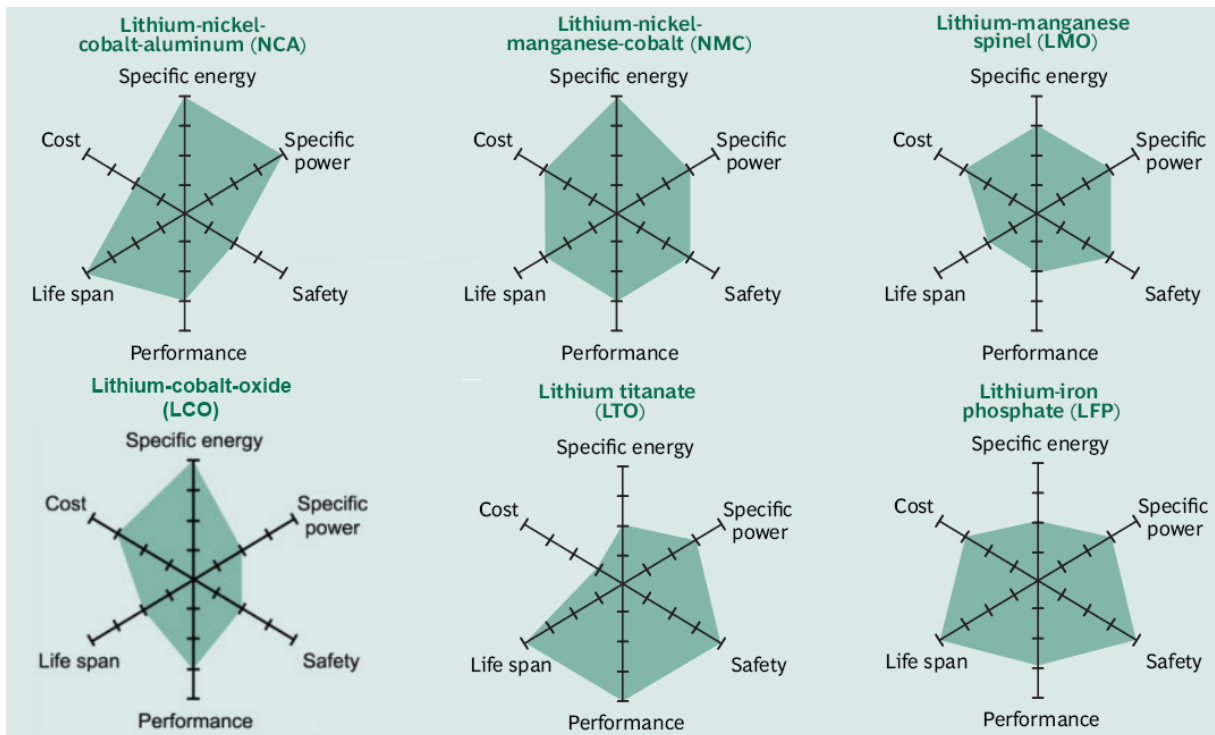


Figure 3.2: A comparison of various EV suitable Li-ion types in the most important criteria. The farther the coloured shape extends along a given axis, the better the performance in that area is [21][22]. So the farther the shape extension in the cost area, the lower the costs.

Performance in figure 3.2 is referring to the peak power and capacity at low temperatures, SoC measurement and thermal management. The different Li-ion types are all referring to a different cathode material except for LTO, which is a different anode material. Figure 3.2 shows that each type has its advantages and disadvantages, and a trade-off must be made between the properties of the Li-ion types.

3 Degradation mechanisms of Li-ion cells

The most common Li-ion type in small consumer electronics is lithium-cobalt-oxide ($\text{LiCoO}_2/\text{LCO}$). This type is often found in laptop and cell phones due to its high specific energy. Because of safety issues, low specific power and life span this type is not preferred in EVs. Nonetheless, Tesla Motors uses laptop sized LCO cells in their BEVs combined with a liquid cooling system [23]. The Li-ion types lithium-nickel-cobalt-aluminium-oxide ($\text{LiNiCoAlO}_2/\text{NCA}$) and lithium-nickel-manganese-cobalt-oxide ($\text{LiNiMnCoO}_2/\text{NMC}$) have a specific energy close to LCO; for the same cell weight these Li-ion types have a higher capacity than the other types and thus higher driving range. Nevertheless, these Li-ion types can experience thermal runaway as shown in figure 3.3, which can lead to unacceptable dangerous situations.

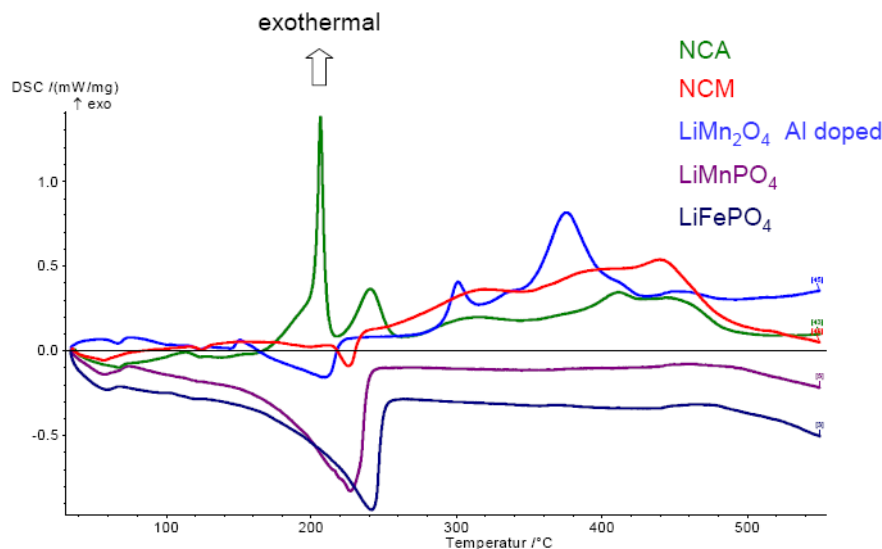


Figure 3.3: The results of a differential scanning calorimetry (DSC) measurement done on various Li-ion cathode materials in a charged state [24].

Figure 3.3 shows that in NCA and NMC cells exothermic reactions take place at higher temperatures, which can lead to thermal runaway of the cell; high temperatures cause chemical reactions which raise the temperature on their turn. Lithium-iron-phosphate ($\text{LiFePO}_4/\text{LFP}$) will not experience thermal runaway, because endothermic reactions take place in the cathode. Furthermore, LiFePO_4 cells have almost no fire hazards, since no oxygen is released at high temperatures [24].

In terms of costs LiFePO_4 and lithium-manganese-oxide ($\text{LiMn}_2\text{O}_4/\text{LMO}$) cells are the most beneficial, since no nickel or cobalt is used in the cells. This comes at the cost of lower specific energy. LiFePO_4 cells have the lowest costs per Ah [24] and kW [25], good life span, good power capabilities and are extremely safe. The disadvantages of LiFePO_4 cells are, however, the low specific energy and poor performance at low temperatures.

LMO cells are safer than NCA and NMC cells, but still suffer from minor safety issues and low life span due to low active material stability, which is why a manufacturer combined the LMO cathode with a lithium-titanium-oxide ($\text{Li}_4\text{Ti}_5\text{O}_{12}/\text{LTO}$) anode. LTO anodes have an extremely high cycle life and no solid electrolyte interphase (SEI) layer is formed on the anode [24]. Furthermore, LTO anodes have a high ionic conductivity and do not suffer from lithium plating, resulting in high C-rate capabilities, even at low temperatures. LMO/LTO cells also have an improved safety due to the stability of LTO. The disadvantages are, however, a severe increase in costs, low nominal voltage of 2.5V and decrease in specific energy.

Li-ion polymer (LiPo) cells

Just like the cathode or anode material in cells, the electrolyte in the cell can also be made of a different material. By using polymers as an electrolyte instead of liquid salts, LiPo cells are created. LiPo cells with a solid polymer have poor conductivity at room temperature and can only operate at high temperatures. For that reason nowadays LiPo cells with a gelled polymer are used; liquid electrolyte is infused into the polymer and becomes a gel [26]. LiPo cells offer a higher flexibility in design, higher electrolyte stability and higher energy density, since no external metal container is necessary. LiPo cells are however more expensive and can experience swelling without a metal container. In EV applications gelled polymer electrolytes are used with LMO cathodes by several large EV manufacturers [27].

Despite the current popularity for LMO polymer cells, the author's expectation is that LiFePO₄ cells will be used in most BEVs in the short term future. One of the largest hurdles for BEVs is currently the high costs of BEVs. LiFePO₄ cells are the cheapest in terms of unit power and unit capacity. A greater life span will contribute to the reduction of costs, since EV manufacturers can oversize the battery pack less to be able to guarantee the driving range for a given period.

Another very important issue is the safety of the battery pack, since possible thermal runaway and fire hazards are unacceptable. LiFePO₄ cells can guarantee this safety, since no oxygen will be released from the cells and endothermic reactions take place in the LiFePO₄ cathodes.

The problem with bad performance at low temperature can be solved with heating of the battery pack. The low specific energy is a problem if BEVs are used for long distance trips, but the expectation is that BEVs will initially be a city vehicle. Field studies have shown that BEVs have more than enough driving range [28][29]. With a sufficient charging infrastructure the low specific energy of LiFePO₄ will not be a great problem. It is therefore concluded that LiFePO₄ cells will be used in most BEVs in the near future. Due to its high cycle life and low price, other EV types are also expected to use LiFePO₄ batteries in the near future.

3.3 Normal degradation of Li-ion cells due to cycling

The main mechanisms for capacity fading during normal use are the loss of lithium ions and active material. This can be described by splitting the capacity fading with cycling in a Li-ion cell into four stages, which gives a general shape as shown in figure 3.4.

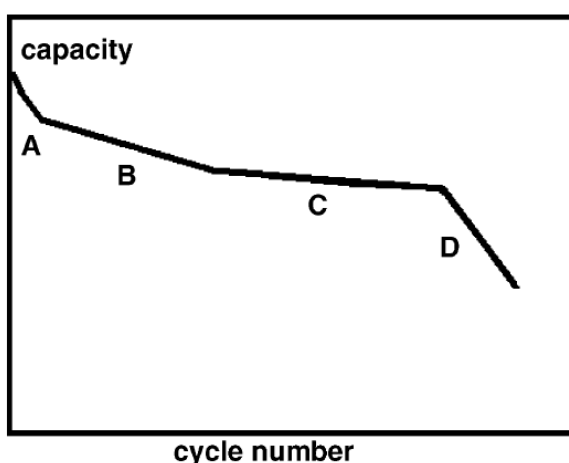


Figure 3.4: The general trend of capacity fading of a Li-ion cell vs. cycle number [30].

3 Degradation mechanisms of Li-ion cells

The initial capacity loss in region A is high, but does not continue many cycles as can often be seen from manufacturer data. The end of life (EoL) of a Li-ion cell, 80% of its nominal capacity, occurs in region C. So the operating region for a Li-ion cell during its lifetime is mainly region B and C and the capacity fading can be approximated by a linear function [30]. Nevertheless, the four stages of capacity fading in Li-ion cells will be explained.

Stage 1: The fast decrease of capacity in the first stage can be explained by the loss of lithium ions to the film formation. On the interphase of the anode with the electrolyte of the separator a Solid Electrolyte Interphase (SEI) film will form as a side reaction. The side reaction rate will gradually decay as the cell is cycled more, because the gradually growing SEI film on the anode will partially impede further occurrences of SEI film forming [31]. A schematic representation of a Li-ion cell with SEI layer is given in figure 3.5.

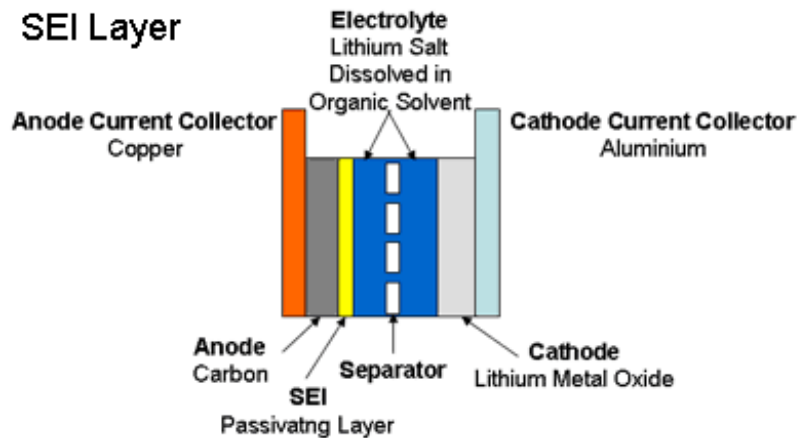


Figure 3.5: A schematic representation of a Li-ion cell with SEI film layer [32].

It has been reported in [14] that in the first stage the capacity fading rate for lower C-rates is more severe than higher C-rates. This is counterintuitive, because higher currents will stress the battery more. This can be explained if the excess lithium ions in the cell are seen as a 'reservoir' [14]. Cells discharged at a lower C-rate have a higher capacity, so more lithium ions are intercalated and more 'reserved' lithium ions are used in the SEI film forming. Higher C-rates induce a higher voltage drop over the internal resistance of the cell. The cut-off voltage is reached at a higher state of charge (SoC) than at lower C-rates, so the capacity is lower and less 'reserved' are used. In region B the 'reservoir' is depleted and the loss of lithium ions will be the similar for all C-rates.

Stage two: In stage two the limiting electrode is the anode [31]. Due to the SEI film layer formed on the anode, less active material is available and less lithium ions are intercalated into the anode during charging. As a result the loss rate of lithium ions will be slower, and the SEI layer protects the anode from reduction reactions with the electrolyte. During continuous intercalation and deintercalation the SEI layer cracks and more active material will be exposed. This will cause more side reactions and the SEI layer will continue to grow, leading to a less porous SEI layer and loss of lithium ions. The consumption of lithium ions results in a non-fully intercalated cathode.

Stage three: In the third stage the degradation rate of the active cathode material will be higher than the loss of lithium ions. On the cathode/electrolyte interphase layer similar to the SEI layer is formed, which is named the Solid Permeable Interphase (SPI) [33]. This layer will also grow

due to cycling and limit the active cathode material. Due to fatigue the cathode will be deformed as well, which causes happens at a faster rate than the loss of lithium ions [31]. The anode is however still the limiting electrode in this stage, as there is still more active cathode material available than lithium ions.

Stage four: Due to the high degradation rate of the cathode, in the fourth stage the cathode becomes the limited electrode. Less active cathode material is available than the amount of 'cycleable' lithium ions [31]. Not all the lithium ions that were intercalated into the anode during charging can be intercalated into the cathode during discharge. More and more lithium ions are stuck inside the anode. The cathode will be fully intercalated during discharge now, which raises the active cathode material loss rate. These added effects cause an accelerated capacity fading and the capacity will rapidly decrease.

The severity of all stages is not the same for different types of Li-ion cells. The most important capacity fading mechanism for LiFePO₄ cells is the loss of lithium ions by the lithium ion consuming SEI film later formation, which also results in a loss of active anode material [14]. Loss of cathode material happens at a lower rate for LiFePO₄ cells, since neither cycling nor temperature change enhances the formation of the SPI layer [33]. This causes LiFePO₄ cells to have a much higher cycling life compared to other chemistries.

Power fading is coupled to capacity fading. The growth of the SEI layer results in the internal impedance rise of the battery cell and the deformation of the electrodes in a lower conductivity. As a result the power fading occurs due to the loss of active material.

From the four stages it is clear that capacity fading primarily occurs on the electrode/electrolyte interphase under influence of intercalation and deintercalation of lithium ions. Under ideal conditions these are the only mechanisms that degrade a Li-ion cell. Conditions are however almost never ideal in practice. Non ideal conditions introduce other degradation mechanisms which will accelerate the capacity fading and cause additional cell life decay.

3.4 Accelerated degradation of Li-ion cells due to cycling

In real-life applications Li-ion cells experience accelerated degradation next to the normal degradation mechanisms. Nonideal temperatures, large C-rates, high SoC and deep DoDs will have a negative impact on the cell capacity. Some degradation factors result in a temporary loss of capacity, which will be restored again when ideal conditions are reached. Other factors will reduce the capacity permanently or even damage the cell.

The effects of the nonideal conditions of temperature, C-rate, SoC and DoD will be described respectively. A distinction will be made between temporary and permanent effects, and only the permanent effects are considered to be capacity fading and have an impact on the cell life.

The severity of the accelerated degradation mechanisms is not equal for all types of Li-ion cells. For LiFePO₄ cells low temperature strongly affects the performance and capacity of the cell [34], and used to have poor C-rate performance. However, the C-rate performance has been improved by changing the manufacturing process [35][36], using nanostructured material [37] or coating the cathode with carbon [38][39]. Furthermore, it has been reported in [40] that the DoD has no influence on the capacity fading, but the charge or energy processed is the determining factor.

3 Degradation mechanisms of Li-ion cells

3.4.1 Temperature

Temperature has a very strong influence on the capacity of a Li-ion cell. Li-ion cells have an optimal temperature operating range just like any other battery type. Outside this range the battery cell experiences severe loss of capacity, which is partly temporary and partly permanent.

Manufacturers usually specify a temperature operating range in which the operation of the cell is guaranteed. However, this does not mean that the capacity of the cell is guaranteed, and even within this specified range the battery can experience accelerated degradation. So the temperature range for optimum cycle life is even narrower than the range in the datasheet. In figure 3.6 an example of the temperature range for optimal cycle life is given. From figure 3.6 it can be seen that the decay of cycle life is different for high and low temperatures, as different degradation mechanisms deteriorate the battery.

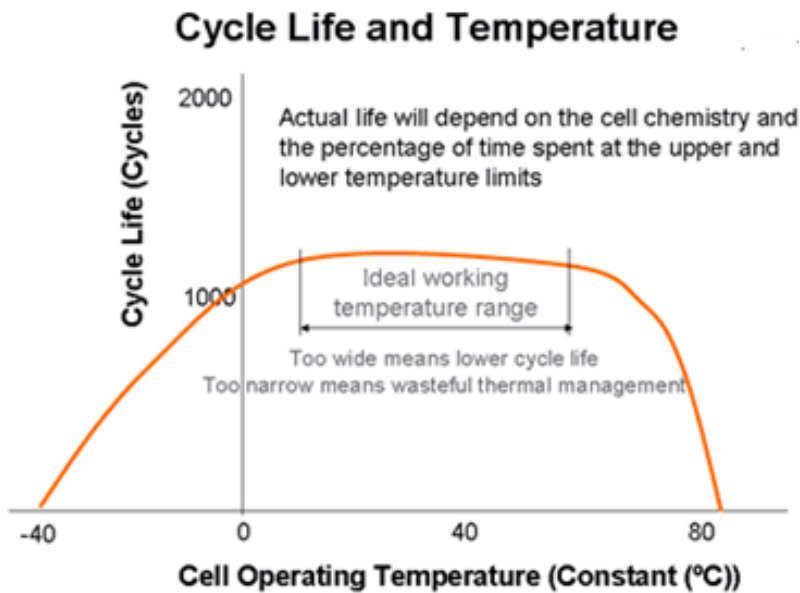


Figure 3.6: An example of a battery cell's temperature range for optimal cycle life [41].

3.4.1.1 High temperature

High temperatures will initially increase the power and discharge capacity of Li-ion cells. The activation energy for the chemical reaction will be lowered and more intercalation and deintercalation can take place in the cell, resulting in a higher cell voltage. Due to the higher temperatures lithium ions can diffuse faster, which means a higher current can flow. These two effects result in a higher power capability. Since more energy is stored in the cell due to more intercalation, the cell can also discharge deeper and deliver more energy.

The increase of temperature may seem to have a positive effect, but in the long term the cell is severely damaged. In figure 3.7 an example of capacity fading at different temperatures is given. It can be clearly seen that increasing temperatures result in higher capacity fading. This is not the result of a single degradation mechanism, but an addition of several mechanisms.

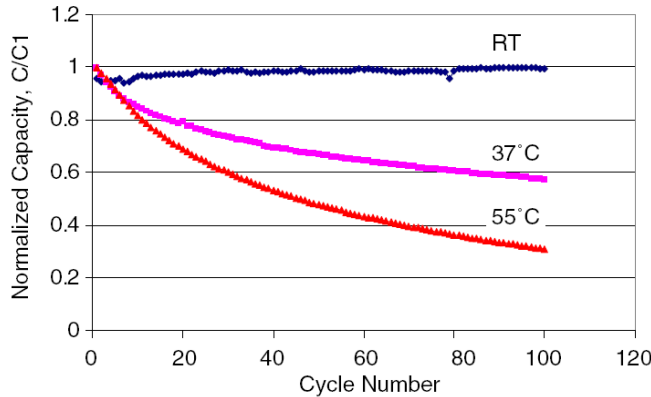


Figure 3.7: The accelerated capacity fading due to high temperatures [42].

Due to high temperatures the SEI layer will slowly deteriorate and starts to break down or dissolve into the electrolyte [43]. The active material of the anode will be partly exposed to the electrolyte again, causing the side reactions. The damaged SEI layer will be restored due to the side reactions or a precipitation of the dissolved SEI particles will take place. In the restored SEI layer some metastable organic SEI components are converted into stable inorganic molecules due to higher temperatures, which are more stable and less porous [43]. Also parts of the cathode can dissolve into the electrolyte and incorporated into the SEI layer. As a result the intercalation at the anode will be more difficult and the ionic conductivity will be lowered. The same degradation mechanism happens at the cathode side with the SPI layer. The process for the anode is visualized in figure 3.8.

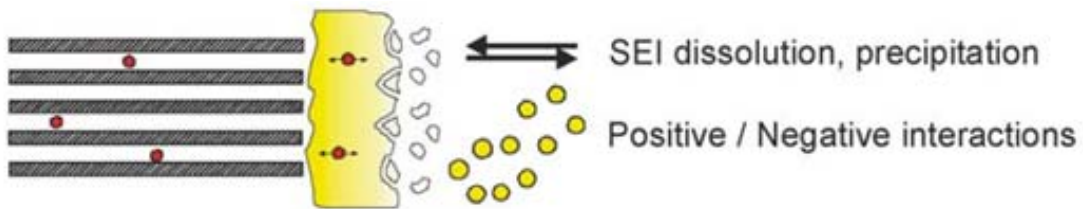


Figure 3.8: The break down and dissolution of SEI layer components and restoration of the SEI layer due to precipitation and new side reactions [43].

Another degradation mechanism due to high temperatures is the deformation of the anode. Lithium ions are solved in the electrolyte, and at higher temperatures this solvent has a higher energy. Because of the higher energy sometimes intercalation of the entire solvent will take place [43]. This will deform and crack the anode. This mechanism is displayed in figure 3.9. The same mechanism also occurs at the cathode side, leading to structural damage of the active cathode material.

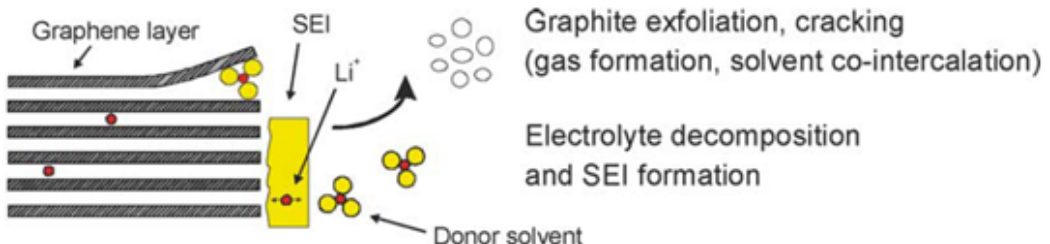


Figure 3.9: Cracking of the anode due to intercalation of the solvent and gas formation as a result of electrolyte decomposition [43].

3 Degradation mechanisms of Li-ion cells

In figure 3.9 gas formation is described. Depending on the type of cathode, gas formation can result from the formation of a lithium/oxygen-deficient sub-surface layer from which oxygen is released [43]. Gas formation also occurs as a result of electrolyte decomposition at high temperatures, and bad ion conductors are left as decomposition products [44]. This means less lithium ions can be transported to the cathode and anode, which decreases the cell conductivity and eventually capacity.

Not only will the electrolyte decompose as a result of high temperatures, but the separator in the electrolyte as well. When the separator has disappeared, the battery cell is more prone to short-circuit. Lithium plating and corrosion can cause the cell to short-circuit, which will be explained in paragraph 3.4.1.2 and 3.4.3.2 respectively.

Between the electrodes and current collectors a binder is present to keep the two connected. At high temperatures the binder will decompose and the contact between the binder and current collector will worsen [43]. This will cause a lower conductivity of the cell and results in power fading, as many other degradation mechanisms at high temperatures do.

Raising the cell temperature results in a temporary capacity increase, but the coupled disadvantages are much more severe. It is, however, very hard to determine the temperature of the battery cell. The temperature on the surface is much lower than the temperatures of the electrodes, which is where the chemical reactions occur [45]. To minimize the temperature difference and accelerated degradation, good thermal management of the battery is required.

3.4.1.2 Low temperature

At low temperatures the activation energy needed for the chemical reactions to be able to occur will be higher. The intercalation and deintercalation at the electrodes will require more energy, so less lithium ions can participate in the active cell process. This will result in a temporary loss of capacity.

Less intercalation and deintercalation also means a lower cell voltage, which influences the power the cell is able to deliver. Due to the low temperature the diffusion of lithium ions will be slower. As a result the currents the cell is able to provide will be lower, which will also result in a loss of power.

The effects mentioned above are, however, temporary; when the temperature is restored to nominal level, the capacity and power capabilities will be recovered. Under normal discharge low temperature on its own does not have any influence on capacity fading.

Figure 3.6 shows that low temperatures do have influence on the cycle life. This influence is the result of a degradation mechanism during charging, namely lithium plating. The intercalation of lithium ions into the anode during charging cannot happen as fast as the electric energy transferred and lithium ions diffused to the anode. The anode will be polarized to potentials able to cause lithium ions to react to lithium metal [46]. The lithium metal is deposited on the anode and blocks the pores of the SEI layer. Less lithium ions can intercalate into the anode and lithium ions are transformed into lithium metal; as a result capacity fading occurs. The reason that lithium plating is more likely to occur during charging than discharging, is because the intercalation rate at the anode is inherent slower than the deintercalation rate [47].

The slow diffusion of the lithium ions together with lithium plating will cause the deposited lithium metal to slowly grow [43]. Lithium metal dendrites are formed, which slowly grow to the cathode. Due to corrosion lithium metal is inserted in the electrolyte and can puncture the

separator. As a result a conductive path between the cathode and anode can be formed and the cell short-circuits. Lithium plating, lithium dendrite growth and corrosion are shown in figure 3.10.

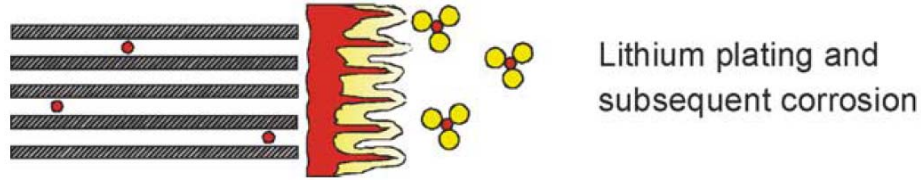


Figure 3.10: Lithium plating, lithium dendrite growth and subsequent corrosion due to low temperatures [43].

The overpotential at the anode/electrolyte interphase, which causes lithium plating, is not only caused by low temperatures. High C-rates, an excess of cathode material and non-uniformity of electrodes will enhance lithium plating [46]. The effect of high C-rates will be explained in paragraph 3.4.2.

3.4.2 C-rate

The C-rate is the current in the cell scaled to the nominal capacity. A high C-rate is thus a high current. The process of discharging and charging at an electrode/electrolyte interphase is explained by figure 3.11.

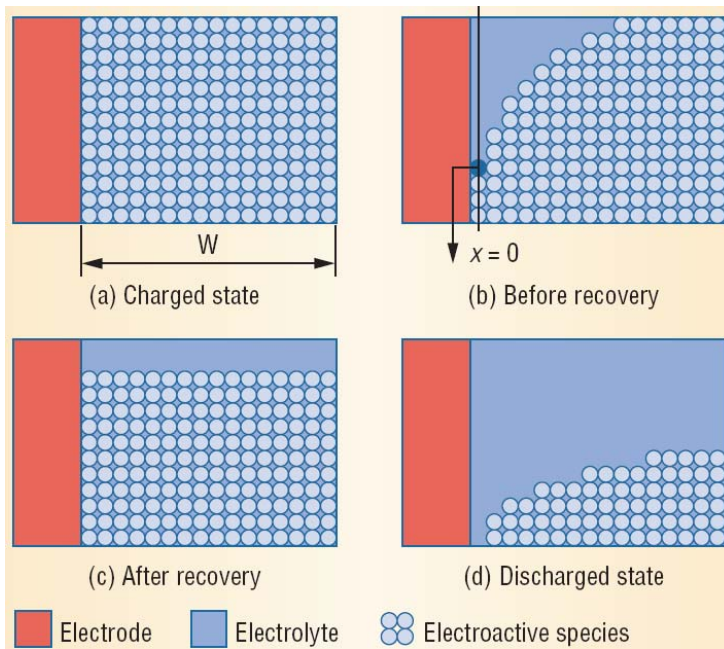


Figure 3.11: The process of charge/discharge at an electrode with (a) all the lithium ions available, (b) chemical reaction for intercalation before recovery, (c) after recovery and (d) not enough lithium ions available for chemical reactions to support the C-rate [48].

When all lithium ions are still available in the electrolyte as in figure 3.11a, the surface near the electrode will be filled with lithium ions. During intercalation the lithium ions near the surface leave the electrolyte as shown in figure 3.11b. The chemical reaction associated with intercalation cannot be sustained over the entire surface anymore as the diffusion rate is lower than the reaction rate. As a result a concentration gradient builds up in the electrolyte [48]. This is seen as a rise of the internal impedance of the cell. When this is kept up for a long time, damage to the cell can occur due to local overpotential. Lithium ions from the bulk electrolyte

3 Degradation mechanisms of Li-ion cells

diffuse to the area with the least lithium ions and after a recovery period the lithium ions are spread out over the electrode surface again as in figure 3.11c. In figure 3.11d all the lithium ions at the surface are intercalated and the current will stop, even though there are still lithium ions present in the bulk. This will result in a temporary capacity loss. The capacity can be recovered after a resting time or when a lower current is used. So the higher the C-rates are, the higher the temporary capacity loss is.

The insufficient diffusion rate causes the diffusion polarisation voltage drop to rise; together with the ohmic and activation polarisation voltage drop, the total voltage drop over the cell is determined. Higher C-rates induce higher voltage drops as described by Ohm's law and is shown in figure 3.12. The cut-off voltage will be reached faster than with lower C-rates, resulting in a loss of capacity. This can be recovered by discharging at a lower C-rate.

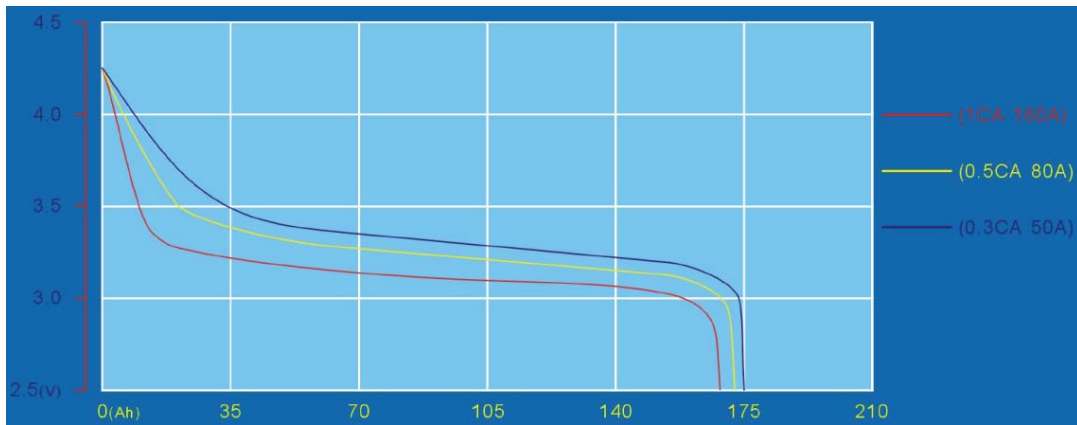


Figure 3.12: An example of the terminal cell voltage at different discharge C-rates [49].

For charging at high C-rates the maximum terminal voltage will be reached at a lower SoC, as the voltage drop over the internal resistance will be added to the terminal voltage with charging. Most battery cells are therefore charged with the constant current constant voltage (CCCV) protocol. This means that the battery will be charged with a constant current up to the maximum terminal voltage. Then the cell is charged with a constant voltage by slowly reducing the current. For fast-chargers, which only charge to the maximum voltage with constant current, the higher the C-rate is, the lower the charged capacity will be.

Since for both discharge and charge modes the voltage drop over the internal resistance will be larger for higher C-rates, the energy efficiency will be lower. The lost energy will be mainly dissipated into heat, as described below.

Large continuous currents will not only cause temporary loss of capacity, but also damage the cell and cause capacity fading. During operation the internal cell impedance causes a voltage drop V_{int} over the cell. The power dissipation generated by ohmic heating will be $P_{dis} = I_i^2 R_i$ with R_i the internal resistance of the cell and I_i the current through the internal resistance. In practice the current through each internal resistance element is different, so the total power dissipation is a summation of the power dissipation in each resistance element. Consequently, a higher current will generate more heat and cause the temperature of the cell to rise. This will invoke the high temperature degradation mechanisms described in paragraph 3.4.1.1 as a consequence.

Large continuous currents can also cause overpotential of the electrodes. The diffusion of lithium ions is not fast enough, causing the electrolyte near the electrode to be charged compared to the electrolyte in the middle of the cell. The maximum voltage for the cell is reached at an earlier stage at certain areas of the cell, causing local overcharge. The degradation

mechanism associated with overcharge will be described in paragraph 3.4.3.1. The intercalation and deintercalation of lithium ions can also not happen fast enough, with lithium plating and corrosion as a result for high charging currents [50]. All these effects will decrease the capacity of the cell.

Short pulses on the contrary hardly damage the cell. Short pulses will only cause the lithium ions on the surface of the electrode to react. If the recovery periods are sufficiently long for the lithium ions to diffuse to the electrode/electrolyte interphase, local overpotential on the electrodes is prevented. Furthermore, if the cell has a large thermal capacity, the temperature rise can be neglected. Due to the short pulses the heating energy resulting from ohmic heating will be low and the degradation mechanisms associated with high temperature will not occur.

Except for local overpotential and temperature rise, high C-rates will also cause the SEI layer on the anode to crack faster. More active anode material is exposed and the SEI layer will restore itself, reducing lithium ions from the battery cell process. High C-rates will furthermore cause additional strain on the electrode materials, resulting in increased deformation and loss of active material [43]. These effects will all result in capacity and power fading. High continuous C-rates must therefore be avoided for a long battery cell life.

3.4.3 State of charge (SoC)

The state of charge (SoC) is an indication of the amount of energy left in the battery cell as a percentage of the current capacity. The higher the SoC, the more energy is stored in the cell. This will mean the battery cell is more reactive, which will accelerate degradation of the cell.

At a high SoC the anode will be highly lithiated and energized. Due to the high energy content in the cell the self-discharge will also be higher. More reactions will take place and the SEI layer will grow faster. Deformation of the cathode can also occur, since it will be in a highly delithiated state and experiences thermodynamic instability [43]. Furthermore, electrolyte oxidation occurs at high SoC, leading to impedance increase [51]. These effects result in capacity and power fading.

The effects of high SoC mentioned above are more profound during storage for a long time, but with cycling the influence of high SoC vary a lot. The amount of time spend at a certain SoC is very short, as the SoC quickly varies. The influence of high SoC can be limited if the cells are cycled at a low SoC. This is under the assumption that the cell will operate within the specified voltage range given by the manufacturer. In case of overcharge or overdischarge, which will be described respectively, other degradation mechanisms will be introduced and shorten the cell life.

3.4.3.1 Overcharge

Overcharge means that the cell is charged over the specified voltage and will operate above its maximum stress point. A small increase in capacity is initially obtained, but the cycle life is strongly reduced. This effect is stronger as the end of charge voltage increases, as shown in figure 3.13. During overcharge electrical energy is pumped into the battery, but hardly any intercalation can take place anymore. This will be represented by a sharp increase of internal resistance. The electric energy will be dissipated and the temperature of the battery rises, causing all the high temperature degradation effects described in paragraph 3.4.1 [10].

3 Degradation mechanisms of Li-ion cells

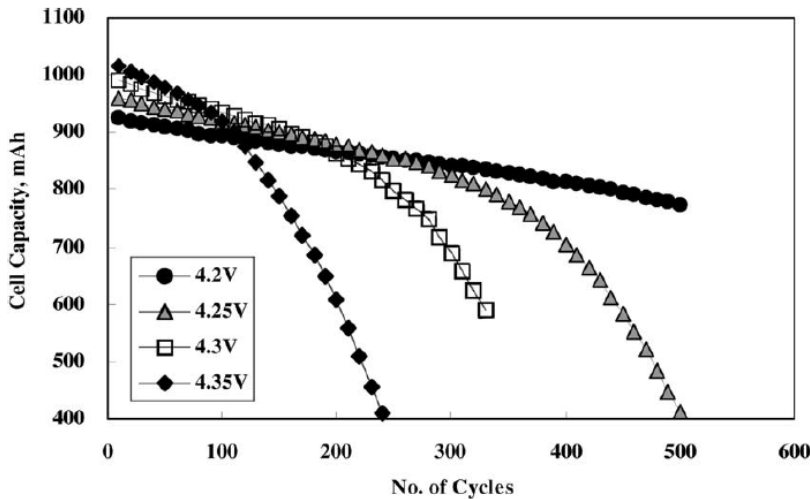


Figure 3.13: Strong decrease of cycle life with increasing maximum charging voltages [52].

Decomposition of the binder and electrolyte will also take place. The decomposition of electrolyte forms insoluble products, blocking the pores of the electrodes, and causes gas generation [53]. The gas generation raises the pressure in the cell and forms a safety hazard.

Overcharge does not only influence the electrolyte. Oxidation of the cathode and lithium plating on the anode will occur. Oxidation of the cathode reduces the active cathode material, and lithium plating reduces active anode material and lithium ions in the cell. Overcharge must therefore be avoided at all times.

3.4.3.2 Overdischarge

When the cell is discharged under the specified cut-off voltage, essentially negative SoC, two degradation mechanisms will severely damage the cell. The main cause of capacity fading due to overdischarge is corrosion of the copper current collectors and dissolution into the electrolyte [54]. The copper current collectors are the current collectors at the anode side. The copper ions will not only block the active electrode materials, but will also migrate to the separator. The separator will be degraded and punctured by the copper ions, which continue to migrate to the cathode. This will form a conductive path and the cell will be short-circuited due to copper shunts. The corrosion will also lead to a loss of contact with the anode and poor electronic conductive corrosion products, resulting in power fading. The corrosion products cause the current to flow through the conductive copper parts, increasing the local current density. Localised overpotential can occur and make the cell more susceptible for lithium plating [55].

The second degradation mechanism is the decomposition of the SEI layer on the anode [56]. The high anode potential will cause dissolution of the SEI layer. Upon recharge the exposed active material will cause side reactions to restore the SEI layer and reducing lithium ions, causing capacity fading.

Overdischarge can cause severe capacity fading or even destroy the battery cell. If copper shunts have formed in the cell, the cell is short-circuited and will heat up rapidly upon recharge. This is a safety hazard, and overdischarged cells must be carefully recharged.

3.4.4 Depth of discharge (DoD)

The depth of discharge (DoD) is the percentage of the current cell capacity that is discharged in a cycle. The cycle life of a cell is strongly dependent on the DoD. An example of a number of

possible cycles against the DoD is given in figure 3.14. Similar cycle number vs. DoD graphs as in figure 3.14 are always obtained from cells discharged from an initial SoC of 100%. The cell is discharged at a constant current to the appropriate DoD and fully charged again. The deeper the discharge, the more intercalation and deintercalation has taken place in the electrodes. The loss of lithium ions and active electrode material described in paragraph 3.3 will be higher for larger DoD cycles. More capacity fading per cycle occurs and fewer cycles are possible.

If no other degradation mechanisms occur at high DoDs, the charge or energy throughput of the cell will be equal for all DoDs and no additional capacity fading is experienced. However, at low SoCs, i.e. high DoDs, additional degradation mechanisms can occur in the cell during cycling. At low SoCs the cathode will be highly lithiated. Due to the high concentration of lithium ions intercalated into the cathode, the structure of the cathode can be distorted as a result of the Jahn-Teller effect [56]. Also decomposition and dissolution of the cathode material into the electrolyte can occur [43]. The active cathode material is reduced and results in capacity fading. Whether the DoD has an influence on the capacity fading is therefore strongly dependent on the cathode material.

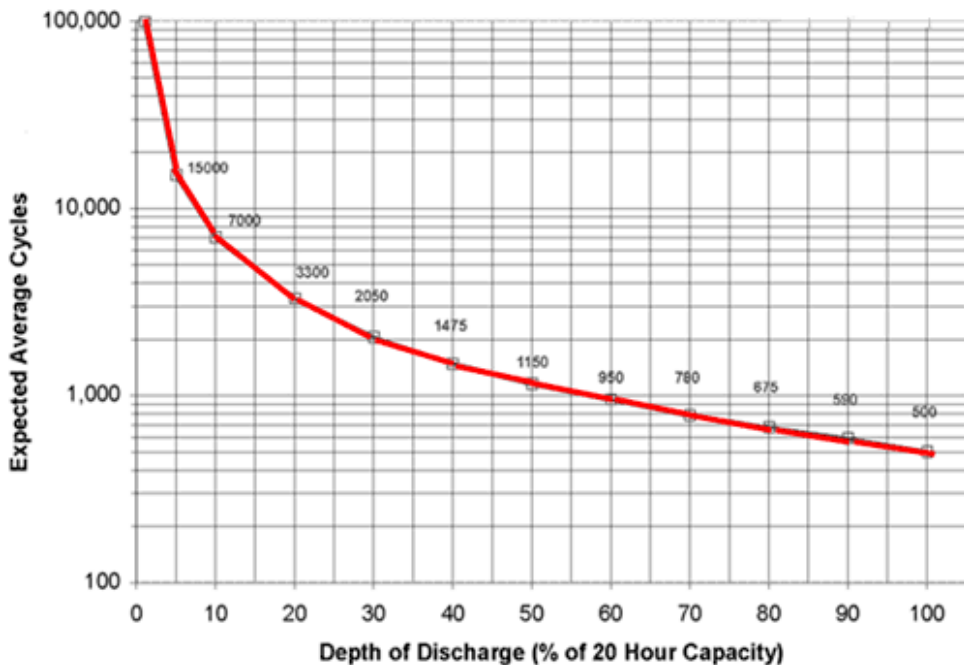


Figure 3.14: An example of a typical cycle number vs. depth of discharge (DoD) curve of a Li-ion cell [57].

3.5 Degradation of Li-ion cells due to storage

Li-ion cells do not only degrade as a result of usage, but also when the cells are not used and stored. The active anode material is still exposed to the electrolyte through the porous SEI layer, and side reactions will enhance this SEI layer. Cells stored under the right conditions exhibit minimal capacity fading, but at high SoCs or high temperatures the capacity fading will be more severe. An example of the capacity fading at different SoCs and temperatures is given in figure 3.15. From figure 3.15 it can be seen that the cell voltage, i.e. SoC, at which the cell is stored has an influence on the capacity fading. Even without usage chemical reactions will still occur in the cell.

3 Degradation mechanisms of Li-ion cells

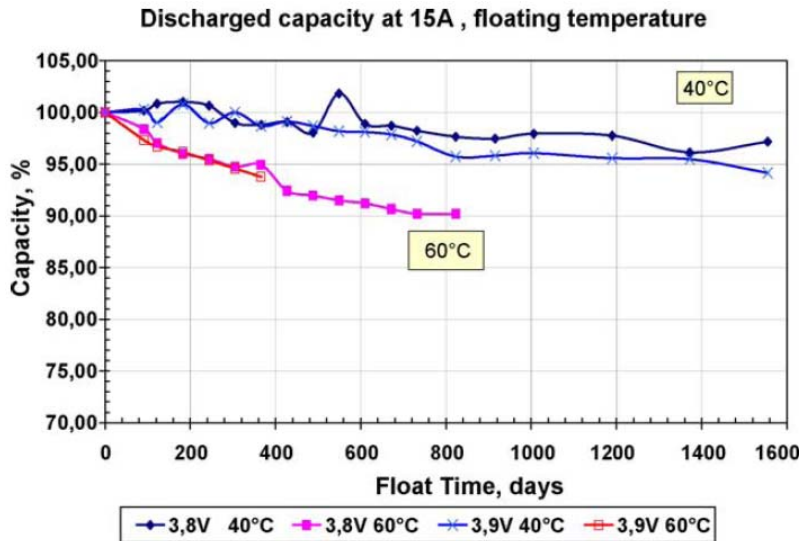


Figure 3.15: An example of capacity fading due to storage at different voltages (SoC) and temperatures [58].

At higher temperatures the capacity fading strongly depends on the oxidation properties of the cathode with the electrolyte [58]. The activation energy for the chemical reactions is lowered with increasing temperature and reactions occur faster and more easily. At higher SoCs the cathode has more lithium ions intercalated and as a result the cell voltage is higher. The cell has more energy stored inside and is thus more reactive. The degradation mechanisms for high temperature and high SoC that occur are respectively described in paragraph 3.4.1.1 and 3.4.3. High temperature or SoC will also lead to resistance growth in the cell, which results in power fading. This is shown in figure 3.16.

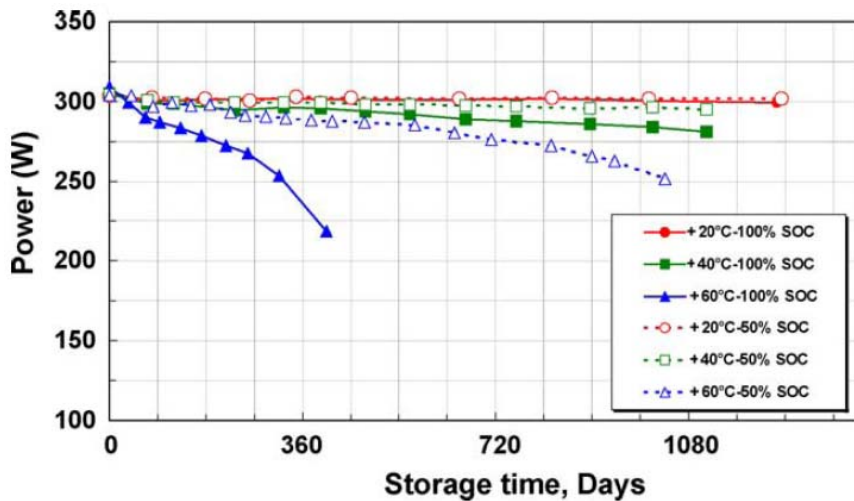


Figure 3.16: An example of power fading due to storage at different SoCs and temperatures [58].

Li-ion cells are optimally stored at low temperatures and low SoC to slow down the electrochemical processes in the cells. However, due to the self-discharge of a Li-ion cell, cells cannot be stored at very low SoCs. This would result in overdischarge and damage the cell as described in paragraph 3.4.3.2. Storage at 40% SoC and 15°C has been suggested for optimal battery life [59].

4 Capacity fading model for state of health determination

The severity of battery cell wear can be quantified by the state of health (SoH) of a battery cell. The SoH reflects in percentages how healthy a cell is, with 100% for a new cell and 0% when the end of life (EoL) of a cell is reached. The SoH of a cell is determined by using life estimation models, which can be divided into two different approaches [4] :

- Performance-based models; by continuously monitoring the changes in performance values of the battery cell such as voltage, current, power or capacity, the SoH of the battery is determined. When the performance drops under a certain threshold value or meets a certain condition, the EoL of the battery cell is reached. Performance based models consists of artificial neural network, electrochemical, equivalent circuit, (semi-) empirical and analytical models [4].
- Weighted-throughput models; the EoL of a battery cell is reached when the weighted throughput of a chosen parameter in respect to the reference conditions is fulfilled. Depending on the throughput parameter, the value of the throughput parameter under certain conditions is sometimes given by the manufacturer. Throughput parameters are the charge (Ah) processed, energy (Wh) processed, number of cycles (cycle counting) or time of operation. By registering the conditions under which these data are acquired, the effective throughput and EoL throughput under reference conditions can be determined.

For SoH determination in reference to capacity fading both performance-based models and throughput models will be evaluated. Out of the performance based models, the models of interest are mostly (semi-) empirical models for capacity fading. These models capture the general trend of capacity fading including changing operating conditions with the lowest complexity. Electrochemical models will be used to extract equations which can be used in combination with the (semi-)empirical models and gain a better understanding of the processes in the cell. In the next chapter an equivalent circuit-based model will be used to describe the other performance parameters of the cell. Analytical models and artificial neural networks do not describe the processes in the cell and are not relevant in this work.

Since capacity fading has been chosen as the parameters for SoH determination in this work, different definitions of cell capacity and capacity fading have to be understood. Capacity fading can be contributed to two phenomena: true capacity fading and rate capability losses [60]. True capacity fading represent the loss of lithium ions and active material, while rate capability losses are caused by the growth of internal impedance in the cell and are current dependent. The useable capacity is defined as the initial useable capacity minus the true capacity fading. The apparent capacity includes both true capacity fading and rate capability losses. This chapter will only consider true capacity fading. Unless mentioned otherwise, capacity fading in this chapter will indicate true capacity fading only. The rate capability losses are dependent on the internal impedance, which can be modelled by circuit components in the equivalent circuit-based model and is discussed in the next chapter.

In this chapter first a literature review will be conducted on the available capacity fading models, which is followed by a short analysis of the available models. Then the performance-based damage accumulation model and throughput-based Palmgren-Miner rule model will be explained and a comparison of the both SoH models will be given. From literature a capacity

fading rate model will be determined and both SoH models will be evaluated according to the capacity fading rate model. For battery cell usage under changing operating conditions, the capacity fading rate will be constantly changing. An overview of the stress factor models for the changing operating conditions will be given, and the relevant stress factors will be chosen. Finally the complete literature-based capacity fading model will be proposed and several SoH determination methods are given.

4.1 Capacity fading models: a literature review

Permanent loss in capacity can be divided into calendar and cycling losses. Broussely [51] explored the relation of capacity fading with calendar life on Li-ion cells. The Arrhenius equation was found to fit the experimental data conducted at different temperatures. The capacity fading due to storage showed a square root of time dependence, which is consistent with the surface film growth rate mentioned in literature. Ploehn. et al. [61] have also found that the Solid Electrolyte Interphase (SEI) thickness was linearly dependent on the square root of time. Bloom et al. [62] discovered that the same relation holds for power fading.

Capacity fading as a result of calendar losses has also been observed by Liaw et al. [63] to behave according to the Arrhenius equation. NCA cells were tested and capacity fading was found to be dependent on temperature and SoC. The activation energy differed for changing SoC, where the difference was smaller after longer ageing times. The capacity fading was discovered to be related to the impedance rise. The more the impedance rose, the lower the activation energy would be.

Spotnitz [30] considers the SEI formation also the main cause of capacity fading for cycling. The capacity fading is described on a molecular level with the loss of lithium ions, where the loss of ions is depend on the SEI formation rate. The temperature dependence of the formation rate followed the Arrhenius equation. Disruption of the SEI layer due to intercalation will enhance SEI formation and results in capacity fading. This was described by a model describing the loss of lithium ions.

Rong & Pedram [64] has also contributed the main cause for capacity fading to the electrode film growth. The model consists of a film growth equation, which is dependent on the cycle number and temperature. A lithium-ion cell has been cycled at room temperature and the capacity fading versus cycle number was found to be linear.

To model the cycling losses, Zhang & Wang [65] have conducted cycling tests on NCA cells at different temperatures. The capacity fading was found to consist of a parabolic and a linear region, where the switch from parabolic to linear region is different for each temperature. The capacity fading is then modelled as an addition of a radical and linear function. The capacity of the cells follows the Arrhenius equation. From the tests it was found that the activation energy drops with increasing cycling, which implies that the degraded cathode is less sensitive to temperature.

The same capacity fading behaviour was seen in Guena & Leblanc's life cycle tests [66] on lithium metal polymer (LMP) cells. The tests showed that the Δ DoD has a large influence on capacity fading. An increase of three times more Ah processed in the case of 50% Δ DoD is observed in comparison to 100% Δ DoD with the same amount of capacity faded. Micro-cycling was tested as well, with Δ DoD of 0.5% at 100% SoC. This was compared to capacity fading due to calendar losses, and micro-cycling seems hardly to have any effect on the capacity fading.

Smith et al. [67] collected data from experiments done with NCA cells to set up a semi-empirical model for capacity fading. The true capacity fading was observed to decrease linearly

4 Capacity fading model for SoH determination

with the ΔDoD . The impedance growth was also observed to be linearly dependent on the ΔDoD , and cycling suppressed the negative effects of storage. This resulted in an addition of a linear and radical equation. The impedance was also observed to grow with the SoC dependent Tafel equation and temperature dependent Arrhenius equation. This impedance growth was added to the true capacity fading equation, resulting in a total capacity fade model consisting of a linear and radical equation.

Doerffel [68] observed a linear relation for the capacity fading from experiments. The capacity fading of a LiFePO₄ cell for EV applications has been tested under various conditions. The tests have however been done on the same battery, making it very hard to determine how much influence on the capacity each ageing factor has. The capacity fading was found to be linear with the number of cycles.

However, the experiments mentioned above did not differentiate between true capacity fading and rate capability loss. Tredeau & Salameh [69] have tested an EV LiFePO₄ cell to find the amount of true capacity fading. The true capacity fading was found by not only charging the cell with a CCCV-protocol, but also using the same protocol for discharge. A linear decrease of capacity was observed.

To quantitatively distinguish between true capacity fading and rate capability loss, Ramadass et al. [60] split the capacity fading into three components: increasing resistance at the electrodes, loss of active electrode material and loss of active lithium ions. The resistance increase due to film formation was found to increase radically with the cycle number, which is responsible for the rate capability loss. The anode was taken as the limiting electrode, which the loss of active material and lithium ions was contributed to. From experiments with a LiCoO₂ cell a semi-empirical equation was constructed, which described cycling under adverse conditions with a quadratic function and cycling under reference conditions as linear.

Santhanagopalan et al. [70] developed a model for capacity fading with experiments on a LiCoO₂ cell, only considering true capacity fading. A distinction is made between loss of lithium ions and active materials, both at the cathode and anode. Mathematical equations describing the electrochemical reactions in the cell are used and parameters are estimated by conducting tests. The loss of lithium ions is the determining capacity fading factor for the cathode. For the anode loss of lithium ions is at low temperatures initially the main contribution to capacity fading, but at high temperatures and higher cycle numbers the loss of active material becomes more important. This last result is the limiting factor for the cell capacity.

In literature ΔDoD was always assumed to have a large influence on the cycle life. Modelling of the influence of ΔDoD has been described by empirical equations, which were extracted from manufacturer data. Thaller & Lim [71] have used both an exponential function and rational function to describe the influence of ΔDoD on the cycle life for a lead-acid and NiCd cell. Drouilhet & Johnson [72] have expanded this equation with a rational term, also deducted from NiCd cell data. The larger the ΔDoD of the cycle is, the shorter the cycle life of the cell is. Rosenkranz [73] used data from several types of battery cells including Li-ion, and described the ΔDoD dependence of all types with a rational equation.

Ning & Popov [74] have tested LiCoO₂ cells for the influence of SoC and ΔDoD on the cycle life. The anode was considered as the limiting electrode, and the surface film formation was due to the parasitic reaction on the anode surface. The loss of lithium ions, and thus capacity fading was completely contributed to the parasitic reaction in this model. The exchange current of the parasitic reaction determined the loss of lithium ions. This was found to be dependent on the

time of discharge and overpotential of the anode, which was described by the Tafel equation. The time of discharge corresponds to the ΔDoD . Capacity fading was found to be linear with cycle number under equal conditions. Higher end of charge voltages and higher ΔDoD contributed to a higher capacity fading.

All the ΔDoD and SoC influences were, however, obtained with constant current discharge experiments. Millner [3] proposed a model for capacity fading including ΔDoD fluctuations on different SoC, whereas other capacity fading models including ΔDoD influence presume the battery cell is discharged from a fully charged state. Millner's model can be easily applied in a practical system and differentiates between influences on the capacity fading rate due to SoC and ΔDoD . The influence of discharging from different SoCs is described by the average SoC over a certain period of time using SoC_{avg} . The ΔDoD is taken into account using SoC_{dev} , the normalised deviation from SoC_{avg} . Zhurkov's model for crack propagation [75] is used to derive an exponential relation between the capacity fading and SoC_{dev} and SoC_{avg} . Then the amount of capacity fading is scaled against the capacity fading already received by the battery cell. With the combination of Arrhenius equation the model described the effect of SoC, ΔDoD and temperature on capacity fading.

Choi & Lim [52] have tested a LiCoO₂ cell under constant current discharge and concluded that the ΔDoD does not have an influence on the cycle life. The capacity of the cells discharged from 100% SoC decreases linearly with the same rate for all ΔDoDs . On the other hand overcharge and high charge or discharge currents did introduce an accelerated capacity fading.

Peterson et al. [40] have tested state-of-the-art LiFePO₄ cells under both varying and constant current discharge and also concluded that increasing ΔDoD also does not introduce more capacity fading for the tested types of Li-ion cells. The cells were tested with a dynamic profile simulating driving with regenerative braking and a constant current profile simulating vehicle to grid discharge. Each cell experienced a different ΔDoD . The capacity fading was found to be linear with the amount of charge or energy processed in the cells, with the dynamic profile causing more than twice as much capacity fading as the constant current profile.

To account for the different degradation factors influencing the capacity fading of a cell, Marano et al. [4] proposed a weighted Ah-throughput model. A Li-ion cell can process a certain amount of Ah under reference conditions before the EoL is reached. Weighting factors are used to calculate the equivalent processed amount of Ah under reference conditions. This prognostic model can then be used to predict the EoL under current operating conditions. A prognostic model based on mechanical fatigue of materials is used, which could be described by the Palmgren-Miner (PM) rule or damage accumulation model. Both models are equivalent under certain conditions.

Safari et al. [76] have approached the problem of life prediction of Li-ion cells in the same way as [4]. With the use of an electrochemical model for a LiCoO₂ cell, the difference between the PM rule and damage accumulation model was investigated. Dummy ageing experiments were conducted at different SoCs with microcycling at different C-rates. From experiments it could be concluded that high SoC and C-rate cause increased capacity fading, and that the PM rule is more accurate than the damage accumulation model.

In a second paper Safari et al. [77] tested the PM rule and damage accumulation model on simulated models with a varying current profile. Empirical equations were used to model both models. The damage accumulation was modelled with two 2nd order equations for the SoC and C-rate and one correlation term; the parameters were all dependent on time, and each parameter

4 Capacity fading model for SoH determination

was modelled with a 3rd order equation. The PM rule time was modelled the same way, only the parameters were dependent on damage and followed an addition of linear, radical and logarithmic relation. Different parameters were obtained for charging and discharging. The effect of charging was found to have a larger effect on capacity fading than discharging. The damage to the cell or remaining lifetime of the cell is respectively found with a summation of the amount of damage accumulated or time passed during each event. Each event is a period in which the operating conditions do not change.

Analysis literature review

From literature research on capacity fading models it can be concluded that there is not one general model for Li-ion cells. Many models only include some of the degradation factors, and none have included all. In some models the capacity fading including rate capability losses is measured, while others make a clear distinction between true capacity fading and rate capability loss. The rate of capacity fading is also not the same for all models. Some authors only observed a linear decrease with cycle number, while others saw a combination of a linear equation with either a radical or quadratic equation. Authors measuring the capacity fading with rate capability loss described the capacity fading with a radical equation, while authors making a distinction in capacity fading used quadratic equations.

In modelling the capacity fading factors all authors agree the temperature dependent degradation can be modelled with the Arrhenius equation. As for the ΔDoD, different models have been developed in literature. Some authors use an exponential equation, while others use a rational equation. One author proposed the use of crack propagation theory, which is also an exponential equation. Other authors even observed that the degradation does not worsen with increased ΔDoD at all. Overcharge was also observed as an important capacity fading factor, and high SoC also introduced capacity fading. The capacity fading due to high SoC was modelled with the Tafel equation for storage, but has not been validated for cycling. Capacity fading due to high currents was also measured, but no model was developed to describe this effect. It is also not clear whether true capacity fading or rate capability losses will result from cycling with high currents.

With capacity fading models a prognostic model for the SoH of a cell can be developed. The capacity damage caused by each event or the time spent under certain stress levels is scaled to reference conditions and added to be compared to the total tolerable damage or time. Consequently, the SoH of the cell can be determined and the amount of time or energy that the cell can still spend under the same conditions can be estimated.

4.2 SoH models on capacity fading

Models considering capacity fading as the state of health (SoH) indicator can be divided into two categories: models using the Palmgren-Miner (PM) rule i.e. weighted throughput models, and damage accumulation models i.e. performance-based models [4]. The PM rule gives the decrease of the life fraction at the end of each event by defining the end of life (EoL) conditions beforehand. The damage development rate will be dependent on the chosen throughput parameter. The damage accumulation models determine the amount of capacity fading occurred during each event, in which the damage sustained is the monitored performance parameter. An event is a period of time in which the operating conditions are considered to be constant. For the PM rule a summation of the life fraction decreases will give the SoH immediately, while for a

damage accumulation model the summation of the capacity fading during each event has to be scaled with the desired EoL condition.

4.2.1 Palmgren-Miner rule model

The PM rule approach is used in the modelling of mechanical fatigue in the ageing of mechanical components. The rule states that the life of a component under a variable load is reduced each time by a finite fraction [4]. This fraction corresponds to the ratio between the time the component spent under a given constant load and the life time of the component if it would be subjected to the same load. Expressed in an equation, the EoL of the component is reached when

$$\sum_{i=1}^E \frac{\Delta t_i}{t_i^f(\sigma_i)} = 1 \quad (4.1)$$

with t_i^f the time it would take for a component to reach its EoL under a constant stress factor σ_i , Δt_i the duration of the event and E the number of events when the EoL condition is reached. The stress factor is considered to be constant within an event. Equation 4.1 states that the EoL of a component is reached when the cumulative fractions of life time reduction has reached unity. For averaged stress factors within a cycle, equation 4.1 can be expressed as [4]

$$\sum_{i=1}^E \frac{n_i}{N(\sigma_i)} = 1 \quad (4.2)$$

with n_i the number of cycles spent under stress factor σ_i and $N(\sigma_i)$ the total number of cycles for the EoL to be reached. For battery cells the Ampere-hours (Ah) discharged are also used often as a measure for the life fraction left [13]. Battery cells can also be assumed to have a certain amount of Ah-throughput under certain conditions before the EoL is reached. By substituting the time in equation 4.1 by Ah, an Ah-throughput model is obtained

$$\sum_{i=1}^E \frac{Ah_i}{Ah_f(\sigma_i)} = 1 \quad (4.3)$$

where Ah_i is the Ah discharged during the event and Ah_f the total Ah to be discharged for the EoL is reached under stress factor σ_i . Equation 4.3 can be normalised to a reference conditions, resulting in a weighted Ah-throughput model [4][72]:

$$\frac{\sum_{i=1}^E Ah_{ef,i}}{Ah_{total}} = \frac{\sum_{i=1}^E n_i \cdot \sigma_i \cdot Ah_i}{Ah_{total}} = 1 \quad (4.4)$$

Here n_i is the number of events under event i , $Ah_{ef,i}$ is the effective Ah discharged under reference conditions and Ah_{total} is the total Ah discharged to reach the EoL under reference conditions. Using equation 4.4 only the EoL Ah-throughput for reference conditions has to be determined. The stress factor σ_i consists of multiple stress factors that have effect on the capacity fading of a cell, which have to be determined experimentally.

4.2.2 Damage accumulation model

The damage accumulation model is a summation of the damage occurred in a life time of the object. Just like the PM rule, the damage accumulation model is also often used in mechanical

4 Capacity fading model for SoH determination

fatigue analysis [13]. The amount of capacity fading of a battery cell is modelled as damage in the damage accumulation model. The rate at which the damage develops can be described by

$$\frac{d\xi(t)}{dt} = \varphi(\xi, \sigma) \quad (4.5)$$

where ξ is the amount of damage and φ is a function of ξ and stress factor σ . This means that the variation of the damage is a function of the current amount of damage and stress factor σ . When the damage and stress factor are considered to be constant during a cycle, e.g. averaged temperature and C-rate of a cycle, equation 4.5 will become [4]

$$\frac{d\xi(n)}{dn} = \varphi(\xi, \sigma) \quad (4.6)$$

with n as the cycle number. Similar to equation 4.6, the damage rate can also be modelled with an Ah or Wh dependency instead of time. Taking equation 4.5 as an example, the total damage can be calculated by

$$\xi = \sum_{i=1}^E \left(\int_{t_{i-1}}^{t_i} d\xi_i(t) \right) = \sum_{i=1}^E \left(\int_{t_{i-1}}^{t_i} \varphi(\xi_i(t), \sigma_i) dt \right) \quad (4.7)$$

where t_{i-1} is the starting time of an event, t_i the end time of the event, E the total number of events and ξ_i is the damage development with time at a constant stress factor σ_i . A linearization to determine the total damage has been proposed by [76], which changes equation 4.7 to

$$\xi = \sum_{i=1}^E \left(\left(\frac{d\xi_i}{dt} \right)_{\sigma_i} \Big|_{(t_{i-1}+t_i)/2} (t_i - t_{i-1}) \right) \quad (4.8)$$

where $t_i - t_{i-1}$ can be written as the time interval Δt_i . Equation 4.8 states that the damage occurred during Δt_i is the damage rate at the median of the time interval multiplied by Δt_i , under the assumption that the stress factor is constant during Δt_i . For equation 4.8 the time passed from zero damage has to be used to determine the damage rate if the damage development is nonlinear. If the amount of time passed is unknown, the amount of damage sustained can be used to calculate the time passed.

4.2.3 Choice of SoH model

The PM rule model is a throughput model and for battery cells it can use either time, cycle, Ah or Wh as throughput parameter. The damage accumulation model is a performance based model and the capacity faded is the SoH parameter. Todinov [78] has shown that the PM rule model and damage accumulation model are compatible, if the damage rate can be factorised. Using equation 4.6 this is show by [78]

$$\frac{d\xi(n)}{dn} = \varphi(\xi, \sigma) = \varphi_1(\xi)\varphi_2(\sigma) \quad (4.9)$$

According to equation 4.9 the stress factors have to be independent from the current state of damage for the damage rate to be factorised. If the damage rate cannot be factorised, the PM rule model will not produce the same results as the damage accumulation law. The PM rule model is often used in cases where the damage rate is unknown or too complicated due to its

simplicity [78]. If the damage rate is linear, the PM rule model and damage accumulation model will be equivalent [76].

Safari et al. [77] have simulated capacity fading with both throughput models on dummy batteries and concluded that the PM rule model produced more accurate results. A possible reason is that the proposed damage rate equation is not as accurate as the PM rule equation. The disadvantage of the PM rule model is that the entire development of the capacity fading rate until the EoL has to be known to be able to accurately determine the SoH [78]. For the damage accumulation model the SoH is accurately determined up to the point tests have been conducted, since the SoH can be calculated with the ratio between the damage sustained and EoL damage.

In the case that the PM rule and damage accumulation model are not compatible, the damage accumulation model is more desirable in SoH determination. This is under the condition that the damage development rate can be determined. By convention the EoL condition for rechargeable battery cells is set to 80% of its rated capacity, but depending on the requirements this could be changed. The advantage of the damage accumulation model is that the SoH can be directly determined if the EoL conditions are changed. Also testing the cells until the EoL conditions are reached is undesirable, since this could take a very long time. Finally, if the rate capability losses are taken into account, the PM rule model needs to be completely changed. In the damage accumulation model an addition of the rate capability losses and true capacity fading directly determines the SoH. Therefore the damage accumulation will be chosen.

4.3 Capacity fading rate model

In datasheets and literature the end of life (EoL) of a battery cell is given in number of cycles, which is dependent on the ΔDoD . The EoL condition is reached when the capacity of the cell drops 80% of its rated capacity. The development of the capacity fading from a fresh cell to the EoL condition is however often not known. Consequently, to be able to determine the state of health (SoH) at any point of the cells life time, the capacity fading rate has to be determined. The capacity fading rate is differentiated into calendar losses due to storage and cycling losses due to usage, which will be described respectively.

4.3.1 Calendar loss rate

The capacity fading due to storage has been observed to be linear dependent on the square root of time, and can therefore be described with a radical function [51][72]:

$$Q_{cal} = k_{cal}(\sigma)t^{1/2} \quad (4.10)$$

where Q_{cal} is the calendar loss and k_{cal} a parameter dependent on the stress factor σ . Previous works have determined the timescale of t to be in weeks. So it will take a very long time to determine and verify the calendar loss rate. Furthermore, the calendar loss rate is very low compared to the cycling loss rate and has a much lower impact than cycling losses during real-life operation. Therefore the calendar losses are ignored in this first approximation.

4.3.2 Cycling loss rate

Many different empirical equations have been found describing the cycling loss rate of a Li-ion cell. Zhang & Wang [65] and Smith et al. [67] conducted experiments to determine the development of capacity fading in a life time of a NCA cell. They observed that the capacity fading versus cycle number developed with a combination of a radical equation and linear

4 Capacity fading model for SoH determination

equation. Guena & Leblanc [66] observed the same behaviour with LMP cells. The observed capacity fading can be described with:

$$\xi = k_1 n + k_2 \sqrt{n} + \xi_0 \quad (4.11)$$

where ξ is the amount of capacity fading, k_1 and k_2 the stress factor dependent parameters, n the number of cycles and ξ_0 the damage on the cell at the start of the measurement. For a fresh cell ξ_0 is zero. To determine the capacity at a certain point in time, the cells were discharged with a constant current. When the end of discharge (EoD) voltage was reached, the current was cut off. With this method, the rate capability losses are also taken into account. A distinction between the rate capability losses and true capacity fading cannot be made.

Ramadass et al. [60] did make a distinction between the rate capability losses and the true capacity fading using LiCoO₂ cells. Since the SoH will be initially be determined with only true capacity fading, in this chapter only the true capacity fading is of importance. Therefore the capacity fading model of [60] is chosen and the true capacity fading rate was found to be

$$\frac{d\xi}{dn} = k_1 + k_\sigma n \quad (4.12)$$

where k_1 is the parameter for cycling under reference conditions, k_σ the parameter for cycling under adverse conditions and n the number of cycles. Under changing temperatures or C-rates, k_σ will change, but k_1 will remain the same. Since the capacity fading due to adverse conditions is not linear, the capacity fading rate is dependent on the previous state of the cell. With the use of equation 4.6, equation 4.12 can be expressed as

$$\frac{d\xi}{dn} = \sqrt{k_1^2 + 2k_\sigma \xi} \quad (4.13)$$

in which the stress factor dependent parameter is expressed as k_σ . Equation 4.13 cannot be factorised as described in equation 4.9. Therefore the PM rule model will not be equivalent to the damage accumulation model for the capacity fading rate, and the damage accumulation model is chosen. Peterson et al. [40] showed that the capacity fading rate expressed in the charge or energy processed in the cells is more desirable, since in electric vehicle (EV) applications the charge or energy processed in each cycle is different due to regenerative braking. The cells which the model in [60] was based on were cycled with the same ΔDoD and C-rate, so an equal amount of charge was processed. Therefore equation 4.12 can also be expressed in Ah. Applying equation 4.7, the amount of capacity fading for a charge interval with constant stress factors is given by:

$$\Delta\xi_i = \frac{1}{2} k_\sigma \cdot \Delta Ah_i (cf_i)^2 + \Delta Ah_i (cf_i) \cdot \sqrt{k_1^2 + 2k_\sigma \xi_{i-1}} \quad (4.14)$$

where i is an event in which the stress factors are constant, $\Delta\xi_i$ the capacity fading occurred in event i , ΔAh_i the amount of energy processed in that event, cf_i the correction factor for a constant current or dynamic profile [40] and ξ_{i-1} the capacity fading at the start of the event. The correction factor will be omitted in the description of equations that come to follow. The total capacity fading will be a summation of the capacity fading occurred during each event.

4.4 Modelling stress factors of capacity fading

From chapter 3 several factors were identified to have an impact on the rate of capacity fading of a Li-ion cell. In literature different equations have been found to model each stress factor. The focus in this work lies mostly in empirical or semi-empirical equations, as these are easier to understand for an electrical engineer without much chemical background knowledge.

In this paragraph equations for the stress factors found in literature will be described. The stress factors are temperature, ΔDoD , overcharge/SoC and C-rate, and will be expressed as σ , each with a different subscript. From the equations found only a few equations are chosen to model the capacity fading. The chosen equations will be combined into a complete capacity fading model, in which the parameters have to be experimentally determined.

4.4.1 Stress factor: temperature

Temperature has a large influence on the amount of capacity fading in a Li-ion cell. Higher temperatures not only cause the active cell process to occur faster, but also the unwanted side reactions. Also new degradation mechanisms are introduced, which are described in paragraph 3.4.1.1. The capacity fading in Li-ion cells is strongly temperature dependent, which is described by the well-known Arrhenius equation:

$$A = A_0 \cdot e^{\left(-\frac{E_a}{RT}\right)} \quad (4.15)$$

where A is the quantity of interest, A_0 the pre-exponential term, E_a the activation energy, R the gas constant and T the temperature in Kelvin. In this work A is the amount of capacity fading occurred in the cell. The Arrhenius equation was found to be valid for both cycling and storage in tested Li-ion cells [3][30][63]. The activation energy E_a was found to be dependent on the SoC at which the cell was kept at during ageing and the duration of the ageing [63]. At high SoCs E_a was lower than for low SoCs, and the E_a lowered with increasing ageing time. This means that unwanted reactions resulting in capacity fading will occur more easily at high SoCs and the amount of degradation will increase with increasing capacity fading.

From the experimental data obtained in [63], a clear decrease of activation energy for the capacity fading cannot be seen. The capacity fading relative to their initial capacity at different temperatures is measured as a function of time. The amount of capacity fading at different times is fitted with the Arrhenius equation, but the lowest temperature capacity fading deviated from the other temperatures. First the activation energy decreased with time, but increased again at a later stage. A pattern could not be derived from the development of the activation energy.

The activation energy shows a dependency on degradation, but it is not clear what this dependency is. By taken the degradation dependency into account and with the use of equation 4.15, the temperature stress factor can be expressed as:

$$\sigma_T(T, \xi) = \sigma_{Tref} \cdot e^{\left(\frac{-E_a(\xi)}{R} \left(\frac{1}{T} - \frac{1}{T_{ref}}\right)\right)} \quad (4.16)$$

with σ_T the stress factor at the current temperature and capacity faded, σ_{Tref} the stress factor at reference conditions, ξ the amount of capacity fading, T_{ref} the reference temperature and the other parameters as mentioned before. The temperature stress factor represents the change in capacity fading rate compared to the reference condition as a result of temperature fluctuations.

4 Capacity fading model for SoH determination

4.4.2 Stress factor: ΔDoD

Capacity fading occurs more profound when Li-ion cells are discharged deeply. The deeper a cell is discharged in a cycle, the more the cell is stressed in that cycle. Therefore the number of possible cycles in the lifetime of a cell, the cycle life, is strongly dependent on the ΔDoD. With the use of a cycle number versus ΔDoD curve, the cycle life of a cell can predicted. An example of such a curve is given in figure 4.1. The data for the curve in Figure 4.1 is mostly obtained from manufacturers. However, in reality manufacturers are very reluctant in providing such a curve, and only publish the cycle life for 80% or 100% ΔDoD.

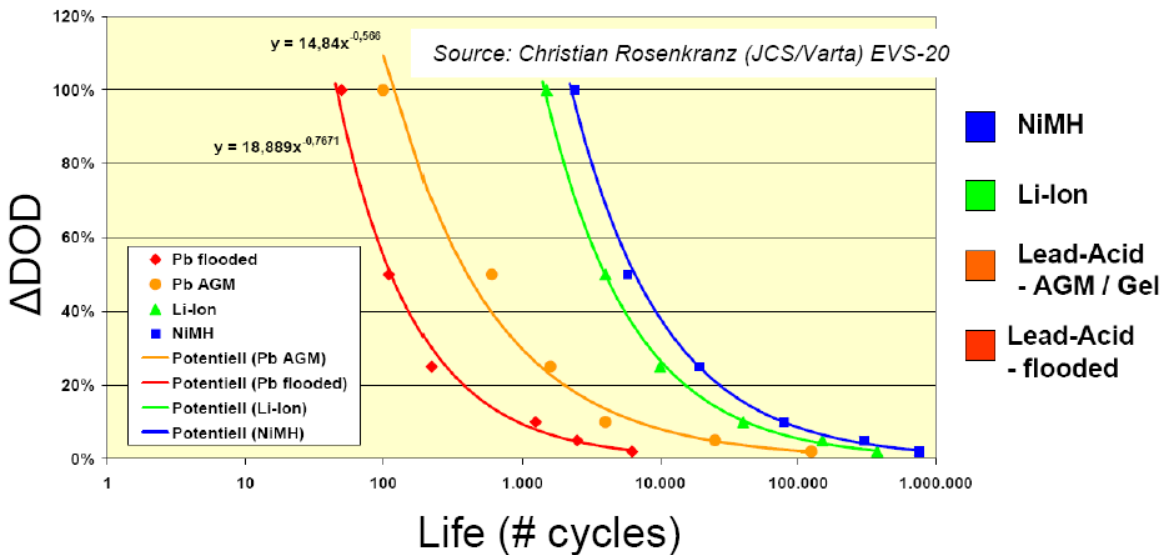


Figure 4.1: An example of cycle life vs. ΔDoD curve for different battery cell chemistries [73]

To be able use the very scarce information provided by the manufacturers, several equations have been developed for the relation between cycle life and ΔDoD. Thaller & Lim [71] have summarised the most popular equations describing the cycle life vs. ΔDoD in their literature research. The equations were primarily used to describe the cycle life of NiCd cells, but have also been applied on lead-acid cells. The most popular equation was

$$N(\Delta DoD) = N_0 \cdot e^{\alpha(1-\Delta DoD)} \quad (4.17)$$

where N is the cycle life for a given ΔDoD, and N_0 and α constants which have to be determined with cycle life data. Another equation which was used to describe the cycle life of NiCd cells is [71]:

$$N(\Delta DoD) = B \cdot \frac{1 - \Delta DoD}{\Delta DoD} \quad (4.18)$$

with B as a constant. Drouilhet & Johnson [72] also proposed a model for the cycle life of NiCd cells. In their model it is assumed that not only the cycle life of the cells is dependent on the ΔDoD, but the charge-throughput as well. The amount of charge a cell can process in its lifetime is assumed to become less when the cell is discharged deeper. A reference ΔDoD is chosen and the charge-throughput is determined from the reference condition. The cycle life was then calculated with a best-fit equation for the manufacturer data, which was a combination of equation 4.17 and 4.18 [72]:

$$N(\Delta DoD) = u_2 \left(\frac{\Delta DoD_R}{\Delta DoD} \right)^{u_0} e^{u_1 \left(1 - \frac{\Delta DoD}{\Delta DoD_R} \right)} \quad (4.19)$$

where u_0 , u_1 and u_2 are constants and the reference ΔDoD is given by ΔDoD_R . Rosenkranz [73] also used manufacturer data to model the cycle life of a cell, but for a few different cell chemistries including Li-ion. The following equation was proposed and fitted over data obtained from manufacturers [73]:

$$N(\Delta DoD) = \frac{u_0}{(\Delta DoD)^{u_1}} \quad (4.20)$$

with u_0 and u_1 as fitting parameters. All the above equations are, however, obtained from tests in which fully charged cells are discharged with the desired ΔDoD . So it is unclear if cycling at a lower SoC will produce the same curves. Furthermore the tests do not account for regenerative braking, which will frequently occur in EV applications. Finally, a cycle is defined as a discharge from 100% SoC with a certain ΔDoD , followed by a full recharge. A cycle is not defined in the case of cycling at lower SoC with shallow ΔDoD .

Millner [3] proposed a model based on crack propagation, which was capable of modelling cycling at lower SoC and regenerative braking. To differentiate between capacity fading due to high SoC and deep discharge, the average SoC over an arbitrary period and the deviation from that average SoC are used as parameters. The average SoC and SoC deviation is defined as [3]

$$SoC_{avg} = \frac{1}{\Delta t_m} \int_{t_{m-1}}^{t_m} SoC(t) dt \quad (4.21)$$

$$SoC_{dev} = 2\sqrt{3} \cdot \sqrt{\frac{1}{\Delta t_m} \int_{t_{m-1}}^{t_m} (SoC(t) - SoC_{avg})^2 dt} \quad (4.22)$$

where SoC_{avg} and SoC_{dev} are respectively the average SoC over a time interval and SoC deviation from the average SoC during the time interval. SoC_{dev} varies between 0 (0% ΔDoD) and 1 (100% ΔDoD). The time interval Δt_m is the time between t_m and t_{m-1} , where Δt_m is arbitrary chosen. The chosen time interval must include both discharge and recharge, but it is possible to contain multiple cycles of discharging and charging. In this model a cycle is defined as period of discharge followed by a period of recharge up to the point discharge starts again. To account for multiple cycles in a time interval, the number of cycles equivalent to a full discharge and recharge, i.e. effective throughput cycles, is used. To determine the number of effective throughput cycles in Δt_m , the following equation is used [3]:

$$n_m = \int_{t_{m-1}}^{t_m} \frac{|I(t)|}{2Q_R} dt \quad (4.23)$$

with n_m as the effective throughput cycle in time interval Δt_m , $SoC_{dev,m}$ the SoC deviation in that time interval, I the current and Q_R the rated capacity of the cell. The factor 2 is due to the fact that both discharge and charge currents are integrated. With the use of Zhurkov's model for crack

4 Capacity fading model for SoH determination

propagation [75], [3] proposed an equation for the incremental capacity fading for cycles centred at 50% SoC:

$$\xi_1 = K_{co} \cdot n_m \cdot e^{\left(\frac{(SoC_{dev}-1)}{K_{ex}} \cdot \frac{T_{ref}}{T}\right)} + 0.2 \frac{\Delta t_m}{t_{life}} \quad (4.24)$$

where K_{co} and K_{ex} are constants, T_{ref} the reference temperature and T the cell temperature, both in Kelvin, t_{life} the estimated calendar life at reference temperature, and ξ_1 is the incremental capacity fading. Equation 4.24 does not account for the influence of the average SoC, which is taken into account by the following equation:

$$\xi = \xi_1 \cdot e^{\left(K_{soc} \left(\frac{SoC_{avg}-0.5}{0.25}\right)\right)} \cdot (1 - L) \quad (4.25)$$

in which K_{soc} is a constant and L is the life ageing parameter. The life ageing parameter is defined as the fraction of rated capacity that has faded. So a life ageing parameter of 0.2 corresponds to 80% rated capacity left at reference conditions. With the life ageing parameter equation 4.25 takes the concentration of lithium ions left in active form into account that can still contribute to capacity fading. Equation 4.25 corresponds to the Tafel equation, which is used to model overcharge and high SoC. This will be described in paragraph 4.4.3.

Up to this point all the equations in this paragraph assume that the capacity fading is worse when ΔDoD is larger. However, in [52] LiCoO₂ cells have been tested under constant current discharge with different ΔDoD and the capacity fading in all cells was observed to occur at the same rate.

Peterson et al. [40] also came to the conclusion that the ΔDoD was not a factor in accelerating capacity fading. State of the art LiFePO₄ cells were cycled with different ΔDoD under a dynamic current profile and a constant current profile. The dynamic profile simulates a real driving cycle with regenerative braking. The tests have been conducted at room temperature with pulses up to 3C. The capacity fading was found to be linearly decreasing with the amount of charge in Ah or energy in Wh the cell had processed independent of the ΔDoD . The capacity fading from the constant current profile was observed to be less than for the dynamic profile, with approximately a factor two difference. Consequently, the charge or energy processed with a constant current profile were multiplied by a correction factor cf .

4.4.3 Stress factor: overcharge/SoC

When the SoC of a battery cell is high, the cell contains more energy and is therefore more reactive. Furthermore, when a cell is overcharged, unwanted side reactions occur. The side reactions are described in paragraph 3.4.3.1. In literature both effects are described using the Tafel equation [67]:

$$\sigma_{SoC} = \sigma_{SoC,0} \cdot e^{\left(\frac{\alpha F}{RT}V\right)} \quad (4.26)$$

where σ_{SoC} is the stress factor for the SoC, $\sigma_{SoC,0}$ is a constant, α the charge transfer coefficient, F the Faraday constant, R the gas constant, T the temperature in Kelvin and V the cell voltage instead of the overpotential. The higher the SoC of the cell, the higher the cell voltage will be and more severe capacity fading will occur. During storage the cell voltage, which occurs at high SoC, has a large negative influence on capacity fading. So when the cell is kept at a high SoC, the stress factor will be large.

Cells which are continuously cycled will less influence from high SoC. For Li-ion cells the discharge curve has a large linear region and is very flat. High cell voltage will therefore only be experienced in a small region near 100% SoC. To optimize cycle life, manufacturers specify a maximum charging voltage. The battery management system (BMS) will make sure the cell voltage will not exceed the maximum voltage level, so no overcharge will occur. Furthermore, due to the continuously changing SoC during cycling, the average SoC is assumed to be constant in this first approximation. The constant stress factor σ_{SoC} will then be incorporated in the capacity fading rate and does not have to be modelled separately.

4.4.4 Stress factor: C-rate

Large currents, and thus large C-rates, can cause unwanted side reaction in Li-ion cells. These side reactions are described in paragraph 3.4.2. In figure 4.2 an example of capacity fading due to high C-rates is given. However, in the experiment a distinction between rate capability loss and true capacity fading is not made [52]. The capacity fading due to high C-rates could be a result of rate capability loss. It could also be attributed to the temperature degradation mechanisms, since a higher C-rate will cause ohmic heating, resulting in temperature rise.

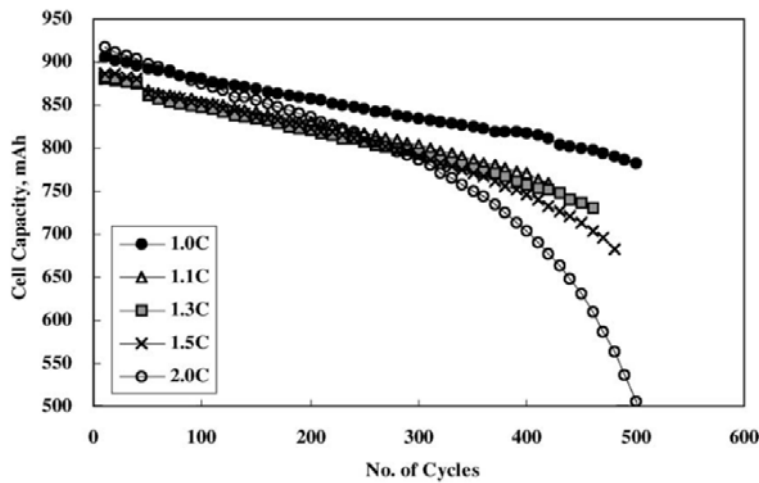


Figure 4.2: An example of accelerated capacity fading due to higher C-rates [52].

Lithium plating, resulting from high charging currents, is rarely taken into account in existing capacity fading models. This effect will also occur during charging at low temperature and overcharge, as described in paragraph 3.4. In literature no equation has been found describing lithium plating. Also no semi-empirical equations have been found describing accelerated capacity fading as a result of high C-rates that make a distinction between rate capability loss and true capacity fading. Nevertheless, to take the effect of high C-rates into account, a second order equation as proposed by [77] is used:

$$\sigma_I = k_3(\xi) + k_4(\xi) \cdot I + k_5(\xi) \cdot I^2 \quad (4.27)$$

with σ_I as the C-rate stress factor, k_3 , k_4 and k_5 as parameters dependent on the amount of capacity fading and I the current in C-rate. Equation 4.27 is purely empirically and has no physical meaning, since no model has been found in literature describing the C-rate stress factor. Therefore the C-rate stress factor is often neglected [4]. For low temperature charging and high charging rates the C-rate effect can, however, not be neglected, since it will have a significant effect on the capacity of the cell [50].

4 Capacity fading model for SoH determination

4.4.5 Modelling choice of stress factors

Many degradation mechanisms cause capacity fading in a battery cell. These degradation factors are accelerated or induced by the stress factors temperature, ΔDoD , SoC/overcharge and C-rate. The influences of some stress factors are more profound than others, and this will be reflected in the capacity fading. Therefore some stress factors will be ignored or simplified in the capacity fading model, while others have to be taken into account.

From literature the temperature was determined to be an important stress factor on capacity fading, which was modelled with the Arrhenius equation. The activation energy in the Arrhenius equation has been found to change with the amount of capacity fading, but a clear relation was not distinguishable. Therefore the activation energy will be taken as a constant for the first approximation.

The literature on the ΔDoD dependence of Li-ion cells has been contradictive. Some authors claim the ΔDoD plays an important role in accelerated capacity fading, while others claim that high ΔDoD does not have an accelerated effect and the capacity fading is only dependent the charge or energy processed. A possible reason is the different Li-ion chemistries used in the experiment. The capacity fading as a function of charge or energy processed has, however, not been measured by the authors stating the accelerated capacity fading influence of ΔDoD . Also these experiments were conducted at a constant current discharge from 100% SoC, ignoring regenerative braking and partial recharge.

However, the energy processed is an ambiguous parameter; the energy processed can be determined based solely on the open-circuit voltage (OCV) or include the power dissipation by the internal cell impedance. The energy processed determined with the terminal voltage does not include the power dissipation, and the voltage drop during discharging is compensated with a voltage rise during charging. However, the internal cell impedance for discharging and charging are not the same, and the energy processed determined with the terminal voltage will lead to offsets compared to the energy processed determined with the OCV. So the actual energy processed with or without the power dissipation cannot be directly measured. On the other hand, the charge processed can be directly measured and with a coulombic efficiency of approximately 100% the measured charge processed by the cell is practically equal to the actual charge processed by the cell. Therefore the ΔDoD stress factor will initially be ignored and the capacity fading will be dependent on the charge processed.

It is clear that when cells are overcharged, the life of the cell is strongly reduced. In the model the battery cells are assumed to be controlled by a BMS, which will keep the cell within the specified voltage levels and prevent overcharging. High SoC will also induce accelerated capacity fading, which has been shown for storage. On the other hand, during cycling the SoC varies constantly and the average SoC is assumed to be constant; it is difficult to determine the effect of the SoC. Therefore the SoC influence is ignored as a first approximation.

From experiments the C-rate was shown to have a large influence on the capacity fading. Some authors neglect the C-rate effect and contribute the accelerated capacity fading to the temperature stress factor. In other experiments high C-rates at low temperatures were observed to cause a different degradation mechanism than the temperature rise degradation. So the C-rate stress factor cannot be ignored. However, no semi-empirical or empirical equation describing the effect of high C-rates has been found in literature. A second order polynomial will therefore

be used just like [77], but neglecting the capacity fading dependence of the parameters as a first approximation.

From the analysis of stress factors, the temperature and C-rate are chosen to be taken into account in the capacity fading model. The stress factors are initially assumed to be independent of each other, so the stress factor coefficient is a multiplication between several factors. By combining equation 4.16 and 4.27, the stress factor coefficient becomes

$$k_\sigma = k_2 \sigma_I \sigma_T = k_2 \cdot (k_3 + k_4 I + k_5 I^2) \cdot e^{\left(-\frac{E_a}{R} \left(\frac{1}{T} - \frac{1}{T_{ref}}\right)\right)} \quad (4.28)$$

where k_2 is a scaling constant for reference conditions and stress factors σ_T and σ_I will be 1 under reference conditions. The parameters for the stress factor coefficient have to be determined experimentally and are different for each type of Li-ion cell. Even if the Li-ion cell types are the same, the parameters will most likely differ for different manufacturers. By conducting capacity fading experiments under different influences, the parameters can be extracted from the measurement results.

4.5 Chosen literature-based capacity fading model for SoH determination

In capacity fading a distinction between rate capability losses and true capacity fading can be made. Rate capability losses are dependent on the current and become larger as the internal resistance of the cell grows. True capacity fading is not dependent on the current, and reflects the loss of lithium ions and active material.

In this chapter true capacity fading rate models have been investigated and combined to construct a complete model based on existing models in literature. The constructed model is able to describe the rate of capacity fading under the relevant stress factors. For a given end of life (EoL) condition, the state of health of a battery cell can then be determined using the capacity fading model. Several definitions exist for the SoH, which produce different results. The desired definition for the SoH depends on the requirements, application or parameter of interest.

4.5.1 Chosen capacity fading model

From the different SoH throughput models on capacity fading, the damage accumulation model is chosen to determine the capacity fading and SoH of the cell. An equation consisting of a quadratic and linear equation was chosen to describe the capacity fading rate, which could not be factorised. Therefore the PM rule model and damage accumulation model are not compatible.

The parameters in the capacity fading rate model are dependent on stress factors. From the stress factors the temperature and C-rate were chosen to be included in the model. Combining the chosen equations 4.14 and 4.28, the capacity fading under different stress factors can be determined by

$$\xi = \sum_i^E \Delta \xi_i (\Delta Ah_i, \xi_{i-1}) = \sum_i^E \left(\frac{1}{2} k_{\sigma,i} \Delta Ah_i^2 + \Delta Ah_i \sqrt{k_1^2 + 2k_{\sigma,i} \xi_{i-1}} \right) \quad (4.29)$$

$$k_{\sigma,i} = k_2 \sigma_{I,i} \sigma_{T,i} = k_2 (k_3 + k_4 I + k_5 I^2) e^{\left(-\frac{E_a}{R} \left(\frac{1}{T,i} - \frac{1}{T_{ref}}\right)\right)} \quad (4.30)$$

4 Capacity fading model for SoH determination

The total capacity fading ξ is the amount of capacity fading sustained under reference conditions. Parameters k_1 to k_5 are constants and do not change with changing stress factors. The total capacity fading will be a summation of the capacity fading sustained of E events. During each event the stress factors are constant and are assumed to be independent of capacity fading. After the parameters in equation 4.29 and 4.30 have been determined, the capacity fading can be calculated from the charge processed and sustained capacity fading. Also the capacity fading for a given load profile can be predicted.

4.5.2 SoH determination with capacity fading

In this work capacity fading is chosen for the SoH determination of a battery cell. With equation 4.29 and 4.30, the SoH of a cell can be calculated with a predetermined EoL condition. The EoL condition depends on the application, but by convention this is set at 80% of the rated capacity. If the EoL condition is only dependent on the true capacity fading and not the rate capability losses, the SoH in percentages is expressed as:

$$SoH_{\xi} = \left(1 - \frac{\xi}{0.2Q_R}\right) \cdot 100\% \quad (4.31)$$

where Q_R is the rated capacity of the cell, ξ the amount of capacity fading under reference conditions and SoH_{ξ} the state of health of the cell from a capacity fading point of view. From a user's point of view the SoH_{ξ} is the most important, since it reflects the current capacity under reference conditions, which determines the cell runtime. From an owner's point of view, how long the cell will last before the EoL is reached is of greater importance. This is not directly reflected by the SoH_{ξ} unless the capacity fading rate is linear. To obtain the SoH in respect to the charge throughput of the cell, equation 4.31 is adjusted. With equation 4.12 and 4.28 this will become

$$SoH_{Ah} = \left(1 - \frac{Ah(\xi)}{Ah(0.2Q_R)}\right) \cdot 100\% = \left(1 - \frac{-k_1 + \sqrt{k_1^2 + 2k_{\sigma}\xi}}{-k_1 + \sqrt{k_1^2 + 0.4k_{\sigma}Q_R}}\right) \cdot 100\% \quad (4.32)$$

with Ah the amount of charge processed for a given amount of capacity faded and k_{σ} the stress factor coefficient relative to reference conditions. SoH_{Ah} can be determined with the same information as SoH_{ξ} and reflects the charge the cell can still process before the EoL is reached. SoH_{ξ} and SoH_{Ah} are only equivalent if the damage development is linear. To determine either of SoH, the damage rate has to be known. Depending on the application or desired parameter, either the SoH_{ξ} or SoH_{Ah} can be used.

In this chapter the individual effects on true capacity fading have been investigated. The rate capability losses are not taken into account as the losses are dependent on the development of the internal impedance. On the other hand, according to the US Department of Energy (DOE) National Laboratory battery test manual [12], the cell capacity is determined under a constant current discharge until the minimum voltage is reached. Cell capacities tested with US DOE battery test manual include the rate capability losses, which would change the SoH equation 4.31 into:

$$SoH_{\xi} = \left(1 - \frac{\xi + (SoC_{f,Ah} - SoC_{f,0}) \cdot (C_R - \xi)}{0.2Q_R} \right) \cdot 100\% \quad (4.33)$$

where $SoC_{f,Ah}$ is the end of discharge (EoD) SoC after an certain amount of Ah has been processed corresponding to capacity fading ξ and $SoC_{f,0}$ the EoD SoC for a fresh cell. Both the $SoC_{f,Ah}$ and $SoC_{f,0}$ are the thermokinetic SoC, which is not dependent on the current and determined by the OCV. The $SoC_{f,Ah}$ and $SoC_{f,0}$ can be determined using:

$$V_{oc}(SoC) = IZ_{ref}(SoC, Ah) + V_{min} \quad (4.34)$$

Here V_{oc} is the SoC dependent open-circuit voltage, I the current in Amps, Z_{ref} the internal impedance under reference conditions and V_{min} the EoD cut-off voltage which is specified by the manufacturer. The internal impedance Z_{ref} is dependent on the SoC and grows with increasing cycling. After determining the charge processed Ah corresponding to capacity fading ξ , the SoC dependent Z_{ref} can be determined and the EoD SoC can be extracted from equation 4.34. The equations for V_{oc} and Z_{ref} will be given in the next chapter, as this chapter only focuses on the capacity fading.

The conclusion is drawn that no general definition exists for the SoH of a Li-ion cell. The SoH can be determined using the capacity fading SoH or the charge throughput SoH. Only if the damage development is linear with the charge processed, both SoH definitions are equivalent. Furthermore the capacity fading SoH can be divided in the true capacity fading and the capacity fading with rate capability losses. The rate capability losses are dependent on the development of the internal impedance and the amplitude of the testing current. Depending on the application, parameters of interest or requirements, the appropriate SoH definition can be chosen.

5 Practical circuit-based model including ageing effects

In literature many different models predicting the behaviour of Li-ion cells have been developed. However, for an electric vehicle (EV) system engineer an equivalent circuit-based model is most preferable, since the model can be directly connected to electrical circuit models of other components in a system. Electrical circuit models of battery cells are classified as performance-based models [4]. The performance-based models can further be distinguished by their modelling approach. The most common types are impedance-based and Thevenin-based models.

Impedance-based models are mainly used by electrochemical engineers to describe electrochemical processes with an electrical circuit model. Impedance-based models are extracted from Electrochemical Impedance Spectroscopy (EIS) measurement on a battery cell. The impedance response of the cell is measured at a large range of frequencies and modelled to Randles circuit. With the obtained Nyquist plot, the value of each circuit component in Randles circuit can be determined for the conditions the cell was measured at. Each circuit component corresponds with one or more electrochemical processes in the cell and the model becomes more accurate when a higher order Randles circuit is used.

Thevenin-based models are more commonly used by electrical and electronic engineers to describe the voltage behaviour of a cell. By measuring the voltage response of a battery cell to current variations an electrical circuit model is constructed. The order of the circuit is determined by a trade-off between model complexity and accuracy. Furthermore, each circuit component can be described by nonlinear equations, which complexity also depends on the desired accuracy. Consequently, the optimal trade-off between model complexity and accuracy for a practical circuit-based model has to be investigated.

This chapter will start with an extensive literature review on existing electrical circuit models for Li-ion cells and ageing influences on the voltage response. Then the most common electrical circuit models are described in more detail and combined to obtain an accurate practical circuit-based model. Each circuit component consists of nonlinear equations modelling the circuit component value under different operating conditions. An overview of available equations modelling the change in circuit component values is given including ageing effects. Finally practical circuit-based model is constructed based on the equations found in literature.

5.1 Lithium ion cell models including ageing effects: a literature review

The behaviour and performance of Li-ion cells have been described by many different models. It is, however, important that the model can be directly connected to a model of the rest of an electric vehicle (EV) system. Therefore the focus of the literature review will be on equivalent circuit-based models for Li-ion cells, as these can be directly connected to an EV system circuit model and have a low complexity.

A Li-ion cell is, however, an electrochemical system and insight into the electrochemical processes in the cell is required to be able to understand the ageing in a cell. Also empirically based analytical models will provide a description of the performance development in a cell due to ageing. Furthermore, to bridge the gap between electrical circuit-based models and electrochemical models, impedance-based models are used. Impedance models give a simple description of electrochemical processes in a cell with electrical circuit components. Depending on the state of the cell, electrochemical processes will occur at a different rate or different

processes will occur. The changes in the electrochemical processes can then be described by changing the component values in the impedance-based model.

By only taking the relevant Li-ion cell models into account, the literature review can be divided into three parts. First electrochemical and analytical models will be described. Only the models which include ageing effects will be reviewed. Next an overview of impedance-based models will be given, with the focus on impedance-based models including or describing ageing effects. The desired model is an equivalent circuit-based model. To be able to choose the best equivalent circuit-based model for modelling Li-ion cells, existing equivalent circuit-based models will be summarized. Finally an analysis on the investigated models will be conducted.

5.1.1 Electrochemical and analytical models with ageing

Similar to capacity fading, performance ageing effects in Li-ion cells are either the result of storage (calendar ageing) or usage (cycling ageing). Thomas et al. [79] have developed an analytical model to describe the calendar ageing. Experiments have been conducted with NCA cells, which were kept at different SoC and temperatures. The focus of the study was power fading, which was found to be linear with the power of 3/2 over time. The battery kept at 100% SoC did not show the same trends as the other SoCs and degraded more severely, which suggests at high SoC another degradation mechanism was present. It was concluded that higher temperatures or SoC showed faster power fading.

Hartman II [80] proposed an electrochemical model to predict the terminal voltage of a battery cell as a result of cyclic ageing. The model contains first and second order temperature corrected voltage equations. The parameters of the obtained model were determined with the ageing model. The ageing model only took cycling and the maximum charging voltage into account. Overcharge was shown to exponentially decrease the capacity of the battery cell. A quadratic ageing model was used to estimate the remaining capacity of the cell and a linear ageing model was used to derive the parameters for the voltage response model. The model was capable of predicting the terminal voltage of an ageing cell in this manner.

An electrochemical model was also proposed by Rong & Pedram [64] to calculate the terminal voltage. With the use of the Butler-Volmer equation and Arrhenius equation plus some approximations, a closed form expression for the terminal voltage is obtained. This expression is dependent on the C-rate and temperature. In this equation the internal cell resistance is an addition between the initial resistance and film resistance. The film resistance growth is proportional to the cycle number and temperature. This results in a model which is dependent on the C-rate, temperature and ageing. The full charge capacity of the cell is then dependent on the initial internal cell resistance plus film resistance growth, where the design capacity is only dependent on the initial internal resistance. A ratio between the two capacities was determined to be the SoH.

Li et al. [81] have attempted to make a complete ageing model for lithium-ion battery systems by combining electrochemical and analytical models previously developed by other authors. A model for not only one cell, but a whole battery system was developed. Capacity fading was modelled by Solid Electrolyte Interphase (SEI) layer growth, which also raises the internal resistance of the cell. The model of [64] was used to model the capacity fading. The runtime recovery effect and rate capacity effect were also taken into account in the model. Power dissipation of each cell was determined by the current profile and internal resistance. By

5 Practical circuit-based model including ageing effects

determining the heat capacity of each cell and thermal conductance between the cells, the temperature change could be calculated. Finally the runtime charge capacity for a single cell and for the whole battery system was calculated.

5.1.2 Impedance-based models with ageing

Moss [82] has studied the effect of cycling on a Li-ion polymer cell with LiCoO_2 cathode. The impedance-based model of the cell was a modified Randles circuit and consisted of a series resistance for the ionic conductivity, multiple parallel RC pairs in series for the surface film layers, one parallel RC pair describing the charge transfer on the electrode/electrolyte surface and a Warburg impedance for the particle bulk. From cycling tests the increase of the total cell impedance was contributed by the growth of surface films, decrease of ionic conductivity and structural modification of the positive electrode. The charge transfer resistance and diffusion resistance was found to rise with increased cycling.

Zhang & Wang [65] have conducted cycling tests with NCA cells and came to the same conclusion as [82]. The polarisation resistance and Warburg coefficient was found to grow with the square root of the cycles. With a three-electrode impedance measurement the cathode was found to be mainly responsible for the impedance rise due to cycling, with the surface layer resistance R_{SEI} the most influential of the impedances. The charge transfer resistance R_{ct} grew with the fastest rate, but was not as significant as R_{SEI} .

Abraham et al. [83] used NCA cells and concluded that the ohmic resistance was almost invariant with the temperature, whereas the polarisation resistance strongly depended on the temperature with the Arrhenius equation. This resulted from improved electrode interfacial kinetics. The activation energy was not dependent on the temperature and was found to be similar for fresh and aged cells.

Suresh et al. [84] have investigated the low temperature behaviour of a LiCoO_2 cell. The impedance-based model was similar to the other impedance-based models, with an inductance-resistance pair added to the circuit. The inductance was, however, found to be of geometrical origin and not electrochemical, so it was independent from the battery parameters. From experiments the ohmic resistance was found to be invariant with the temperature, whereas the polarisation resistance follows the Arrhenius equation. The polarisation resistance is split into R_{SEI} and R_{ct} , where R_{SEI} was nearly invariant with the SoC and R_{ct} strongly dependent on the SoC. The activation energy of R_{SEI} at high SoC was different than lower SoCs, but nearly invariant for R_{ct} . An equation for the temperature dependence of R_{ct} was obtained with the Butler-Volmer equation.

This behaviour at low temperatures was confirmed by Zhang et al. for a nickel-based mixed oxide cathode Li-ion cell [85] and a commercial LiCoO_2 cell [86]. R_{ct} became significant higher than the ohmic resistance and R_{SEI} at low temperatures, especially at low SoC. This could lead to charging difficulties at low temperatures.

5.1.3 Equivalent circuit-based models

Liaw et al. [87] have proposed a model for Li-ion batteries in the form an ohmic resistance in series with one parallel RC pair, i.e. a first order equivalent circuit-based model. The ohmic resistance was taken as constant over the entire SoC range, whereas the polarisation resistance was an addition of SoC dependent equations. The model was verified with a calendar ageing experiment with NCA cells and the parameters in the polarisation resistance equation were found to be variable with the ageing time.

On the other hand, Haifeng et al. [88] discovered in their research that the polarisation resistance was nearly invariant as a result of cycling, whereas the ohmic resistance rose with increasing cycle number. The ohmic resistance grew nearly linear under ideal conditions and low ΔDoD , while under high ΔDoD , C-rate or temperature the resistance growth was slightly quadratic. The ratio of the ohmic resistance of an aged and new cell was then taken as a measure for the SoH. With second order equivalent circuit-based model the voltage behaviour of the cell was simulated.

Hu et al. [89] proposed an equivalent circuit-based model without the order being fixed and conducted tests with a state of the art LiFePO₄ cell. The open-circuit voltage (OCV) was described by an addition of two exponential functions, dependent on the SoC. The model included the hysteresis effect on the OCV, which was dependent on the temperature and current direction. From experiments it could be concluded that the model parameters for charging differed from discharging.

Benger et al. [90] have linked a Thevenin-based circuit to an impedance-based model. A second order equivalent circuit was used, in which the first parallel RC pair represented the charge transfer interface and the second the drop in voltage due to reduction in active material as a result of the lower diffusion rate; the second RC pair was a simplified representation of the Warburg impedance. The OCV was found to be independent of temperature, current amplitude and current direction.

Chen & Rincón-Mora [91] have combined the Thevenin-, impedance- and runtime-based electrical models into an equivalent circuit-based model to obtain the advantage of each electrical circuit model. Empirical equations for each circuit component were obtained from observing the measurement data of Li-ion polymer cell. This resulted in an addition of an exponential equation and a 3rd order polynomial for the OCV and exponential equations for the other components.

Zhang et al. [92] have adjusted the model in [91] by making the capacitance that represented the battery capacity variable. The current effect and recovery effect were included by adding Rakhmatov et al.'s model [93]. An analytical expression considering the electrochemical interface reaction rate and diffusion rate was added to the original equation for the cell capacity.

Erdinc et al. [94] have also expanded the model in [91] by adding the effects of temperature and capacity fading on a battery cell. The capacity fading was dependent on the calendar losses and cycling losses. Calendar losses followed the Arrhenius equation and were linear dependent on time. Cycling losses were represented by the empirical relations found in [60]. The capacity decreases linear under normal conditions and high temperatures a quadratic term was added. The internal resistance grew with the square root of cycle numbers. The OCV was corrected for different temperatures by adding a potential correction term, which was described in [95].

The equivalent circuit-based model so far only modelled the discharging behaviour of the cell, and did not take the charging behaviour into account. In EV applications, however, regenerative braking occurs during discharging and the charging behaviour also has to be taken into account. Chan & Sutanto [96] recognised the need to model the charging phase of the cell in EV applications, and introduced separate circuit components for discharging and charging. The model was expanded with additional circuit components for modelling in circuit simulation programs by Mischie & Stoiciu [97], but suffered from incapability to model fast transitions between discharging and charging states.

5 Practical circuit-based model including ageing effects

Instead of using separate circuit components for discharging and charging, Kroese & Krein [98] incorporated the current direction effect into the nonlinear circuit components. Furthermore, the model in [91] was expanded into a third order equivalent circuit to increase the accuracy. Additionally, instead of the exponential equations for the circuit components, 6th order polynomials were used. The current effect, OCV correction and cycle losses were reported to be included in the model, but equations were not given.

5.1.4 Analysis literature review Li-ion cell models

Many authors have shown that the performance of Li-ion cells worsens with ageing, but different models have been proposed to describe the ageing effect. The calendar power fading was found to be dependent on the power of 3/2 with time and modelled with analytical expressions. High SoC and temperature contributed to the accelerated calendar power fading. From the electrochemical models and semi-empirical analytical models it can be concluded that high temperature also accelerated cycling ageing. The internal impedance was found to rise by film formation, which was more profound at high temperatures.

Impedance-based models concluded that ageing occurred as a result of the growth of surface films, decrease of ionic conductivity and structural modification of the positive electrode. This resulted in a rise in polarisation resistance and Warburg coefficient, which were found to increase with the square root of cycles. The polarisation resistance can be split up into surface film resistance and charge transfer resistance. The charge transfer resistance was found to be strongly dependent on temperature and SoC, while the ohmic resistance and surface film resistance were less sensitive to either stress factors.

All equivalent circuit-based models investigated were constructed the same way. The circuits consist of an ohmic resistance in series with a number of parallel RC pairs, which determine the order of the circuit. However, the nonlinear equations to describe the circuit components were not similar. The OCV was described with either exponential functions, second to sixth order polynomials, or a combination of those functions. The other circuit elements were described in the same way. Also the influence of several stress factors on the circuit components is differently described by the various authors. Some authors did not observe hysteresis effect or temperature dependence of the OCV, while others did. The polarisation resistance was found to rise with cycling ageing by some authors, while others only observed a rise in the ohmic resistance and not the polarisation resistance. Consequently, from experiments it has to be determined which model is valid and which effects have to be taken into account to achieve sufficient accuracy.

5.2 A practical circuit-based model

Most electrical circuit models for battery cells can be classified into two main types: Thevenin-based and impedance-based circuit models. Another important type of electrical circuit model is a runtime-based circuit model, which is capable of simulating the runtime and DC behaviour of a cell [91]. The circuit models will be respectively described in this paragraph. Each of the electrical circuit types has its advantages and disadvantages. The disadvantages can be overcome by combining the different circuit models, resulting in a practical circuit-based model capable of describing the complete battery cell behaviour and performance.

5.2.1 Thevenin-based circuit models

Thevenin-based circuit models give the cell voltage response for a given load profile. In figure 5.1 an example of a Thevenin-based circuit model is depicted. The model is good at capturing transients, but cannot predict the battery runtime. Also the DC response of the cell cannot be modelled. In its most basic form it consists of an ohmic resistance R_o for the instantaneous

voltage drop and an RC parallel network (R_{trans}, C_{trans}) modelling the transient behaviour. The open circuit voltage V_{oc} is kept at a constant level depending on the state of charge (SoC). Additional components can be added in the model to take either the DC response or battery runtime into account, but not both. For example, the battery run-time can be modelled by adding a capacitor in the circuit, but then the model is not capable of measuring the DC response [80] [88]. Also more parallel RC pairs can be added in series to the model to improve the accuracy of the model.

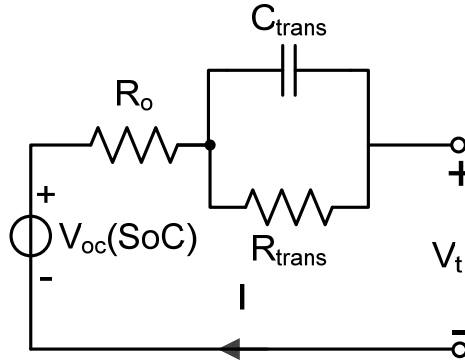


Figure 5.1: An example of a Thevenin-based circuit model

5.2.2 Impedance-based circuit models

An impedance-based circuit model is derived with an EIS measurement to obtain the AC response of a cell over a large range of frequencies. As shown in figure 5.2a, the obtained AC response is plotted on a Nyquist plot, with the real and imaginary axis representing respectively the resistance and reactance of the cell. Each data point corresponds with the impedance response at a certain frequency, and the highest frequencies are on the left side of the plot. With the use of Randles circuit, the obtained impedances can be related to electrochemical processes in the cell, which is shown in figure 5.2b.

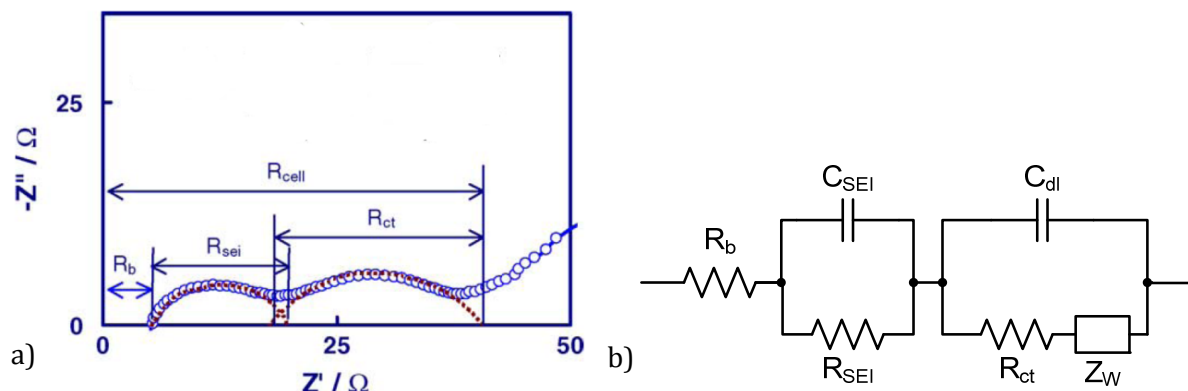


Figure 5.2: a) An example of an EIS measurement with the circuit elements identified in the AC response and b) the corresponding Randles circuit [99].

R_b is the bulk resistance of the cell, accounting for the electric conductivity of the electrolyte, separator and electrodes. R_{SEI} and C_{SEI} represent the resistance and capacitance of the surface film layer on the electrodes e.g. the solid electrolyte interphase (SEI) layer, corresponding to the high frequency impedances. The charge transfer resistance R_{ct} is related to the charge transfer between the electrolyte and electrode, and double layer capacitance C_{dl} is the capacitance between the electrolyte and electrode. These two components account for the medium

5 Practical circuit-based model including ageing effects

frequency response. Finally the Warburg impedance Z_W represents the diffusion of the lithium ions between the active material and electrolyte, corresponding to the low frequency response. Depending on the required accuracy, in the impedance-based circuit model the first parallel RC pair can be approximated with a series resistance [100] or more parallel RC pairs can be added [82]. An inductance is also sometimes added in series with the bulk resistance to describe the positive reactance response at high frequencies [65]. The positive reactance response can, however, be ignored, since its nature is geometrical and not electrochemical [84].

5.2.3 Runtime-based circuit models

Runtime-based circuit models are used to simulate the runtime of a battery. The model uses a complex circuit network to simulate runtime and DC response under a constant discharge current [91]. It can, however, not capture AC response and only a limited transient response can be modelled. An example of a runtime-based circuit model is given in figure 5.3. Runtime-based circuit models are easily to implement in circuit simulation programmes such as PSPICE.

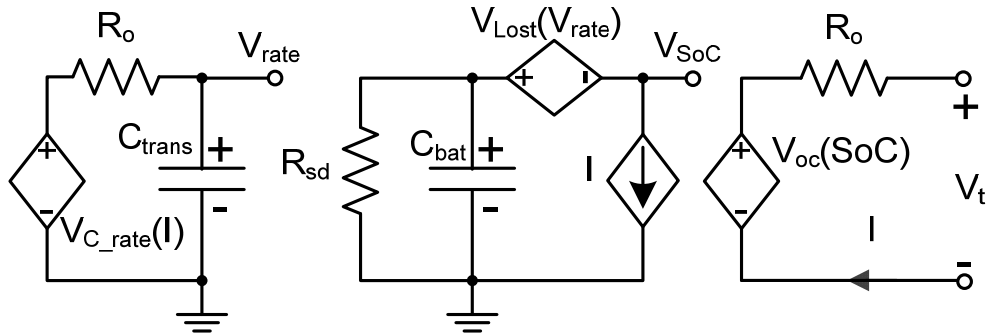


Figure 5.3: An example of a runtime-based circuit model [91]

5.2.4 Compatibility of electrical circuit-based models

An accurate equivalent circuit-based model can be constructed by combining the Thevenin-based, impedance-based and runtime-based circuit models. By combining the impedance-based circuit model with the other two circuit models, the development of the electrochemical processes and cell components can be related to the measured voltage response. Changes in the voltage response are a result of changing operating conditions, which can then be described by equations from electrochemical and analytical models through the impedance-based model.

The Thevenin-based and runtime-based model can easily be combined, since both models are based on the voltage response data. The impedance-based model is, however, extracted from EIS measurements, describing a battery cell based on the electrochemical processes or components in the cell instead of the voltage response. The timescale of the measurements is different and the impedance-based model contains a Warburg impedance. Therefore the circuit components in a Thevenin-based circuit model are not directly equivalent to the circuit components of an impedance-based circuit model.

5.2.4.1 Timescale compatibility for practical applications

To be able to combine the impedance-based circuit model with the two other circuit models, first the timescale of the voltage response and EIS measurements have to be compared. The voltage response for practical applications is measured in seconds. In figure 5.4a a typical voltage response of a current pulse is given, which is used for determining the circuit components in a Thevenin-based circuit model. The EIS on the other hand is conducted with frequencies up to several kilohertz, as shown in figure 5.4b.

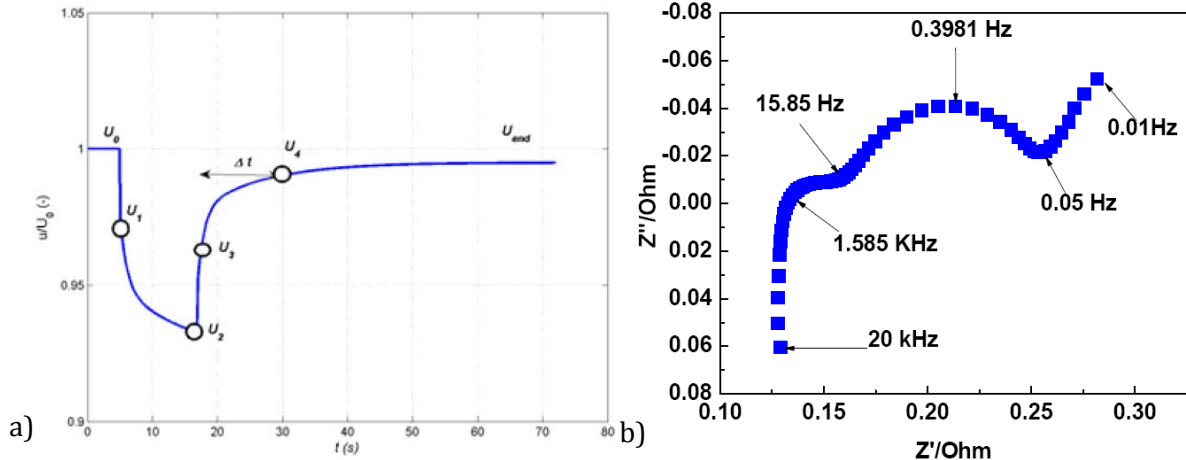


Figure 5.4: a) a typical voltage response from a Li-ion cell of a current pulse for parameter determination of a Thevenin-based model [90] and b) an example of an EIS measurement with given frequencies [82].

The double arches found in figure 5.4b correspond to the R_{SEI} and R_{ct} as described in figure 5.2a and b. From the EIS measurements it can be seen that the frequency region corresponding to the surface film layer resistance R_{SEI} is in range of several kilohertz up to tens of hertz. This means that in a practical application the voltage response of surface film layers will be indistinguishable from the bulk resistance R_b , since the voltage response due to both resistances is measured as an instantaneous voltage drop. Higher sampling rate to differentiate the R_{SEI} from the R_b is possible, but will require more energy from the battery. A trade-off between accuracy and energy usage has to be made. Kroeze & Krein [98] have investigated the influence of time constants smaller than a second and observed no impact to the model. Therefore the sampling time will be approximately one second and the series resistance R_o will contain both the surface film layer resistance and bulk resistance.

5.2.4.2 Warburg impedance for practical applications

From figure 5.2b it can be seen that the impedance-based circuit model contains a Warburg impedance, whereas the Thevenin-based or runtime-based circuit models do not. The Warburg impedance is a constant phase element with a constant phase of 45° and represents the diffusion within a battery cell, which corresponds to the low frequency slope in an EIS measurement. Since the diffusion phenomena and charge transfer phenomena occur in distinct frequency areas, the time constant of either processes can be considered to differ by at least one order of magnitude [100]. The Warburg impedance will then appear in series with the parallel charge transfer RC pair, resulting in a modified Randles circuit shown in figure 5.5a [101]. The Warburg impedance can be analytically described by a hyperbolic tangent function. Kuhn et al. [102] have, however, shown that the Warburg impedance can be simplified to multiple parallel RC pairs in series, which is shown in figure 5.5b.

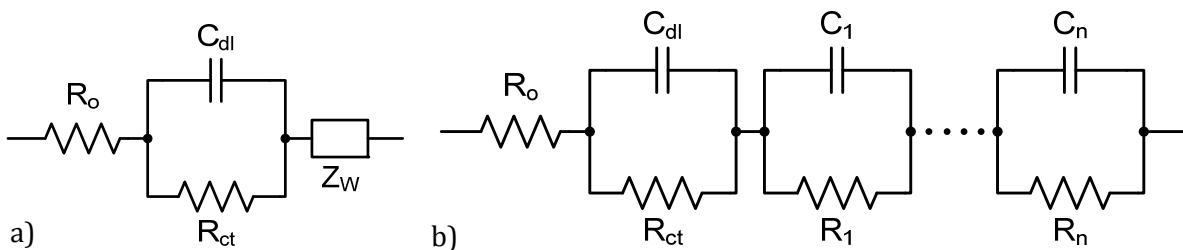


Figure 5.5: a) A modified Randles circuit representing a Li-ion cell [101] and b) a modified Randles circuit using lumped elements representing the diffusion phenomena [102]

5 Practical circuit-based model including ageing effects

The optimal number of parallel RC pairs for modelling the diffusion phenomena has been investigated by Do et al. [101]. From experiments it was concluded that one parallel RC pair accurately models the diffusion phenomena during transient periods, while during steady-state an offset arises. From EIS measurements the usage of three parallel RC pairs for the diffusion phenomena was found to be the best trade-off between accuracy and complexity.

The impedance-based circuit model in figure 5.5b is equivalent to a Thevenin-based circuit model. From the perspective of a Thevenin-based circuit model two parallel RC pairs are the best trade-off between accuracy and complexity, as the modelled voltage response errors are sufficiently low [91]. Consequently, the parallel RC pair for the short time constant represents the charge transfer process, while the RC pair for the long time constant portrays the diffusion phenomena in the cell.

5.2.5 Combined electrical circuit-based model for practical applications

A combination of the Thevenin-based, impedance-based and runtime-based circuit models will result in an equivalent circuit-based model capable of simulating battery runtime, transient, DC and AC responses. Chen & Rincón-Mora [91] have proposed a combined equivalent circuit-based model, which is shown in figure 5.6.

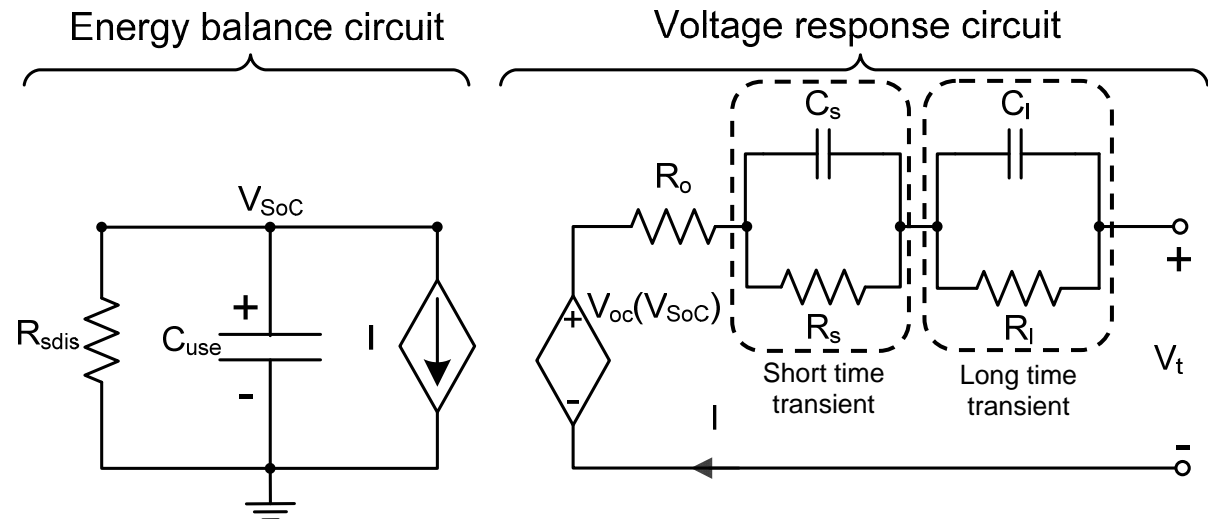


Figure 5.6: An equivalent circuit-based model capable of simulating runtime, transient, AC and DC responses [91] for practical applications.

The circuit is split into an energy balance circuit and a voltage response circuit. The energy balance part models the self discharge, the cell capacity, the amount of energy left in the cell and the battery runtime. The capacity of the battery is described by C_{use} . C_{use} is not a real capacitance, but a circuit embodiment of the useable capacity in a cell, indicated by Q_{use} . The voltage over the capacity V_{soc} is a value between 0 and 1, equivalent to the SoC of the battery cell. Therefore in the rest of this work SoC will be used instead of V_{soc} . The voltage over the capacitance will drop or rise depending on the direction of the cell current I in accordance to the magnitude of I . The resistance R_{sdis} models the self-discharge of the cell.

The voltage response part describes how the cell voltage responds to a given load current I . The open circuit voltage V_{oc} is a dependent voltage source depending on the SoC, given by V_{soc} . The ohmic resistance of the battery cell is given by R_o , which include the bulk resistance R_b and surface layer resistance R_{SEI} . R_s and C_s represent the short time constants in the voltage response, which is related to the charge transfer resistance R_{ct} and double layer capacitance C_{dl} . The long

time constants are accounted for by R_l and C_l , which is linked to a single RC pair Warburg impedance equivalence modelling the diffusion phenomena. In a practical application the circuit will also consist of a series resistance at the terminal voltage V_t representing the contact resistance of the current collectors to the external circuit and wire resistance up to the point the voltage is measured.

5.3 Determination of the nonlinear circuit components

The equivalent circuit-based model in figure 5.6 is capable of accurately simulating a Li-ion cell for any instantaneous moment with the corresponding circuit component values. Unfortunately, the values of the circuit components vary strongly over the runtime period of a cell and are dependent on many operating conditions. Also ageing of the cell will influence the circuit component values. The circuit components are therefore strongly nonlinear and are dependent on many factors. Nonlinear equations for the circuit components are mostly extracted from measurement data and are therefore empirical. The circuit components can, however, be related to the electrochemical processes within a Li-ion.

First an overview of (semi-)empirical models for the energy balance circuit will be given. The energy balance circuit include temporary and permanent capacity loss, which is dependent on many factors. Then existing equations describing the voltage response circuit components will be evaluated. Next equations for the circuit components will be determined from existing models based on a trade-off between accuracy and complexity. Finally a complete equivalent circuit model for practical applications will be proposed.

5.3.1 Energy balance circuit components

The energy balance circuit consists of a current dependent current source, a resistance representing the self-discharge and a capacitance for the useable capacity of cell. The useable capacity is not dependent on the current and related to the OCV of the cell. The capacity apparent to the user can then be numerically determined by both the energy balance circuit and voltage response circuit, as it is also dependent on the rate capability losses. The current source represents the current drawn from or fed back into the cell, i.e. the load profile over time.

5.3.1.1 Cell capacitance C_{use}

The capacitance C_{use} is equivalent to the useable capacity of the cell, for which variable Q_{use} is used. The useable capacity of the cell is dependent on the current true capacity and operating conditions. The current true capacity is the theoretically possible amount of charge that can be discharged from a fully charged cell with an infinitely small current for a given minimum cell voltage at reference conditions, so that the voltage drop over the internal resistance becomes close to zero. As explained in paragraph 3.4.1, the useable capacity of the cell is strongly dependent on the temperature. From capacity measurements in literature at various temperature the capacity of the cell was found to vary with the Arrhenius equation, resulting in [52]

$$Q_{use} = Q_{ref}(\xi) \cdot e^{\left(-\frac{E_{a,q}}{R} \left(\frac{1}{T} - \frac{1}{T_{ref}}\right)\right)} \quad (5.1)$$

where Q_{use} is the useable capacity, $E_{a,q}$ the activation energy, R the gas constant, T the current temperature in Kelvin, T_{ref} the reference temperature in Kelvin and Q_{ref} the current true capacity. The current true capacity is the initial true cell capacity minus the amount of true capacity fading

5 Practical circuit-based model including ageing effects

ξ. The determination of the amount of true capacity fading is described by equation 4.29 and 4.30.

In [52] the activation energy was found to decrease for increasing cycle numbers. Their conclusion is, however, based on comparison of the apparent capacity at a certain cycle number of different cells cycled at different temperatures, and can also be explained differently. Due to increased electrochemical kinetics, the initial capacity at higher temperatures is larger. The capacity fading rate for cells cycled at higher temperatures is worse, which will close the gap between the apparent capacity at high and low temperatures. The decrease of the relative difference of the apparent capacities will result in a decrease of activation energy. To discover the dependence of the activation energy on the capacity fading, one cell should be varied over several temperatures or cells with the same amount of capacity fading should be compared.

In paragraph 3.4.2 it was explained that the capacity of a cell would decrease with increasing C-rates. With high C-rates the diffusion rate of the lithium-ions in the cell is much lower than the electrochemical processes producing the current, resulting in the end of discharge (EoD) condition reached at an earlier stage than with lower currents. A decrease of the useable capacity as a result of increasing current is often modelled by the well known Peukert's law:

$$Q_{use} = I^k t \quad (5.2)$$

with I the current in C-rate, t the actual time to discharge the cell and k the Peukert constant. The value of the Peukert constant is different for each cell type. Equation 5.2 is, however, only valid for constant current discharge, which is rarely the case in practical applications such as electrical vehicles. Rakhmatov & Vrudhula [103] proposed a model for the decrease in useable capacity as a function of current derived from physical principles. The model is capable of modelling variable as constant current, and is given by:

$$Q_{decrease} = I \left(t_s - t_e + 2 \sum_{m=1}^{\infty} \frac{e^{-\beta^2 m^2 (L-t_s)} - e^{-\beta^2 m^2 (L-t_e)}}{\beta^2 m^2} \right) \quad (5.3)$$

The current is assumed to be constant in a certain period. In equation 5.3 $Q_{decrease}$ is the amount of energy drawn from the cell, t_s the starting time of the period, t_e the ending time, β the diffusion coefficient and L the total battery operating time. The decrease of energy in the cell is dependent on the duration of the current plus an analytical term describing the current recovery effect. The current recovery effect is the recovered capacity by discharging at a lower current or resting time. With increasing currents the useable capacity decreases, since the EoD conditions are reached faster. When the current is lowered, the diffusion rate in the cell can accommodate the electrochemical processes for current production better and the EoD conditions are reached at a lower SoC.

5.3.1.2 Self-discharge resistance R_{sdis}

The value of the self-discharge resistance R_{sdis} is a function of the SoC, temperature and the SoH of the cell [91]. At a higher SoC, temperature or cycle damage the self-discharge rate of the battery will be larger, i.e. a lower R_{sdis} . When R_{sdis} is infinite, no current will pass through R_{sdis} , which means that there is no self-discharge. Verbrugge & Conell [104] have proposed the following equation for the self-discharge rate, only taking the SoC of the cell and temperature into account:

$$I_{sdis}(T, SoC) = k_{sdis} \cdot e^{\left(-\frac{E_{a,sdis}}{R} \left(\frac{1}{T} - \frac{1}{T_{ref}} \right) \right)} \cdot SoC_{sdis} \quad (5.4)$$

where I_{sdis} is the self-discharge current, k_{sdis} a constant and SoC_{sdis} the SoC at which the cell was during self-discharge. The self-discharge for most Li-ion cells is, however, very low with only a few percent per month as shown in overview in paragraph 2.3.

5.3.2 Voltage response circuit components

The voltage response circuit contains a dependent voltage source embodying the OCV of the cell, a series resistance representing the contact resistance, bulk resistance and surface layer resistance, one parallel RC pair with a small time constant symbolising the interfacial charge transfer and another parallel RC pair with a long time constant representing the diffusion in the cell. Each circuit component is strongly dependent on the current state of the cell and operating conditions, reflecting the dependency on the voltage response.

5.3.2.1 Open-circuit voltage V_{oc}

The OCV of a cell is the voltage of the cell when it is at electrochemical equilibrium. Depending on the battery size, type and conditions, the time to reach electrochemical equilibrium varies strongly. The OCV of a Li-ion cell varies over the capacity of the cell. The OCV is therefore strongly dependent on the SoC of the cell. In figure 5.7 the OCV of a typical LiFePO₄ cell is shown.

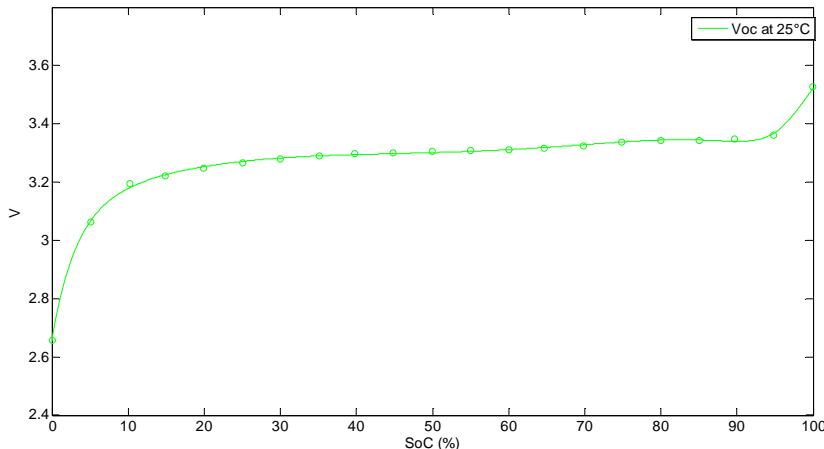


Figure 5.7: The open-circuit voltage of a typical LiFePO₄ cell

To describe the OCV mathematically, several empirical equations have been developed. One way to model the OCV is by using a double exponential function [89]:

$$V_{oc}(SoC) = a_0 + a_1(1 - e^{-a_2 SoC}) + a_3 SoC + a_4 \left(1 - e^{-\frac{a_5}{1 - SoC}} \right) \quad (5.5)$$

where a_0 to a_5 are all constants and V_{oc} the OCV. Another way of modelling the OCV is using a combination of a third order polynomials and an exponential function [91], resulting in

$$V_{oc}(SoC) = a_1 e^{-a_2 SoC} + a_3 + a_4 SoC + a_5 SoC^2 + a_6 SoC^3 \quad (5.6)$$

Instead of using an exponential function for the OCV, a sixth order polynomial has also been proposed [98]. This results in

$$V_{oc}(SoC) = a_0 + a_1 SoC + a_2 SoC^2 + a_3 SoC^3 + a_4 SoC^4 + a_5 SoC^5 + a_6 SoC^6 \quad (5.7)$$

5 Practical circuit-based model including ageing effects

Since equation 5.5, 5.6 and 5.7 are all empirical equations, it cannot be determined which equation fits the OCV the best. Furthermore, each Li-ion battery type has a different OCV behaviour. Depending on the measurements and Li-ion type one equation might yield a smaller error than the other.

From measurements in literature the OCV was found to be dependent on the temperature and exhibits hysteresis. Kroeze & Krein [98] measured a voltage drop for V_{oc} at low temperatures, shown in figure 5.8a. This variation can be approximated by a constant temperature dependent voltage deviation $\Delta V_{oc}(T)$, of which the temperature dependence is shown in figure 5.8b. The OCV can then be described as:

$$V_{oc}(SoC, T) = V_{oc,ref}(SoC) + \Delta V_{oc}(T) \quad (5.8)$$

In figure 5.8b the variation of the temperature dependent constant voltage drop ΔV_{oc} is given as $\Delta E(T)$. A reference temperature is chosen at which the open circuit voltage is determined and at that temperature ΔV_{oc} is set to 0. At lower temperatures ΔV_{oc} will drop and at higher temperatures rise. From figure 5.8b it can be seen that ΔV_{oc} can be described by a 3rd order polynomial, which would result in:

$$\Delta V_{oc}(T) = a_{t1} + a_{t2}T + a_{t3}T^2 + a_{t4}T^3 \quad (5.9)$$

with a_{t1} to a_{t4} constant parameters. Other authors however found the OCV deviation to be very small and chose to ignore it [90].

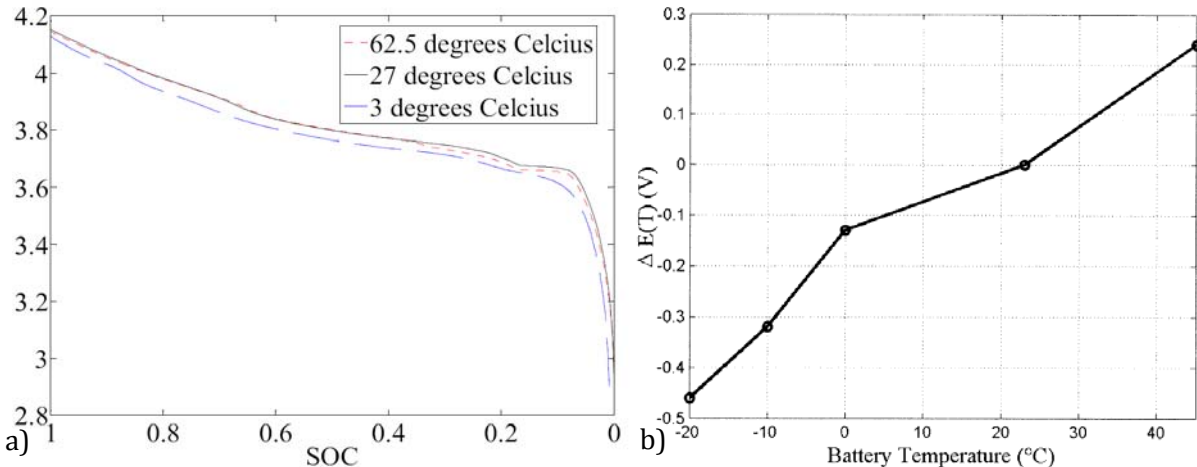


Figure 5.8: a) The open circuit voltage vs. SoC of an arbitrary Li-ion cell at different temperatures [98] and b) an example of the temperature dependent voltage drop on the open circuit voltage of a Li-ion cell [95].

It is also unclear whether the hysteresis effect of the OCV is present in Li-ion cells or that it will have a significant influence in the modelling of Li-ion cells. Hu et al. [89] proposed a first order equation to model the dynamics of the hysteresis voltage:

$$\dot{V}_h = \Gamma(T)|I|(H(SoC, sign(\dot{SoC}), T) - V_h) \quad (5.10)$$

where \dot{V}_h is the change of the hysteresis voltage V_h , \dot{SoC} the change in SoC and Γ the temperature dependent hysteresis transition factor. The hysteresis voltage V_h is added or subtracted from the OCV depending on the direction of the current. Roscher & Sauer [105] have also proposed a model for the hysteresis voltage with a recovery factor λ and hysteresis factor Ψ described by:

$$\lambda(t_{rest}) = e^{\frac{-t_{rest}}{\tau}} \quad (5.11)$$

$$\Psi = k_1 \int \frac{m_1 \cdot I_{cell}}{C_{nom}} dt + k_2 \int \frac{m_2 \cdot I_{cell}}{C_{nom}} dt \quad (5.12)$$

with t_{rest} the resting time of the cell, τ the OCV time constant assuming a first order exponential decay, k_1 , k_2 , m_1 and m_2 fitting parameters for the hysteresis eye and I_{cell} the current. The OCV is then determined by [105]

$$OCV(SoC, \lambda, \Psi) = \Psi \cdot (\lambda \cdot OCV_{1min,c}(SoC) + (1 - \lambda) \cdot OCV_{3h,c}(SoC)) + (1 - \Psi) \cdot (\lambda \cdot OCV_{1min,d}(SoC) + (1 - \lambda) \cdot OCV_{3h,d}(SoC)) \quad (5.13)$$

Here $OCV_{1min,c}$ and $OCV_{3h,c}$ are the values for the OCV determined at the specified SoC for resting times of respectively 1 minute and 3 hours during charging, and $OCV_{1min,d}$ and $OCV_{3h,d}$ in the case of discharging. To investigate whether the equilibrium OCV really experiences hysteresis or is it an effect of the slow diffusion in the cell, Doerffel [68] has tested cells with extremely long resting times during charging and discharging. The equilibrium OCV was shown to exhibit a very small voltage deviation, which could also be contributed to the inaccuracy of the measurement equipment at such a small value. Furthermore, the voltage deviation was insignificantly small compared to the voltage swing, leading to the assumption that the voltage deviation is only due to the slow diffusion rate [68].

The OCV was found to be independent of ageing, as shown in figure 5.9. In figure 5.9 the black lines are the interpolated OCV values determined with a different method than the red lines. If the OCV was plotted relative to the current cell capacity in Ah, a variation of the OCV would be observed due to capacity fading. However, for the OCV versus SoC in percentages as shown in figure 5.9, the OCV for a used cell is approximately identical to the OCV of a new cell.

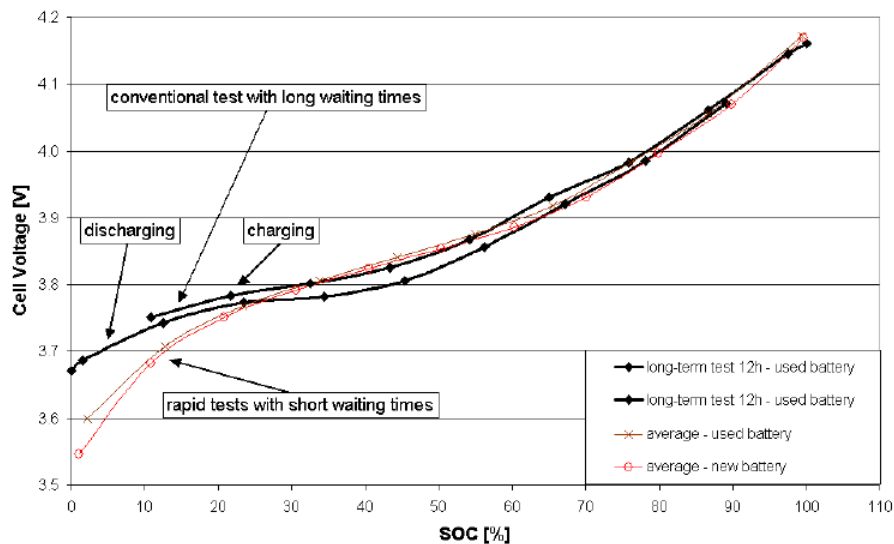


Figure 5.9: Comparison of the OCV vs. SoC in percentages for a new and aged Li-ion cell [68].

From the literature analysis on the OCV of Li-ion cells it can be concluded that the OCV is strongly dependent on the SoC, which can be empirically described by various equations. The OCV was found to be independent of the ageing in the cell for the SoC in percentages. A dependence on the current direction and temperature have, however, been observed by several

5 Practical circuit-based model including ageing effects

authors, which proposed empirical equations describing the OCV variations. Other authors have chosen to ignore the temperature and hysteresis effect. Depending on the required accuracy, the OCV can be described by equations of various complexities.

5.3.2.2 Ohmic resistance R_o

The internal impedance of the cell, consisting of an ohmic resistance and two parallel RC pairs in series, is dependent on many influences such as temperature and ageing. The internal impedance is also dependent on the SoC, as the electrochemical processes related to the internal impedance have a SoC dependence as described in paragraph 3.4.3. Furthermore, the dependence of the electrochemical processes on the C-rate has also been described in paragraph 3.4.2. From measurements by various authors it has been determined that the parameters of the circuit elements for charging and discharging differ from each other [96][98]. Therefore two sets of parameters will be necessary to describe the voltage behaviour of the cell, one for charging and one for discharging.

As described in paragraph 5.2.4, the ohmic resistance in the practical equivalent circuit-based model depicted in figure 5.6 consists of the pure ohmic bulk resistance R_b and high frequency surface layer impedance R_{SEI} . The SoC dependence of the circuit components for a discharging cell is shown in figure 5.10a.

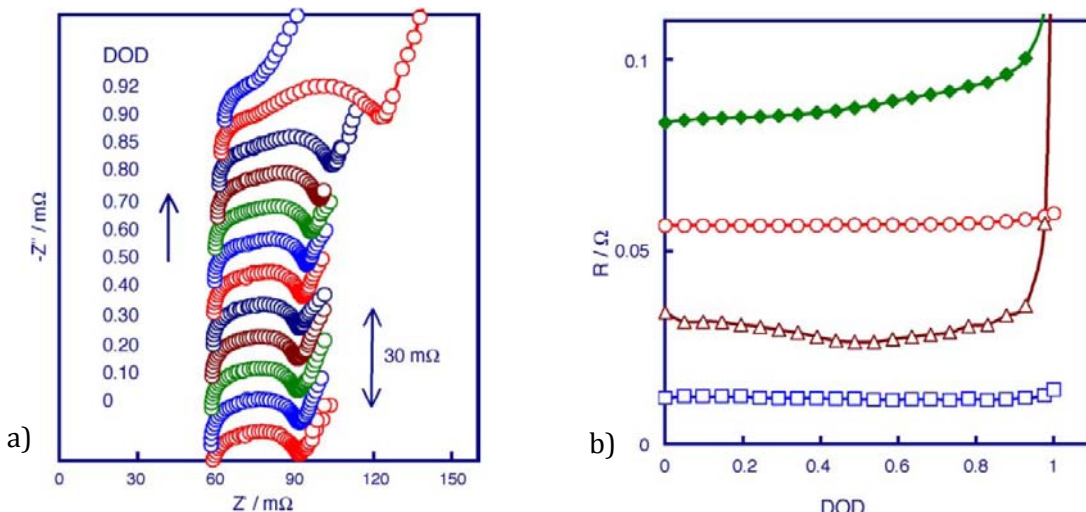


Figure 5.10: a) An EIS measurement of a typical Li-ion cell at different DoDs at 20°C with b) the resistances of the measurement plotted against the DoD with \circ is the bulk resistance R_b , \square the surface layer resistance R_{SEI} , \triangle the charge transfer resistance R_{ct} and the \blacklozenge is the sum of the three resistances [86].

In figure 5.10b the resistances have been extracted from the EIS measurement at 20°C. Here is \circ the bulk resistance R_b , \square the surface layer resistance R_{SEI} , \triangle the charge transfer resistance R_{ct} and \blacklozenge the sum of the three resistances. R_b and R_{SEI} appear to be fairly constant over the entire discharging range, except for a slight increase in value near 100% DoD (0% SoC). R_b is, however, the largest value over the entire SoC range except near 0% SoC, and will therefore greatly determine the cell resistance at room temperature.

To describe the ohmic resistance R_o (R_b+R_{SEI}) quantitatively, Chen & Rincón-Mora [91] have used data acquired from discharging measurements on a Li-ion polymer cell to obtain an empirical equation. The measurement results for the ohmic resistance are shown in figure 5.11. The SoC dependence of the ohmic resistance in figure 5.11 is consist with the EIS measurement results

in figure 5.10b. It can be seen that R_o (R_{series}) displays an exponential behaviour, with the exponential rise at low SoCs. R_o can therefore be expressed as [91]

$$R_o(SoC) = b_1 e^{-b_2 SoC} + b_3 \quad (5.14)$$

where b_1 , b_2 and b_3 are parameters to be determined from the battery cell. Zhang et al. [92] deemed equation 5.14 to be insufficient to accurately describe the ohmic resistance and expanded the equation into

$$R_o(SoC) = b_1 e^{-b_2 SoC} + b_3 SoC^3 - b_4 SoC^2 + b_5 SoC + b_6 \quad (5.15)$$

Another way to describe the SoC dependence of R_o is using a 6th order polynomial similar to equation 5.7 [98]. From figure 5.11 it can also be seen that the value of R_o is current dependent. High currents result in a high ohmic resistance. Using equation 5.14, the influence of the C-rate I can be described by [106]:

$$R_o(SoC, I) = (b_1 + b_4 I + b_5 I^2) e^{-b_2 SoC} + b_3 + b_6 I + b_7 I^2 \quad (5.16)$$

The ohmic resistance is also dependent on the temperature. In figure 5.12 EIS measurements of a Li-ion cell at different temperatures is shown. From the measurements it can be seen that R_b shows almost no change at different temperatures, while R_{SEI} (the first arch) rises at when the temperature drops. To be able to quantify the temperature dependence with the Arrhenius equation, in figure 5.13a $\ln(1/R)$ is plotted against $1000/T$ at a SoC of 60%.

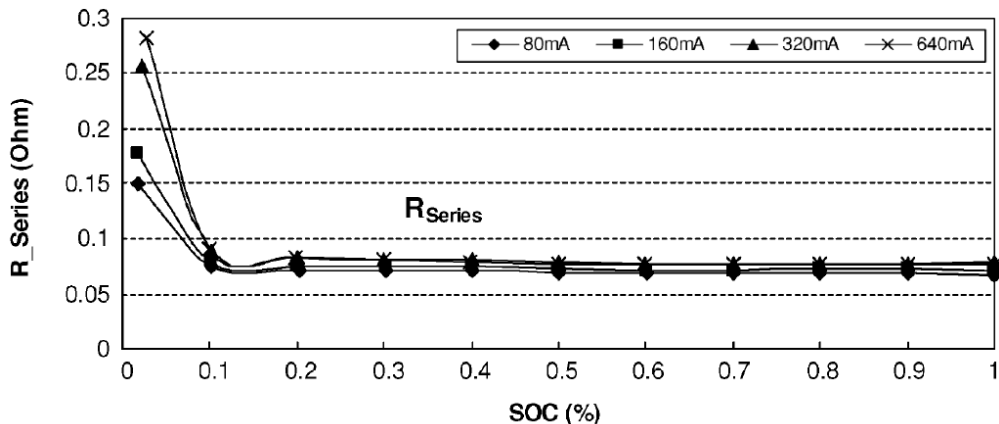


Figure 5.11: An example of the measured ohmic resistance R_o (R_{series}) vs. SoC of a Li-ion polymer cell under different currents [91].

In figure 5.13a the temperature dependences of $1/R_b$ and $1/R_{SEI}$ are curves, which suggest that they behave like the Vogel-Tamman-Fulcher (VTF) equation [86]:

$$A = A_0 e^{\frac{-B}{T-T_0}} \quad (5.17)$$

Here A_0 , B and T_0 are the parameters which have to be determined and T is the temperature. At around -15°C and higher the $1/R_b$ and $1/R_{SEI}$ start to show a linear relationship with the temperature behaviour. Since the application of the Li-ion batteries is almost exclusively at -15°C or higher, for a sufficiently high temperature the VTF equation will behave as the Arrhenius equation [107]. $1/R_b$ will be nearly invariant with the temperature, which is also confirmed by the EIS measurements in figure 5.12. Therefore the temperature behaviour of R_o is primarily determined by R_{SEI} .

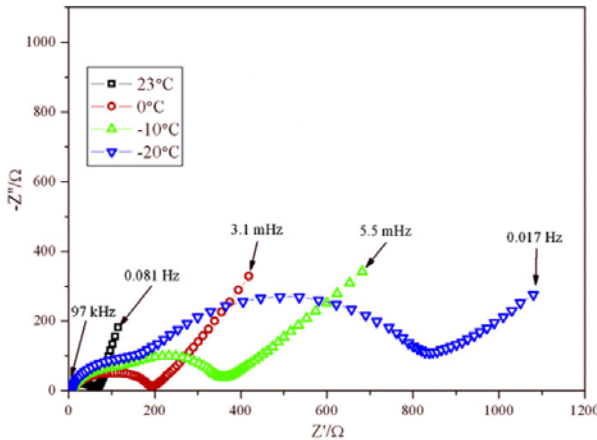


Figure 5.12: An EIS measurement of a Li-ion cell at a constant SoC at different temperatures [34].

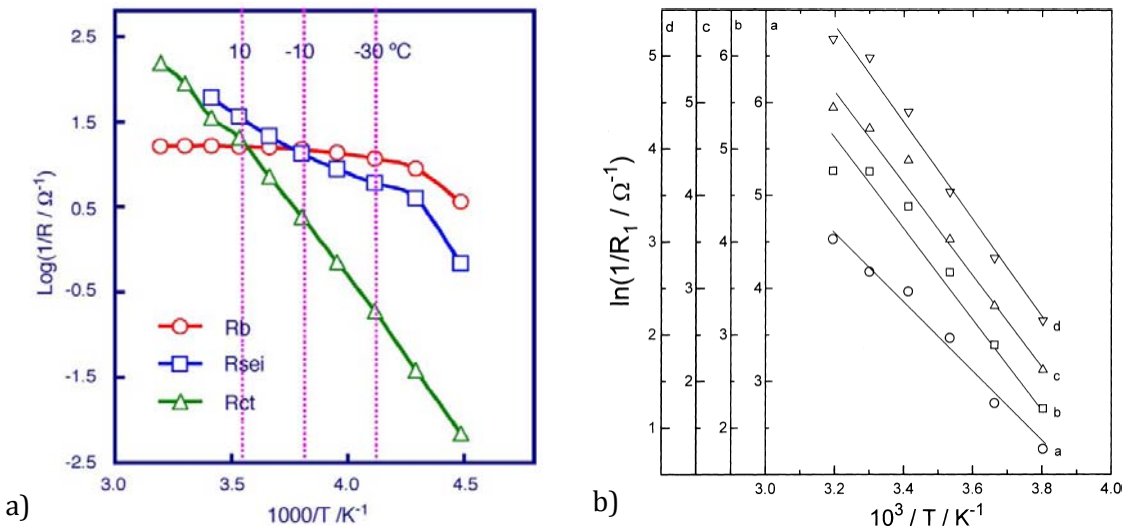


Figure 5.13: a) The temperature dependence of resistances R_b , R_{SEI} and R_{ct} for a typical Li-ion cell at 60% SoC [86] and b) the temperature dependence of R_{SEI} (R_t) at a.100% SoC b.80% SoC c.50% SoC and d.20% SoC with their corresponding vertical axis [84].

In figure 5.13b the temperature dependence of R_{SEI} (R_t) is plotted at different SoCs. From the plot it can be seen that the slope of b , c and d , which are measured at respectively 80%, 50% and 20% SoC, are similar in contrast to a (100% SoC). The slope represents the activation energy in the Arrhenius equation. The activation energy is therefore constant over the entire SoC range except near 100% SoC. Since the cell does not spend much time at 100% SoC during operation, the activation energy is taken as a constant. The ohmic resistance R_o can then be expressed as

$$R_o(SoC, I, T) = R_o(SoC, I) \cdot e^{\left(\frac{E_{a,o}}{R} \left(\frac{1}{T} - \frac{1}{T_{ref}}\right)\right)} \quad (5.18)$$

where $E_{a,o}$ is the activation energy, R the gas constant and T_{ref} the reference temperature. Equation 5.18 represents the reversible variation of the ohmic resistance. The ohmic resistance also experiences an irreversible growth as a result of cycling and storage, similar to capacity fading. The growth of the ohmic resistance will result in rate capability losses and power fading.

To model the rise of R_o due to cycling, the analysis of R_o is split into R_b and R_{SEI} . Haifeng et al. [88] observed a linear rise of the ohmic resistance, which only included R_b and not R_{SEI} . The measurement results are shown in figure 5.14. Under reference conditions R_b rises linearly, but

under adverse conditions R_b start to exhibit a slight parabolic behaviour. This can be described using a similar equation as equation 4.12:

$$R_{b,n}(\sigma, n) = b_{b1}n + b_{b2}(\sigma)n^2 \quad (5.19)$$

with b_{n1} a constant parameter, b_{n2} a parameter dependent on stress factor σ and n the number of cycles. Other authors have however determined that R_b is nearly invariant with increased cycling [65][83] or only increases linearly [80].

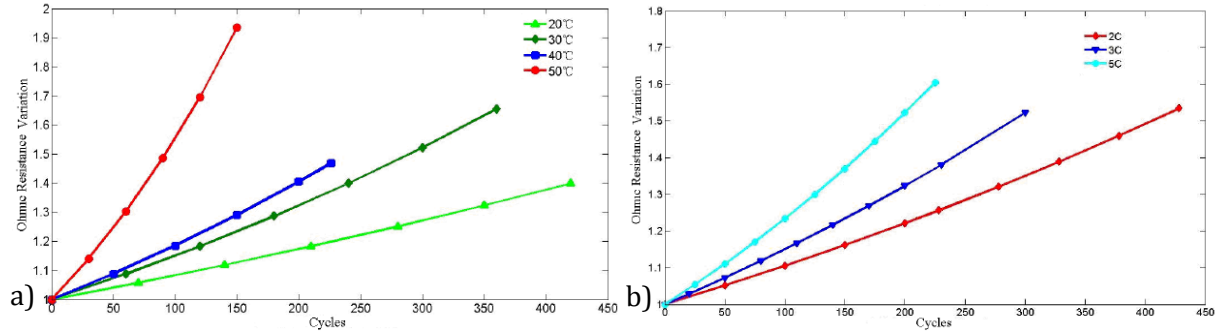


Figure 5.14: The linear behaviour of the ohmic resistance with cycle number at a) different C-rates and b) different temperatures [88].

Several authors have determined that the growth of the SEI layer is dependent on the square root of the cycle number. In figure 5.15 the development of R_{SEI} is given. From figure 5.15 it can be seen that R_{SEI} is linear dependent on the square root of the cycle number. R_{SEI} can be expressed as [65]

$$R_{SEI,n}(n, \sigma) = b_{SEI}(\sigma)\sqrt{n} + b_{SEIo} \quad (5.20)$$

where b_{SEI} and b_{SEIo} are parameters depending on the stress factors. According to Zhang & Wang [65] R_{SEI} is solely contributed by the positive electrode. Ramadass et al. [60] also used equation 5.20 to express the R_{SEI} growth as a function of cycle number, but found the limiting electrode to be the negative electrode. The film growth has also been found to be adequately described by a linear function [64] or the polarisation resistance ($R_{SEI} + R_{ct}$) to be invariant with cycle numbers [88]. Therefore similar to R_b , inconsistencies in literature exist on the R_{SEI} growth as a result of cycling, most likely due to validation on different Li-ion types.

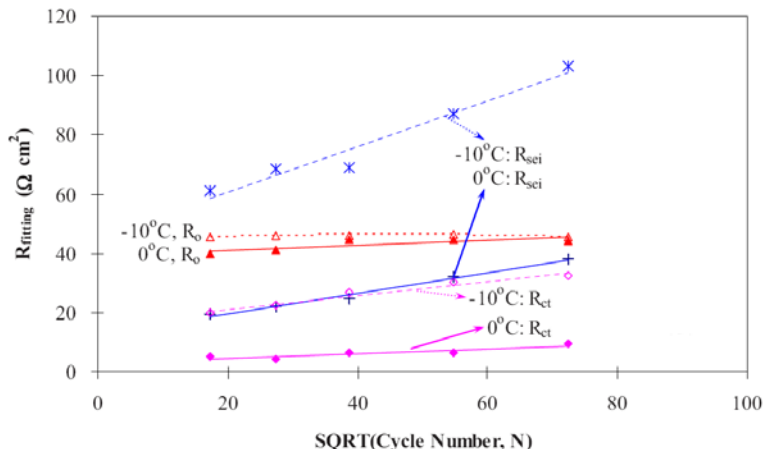


Figure 5.15: The resistances R_b (R_o), R_{SEI} and R_{ct} from an EIS measurement on an NCA cell vs. the square root of cycle numbers [65].

5 Practical circuit-based model including ageing effects

From figure 5.14a it can be seen that increasing temperature will increase the ohmic resistance growth. This can be described by the Arrhenius equation [64], which is also used to describe temperature dependence of the capacity and the reversible temperature effect on the ohmic resistance. Figure 5.14b shows that high currents also accelerate the resistance growth. The current dependence of the resistance growth has, however, not been described quantitatively in literature. Therefore a second order polynomial will be used as a first approximation as in equation 4.27, leading to the following equation to describe the irreversible growth of R_o due to cycling:

$$R_{o,n}(n, T, I) = (b_{n1} + b_{n2}I + b_{n3}I^2)(R_{b,n} + R_{SEI,n})e^{\left(-\frac{E_{a,on}}{R}\left(\frac{1}{T} - \frac{1}{T_{ref}}\right)\right)} \quad (5.21)$$

where b_{n1} , b_{n2} and b_{n3} are constants and $E_{a,on}$ the activation energy of the temperature dependent R_o growth. No evidence was found that higher Δ DoDs would cause more severe resistance growth. Using equation 5.18 and 5.21 the total ohmic resistance can then be expressed as

$$R_o(SoC, T, I, n) = (R_o(SoC, I) + R_{o,n}(n, T, I)) \cdot e^{\left(\frac{E_{a,o}}{R}\left(\frac{1}{T} - \frac{1}{T_{ref}}\right)\right)} \quad (5.22)$$

Other than resistance growth due to cycling, the resistance will also grow during storage. Thomas et al. [79] found the power fading, which is directly related to the internal resistance of the cell, to be dependent on the 3/2 power over time. High temperatures according to the Arrhenius equation and SoC according to the Butler-Volmer equation will accelerate the power fading. No distinction is however made between R_b , R_{SEI} , R_{ct} and the resistance resulting from slow diffusion, making it not possible to identify the contribution of each resistance to the internal resistance rise. Liaw et al. [87] on the other hand assumed the ohmic resistance was invariant with storage time, and therefore the resistance growth due to storage will not be taken into account.

5.3.2.3 Short time transient RC pair R_s and C_s

The circuit components R_s and C_s are not equivalent to the charge-transfer resistance R_{ct} and double layer capacitance C_{dl} , since R_s and C_s are determined empirically. Nevertheless, R_s and C_s can be related to R_{ct} and C_{dl} in a practical model. Therefore results found in literature for R_{ct} and C_{dl} will be used to model R_s and C_s as well. From figure 5.10a and b it can be seen that R_{ct} is dependent on the SoC, and exhibits an exponential behaviour. This is reflected in the measurement results for R_s and C_s as shown in figure 5.16. Using a similar equation as equation 5.14, R_s and C_s can be expressed as [91]

$$R_s(SoC) = c_1 e^{-c_2 SoC} + c_3 \quad (5.23)$$

$$C_s(SoC) = d_1 e^{-d_2 SoC} + d_3 \quad (5.24)$$

with c_1 , c_2 and c_3 parameters to be determined for R_s and d_1 , d_2 and d_3 parameters to be determined for C_s . Instead of equation 5.23 and 5.24, it has also been proposed to describe R_s and C_s with a 6th order polynomial [98]. From figure 5.16 it can be seen that R_s and C_s are also current dependent. Using equation 5.23, a way to describe the current dependency is [106]

$$R_s(SoC, I) = (c_1 + c_4 I + c_5 I^2) e^{-c_2 SoC} + c_3 + c_6 I + c_7 I^2 \quad (5.25)$$

where c_4 , c_5 , c_6 and c_7 are constants for the current dependency. The current dependency of C_s can be described in the same way by modifying equation 5.24.

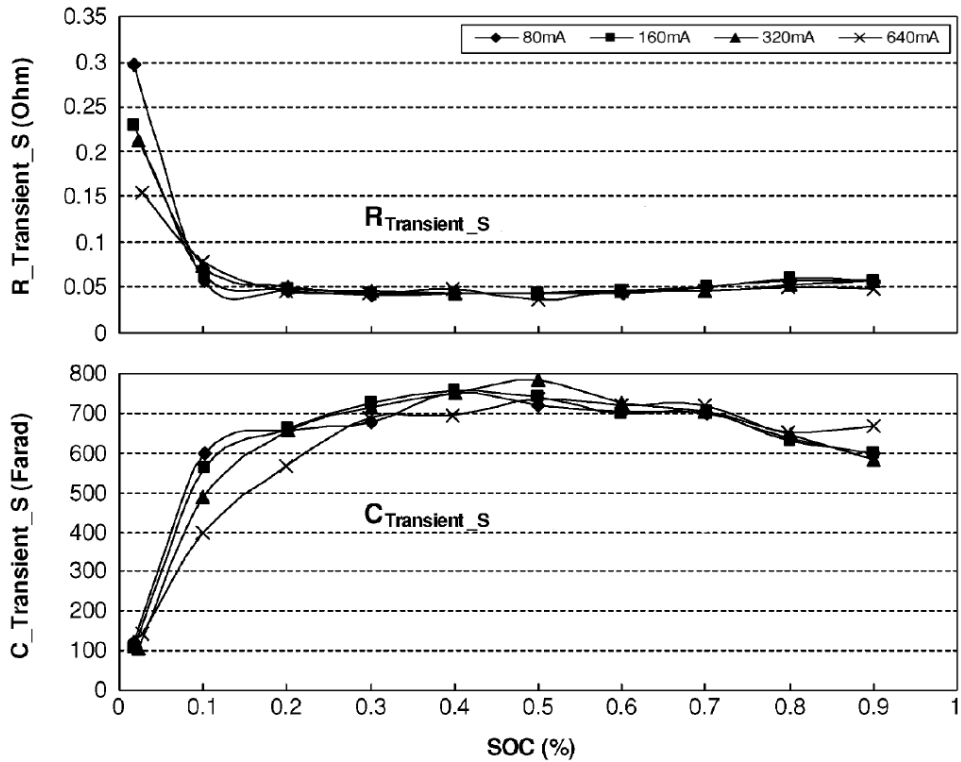


Figure 5.16 An example of the measured short time transient RC pair R_s and C_s vs. SoC of a Li-ion polymer cell discharged with different current levels [91]

From figure 5.12 a strong temperature dependency of R_{ct} is visible on the EIS measurement, which corresponds to the second arch in the Nyquist plot. Figure 5.13a shows that R_{ct} exhibits a very strong temperature according to Arrhenius equation, but shows a non-linearity at higher temperatures. In figure 5.17 instead of $1/R_{ct}$, R_{ct}/T has been plotted against $1000/T/K^{-1}$.

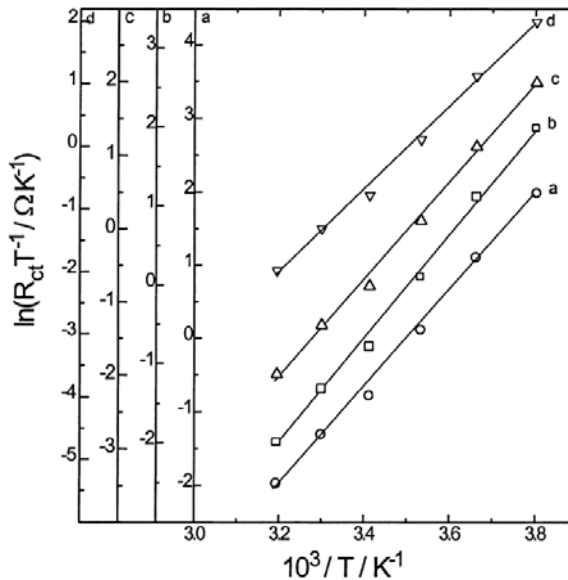


Figure 5.17: The temperature dependence of R_s (R_{ct}) at a. 100% SoC b. 80% SoC c. 50% SoC and d. 20% SoC with their corresponding vertical axis [84].

5 Practical circuit-based model including ageing effects

Figure 5.17 shows that R_{ct} follows the modified Arrhenius equation with nearly a constant slope for different SoCs, indicating a constant activation energy over the entire SoC range. The modified Arrhenius equation has been developed using the Butler-Volmer equation, and using that relation for R_s , the temperature dependence is expressed as [84]

$$R_s(SoC, I, T) = R_s(SoC, I) \cdot T e^{\left(\frac{E_{a,rs}}{R} \left(\frac{1}{T} - \frac{1}{T_{ref}}\right)\right)} \quad (5.26)$$

The charge transfer resistance also experiences irreversible resistance growth due to cycling. In figure 5.15 it can be seen that the R_{ct} varies with the square root of cycle numbers, which can be expressed as

$$R_{s,n}(n, \sigma) = c_n(\sigma) \sqrt{n} \quad (5.27)$$

where c_n is the stress factor σ dependent parameter. Using equation 5.27 the R_s growth due to cycling can be expressed as

$$\Delta R_{s,n} = \sqrt{R_{s,n}^2 + c_n^2 \Delta n} - R_{s,n} \quad (5.28)$$

with $\Delta R_{s,n}$ the change in R_s during Δn cycles under constant stress factors and $R_{s,n}$ taken before the growth determination. The total R_s growth due to cycling is the summation of $\Delta R_{s,n}$. Increased temperatures will make the electrodes degrade faster and less active material will be available for intercalation. The charge transfer on the electrode/electrolyte interface will then experience more resistance. No indication of increased R_s growth due to high currents has been found. By including the temperature dependency of the R_s growth, the parameter c_n can be expressed as

$$c_n(T) = c_{n0} e^{\left(-\frac{E_{a,rsn}}{R} \left(\frac{1}{T} - \frac{1}{T_{ref}}\right)\right)} \quad (5.29)$$

The total short transient resistance can then be expressed as

$$R_s(SoC, T, I, n) = (R_s(SoC, I) + R_{s,n}(n, T)) \cdot T e^{\left(\frac{E_{a,rs}}{R} \left(\frac{1}{T} - \frac{1}{T_{ref}}\right)\right)} \quad (5.30)$$

In literature very little attention has been paid to the development of the double layer capacitance C_{dl} due to cycling, as this parameter has no direct influence on the performance of a battery cell. C_s was found to decrease with increasing cycle numbers, but the change has not been quantified [82]. Since C_s is considered a pair with R_s describing the short time transient behaviour of the voltage, the C_s drop will be described in the same way as the R_s growth using equation 5.27, 5.29 and 5.30.

5.3.2.4 Long time transient RC pair R_l and C_l

The long time transient circuit components R_l and C_l are used to model the diffusion phenomena within the Li-ion cell. In EIS measurements very little attention has been paid to the diffusion phenomena, mostly only mentioning that the low frequency tail can be modelled with a constant phase element. As described in paragraph 5.2.4.2 the constant phase element can be expanded into multiple parallel RC pairs, and approximated by one RC pair representing the long time transient. The SoC dependence of the long time transient components R_l and C_l are shown in figure 5.18.

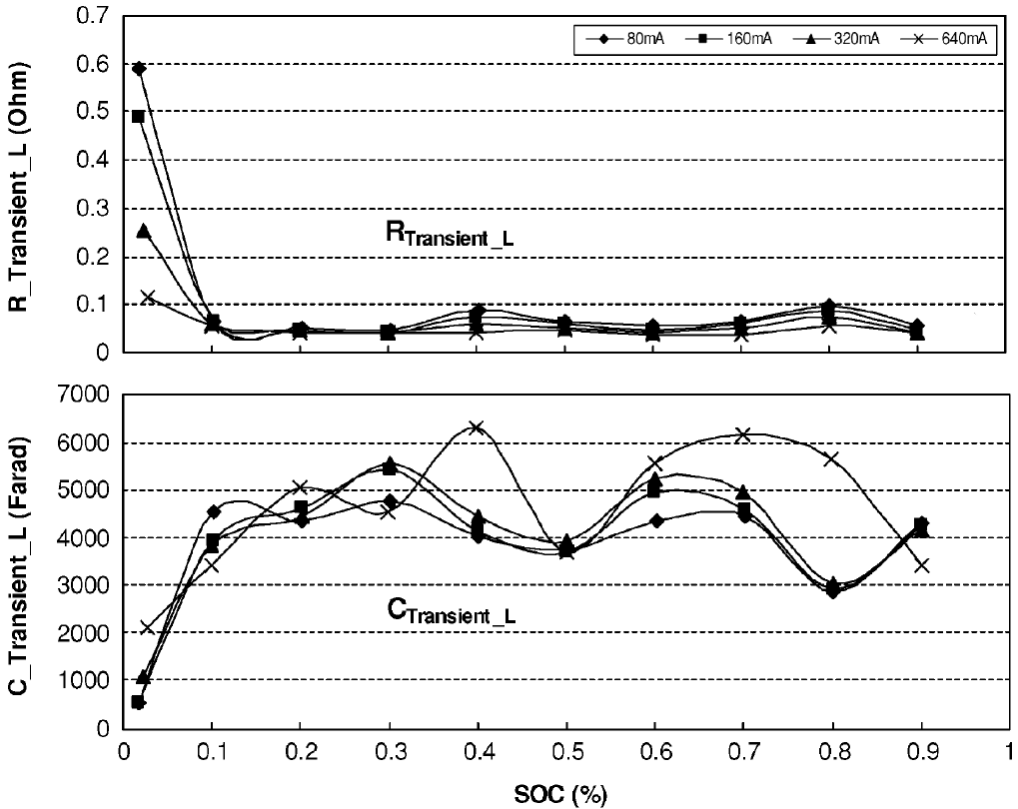


Figure 5.18: An example of the measured long time transient RC pair R_l and C_l vs. SoC of a Li-ion polymer cell discharged with different current levels [91].

A possible way to describe the SoC dependence is using exponential equations [91]:

$$R_l(SoC) = g_1 e^{-g_2 SoC} + g_3 \quad (5.31)$$

$$C_l(SoC) = h_1 e^{-h_2 SoC} + h_3 \quad (5.32)$$

with g_1 , g_2 and g_3 parameters to be determined for R_l and h_1 , h_2 and h_3 parameters to be determined for C_l . Another possible equation to describe R_l and C_l has been proposed by [98] using a 6th order polynomial. In figure 5.18 it can be seen that R_l is smaller for larger currents, just like for R_s . Also C_l shows a dependency on the current. For R_s the current dependency can be expressed as [106]:

$$R_l(SoC, I) = (g_1 + g_4 I + g_5 I^2) e^{-g_2 SoC} + g_3 + g_6 I + g_7 I^2 \quad (5.33)$$

C_l can be modelled in a similar way as equation 5.33 using equation 5.32. The diffusion of lithium ions in a Li-ion cell is very dependent on the temperature [108]. Higher temperatures will cause the lithium ions to diffuse much faster, resulting in a lower R_l . A possible way to describe the temperature dependency is using the Arrhenius equation, leading R_l to change to

$$R_l(SoC, I, T) = R_l(SoC, I) \cdot e^{\left(\frac{E_{a,rl}}{R} \left(\frac{1}{T} - \frac{1}{T_{ref}}\right)\right)} \quad (5.34)$$

Very little research has been done in changes of the diffusion phenomena in a Li-ion cell, since the SEI layer growth has been identified as the primary source for resistance growth. Hartman II [80] used the voltage response to a step current to determine the parameters in a 1st order Randle's circuit, which only includes one RC pair. The time constant was larger than 30 seconds,

which corresponds to the time constant of the diffusion phenomena as seen in EIS measurements [80]. The determined RC pair values therefore correspond to R_l and C_l . R_l and C_l were found to fluctuate with cycle numbers, but did not show a trend and were approximated as constants. Zhang & Wang [65] have, however, measured a change in the Warburg coefficient, which is related to the diffusion phenomena. The Warburg coefficient rises with increasing cycle number, which indicates that the diffusion undergoes more resistance, resulting in a higher R_l . As a first approximation R_l and C_l are assumed not vary with the cycle number. Consequently, equation 5.34 and the C_l equivalent are sufficient to describe the long time transient of the voltage response.

5.3.3 Chosen non-linear circuit component models

Many equations are capable of describing the non-linear circuit components, and a trade-off between complexity and accuracy has to be made to determine which equations are sufficient for practical applications. In the previous two paragraphs several empirical equations found in literature have been given to describe the circuit components, from which equations for the literature-based practical equivalent circuit-based model will be chosen. The final circuit component equations will be given in the next paragraph together with the corresponding nonlinear equations for the circuit components.

5.3.3.1 Chosen energy balance circuit component models

The cell capacity Q_{use} describes the amount of energy in the Li-ion cell and is also capable of modelling the decrease in apparent capacity with increasing currents using equation 5.2 (Peukert's law) or equation 5.3. A Li-ion cell is set to operate between a maximum and minimum voltage to prevent damage to the cell. Higher currents result in higher voltage drops, causing the minimum voltage to be reached at a higher SoC than 0%. This causes a decrease in apparent capacity. The decrease in apparent capacity can, however, also be modelled with the resistances in the voltage response circuit, making it unnecessary to use equations 5.2 or 5.3. Furthermore the activation energy is assumed to be constant over the lifetime of the cell. So using equation 5.1, 4.29 and 4.30 the useable capacity can be modelled. By using the voltage response circuit the apparent capacity can be subsequently modelled.

The self-discharge rate of Li-ion is very low, in the order of a few percent per month. The self-discharge of a daily used cell is therefore hardly noticeable and will be neglected as a first approximation. Consequently, the value of R_{sdis} will be infinite.

5.3.3.2 Chosen voltage response circuit component models

The open circuit voltage V_{oc} is modelled using a combination of polynomials and exponential functions. From figure 5.7 it can be seen that the OCV exhibits an exponential behaviour at high and low SoC, while in the middle region it fluctuates lightly. The solid line in figure 5.7 is a curve fit from a combination of equation 5.5 and 5.6, which results in an accurate fit. The OCV can, however, also be quite accurately described by equation 5.5 alone. Two exponential functions describe the behaviour at high and low SoCs and a linear function is used for the middle region.

The temperature and hysteresis effect of the OCV are modelled by some, but ignored by others. If the temperature swing of the cells is not too large, the temperature effect could be ignored. The hysteresis effect can also be an effect of the slow diffusion within a cell, which is modelled by the long time transient RC pair. Therefore the temperature and hysteresis effect are ignored as a first approximation. Finally, ageing was found not to have any effect on the OCV.

In figure 5.11 the ohmic resistance R_o exhibits an exponential behaviour as a function of the SoC. A current dependency of R_o is also visible in figure 5.11 and from temperature measurements R_o was found to be dependent on the Arrhenius equation. Therefore R_o can be modelled with equation 5.16 and 5.18. The ohmic resistance R_o in the model consists of the bulk resistance R_b and surface layer resistance R_{SEL} , for which different ageing rates have been found. The growth of both resistances have been approximated with a linear dependence on the cycle number, so as a first approximation the irreversible resistance growth of R_o will also be modelled with a linear dependency on the cycle number. A current and temperature dependency of the R_o growth was observed, which can be modelled with equation 5.21. The complete ohmic resistance is then given by equation 5.22.

The short time transient RC pair also exhibits an exponential behaviour as a function of SoC. At high SoCs, however, a SoC dependent rise in R_s and drop in C_s can be seen in figure 5.16. This can be modelled with an additional 1st order polynomial to equations 5.23 and 5.24 for respectively R_s and C_s . To model the current and temperature dependency equation 5.25 and 5.26 are used. R_s was found to grow linearly with the square root of the cycle number and the growth rate was found to be temperature dependent. This is modelled by equation 5.29 and 5.30. Since C_s forms the short time transient RC pair with R_s , the ageing rate of C_s is assumed to be similar to R_s . R_s is finally calculated with equation 5.30.

Similar to R_o and R_s , R_l also exhibits an exponential behaviour as shown in figure 5.18. Also a current dependency is seen and from literature it is known that R_l is also dependent on the temperature. The current and temperature dependency are modelled by equation 5.33 and 5.34. From figure 5.18 it can, however, be seen that C_l experiences a lot of change over the entire SoC range and can therefore not be accurately modelled by equation 5.32. The other approach of using a 6th order polynomial will most likely produce more accurate results. The values of the long time transient RC pair were found not to change with ageing of the cell, so R_l and C_l are not dependent on the cycle number.

The equations for the circuit components R_o , R_s , C_s , R_l and C_l were determined with results from discharging experiments, since in most applications only the discharge behaviour of battery cells is important. In EV applications however regenerative braking occurs and the charging behaviour of the cells also becomes critical. The circuit components in the voltage response circuit, however, do not behave the same for charging as for discharging, which is not taken into account in most existing models. The chosen circuit components models will then either contain different parameters for charging [98] or different equations will be used for charging.

5.4 Chosen literature-based practical circuit model including ageing

From the analysis of equivalent circuit-based models and their non-linear circuit components found in literature, a practical equivalent circuit-based model including ageing effects is constructed. This model is shown in figure 5.19. In figure 5.19 it can be seen that the self-discharge resistance R_{sdis} is left out from the model in figure 5.6. Also every circuit component is made variable, as the circuit components depend on the internal factors SoC and ageing, and the external factors C-rate and temperature. V_{SoC} is the normalized voltage over capacitance C_{use} and is the circuit representation of the SoC of the cell. I is the current in Amps and not C-rate.

5 Practical circuit-based model including ageing effects

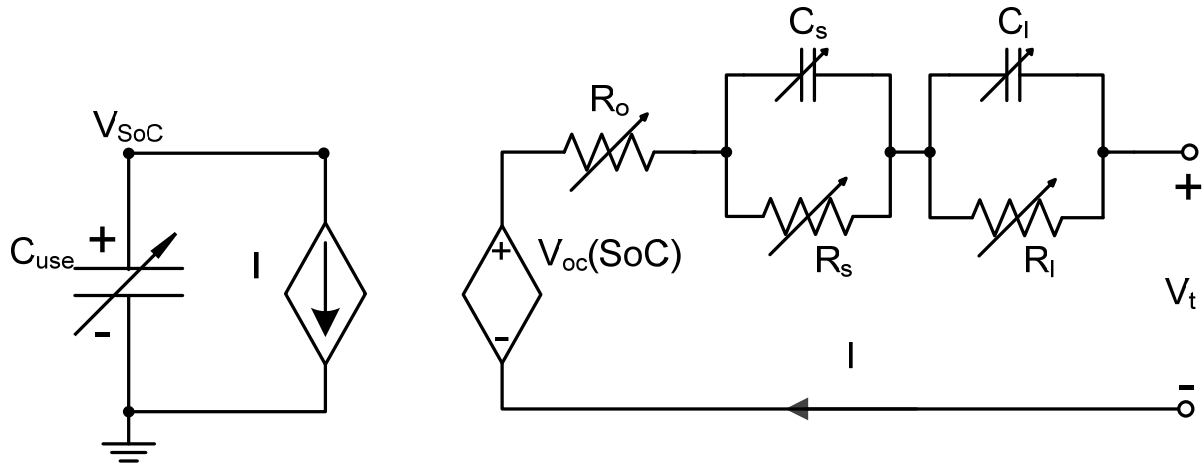


Figure 5.19: The chosen equivalent circuit-based model including ageing effects for Li-ion cells.

The value of C_{use} is equal to the useable capacity of the cell Q_{use} , which is expressed by equation 5.1 and becomes:

$$C_{use} = Q_{use}(\xi, T) = (Q_{nom} - \xi) \cdot e^{\left(-\frac{E_{a,q}}{R} \left(\frac{1}{T} - \frac{1}{T_{ref}}\right)\right)} \quad (5.35)$$

where Q_{nom} is the initial true capacity at reference temperature. The capacity fading ξ can be calculated by equation 4.29 and 4.30. The OCV is expressed in the form of equation 5.5, in which the temperature and hysteresis effect are ignored:

$$V_{oc}(SoC) = a_1 e^{-a_2 SoC} + a_3 + a_4 SoC + a_5 e^{-\frac{a_6}{1-SoC}} \quad (5.36)$$

Since the capacity fading was found to be independent of the SoC and Δ DoD for a dynamic current profile including regenerative braking and only dependent on the charge processed, it is assumed that the resistances and capacitances in the voltage response circuit are also only dependent on the charge processed in the cell. Because in literature cycling experiments to obtain the empirical equations of the circuit components were conducted under constant initial SoC and Δ DoD, the ageing rate due to cycling in cycle numbers n and charge processed Ah are similar. The ohmic resistance R_o is then expressed as

$$R_o(SoC, T, I, Ah) = (R_o(SoC, I) + R_{o,n}(Ah, T, I)) \cdot e^{\left(\frac{E_{a,o}}{R} \left(\frac{1}{T} - \frac{1}{T_{ref}}\right)\right)} \quad (5.37)$$

$$R_o(SoC, I) = (b_1 + b_4 I + b_5 I^2) e^{-b_2 SoC} + b_3 + b_6 I + b_7 I^2 \quad (5.38)$$

$$R_{o,n}(Ah, T, I) = \sum_{i=1}^E \left((b_{n1} + b_{n2} I_i + b_{n3} I_i^2) \cdot b_n \Delta Ah_i \cdot e^{\left(-\frac{E_{a,on}}{R} \left(\frac{1}{T_i} - \frac{1}{T_{ref}}\right)\right)} \right) \quad (5.39)$$

where i is an event and E the total number of events. An event is defined as a period of time in which the current and temperature are constant or averaged over the period. In a similar way the short time transient RC pair is expressed as a function of the charge processed instead of cycle number by

$$R_s(SoC, T, I, Ah) = (R_s(SoC, I) + R_{s,n}(Ah, T)) \cdot T e^{\left(\frac{E_{a,rs}}{R} \left(\frac{1}{T} - \frac{1}{T_{ref}}\right)\right)} \quad (5.40)$$

$$R_s(SoC, I) = (c_1 + c_5 I + c_6 I^2) e^{-c_2 SoC} + (c_3 + c_7 I + c_8 I^2) + c_4 SoC \quad (5.41)$$

$$R_{s,n}(Ah, T) = \sum_{i=1}^E \left(\sqrt{R_{s,ni}^2 + \left(c_{n0} e^{\left(-\frac{E_{a,rsn}}{R} \left(\frac{1}{T_i} - \frac{1}{T_{ref}}\right)\right)} \right)^2 \Delta Ah_i} - R_{s,ni} \right) \quad (5.42)$$

$$C_s(SoC, T, I, Ah) = (C_s(SoC, I) + C_{s,n}(Ah, T)) \cdot T e^{\left(\frac{E_{a,cs}}{R} \left(\frac{1}{T} - \frac{1}{T_{ref}}\right)\right)} \quad (5.43)$$

$$C_s(SoC, I) = (d_1 + d_5 I + d_6 I^2) e^{-d_2 SoC} + (d_3 + d_7 I + d_8 I^2) + d_4 SoC \quad (5.44)$$

$$C_{s,n}(Ah, T) = \sum_{i=1}^E \left(\sqrt{C_{s,ni}^2 + \left(d_{n0} e^{\left(-\frac{E_{a,csn}}{R} \left(\frac{1}{T_i} - \frac{1}{T_{ref}}\right)\right)} \right)^2 \Delta Ah_i} - C_{s,ni} \right) \quad (5.45)$$

The value of $R_{s,ni}$ is $R_{s,n}$ at the start of event i . The long time transient RC pair is assumed to be constant with the cycle number, so no dependency on the charge processed is modelled either. The long time transient RC pair is then expressed by

$$R_l(SoC, I, T) = R_l(SoC, I) \cdot e^{\left(\frac{E_{a,rl}}{R} \left(\frac{1}{T} - \frac{1}{T_{ref}}\right)\right)} \quad (5.46)$$

$$R_l(SoC, I) = (g_1 + g_4 I + g_5 I^2) e^{-g_2 SoC} + g_3 + g_6 I + g_7 I^2 \quad (5.47)$$

$$C_l(SoC, I, T) = C_l(SoC, I) \cdot e^{\left(\frac{E_{a,cl}}{R} \left(\frac{1}{T} - \frac{1}{T_{ref}}\right)\right)} \quad (5.48)$$

$$C_l(SoC, I) = h_1 SoC^6 + h_2 SoC^5 + h_3 SoC^4 + h_4 SoC^3 + h_5 SoC^2 + h_6 SoC + h_7 + h_8 I + h_9 I^2 \quad (5.49)$$

A complete overview of the literature-based circuit model is given in appendix A.1. The parameters equations 5.35 to 5.49 have to be determined from measurements on the Li-ion cell of interest. While the parameters for the instantaneous change of the circuit component values can be determined in one full cycle, the parameters for the ageing rate will require more experimental data. Finally it has to be noted that equation 5.37 to 5.49 are for a discharging Li-ion cell, and will contain different parameters for a charging Li-ion cell. It is also possible that the voltage response circuit equations for a discharging cell are different from a charging cell, which has to be determined experimentally as this is not documented in literature. This will result in doubling of the number of equations for the voltage response circuit.

6 Empirical development of an improved practical circuit-based model

In chapter 5 a practical circuit-based model including ageing effects has been proposed for lithium ion (Li-ion) cells. The model consists of an energy balance circuit to model the cell capacity and a voltage response circuit to model the voltage behaviour of the cell. In the model each circuit component was constructed from empirical equations and experimental data found in literature. However, the results from the experiments found in literature were conducted with various types of Li-ion cells, which behaviour and properties may not be similar. In this thesis the focus lies on lithium iron phosphate (LiFePO₄), since this Li-ion cell type is expected to be used in many electric vehicle (EV) in the near future. Therefore the validity of the model will be tested with LiFePO₄ cells. From the test results an improved model will be extracted which will be able to model the behaviour of LiFePO₄ cells with sufficient accuracy and the least complexity.

The EVs in the project use high capacity automotive LiFePO₄ batteries cells. In the best-case scenario the battery cells used in the EV or at least from the same manufacturer have to be used for the experiments and empirical development of the model, so the model can be compared to. Unfortunately, the smallest LiFePO₄ battery cell of the same manufacturer is 40 Ah. During operation the EVs can draw up to 2.5C from the each cell and has an average discharge rate of 0.7C, which corresponds to peak currents of 100A and an average current of 28A for the smallest cell of the same manufacturer. The high currents require expensive equipment to run experiments, especially when multiple cells are tested in parallel. Nonetheless, since current capabilities of battery cells are rated by their C-rate, LiFePO₄ cells with much lower capacities will yield comparable test results.

In this chapter first the experimental set-up is described. To test different stress factors, multiple LiFePO₄ cells are tested at the same time. Each cell is tested according a general and cell specific test procedure, which will be described respectively. The obtained capacity fading and circuit component development measurement will be given, which will or will not correspond to the literature based model. Finally the model is modified and expanded with the obtained measurement data.

6.1 Experimental setup

The experimental setup consists of the following components: multiple LiFePO₄ cells, a temperature controlled environment, energy source, load, test procedure controller and programmer, voltmeter, current probe and a data logger. The setup is shown in figure 6.1. The Maccor Series 2000 automated battery tester serves as the energy source, load, measurement equipment and test procedure controller. A PC with Maccor software is used to program the test procedures and logs the measurement data.

The LiFePO₄ cells used in the experiment are A123 Systems' APR18650m1 with a nominal capacity of 1.1 Ah obtained from a third party vendor. The obtained cells were unused, but had a lower capacity than the nominal capacity. Since the goal is not to evaluate the performance of a specific cell manufacturer, but to identify and quantify the behaviour and ageing stress factors of LiFePO₄ cells, unused cells of the same type and manufacturer will give sufficient results. The cells were placed in continuous temperature controlled ovens with a metallic surface, so the heat

generated by the cells during operation will have very little influence on the temperature of the cells. The surface temperature of the cells was initially monitored, but temperature variations were very small during cycling. Therefore the temperature of the cells is considered to be constant.

The Maccor Series 2000 automated battery tester has 16 independent channels with a maximum rating of 10V and 2A. Each channel can be programmed with its own test procedure, which is run from the automated battery tester. The test procedure are programmed with the Maccor Test Editor and uploaded to the battery tester via the Maccor software on the PC. The battery tester logs the data on its own internal memory and writes it occasionally to the PC.

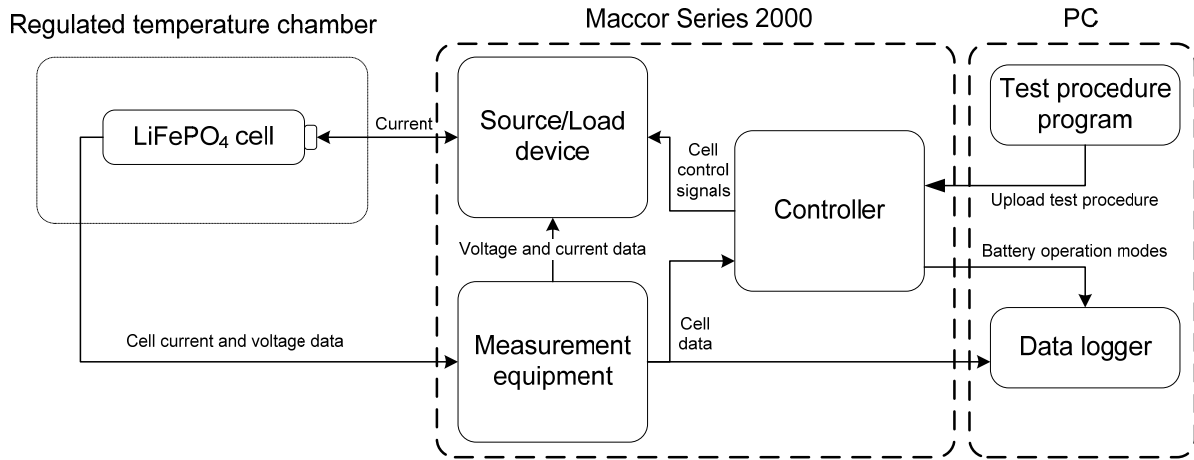


Figure 6.1: The experimental setup used to verify and develop an equivalent circuit-based model with ageing effects for Li-ion cells.

6.2 Test procedure

To test the influence of various stress factors on the ageing of Li-ion cells, each cell has been tested under a different temperature, C-rate, SoC and/or Δ DoD. The cells follow the test procedure shown in figure 6.2.

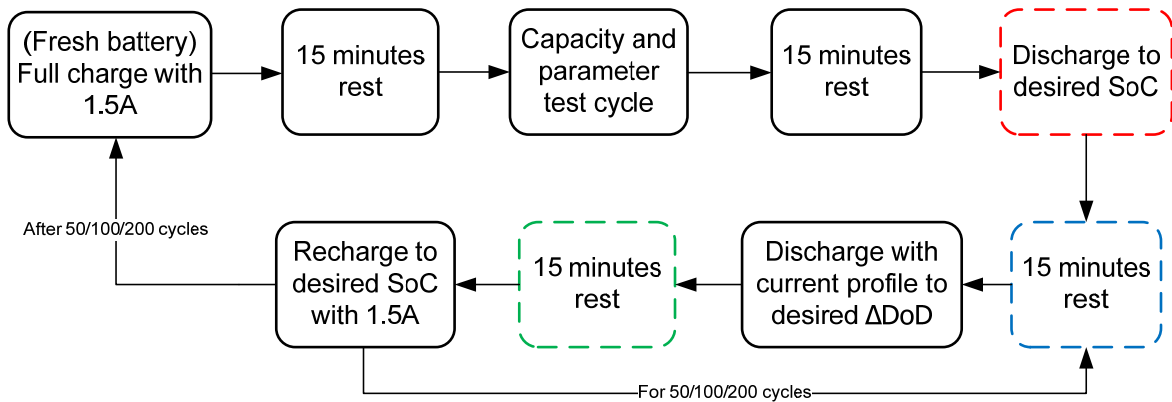


Figure 6.2: The test procedure employed in the experiment to test the influence of various stress factors on ageing, where the cycle number and dashed blocks are test condition dependent.

Depending on the test conditions, the bottom row of the test procedure in figure 6.2 is cycled for 50, 100 or 200 cycles and the coloured dashed blocks are skipped. The resting time of 15 minutes is arbitrarily determined as a trade-off between the one hour resting time suggested by the United States Advanced Battery Consortium (USABC) PHEV battery test manual and

6 Empirical development of an improved practical circuit-based model

available test time [12]. Experiments have determined that a resting time of 15 minutes is sufficient to have minimal influence on the capacity and parameter determination in the SoC range of interest. The charging current of 1.5A is the recommended charging current from the datasheet of cells [109], and the maximum cell voltage is 3.6V.

The goal of the tests is to verify and expand the proposed practical circuit-based model including ageing effects for a current profile which include regenerative braking. In many studies, however, cells are discharged under a constant current and regenerative braking is not included. Therefore first a current profile for cycling will be proposed which does include regenerative braking. Then the capacity and parameter test cycle shown in figure 6.2 will be explained. Finally the test conditions for each cell will be given.

6.2.1 Proposed cycling current profile

Most studies conduct life cycle tests under a constant discharge current. Nevertheless, there are a few studies that conduct life cycle tests with a dynamic profile and have included regenerative braking [40][110]. However, these studies did not investigate a possible increase in ageing due to high C-rates. The dynamic profiles used in the studies are shown in figure 6.3 and figure 6.4. The dynamic profile in figure 6.3a was obtained from the old USABC EV battery test procedure, which is similar to the profile currently suggested by the new USABC PHEV battery test manual shown in figure 6.3b [12]. Negative power is discharge in figure 6.3a and charging in figure 6.3b. The profile in figure 6.4 was obtained from a driving cycle with positive current for discharge.

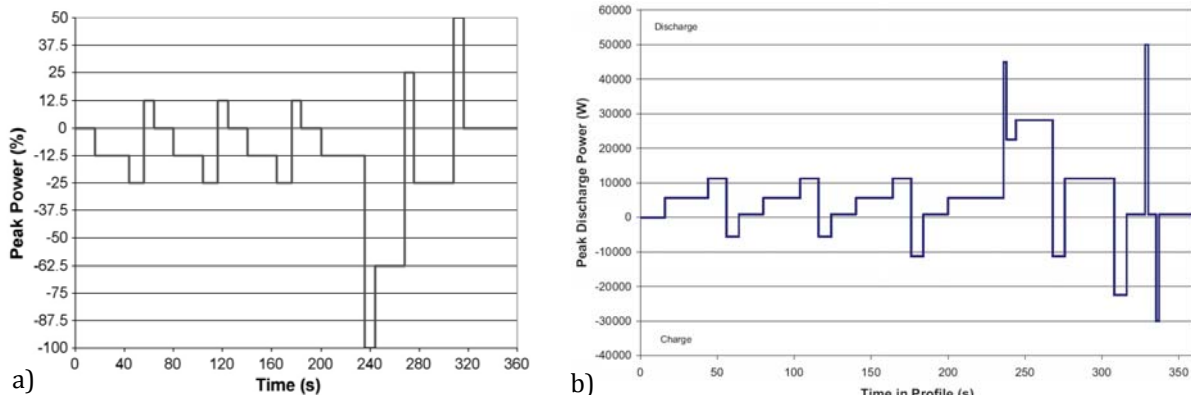


Figure 6.3: a) The profile used in a study on capacity fading under a dynamic profile [110] and b) the dynamic profile for life cycle tests provided by the USABC PHEV battery test manual [12].

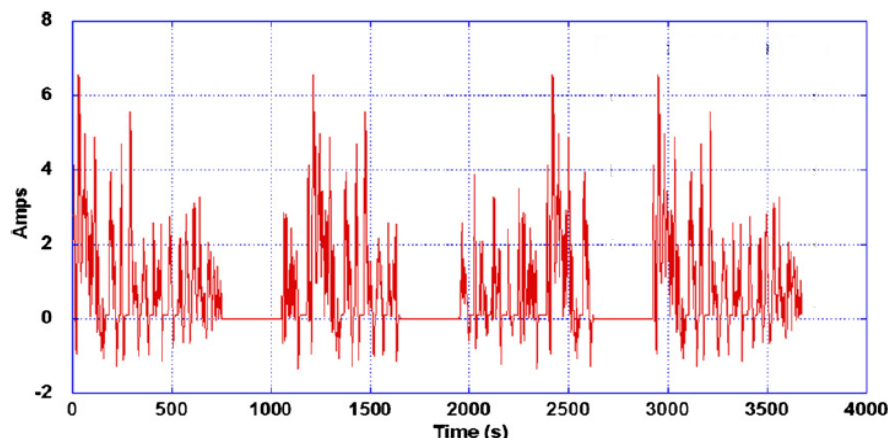


Figure 6.4: The dynamic profile used in a study to determine the Δ DoD dependence of cycling losses in a Li-ion battery cell [40].

The disadvantage of the dynamic profiles in figure 6.3 and figure 6.4 is that different current levels are included in the profile, making it not possible to observe whether high C-rates will introduce additional ageing or not. To overcome this problem, a new cycling current profile is proposed in figure 6.5. A positive current is discharge. The value and length of the discharge and recharge current are the mean value of discharge and regenerative braking in current profiles obtained from field tests with the EVs in the project. For discharging the mean value was 0.67C and for recharging 0.22C. The profile consists of a period of constant current discharge, directly followed by a period of constant current charging and is repeated until the end conditions of the tests have been reached. In the tests only the current levels will be varied, but the length of the discharge and charge period remains constant.

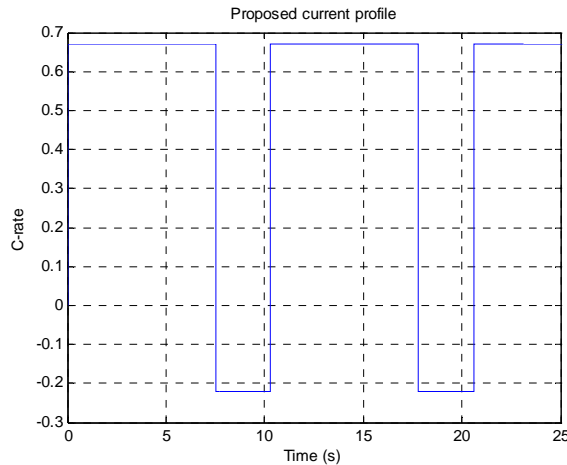


Figure 6.5: The proposed current profile including regenerative braking used in the cycling tests.

6.2.2 Capacity and parameter test cycle

To be able to determine the capacity and parameters for the equivalent circuit components, every few cycles a capacity and parameter test cycle has to be conducted. The test cycle employed is similar to the method in [111] and is shown in figure 6.6.

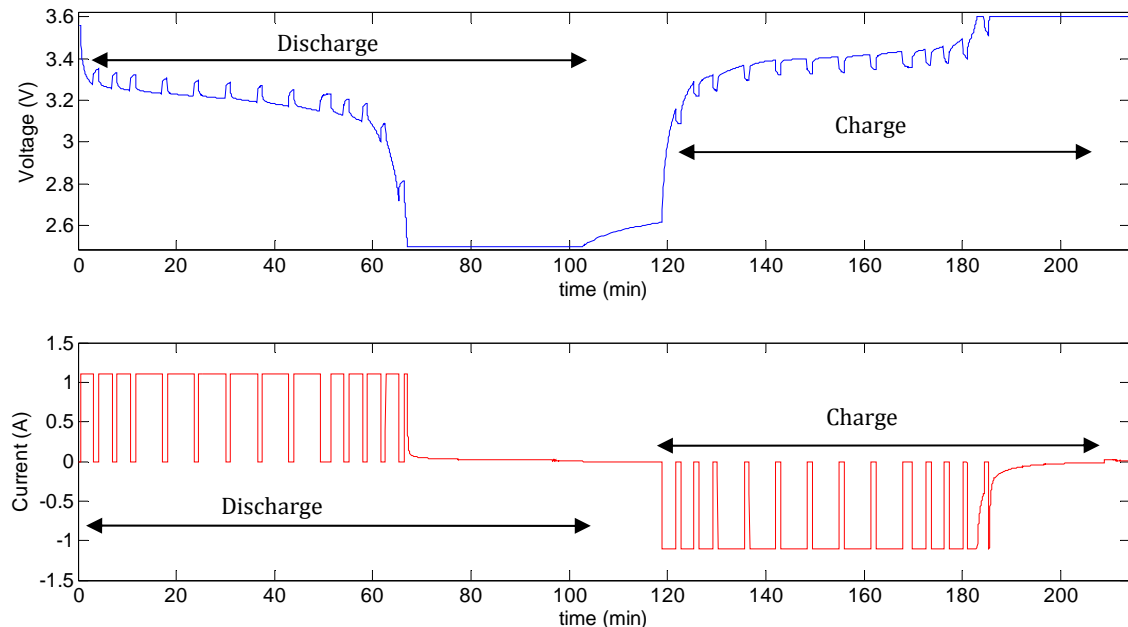


Figure 6.6: The test cycle for determining the capacity and parameter of the equivalent circuit components of a cell under test.

6 Empirical development of an improved practical circuit-based model

Each cell is fully charged with the constant current constant voltage (CCCV) method to a maximum voltage of 3.6V and rested before a test cycle occurs. Starting with a fully charged cell, the cells are discharged at 1C in steps of 0.05 Ah and rested for 1 minute in the non-linear voltage region. In the linear voltage region cells are discharged at 1C in steps of 0.1 Ah before rested for 1 minute. The cells are then rested for 15 minutes before the charging test cycle begins, which is similar to the discharging test cycle. The one minute rest is employed to determine the parameters of the circuit components at different states of charge (SoCs) and is known as the Current-Off method [17] or Current Pulse Relaxation technique [68].

To be able to model the worst case polarisation at any SoC, ideally the resting periods to determine the circuit components should be as short as possible. However, to be able to make a distinction between the short and long time transient time constants, the resting period should be sufficiently longer than the time constant of the short time transient. As a trade-off a resting period of 1 minute was chosen.

In figure 6.6 it can be seen that during the test cycle the cell has not only been charged with the CCCV method, but also discharged in this manner to approximate the true capacity of the cell. When the minimum voltage of 2.5V is reached, the cell is discharged with a constant voltage of 2.5V until the current is smaller than 0.01C or if the charging step exceeds 100 minutes to prevent excessively long charging times. This way a distinction between true capacity fading and rate capability losses of the cells can be made. In the datasheet [109] 2V is the minimum cut-off voltage for discharge, which is determined under a certain current. When the minimum cut-off voltage is reached, the discharge of the cell is stopped immediately. However, the cells in this experiment experience additional constant voltage discharge when the minimum cut-off voltage is reached. The minimum cut-off voltage is therefore set to 2.5V to prevent overdischarge as recommended by [40] and several vendors.

6.2.3 Test conditions

Each test condition investigates the influence of one stress factor or the influence of regenerative braking. At the time of the experiments 15 of the 16 channels were available to be subjected to different test conditions, which all follow the test procedure described in figure 6.2. The coloured dashed boxes and cycle number are test condition dependent. In table 6.1 an overview of the test conditions is given, which is followed by an explanation of the test conditions.

It has been reported that a dynamic profile including regenerative braking will cause accelerated capacity fading, but this was under the profile shown in figure 6.3a [110]. The accelerated capacity fading might also be caused by high C-rates, and it is therefore not clear if regenerative braking will actually cause accelerated ageing. To investigate the influence of regenerative braking, the capacity fading of a cell cycled with the proposed current profile is compared to a cell cycled with resting periods instead of regenerative braking and a cell cycled with a constant current. The cells are discharged with 100% ΔDoD at 25°C (room temperature) at current levels of the proposed profile, i.e. 0.67C discharge and 0.22C recharge. The red dashed block in figure 6.2 is skipped and after every 50 cycles a test cycle occurs.

The stress factors tested in the experiments are deducted from real-life usage of EVs. The reference conditions are set to 90% SoC, 25% ΔDoD, 25°C and C-rate values shown in figure 6.5. The initial 90% SoC is the maximum charging SoC to which some car manufacturers configures the battery management system (BMS) to extend the battery life and 25% ΔDoD is the average daily usage of the battery obtained from real-life tests [28] [29].

The chosen test temperatures apart from the reference temperature are 40°C and -20°C, approximately possible extreme temperatures in the Netherlands [112], and 0° C, an arbitrarily chosen low temperature. The discharging C-rate is varied to 1C and 2A at 25°C. The regenerative braking C-rate is varied to 1C at 0°C to investigate whether lithium plating will result from regenerative braking, as it has been reported that low temperatures also cause accelerated capacity fading [34][113]. Cell 12 is charged at 0°C with a modified C-rate, which is scaled to the measured capacity at 0°C instead of the nominal capacity, to investigate whether lithium plating can be modelled as an increase in C-rate.

A ΔDoD of 12.5% is an arbitrarily chosen value for a short trip e.g. to the supermarket and 50% ΔDoD from 90% SoC is when the driver will adjust its driving pattern [114]. From initial 60% SoC with 50% ΔDoD the battery reaches a near empty state where the driver will frantically search for a charging point. So a comparison between 90% and 60% initial SoC, and a comparison between 12.5%, 25% and 50% ΔDoD are made.

	<i>SoC</i>	<i>ΔDoD</i>	<i>C-rate discharge</i>	<i>C-rate charge</i>	<i>Temperature</i>	<i>Skipped blocks</i>	<i>Test condition/stress factor</i>
<i>Cell 1</i>	100%	100%	mean	mean	25°C	red	Proposed profile 100% discharge
<i>Cell 2</i>	100%	100%	mean	NA	25°C	red	Resting instead of regenerative braking periods, 100% discharge
<i>Cell 3</i>	100%	100%	mean	NA	25°C	red	Constant current 100% discharge
<i>Cell 4</i>	90%	25%	2A (1.8C)	mean	25°C	green	C-rate: 2A current discharge
<i>Cell 5</i>	90%	25%	1C	mean	25°C	green	C-rate: 1C current discharge
<i>Cell 6</i>	90%	25%	mean	mean	40°C	green	Temperature: 40°C
<i>Cell 7</i>	90%	25%	mean	mean	0°C	green	Temperature: 0°C
<i>Cell 8</i>	90%	12.5%	mean	mean	25°C	blue every odd cycle, green	$\Delta\text{DoD}: 12.5\%$
<i>Cell 9</i>	90%	50%	mean	mean	25°C	none	$\Delta\text{DoD}: 50\%$
<i>Cell 10</i>	90%	25%	mean	mean	-20°C	green	Temperature: -20°C
<i>Cell 11</i>	90%	25%	mean	mean discharge C-rate	0°C	green	Lithium plating: mean discharge C-rate charging
<i>Cell 12</i>	90%	25%	mean	mod	0°C	green	Lithium plating: modified current charging, scaled to 0°C capacity
<i>Cell 13</i>	90%	25%	mean	mean	25°C	green	Reference condition
<i>Cell 14</i>	60%	25%	mean	mean	25°C	green	SoC: 60%
<i>Cell 15</i>	60%	50%	mean	mean	25°C	none	SoC: 60%, $\Delta\text{DoD}: 50\%$

Table 6.1: The test procedures conducted with each cell. Under *test condition/stress factor* the tested stress factor is given and *Skipped blocks* refers to which procedure block to skip in figure 6.2.

For 12.5% ΔDoD the bottom row procedure in figure 6.2 is cycled 200 times, the green dashed block is skipped and every odd cycle the blue dashed block is skipped as well. For every test procedure with 25% ΔDoD the cycling procedure occurs for 100 cycles before a test cycle and the green dashed block is skipped. At 50% ΔDoD a test cycle is implemented after every 50 cycles. Skipping the test blocks causes every cell with different ΔDoD to be stressed for an equal

6 Empirical development of an improved practical circuit-based model

amount of time before a resting period, so no difference in continuous stressing and resting time exists before a test cycle occurs. It is not possible in the Maccor software test procedure to invoke mathematical functions or save variables, so the desired SoC and ΔDoD have to be manually calculated and have to be programmed in Amp hours in the test procedure file. To ensure the cells are cycled with the appointed SoC and ΔDoD , after every test cycle the amount of Amp hours for the right SoC and ΔDoD have to be manually adjusted in the test procedure file. This means that between two test cycles the cells are cycled with a constant Amp hour discharge, which will result in an offset in the desired initial SoC and ΔDoD for the test. The capacity fading between two test cycles is, however, expected to be so small that the offset is negligible.

6.3 Measurement method

The capacity of a cell can be directly determined from the test cycle described in figure 6.6. Two different capacities are determined from the cell: the 1C capacity and the true capacity. The 1C capacity is the capacity of a cell determined when the cell reaches the discharge cut-off voltage at 1C current and is dependent on the internal resistance of the cell. The true capacity of the cell is the capacity of the cell without influence of the internal resistance. The true capacity of the cell approximated by discharging the cell at the constant discharge cut-off voltage after the 1C capacity has been reached until the current drops below 0.01C. The Maccor software logs the processed Amp hours at the beginning and end of a test cycle in a txt-file, and with a Matlab script the capacity values are extracted.

The determination of the circuit components in the voltage response circuit is less straightforward. First the open-circuit voltage (OCV) of the cell was determined by the test cycle. Instead of 1 minute rest intervals, the rest intervals were 2 hours long, so the cells would reach their close-to-equilibrium (cte) OCV. Furthermore, the data points were taken at every 5% SoC instead of in 0.05Ah or 0.1Ah steps. The data was fitted in Matlab and with the fit of the OCV the other circuit components were determined. In paragraph 6.4.3 the measurement results and the curve fit for the OCV will be analysed.

The other voltage response circuit components are determined using the step response of the cell voltage in the rest interval as explained in [115]. An example of the voltage response is given in figure 6.7. The voltage drop V_o due to the ohmic resistance R_o is the instantaneous voltage drop after the current is cut off. As described in chapter 5, in the practical circuit-based model the voltage drop smaller than one second is considered to be the instantaneous voltage drop V_o . The short-time and long-time transient parallel RC pairs are determined by curve fitting the rest of the voltage response to the following equations:

$$V_{trans} = V_s \left(1 - e^{-\frac{t}{\tau_s}} \right) + V_l \left(1 - e^{-\frac{t}{\tau_l}} \right) \quad (6.1)$$

$$V_s = R_s I \quad (6.2)$$

$$V_l = R_l I = \left(\frac{(V_{oc} - V_i)}{I} - R_s \right) I \quad (6.3)$$

$$\tau_s = R_s C_s \quad \tau_l = R_l C_l \quad (6.4)$$

V_{trans} is the voltage response without V_o . V_s and V_l are respectively the short and long time transient voltage drop with the time constants τ_s and τ_l , V_{oc} the OCV at the measured SoC and V_i

the voltage after the instantaneous voltage drop as shown in figure 6.7. I is the current in Amps before the rest interval, positive for discharging and negative for charging. The voltage response with a time constant within one minute is considered to be the short time transient, and the voltage response from one minute until the OCV is reached results from the long time transient [68].

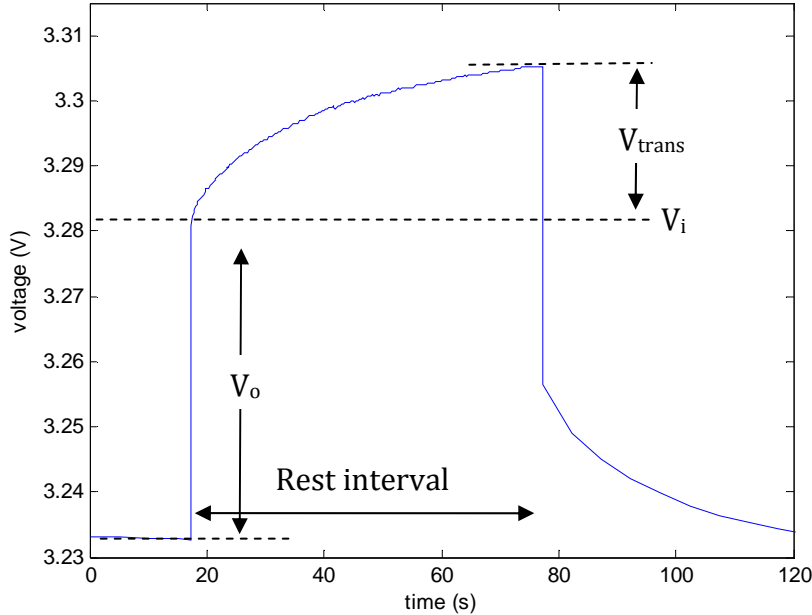


Figure 6.7: An example of the voltage response during a rest interval of a discharge test cycle

By setting a limit on the time constants and choosing the right starting points for the curve fit, the desired short-time and long-time transient time constants are obtained. A non-linear least squares curve fit in Matlab is used to determine the parameters of equation 6.1. This results in a short time constant of approximately 10 seconds and a long time constant of several minutes, which is consistent with findings by other authors [68][91][98]. The voltage response of every rest interval in the test cycle is fitted with equation 6.1 and an adjusted R^2 of at least 0.99 is obtained with an average adjusted R^2 of 0.998, indicating the curve fit is very accurate.

6.4 Measurement and modelling results

The determination of circuit parameters is different for the energy balance circuit and voltage response circuit. The only circuit component in the energy balance circuit which has to be determined is the useable capacity of the cell, which consists of a temporary capacity change and a permanent capacity fading. The temporary capacity change is solely dependent on the temperature, as the capacity in this thesis does not include rate capability losses. The temporary capacity change can be measured by determining the useable capacity at different temperatures. The permanent capacity fading is dependent on many stress factors, and the magnitude of the stress factors is directly related to the capacity fading rate. The true capacity fading can be determined by measuring the capacity discharged by the cell during the test cycle and comparing the result to the initially measured capacity.

The determination of the voltage response circuit parameters, on the other hand, strongly relies on curve fitting. First the open-circuit voltage (OCV) is determined and fitted against empirical equations. With the OCV as a basis, the rest of the circuit parameters are determined with the method described in paragraph 6.3.

6 Empirical development of an improved practical circuit-based model

First the true capacity fading of the measured cells is evaluated. The capacity fading under different stress factors is analysed and the effects are quantified for the model. Then the temporary capacity change is quantified from the measurement data. Next the results from the OCV measurement are discussed and quantified. With the OCV equations the internal cell impedance can be determined. The parameter measurements for all the cells are compared and evaluated. The parameters have also been determined for different temperatures and different C-rates. Furthermore, the measured change in internal cell impedance as a result of life cycle experiments is also analysed. Finally the quantified stress factors are summarised and a practical circuit-based model with known parameters is constructed.

6.4.1 Capacity fading

In chapter 4 many possible stress factors have been found in literature that influences the capacity fading rate. Furthermore, regenerative braking may also have an influence on the capacity fading rate. To confirm whether the possible stress factors and regenerative braking have an effect on the capacity fading rate and to quantify the influences, life cycle experiments have been conducted with LiFePO₄ cells. In figure 6.8 the capacity fading for cells 4 to 15 are shown, which were tested under the conditions described in table 6.1.

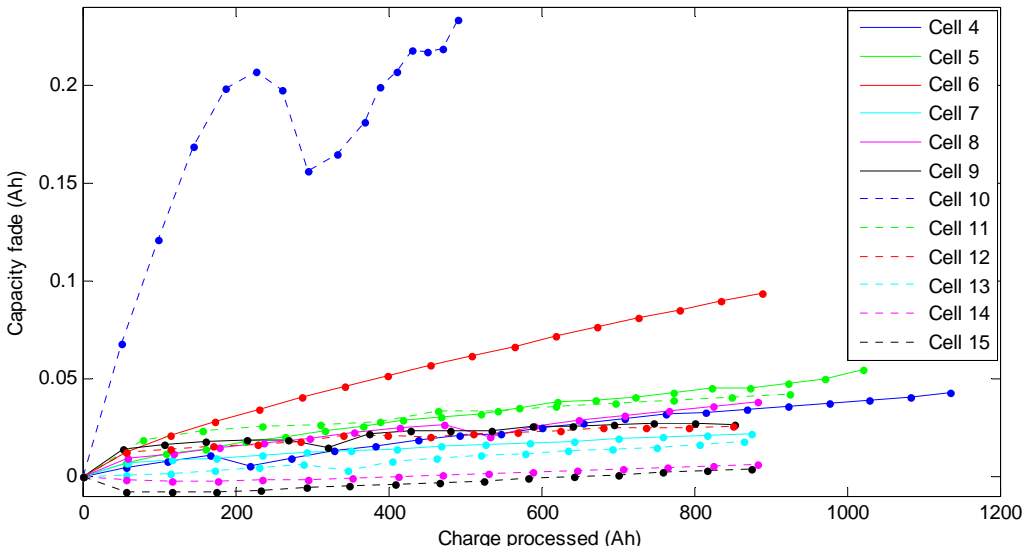


Figure 6.8: The capacity fading for cells 4 to 15 vs. the charge processed in the cells under stress conditions as described in table 6.1.

From figure 6.8 it can be seen that the capacity fading rate is relatively linear with minor saturation as a function of the charge processed. The capacity fading rate can be accurately described by a combination of a linear and radical function, as given by equation 4.11:

$$\xi = k_1 Ah + k_2 \sqrt{Ah} \quad (6.5)$$

Here ξ is the amount of capacity fading, k_1 and k_2 stress factor dependent parameters and Ah the charge processed. Each cell experiences a different capacity fading rate as expected under different stress factors. Since the cells experience discharge and regenerative braking of C-rates, the capacity fading is not modelled with cycle numbers. The amount of charge processed in each cycle is not equal for different ΔDoDs or current profiles, making it not possible to equally compare different cells based on cycle number. Furthermore, a cycle is not clearly defined and has to be calculated, while the charge processed in the cell can be directly measured from the cell current. The capacity fading will therefore be modelled with the charge processed.

In figure 6.8 deviations from the capacity fading trend are observed. The capacity fade of the reference cell 13 is given in figure 6.9, in which two deviations are observed. Firstly the capacity fading rate between the first and second measurement point is different than the general trend. This is explained by the fact that initially the cell is not conditioned in the same way as in the rests of the measured data points. The cell is initially unused and is still in its kick-in period. During the kick-in period the cell will stabilise, while in the other data points the cell has already been stabilised. The second deviation is a spike as a result of the test cycle occurring during a power failure, causing an error in the measured data. The occurrence of the power failure will also be visible in some other cells in the form of a data point deviation.

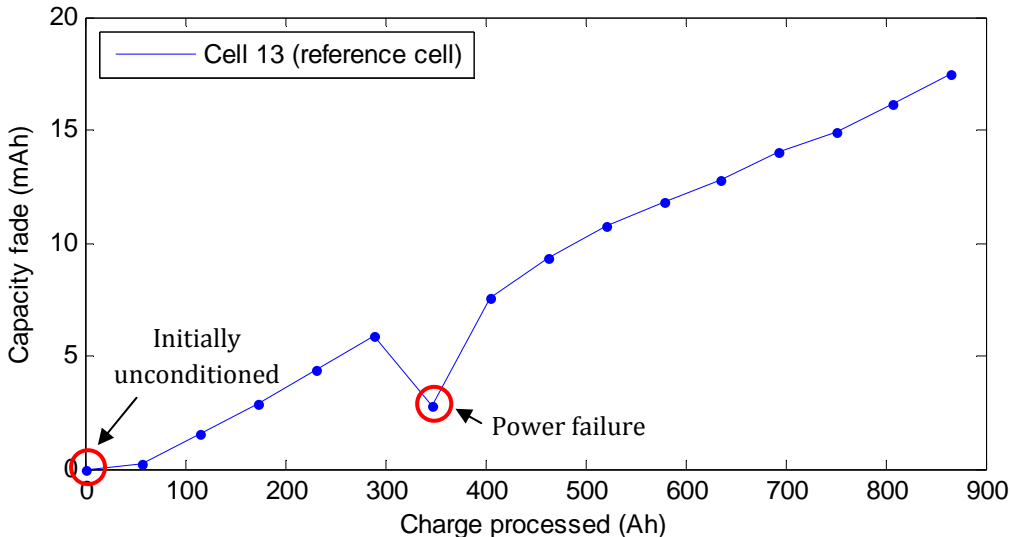


Figure 6.9: The capacity fade of the reference cell Cell 13 with the deviations from the general trends.

Some cells even initially experience negative capacity fade (capacity rise) before capacity fading occurs or exhibit a sudden deviation from the capacity fading trend. The deviations will be explained in the corresponding paragraphs in which these deviations occur. First the influence of different current profiles is analysed. Then the discharge C-rate dependence of the capacity fading rate is investigated, followed by the modelling of the temperature dependence. The recharge C-rate dependency at 0°C is also evaluated. Finally this paragraph concludes with the quantification of the SoC and ΔDoD dependency.

6.4.1.1 Regenerative braking influence

To investigate the influence of regenerative braking on the capacity fading, the capacity fading of a cell cycled with constant current is compared to a cell cycled with the current profile in figure 6.5. Three cells were cycled from 100% SoC with a ΔDoD of 100% and the amount of capacity fade is shown in figure 6.10.

The cells initially experience a capacity gain before the capacity fading occurs. The capacity gain may be caused by a structural change in the cell as a result of cycling the cell to almost 0% SoC. This is considered to be the kick-in period of the cell, in which the cell structure still has to stabilise. The initial 3 data points will therefore not be taken into account in the capacity fading rate modelling. The capacity fading rate for Cells 1, 2 and 3 have been modelled with a linear function as shown in figure 6.11.

6 Empirical development of an improved practical circuit-based model

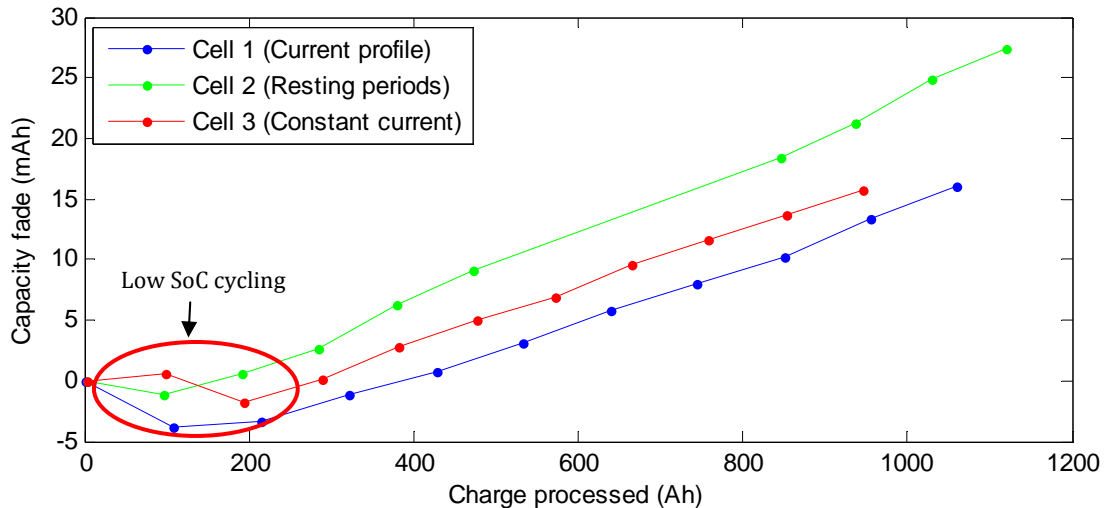


Figure 6.10: The capacity fade vs. charge processed for cells discharged with 100% ΔDoD under different current profiles.

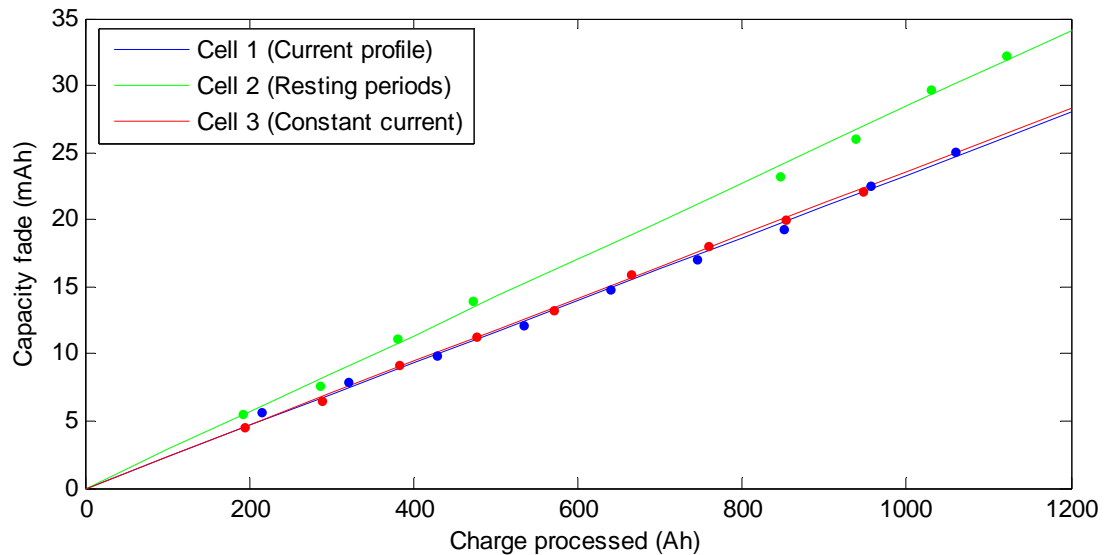


Figure 6.11: The capacity fade of Cells 1,2 and 3 scaled to the curve fit and their linear curve fits.

Figure 6.11 shows that the cells discharged with regenerative braking and constant current have the same capacity fading rate. This means that the capacity fading rate is not influenced by regenerative braking if the capacity fading rate is considered against the charge processed in the cell instead of the number of cycles as done in literature.

The cell with resting periods instead of recharging periods in the profile of figure 6.5 (Cell 2) shows a higher capacity fading rate than the other two cells. Possible reasons are that the short resting periods have a negative influence on the capacity of the cell or that the quality of the tested cell was worse than the other cells. Furthermore, the testing equipment skipped three test cycles during the experiment as seen in figure 6.11. The results of Cell 2 are therefore deemed to be inconclusive. The difference between Cell 2 and the two other cells is that the other cells have been cycled continuously, while Cell 2 experienced resting time between cycling. To test whether resting periods have an influence on the capacity fading rate of the cell, future research may include the cycling of cells with resting periods of different lengths.

From figure 6.11 it can be concluded that the capacity fading rates for constant current discharge or discharge with regenerative braking are equal. The possible additional capacity fading due to short resting periods is ignored in the model, so the capacity fading rate is independent of the current profile type.

6.4.1.2 Discharge C-rate dependence

In the previous paragraph capacity gain is experienced during the kick-in period of the cell as a result of low SoC cycling. This capacity gain does not only occur during the kick-in period of the cell as shown in figure 6.12, but also when the cell has already been cycled for a while. In figure 6.12 cells cycled with different discharge C-rates are plotted against the charge processed. Due to a procedure programming error Cell 4 has been fully discharged and kept on 0% SoC for 58 hours, which resulted in a small capacity rise. A possible explanation for the capacity rise is a structural change in the cell at low SoCs, making it easier to intercalate lithium ions in the previous unused parts of the cell. However, the capacity rise is less than 1% of the rated capacity, so it does not have a large impact on the cell capacity.

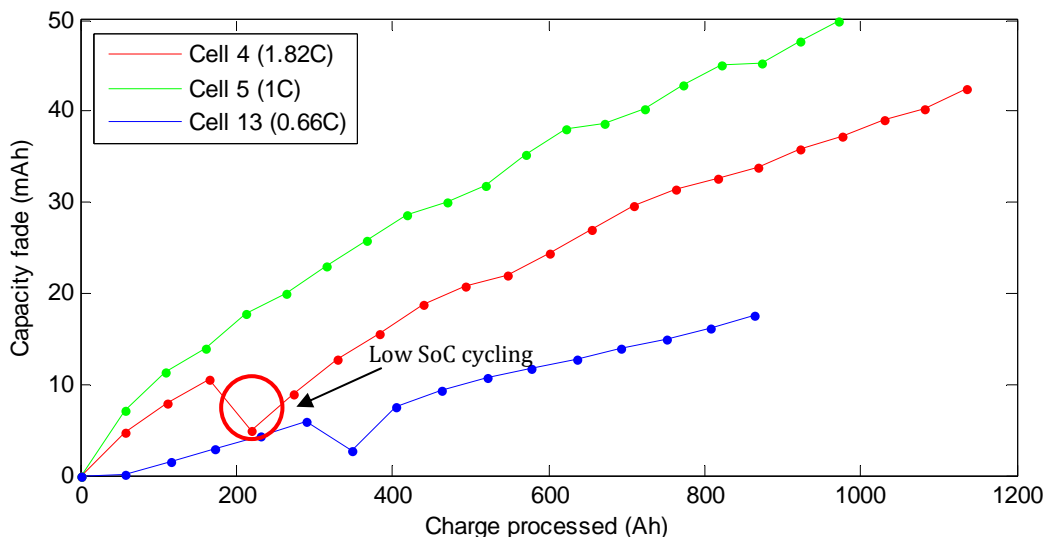


Figure 6.12: The capacity fade vs charge processed of cells discharged with different C-rates and equal recharge rates. The temperature oven of Cell 4 and 5 experienced temperature fluctuations.

From figure 6.12 it can also be seen that the capacity fading rate for a discharge rate of 0.67C is lower than the discharge rates 1.82C and 1C. This would lead to the conclusion that capacity fading is more severe at higher currents. However, the temperature oven of Cell 4 and 5 was not able to keep the cells at 25°C, since the oven was only able to cool with room temperature and the room temperature was higher than 25°C. As a consequence the temperature of the oven with Cells 4 and 5 fluctuated between 28°C and 30°C, which resulted in an increased capacity fading rate as a result of higher temperatures.

Consequently, to investigate the effect of different discharge C-rates on the capacity fading rate, only Cells 4 and 5 can be compared. Since Cell 4 experienced low SoC cycling between the 4th and 5th data point, the cells can only be compared from the 5th data point. In figure 6.13 the data points have been fitted with equation 6.5 with data from the 5th data point.

6 Empirical development of an improved practical circuit-based model

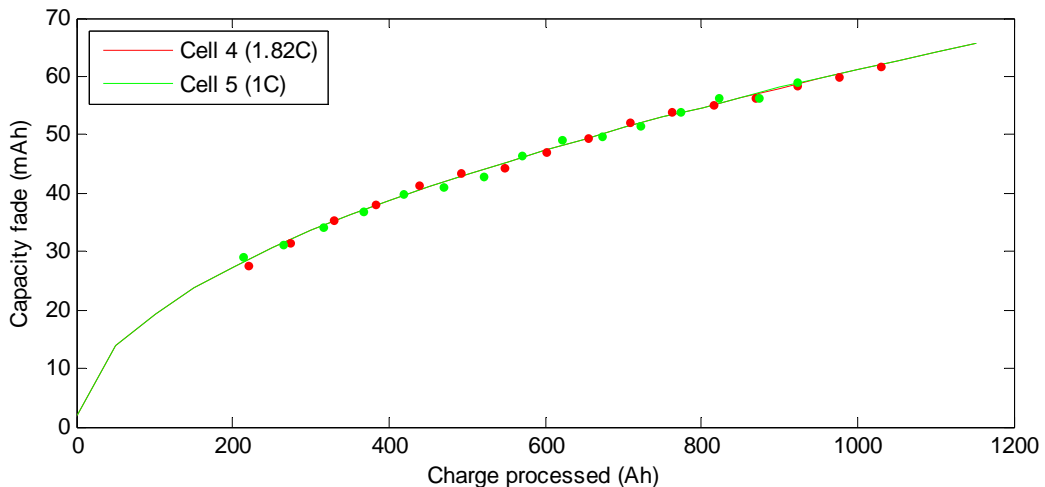


Figure 6.13: The capacity fade of Cell 4 and 5 taken from the 5th data point scaled to the curve fit and their curve fits with equation 6.5.

As can be seen from figure 6.13, the capacity fading rate for both Cell 4 and 5 are overlapping, with a minor difference as a result of temperature fluctuations and curve fitting. It can therefore be concluded that different discharge C-rates around room temperature does not contribute to additional capacity fade, under the condition that the C-rates do not exceed the maximum rating of the cell.

The discharge C-rate is far under the maximum C-rate of 27C (30A), and it is possible that at high C-rates near the maximum will introduce additional capacity fade. Batteries in electric vehicles, however, also operate with a C-rate far under the maximum specifications and are often oversized to have sufficient driving range. The discharge C-rate will therefore most likely not introduce additional capacity fade. This is under the assumption that the battery management system will not let the battery overdischarge. Finally, even though high C-rates itself do not cause additional capacity fade, it does not mean the temperature rise associated with increased power dissipation due to higher C-rates will not.

6.4.1.3 Temperature dependence

To investigate the influence of temperature on the capacity fading rates, cells are cycled in different temperature ovens with a constant temperature. The result of capacity fade at different temperatures is shown in figure 6.14. As can be seen from figure 6.14, every cell except cell 10 (-20°C) follows the general capacity fading trend.

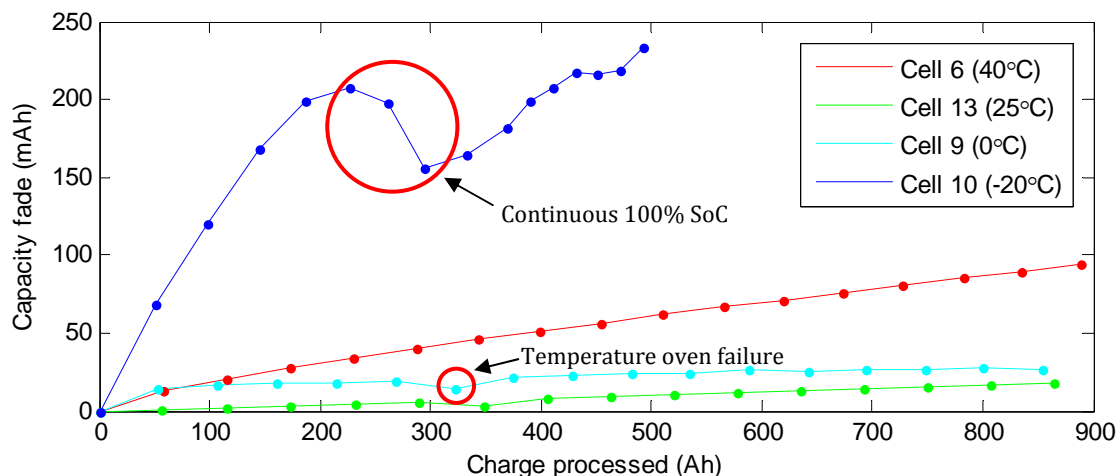


Figure 6.14: The capacity fade at determined at different temperatures.

At -20°C the cell experiences severe capacity fading, which is most likely the effect of lithium plating in the cell and the time limited charging step. At -20°C the electrochemical processes in the cell are very slow, which result in a high internal cell resistance. Due to the high internal resistance the charging step reaches the time limit of 100 minutes and the charging current is cut off before it drops to 0.01C. The end of charge condition is therefore not the same as for cells at higher temperatures and the cell is not charged to 100% SoC.

Due to the large capacity fading between two test cycles, the offset of the SoC between which the cell is cycled is also very large. The capacity keeps decreasing and the cycled SoC range expands at constant Amp hour cycling. This eventually causes the cell to reach 100% SoC before the calculated Amp hours have been charged back by the step 'recharging to the desired SoC' as described in figure 6.2. The cell was kept at 100% SoC for 96 hours and then 45 hours, which most likely caused a structural change in the cell and resulted in capacity rise as shown in figure 6.14.

Since at -20°C another capacity fading mechanism occurs and Cell 10 does not experience the same testing conditions due to the high resistance, Cell 10 is neglected from the temperature stress factor analysis. Furthermore, at the 7th data point of Cell 9 the temperature oven failed to cool, so a small capacity rise was experienced. The temperature of Cell 4 fluctuated between 28-30°C and was mostly around 29-30°C. Since it has been concluded that the discharge C-rate level does not have an effect on the capacity fading rate, Cell 4 can also be included in the temperature analysis and is assumed to be 30°C. By neglecting the data points with equipment failure and the unconditioned first data points of each cell, figure 6.15 is obtained.

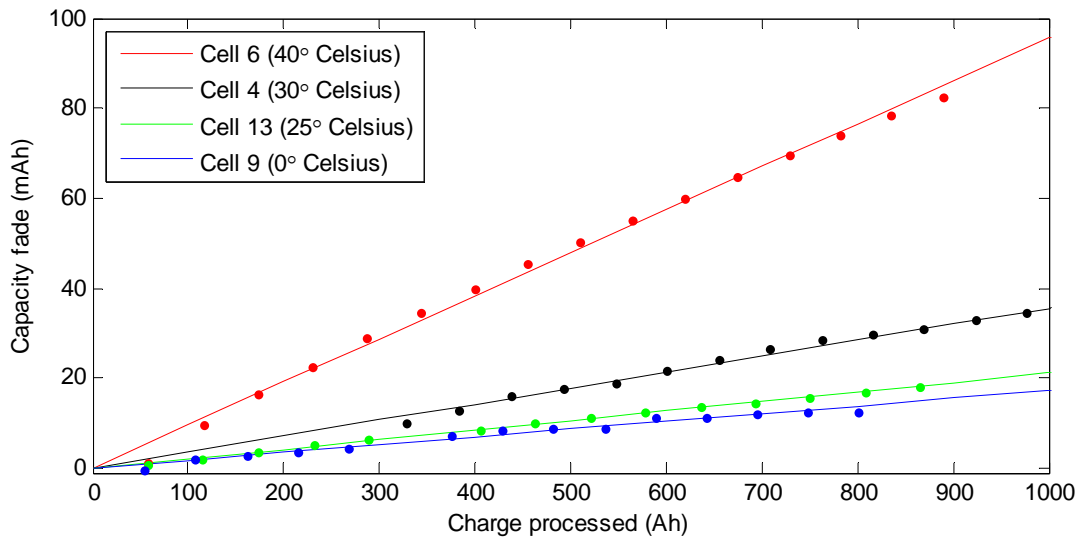


Figure 6.15: The linear approximated capacity fade of cells at 40°C, 30°C, 25°C and 0°C.

In line with the general expectation the cycle life of the cell severely reduces above room temperature. The capacity fading rates shown in figure 6.15 are determined for the cycling temperature. To determine capacity fade at reference temperature, after the cycling tests the cell temperatures have been brought to 25°C and the capacity was measured. The measured capacity at 25°C after the tests was compared to the measurements done before the test and the capacity fading rate was corrected. In figure 6.16 the measured capacity for each test cycle is given for 40°C with a measurement of the capacity at reference temperature before and after the test.

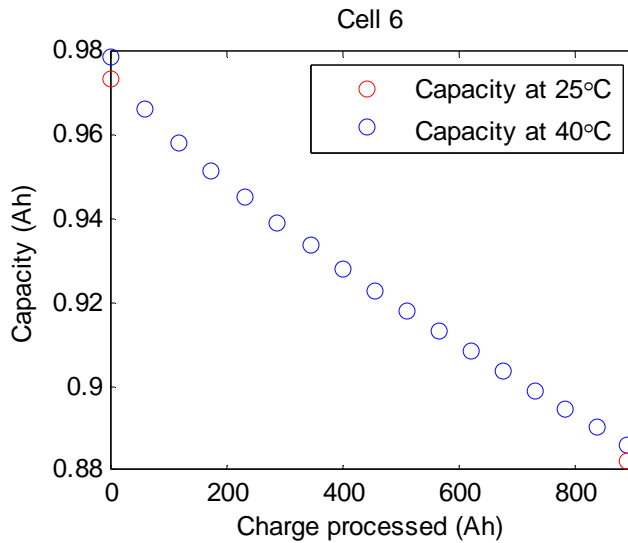


Figure 6.16 The capacity vs. charge processed for cells cycled at 40°C and their corresponding capacities at reference temperature measured at the beginning and end of the cycling test.

The capacity fade at reference temperature was found to be lower by 1.6% of the total capacity fade. Since the cells at 30°C were suppose to cycle at reference temperature, no capacity measurement at reference temperature was taken before and the tests. Because the capacity fading rate for 40°C only differed by 1.6% from the capacity fading rate at reference temperature, the difference of the capacity fading rate at 30°C compared to the rate at reference temperature will be negligible small.

At low temperatures cells do not only experience an irreversible capacity loss, but also possibly reversible capacity loss. To confirm whether the capacity fade at low temperature results in reversible or irreversible capacity loss, the capacity of cells at 0°C (Cell 9, 11, 12) and -20°C (Cell 10) have been measured at reference temperature before and after the cycling tests as shown in figure 6.17.

The temperature dependent capacity variation before and after the cycling tests has been compared for each cell to investigate the irreversible capacity loss. Each cell shows a larger capacity change measured at the end of the cycling test compared to a fresh cell. This indicates that a part of the capacity fade at low temperatures is reversible and the capacity fading rate is lower than determined at the testing temperature. For Cells 10, 11 and 12 the reversible capacity loss is very low with respectively 6%, 11% and 3% of the total capacity fade. However, Cell 9 the reversible capacity loss was measured to be 55%. It has to be noted that measured capacity before the cycling tests were of unconditioned cells and the cells were still in their kick-in period. In this kick-in period the cell structure may not be stabilised yet, causing the measured capacity of each subsequent cycle to possibly deviate from the previous cycle. This results in an inaccurate measurement of the temperature dependent capacity change. To accurately determine the amount of reversible capacity loss, every few test cycles the capacity at reference temperature also has to be measured. Unfortunately, due to practical issues this was not possible.

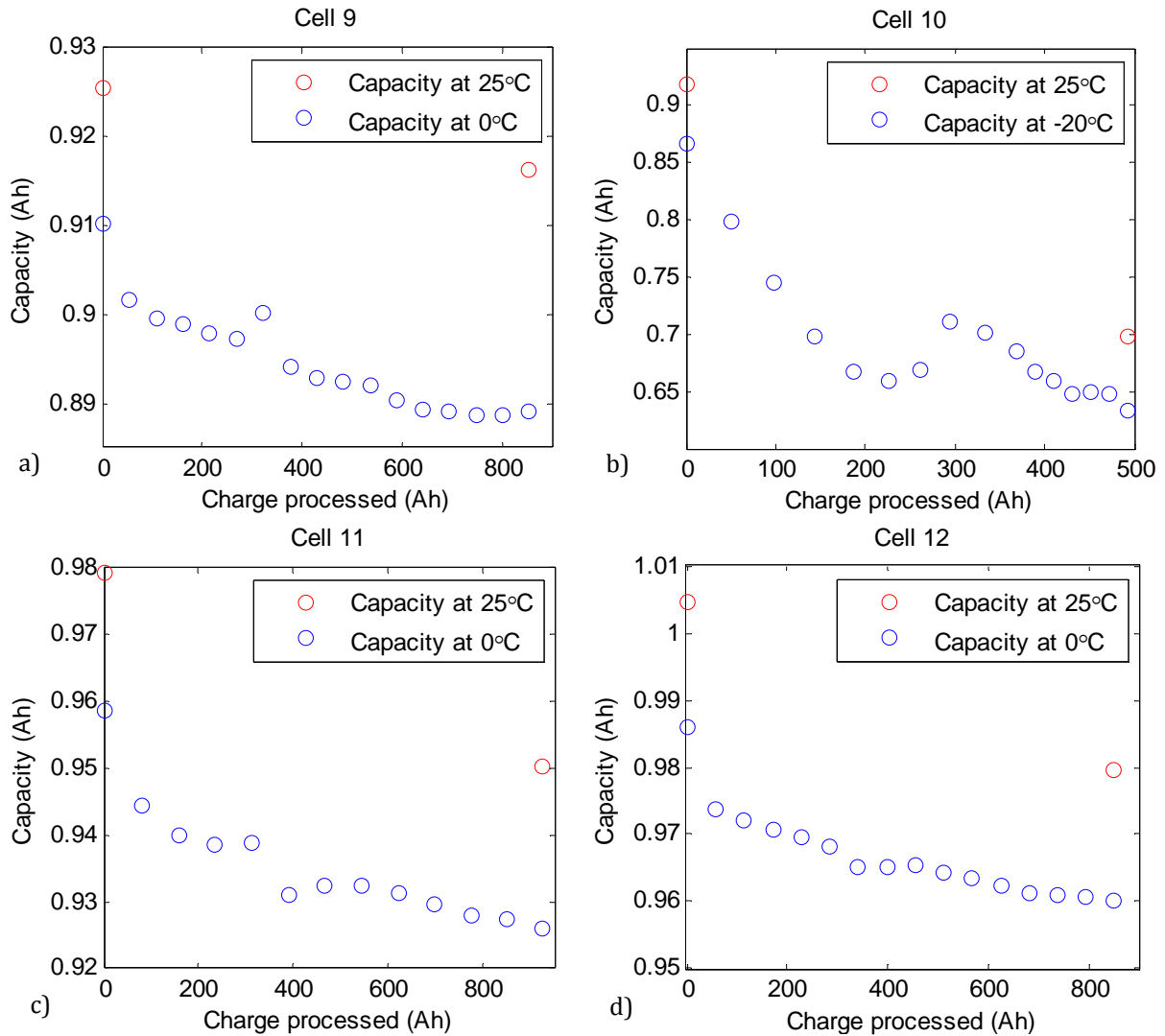


Figure 6.17: The capacity vs. charge processed for a) Cell 9, b) Cell 10, c) Cell 11 and d) Cell 12 cycled at low temperatures and their corresponding capacities at reference temperature measured at the beginning and end of the cycling test.

As described in paragraph 4.4.1, the temperature dependence of the capacity fading rate can be described by the Arrhenius equation:

$$\delta\xi(T) = \delta\xi_{ref} \cdot e^{\left(-\frac{E_a}{R}\left(\frac{1}{T} - \frac{1}{T_{ref}}\right)\right)} \quad (6.6)$$

where $\delta\xi_{ref}$ is the capacity fading rate under the reference conditions (Cell 13), R the gas constant, E_a the activation energy, T the temperature and T_{ref} the reference temperature, both in Kelvin. By plotting the natural logarithm of the capacity fading rates against $1000/T$ in figure 6.18, it is easier to see whether the capacity fading rates follow the Arrhenius equation.

In figure 6.18 both the corrected capacity fading rate for Cells 9 and 12 are displayed, since the testing conditions for Cell 12 are almost equal to Cell 9. From figure 6.18 it can be seen that the capacity fading rate for temperatures above 25°C are linear with $1000/T$, while the capacity fading rate at 0°C does not fit the linear trend. This means that the Arrhenius equation is at least valid for temperatures above 25°C, and at lower temperatures another capacity fading mechanism is present. This is also visible in figure 6.19.

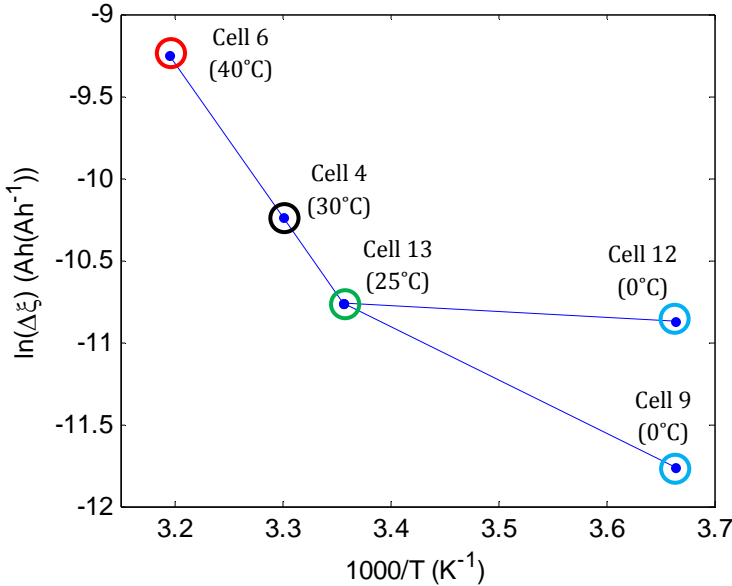


Figure 6.18: The natural logarithm of the corrected capacity fading rate for 25°C caused by cycling at different temperatures vs. 1000/T.

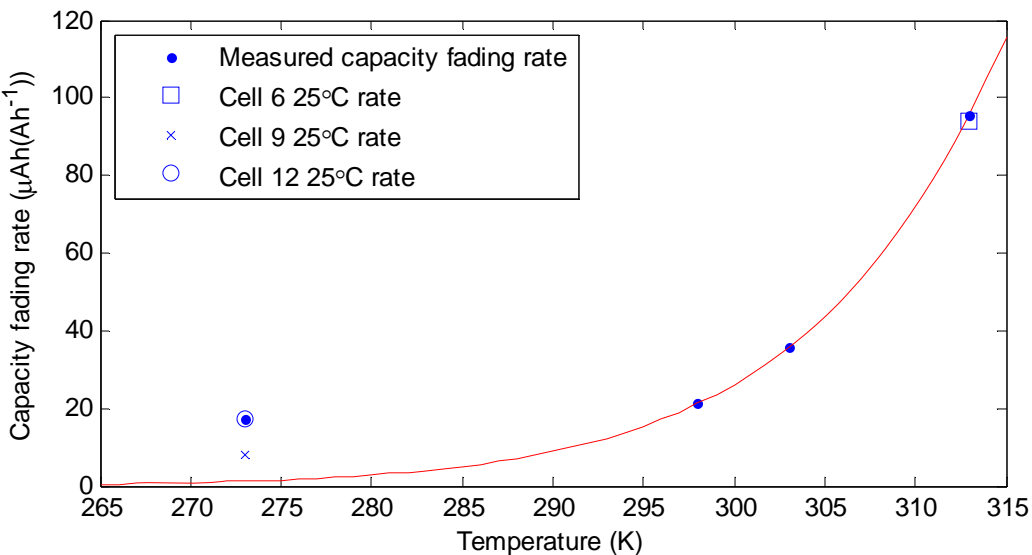


Figure 6.19: Different capacity fading rates vs. temperature, fitted by the Arrhenius equation with an adjusted R^2 of 0.999. The capacity fading rate at 0°C has been excluded from the fit. The capacity fading rate for cells cycled at different temperatures is corrected to the reference temperature.

In figure 6.19 the capacity fading rate at 0°C is excluded from the fit with equation 6.6. $\delta\xi_{ref}$ is the capacity fading rate at reference temperature and E_a is 78.06 kmol/J. In figure 6.19 the corrected capacity fading rates without reversible capacity loss have also been shown. It can be seen that capacity fading rate at 0°C is higher than the rate predicted by the Arrhenius equation, caused by another capacity fading mechanism. This is most likely lithium plating due to the recharge of regenerative braking and normal charging. Therefore the temperature dependent capacity fading rate described by equation 6.6 is certainly valid for temperatures above 25°C, insufficient below 0°C and possibly too optimistic between 0°C and 25°C.

6.4.1.4 Charging C-rate dependence at low temperature

From the temperature analysis it has been concluded that at low temperatures additional capacity fading occurs, most likely due to lithium plating. Lithium plating is dependent on the recharge rate of the cell, and is more severe at higher C-rates. This was also visible from the measurement data shown in figure 6.20.

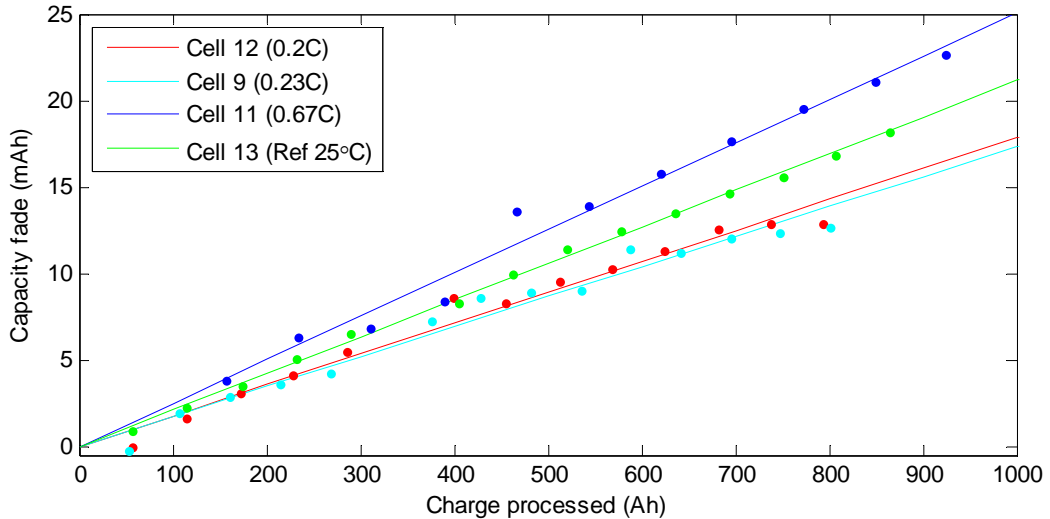


Figure 6.20: A linear approximation of the capacity fade with different recharge C-rates at 0°C and Cell 13 as comparison.

Three different cells have been cycled at 0°C. Cell 12 was to test whether the C-rate can be redefined as relative to the actual capacity of the cell instead of the nominal capacity and model the C-rate influence according to the redefined C-rate. In paragraph 6.4.1.2 it was, however, shown that the discharge C-rate did not introduce accelerated capacity fading and lithium plating is most likely the cause of accelerated capacity fading with increasing recharge C-rate. Furthermore, the difference between the true capacity at 0°C and 25°C is so small that a redefinition of the C-rate has no use, rendering the purpose of Cell 12 obsolete. Cell 12 is then only used as a redundant cell for Cell 9.

From figure 6.20 the influence of an increased recharge C-rate is visible. Since the test conditions of Cell 9 and 12 are nearly similar, the difference can be regarded as a fitting offset. Cell 11 with a higher recharge C-rate clearly shows a higher capacity fading rate. It may be arguable that even though the cells are constantly cooled, higher C-rates can still cause a temperature rise in the cell, which result in a higher capacity fading rate. However, the capacity fading of reference cell 13 is also shown in figure 6.20 and has a lower capacity fading rate than Cell 11. Even if the temperature rises in Cell 11 as a result of a higher recharge C-rate, it cannot explain the high capacity fading rate. It can therefore be concluded that the recharge C-rate does have an influence on the capacity fading rate, which is mostly likely caused by lithium plating. In that case lower temperatures and higher recharge C-rates are expected to cause more capacity fade. Not enough measurements have, however, been conducted to quantify this effect.

6.4.1.5 SoC and ΔDoD dependence

The last stress factors on the capacity fading of a Li-ion cell to evaluate are the SoC and ΔDoD. To prevent influence from different continuous stress times on the measurements, each cell was rested after an equal percentage of SoC was processed in the cell. This means that Cell 7 (12.5% ΔDoD) underwent 2 cycles before it was rested, while Cell 8 (50% ΔDoD) was rested after

6 Empirical development of an improved practical circuit-based model

discharging and after charging as indicated by figure 6.2 and table 6.1. So the measurements on capacity fading under different SoC and ΔDoD result solely from the influence of these stress factors, which are shown in figure 6.21.

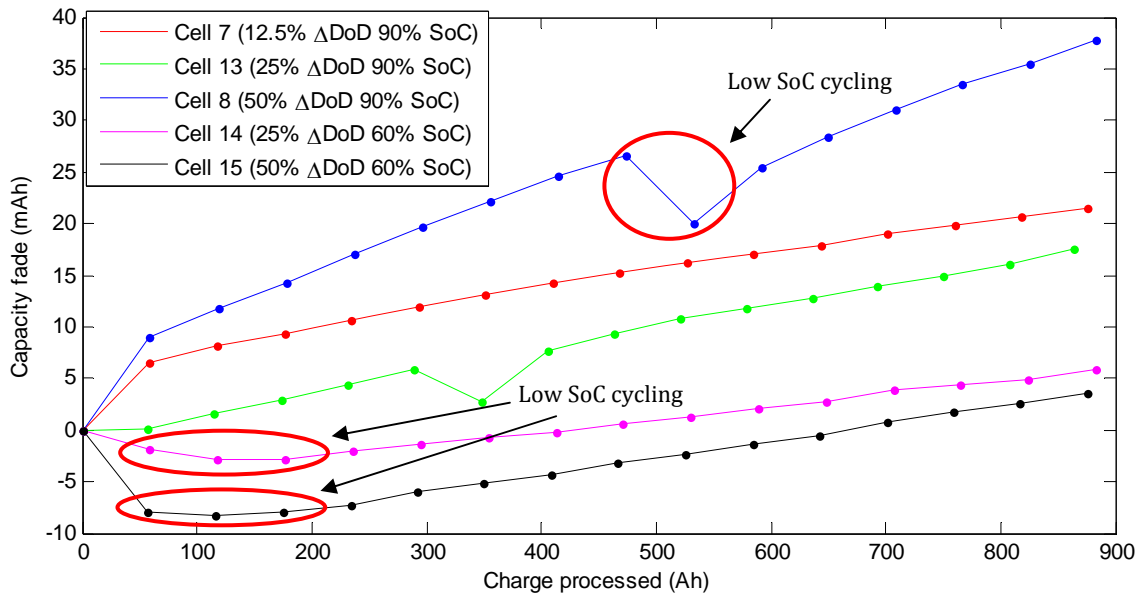


Figure 6.21: The capacity fade determined for cells cycled at different SoC and ΔDoD vs. charge processed.

In figure 6.21 several anomalies are visible. Cell 8 experienced low SoC cycling for tens of cycles due to a test procedure programming error, similar to Cell 4 shown in figure 6.12. Cell 8 was cycled at a dormant part of the SoC range which is only used in the test cycle, most likely resulting in a structural change in the cell and capacity rise.

Cell 14 and 15 also show an increase in capacity for the few initial data points, but are not a result of a programming error. Furthermore, it can also be seen that Cell 15 experiences a larger capacity rise than Cell 14, which may not be completely contributed to the unconditioned first data point. Since Cell 15 reaches a lower SoC (10%) than Cell 14 (35%), more structural change will occur in the Cell 15, which results in an initial capacity rise. However, the capacity rise is less than 1% of the nominal capacity and does not have a large impact on the cycle life of the cell.

By omitting the capacity rises and the unconditioned data points of the cells in the kick-in period, the data points can be approximated by a linear fit and figure 6.22 is obtained. However, the amount of tests conducted was not enough to quantify the capacity fading as a function of SoC and ΔDoD . Therefore additional tests have been conducted at different SoCs and ΔDoD , which are also shown in figure 6.22. Due to practical reasons only four additional tests could be conducted and the testing times was much smaller. The data points in the kick-in periods have also been omitted for the additionally tested cells.

In figure 6.22 the influence of cycling starting from different SoCs with different ΔDoDs can be clearly seen. A high initial SoC will lead to an acceleration of capacity fading, which is visible by comparing Cells 13, 14 and 3a in figure 6.23a for 25% ΔDoD , or Cells 8, 15 and 1a in figure 6.23b for 50% ΔDoD . This is consistent with literature [116], in which the high SoC influence is described with the Tafel equation in the form of end of charge voltage.

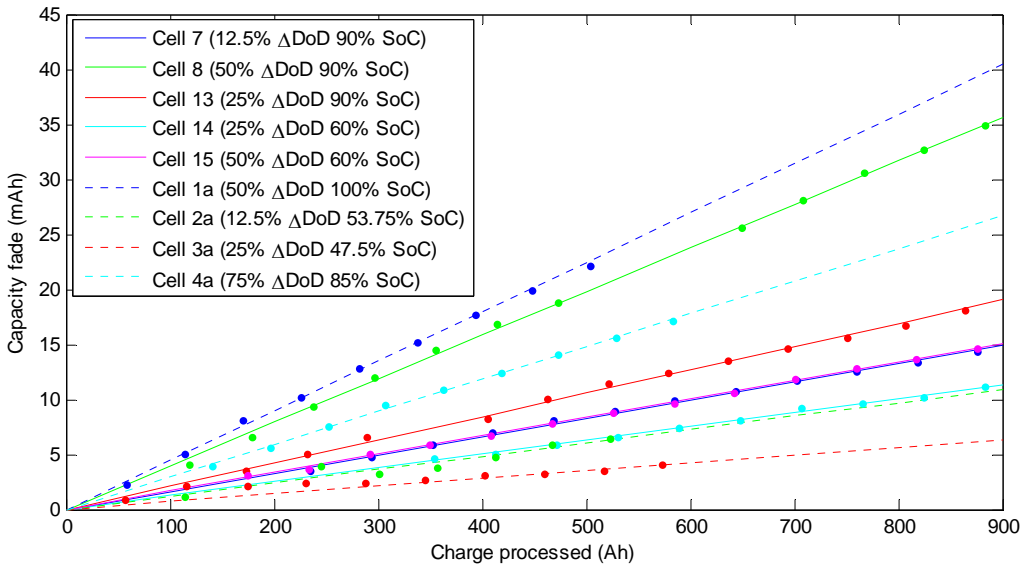


Figure 6.22: A linear fit of the capacity fade at different SoC and ΔDoD vs. charge processed.

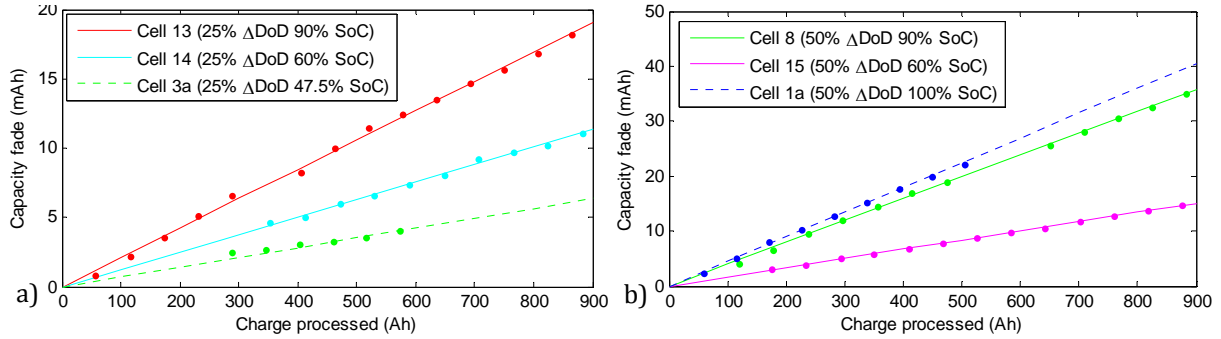


Figure 6.23: The capacity fading for cells cycled from different initial SoCs with a) 25% ΔDoD and b) 50% ΔDoD .

A large ΔDoD will also cause a higher capacity fading rate, which is shown by figure 6.24a. In figure 6.24a Cell 4a is also shown, as the initial SoC is close to the initial SoC of the other cells. Cell 4a shows a lot less capacity fading compared to Cell 8, even though the ΔDoD is much larger, which seems counterintuitive. However, if the cells are compared on the basis of their average SoC over time instead of initial SoC [3] as described by equation 4.21, the lower capacity fading rate for cells cycled with larger ΔDoDs can be explained.

From analysis of the current profile used for cycling it was found that the regenerative braking had very little influence on the slope of the SoC decrease over one cycle, and each cycle is recharged to the same initial SoC. This means that SoC development over one cycle can be approximated as a linear decrease and SoC_{avg} over one cycle is the average of the initial SoC and the final SoC before the cell is recharged. However, only cycling losses have been investigated as a function of charge processed. On the other hand, equation 4.21 is a function of time, which would include calendar losses. Since calendar losses have been neglected in this study, equation 4.21 changes to

$$\text{SoC}_{avg} = \frac{1}{\Delta Ah_m} \int_{Ah_{m-1}}^{Ah_m} \text{SoC}(Ah) dAh \quad (6.7)$$

where Ah_{m-1} is the starting amount of charge processed of the SoC_{avg} determination, Ah_m the final amount and ΔAh_m is $Ah_m - Ah_{m-1}$. Furthermore, the ΔDoD can also be expressed as the normalised

6 Empirical development of an improved practical circuit-based model

SoC deviation SoC_{dev} from the average SoC SoC_{avg} . Since calendar losses have been neglected in this model, SoC_{dev} will be expressed with the amount of charge processed instead of time just like equation 6.7. Additionally, the factor 2 in equation 4.22 is removed, as it is more intuitive to see SoC_{dev} as a deviation from SoC_{avg} instead as ΔDoD . Equation 4.22 will then change to

$$SoC_{dev} = \sqrt{\frac{3}{\Delta Ah_m} \int_{Ah_{m-1}}^{Ah_m} (SoC(Ah) - SoC_{avg})^2 dAh} \quad (6.8)$$

In figure 6.24b the same figure as figure 6.24a is depicted, but with the legend changed to SoC_{avg} and SoC_{dev} . The SoC_{avg} of Cell 4a is much lower than Cell 8, which explains the lower capacity fading rate. On the other hand, the SoC_{dev} of Cell 4a is much higher than the other cells, resulting in a higher capacity fading rate compared to Cell 7 and 13.

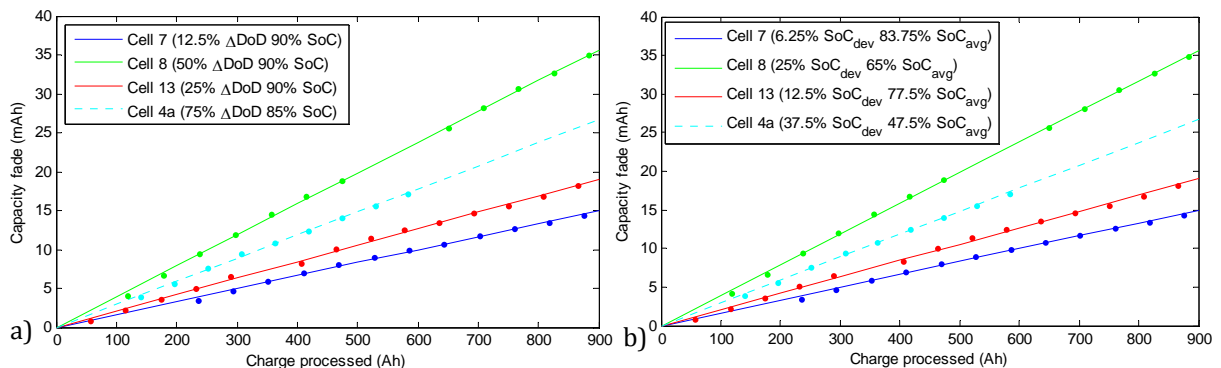


Figure 6.24 The capacity fading for cells cycled with different ΔDoD from the approximately the same initial SoC with a) the conventional legend and b) the ΔDoD and initial SoC expressed in SoC_{dev} and SoC_{avg} .

According to [3], the capacity fading rate dependent on SoC_{avg} can be described by the Tafel equation, which would result in an exponential dependence on SoC_{avg} . By using an exponential equation to curve fit the obtained data of the SoC_{avg} dependence of the capacity fading rate, figure 6.25a is obtained. For the obtained data, the Tafel equation does not seem to be a good fit. On the other hand, at each SoC_{dev} level only a maximum of three data points is available. It can therefore not be determined if the equation is a good fit or not. Nonetheless, a different equation will be chosen to obtain a more accurate fit for the measurement data. In figure 6.25b the capacity fading rates are fitted with the following empirical equation, which was obtained from curve fitting analysis:

$$\delta\xi(SoC_{avg}, SoC_{dev}) = k_{s1}(SoC_{dev}) \cdot e^{(k_{s2} \cdot SoC_{avg})} + k_{s3}(SoC_{dev}) \quad (6.9)$$

where k_{s1} and k_{s3} are the SoC_{dev} dependent parameters, k_{s2} is a constant and SoC_{dev} is a value between 0 and 0.5, corresponding to 0% and 50%. SoC_{dev} cannot be larger than 0.5, as that is the maximum SoC deviation when a cell is cycled between 100% and 0% SoC. Figure 6.25b shows that equation 6.9 is a good curve fit for the measurement capacity fading rates.

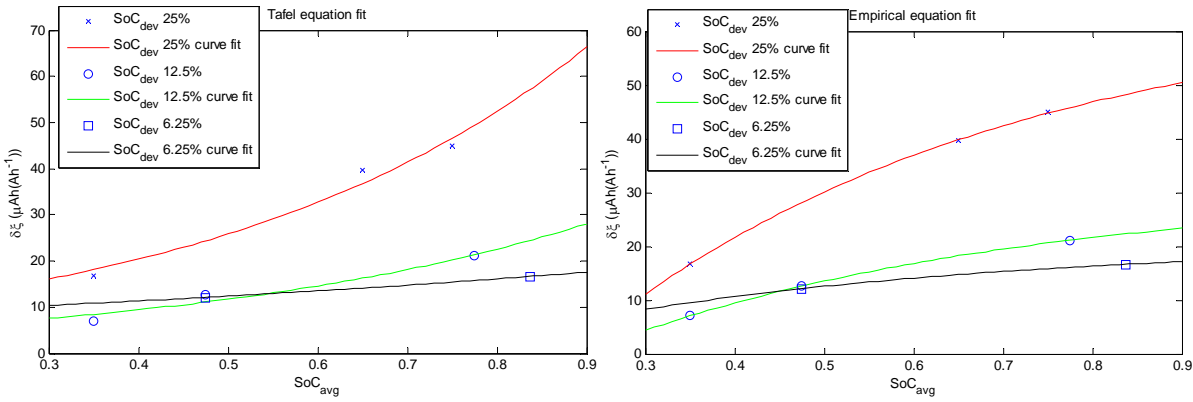


Figure 6.25: The capacity fading rate vs the average SoC over a cycle SoC_{avg} for different values of SoC_{dev}

To describe the SoC_{dev} influence, the crack propagation theory was employed in [3], resulting in the capacity fading rate to be exponentially dependent on SoC_{dev} . The total capacity fading rate was then calculated by multiplying the Tafel equation for the SoC_{avg} and the crack propagation equation for SoC_{dev} . However, the SoC_{dev} dependent parameters in equation 6.9 could not be fitted as a multiplication with another exponential function. By analysing the SoC_{dev} dependent parameters at the measured 25%, 12.5% and 6.25% SoC_{dev} , equation 6.9 turns into the following empirical equation:

$$\delta\xi(SoC_{avg}, SoC_{dev}) = k_{s1}SoC_{dev} \cdot e^{(k_{s2} \cdot SoC_{avg})} + k_{s3}e^{k_{s4}SoC_{dev}} \quad (6.10)$$

with $k_{s1} = -2.046E-4$, $k_{s2} = -2.1665$, $k_{s3} = 1.408E-5$ and $k_{s4} = 3.065$. The problem with both curve fits in figure 6.25 is that the 12.5% SoC_{dev} and 6.25% SoC_{dev} curves cross one another. This suggests that from a certain SoC_{avg} and lower, the cells will have a longer cycle life if a larger SoC_{dev} is experienced, which does not seem intuitive at all. Furthermore, the curve fits may result in a negative capacity fading rate at low SoC_{avg} . The problems are caused by the fact that the capacity fading rate at low SoC_{avg} has not been investigated for certain SoC_{dev} values, resulting in inconclusive capacity fading rates for low SoC_{avg} . Nevertheless, equation 6.10 is sufficient to capture the influence of the SoC_{avg} and SoC_{dev} on the capacity fading behaviour of the cell in most of the SoC region, if ΔAh_m in equation 6.8 is taken over a complete driving cycle. Equation 6.10 is not accurate enough to model the capacity fading rate for small ΔAh_m within a driving cycle, which would result in small SoC_{dev} values over a large range of SoC_{avg} . To obtain a more accurate equation for the capacity fading rate, more cycle life experiments have to be conducted at different SoC_{avg} with different SoC_{dev} , especially at SoC_{avg} or with very small SoC_{dev} . Finally, from the capacity fading analysis of cells discharged from different initial SoC and ΔDoD it can be concluded that a lower average SoC and/or a lower ΔDoD optimises the lifetime of a cell.

6.4.2 Useable cell capacity

The cell capacity does not only change as a result of irreversible capacity loss, but also experiences reversible capacity change. Both the irreversible and reversible capacity changes determine the useable cell capacity. As described in paragraph 3.4.1, the reversible capacity change is strongly dependent on the temperature. To quantify the reversible capacity change, one test cycle has been conducted at each temperature between 40°C and -15°C in steps of 5°C. Since -20°C showed severe capacity fading in paragraph 6.4.1.3, this temperature has been omitted.

6 Empirical development of an improved practical circuit-based model

In literature it was found that the reversible capacity change can be described by the Arrhenius equation. By plotting the natural logarithm of the capacity against $1000/T$ in figure 6.26a it was, however, found that the capacity development does not satisfy the Arrhenius equation. The natural logarithm of the capacity changes with a curve, which suggests that the Vogel-Tamman-Fulcher (VTF) equation can model the reversible capacity change. With the VTF equation the equation for the useable cell capacity becomes:

$$C_{use} = (Q_{nom} - \xi) \cdot e^{k_1 \left(\frac{1}{T-k_2} - \frac{1}{T_{ref}-k_2} \right)} \quad (6.11)$$

where $k_1 = -5.738$ and $k_2 = 2.099E2$. Q_{nom} is the nominal capacity at reference temperature T_{ref} , which was 0.9415 Ah for the tested cell. The curve fit for the capacity is shown in figure 6.26b with the measured capacity.

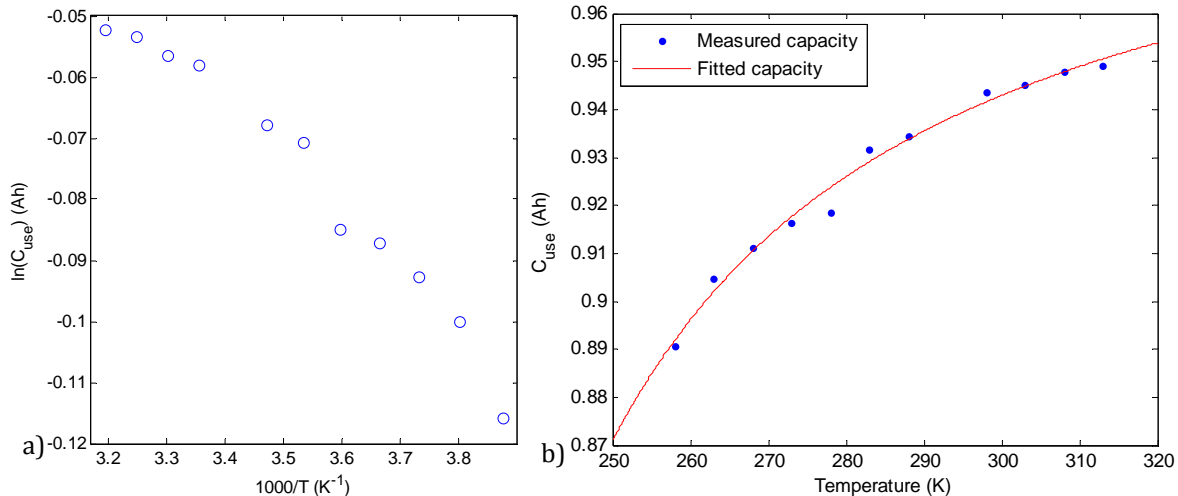


Figure 6.26: a) The natural logarithm of the capacity vs. $1000/T$ and b) the measured temperature dependency of the capacity with the corresponding curve fit according to the VTF equation.

The capacity fading of the cell is assumed to be negligible small during course of the experiment, as at each temperature the cell only experienced one test cycle. The offsets of the curve fit from the measured capacity result from the lower accuracy of the temperature oven and the increasing resistance both at low temperatures. Since the end of discharge/charge condition is when the current becomes lower than $0.01C$, at low temperatures the cell will be less discharged/charged than at higher temperatures due to the increased cell impedance; nevertheless, this effect is neglected in the model as the variations are small and thus equation 4.12 is sufficient to model the useable capacity.

6.4.3 Open-circuit voltage

From literature it was determined that the open-circuit voltage (OCV) is greatly dependent on the SoC and has to be experimentally determined. The OCV has been determined by a procedure similar to the capacity and parameter test cycle shown in figure 6.6, but instead of 1 minute rest intervals the cells are rested for 2 hours during each interval. Also each resting period occurs every 5% SoC instead of in 0.05 or 0.1Ah steps. In figure 6.27 the close-to-equilibrium (cte) OCV at room temperature has been given for charging and discharging.

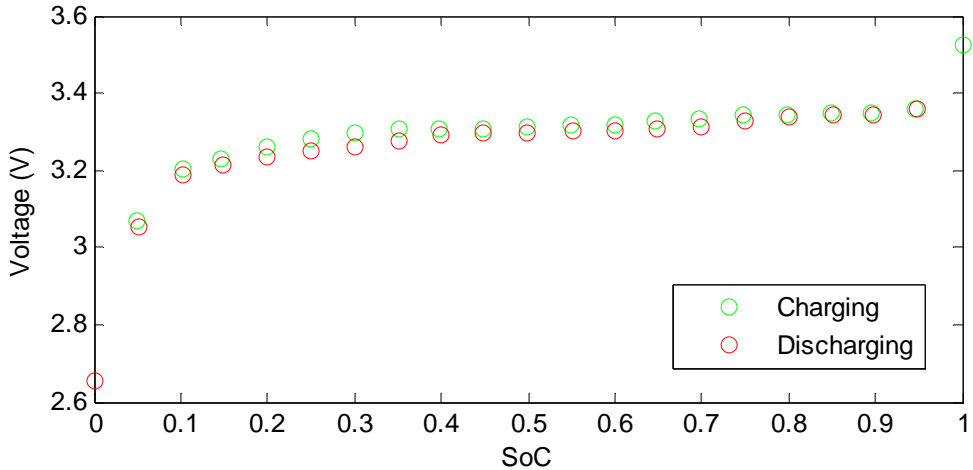


Figure 6.27: The measured charging and discharging cte-OCV at 25°C.

As can be seen from figure 6.27, the 2 hour cte-OCV measurements for charging and discharging are not completely overlapping. The reason is either hysteresis of the OCV or insufficient resting time for the cell to come to a complete equilibrium. As described in paragraph 5.3.3.2, the OCV will be assumed to have no hysteresis and the OCV is obtained by taking the average of the cte-OCV charging and discharging data. This will result in a standard deviation of 9.3mV or 1% of the OCV voltage range with the largest different between charging and discharging being 4% of the OCV voltage range. Any possible hysteresis will then be modelled by the current direction dependency of the internal cell impedance.

The measurement has been conducted for 40°C, 25°C, 0°C and -20°C and the averaged OCV for each temperature are shown in figure 6.28. From figure 6.28 it is seen that the higher the temperatures are, the higher and lower the voltages for respectively 100% and 0% SoC are. This is caused by the charging/discharging cut-off current of 0.01C. Since the internal resistance of the cells is lower at higher temperatures, the end of charge/discharge conditions are reached at a higher/lower SoC. Therefore 100% SoC at e.g. -20°C is slightly less than 100% SoC at 40°C. However, since the voltage rises/drops exponentially at 100%/0% SoC, the SoC difference between different temperatures will be insignificantly small.

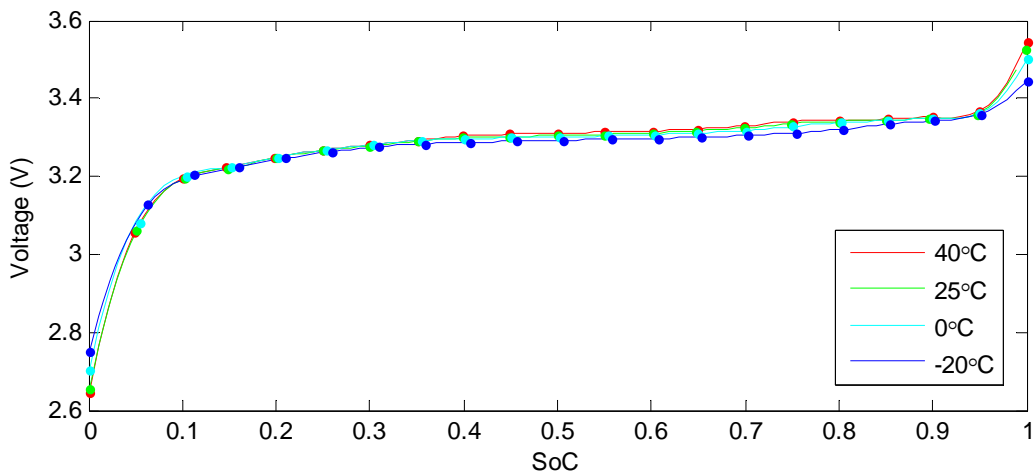


Figure 6.28: The OCV determined for different temperatures.

Furthermore, it can be seen that the OCV is slightly temperature dependent with a constant as described by equation 5.8. The temperature dependent voltage deviation is given in figure 6.29.

6 Empirical development of an improved practical circuit-based model

The deviations from reference temperature were found to be less than 2mV at most temperatures, going up to 8mV at -20°C. This corresponds to a deviation of only 1% or less compared to the OCV range. Since the temperature fluctuations were insignificantly small, the OCV is considered temperature independent.

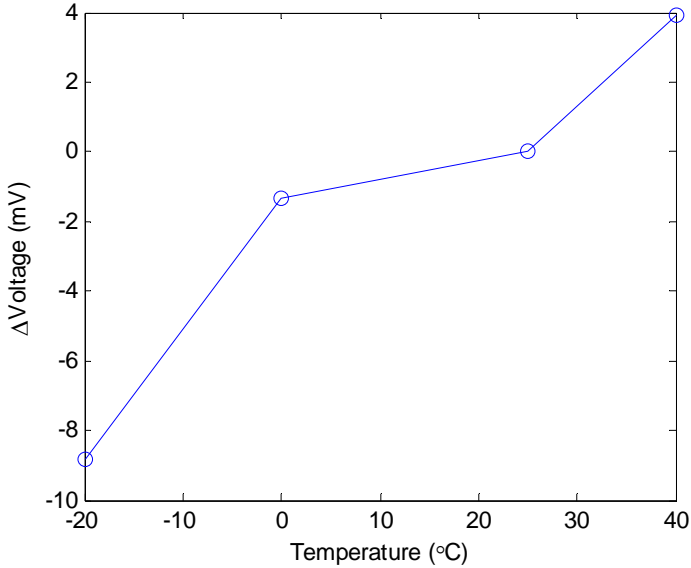


Figure 6.29: The constant voltage different of the OCV at different temperatures with 25°C as reference.

Since room temperature is taken as reference temperature, the OCV measurement data at 25°C will be used to obtain the parameters for the OCV equation. The data is fitted to equation 5.36 with the non-linear least squares method in Matlab 7.7.0 and figure 6.30 is obtained. The OCV is then modelled with:

$$V_{oc}(SoC) = a_1 e^{-a_2 SoC} + a_3 + a_4 SoC + a_5 e^{\frac{a_6}{1-SoC}} \quad (6.12)$$

with $a_1 = -5.863E-1$, $a_2 = 21.90$, $a_3 = 3.414$, $a_4 = 1.102E-1$, $a_5 = -1.718E-1$ and $a_6 = 8.000E-3$. Equation 6.12 is a good fit for the OCV and will be used to obtain the parameters of the other circuit components in the equivalent circuit-based model.

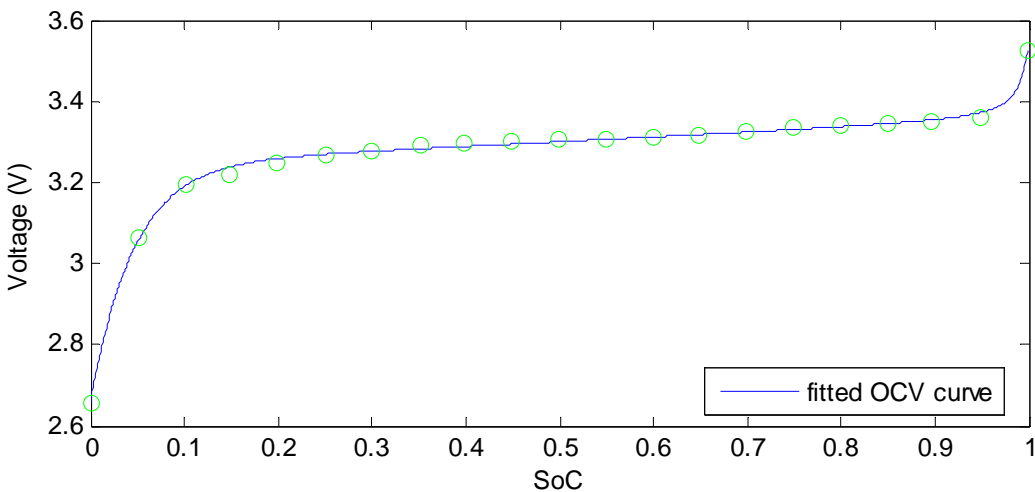


Figure 6.30: The OCV data at 25°C fitted with equation 6.12.

6.4.4 Internal cell impedance

Now an equation for the OCV has been obtained, the values for the internal cell impedance can be determined. The internal cell impedance consists of one ohmic resistance and two parallel RC pairs in series as depicted in figure 5.19. As described in paragraph 5.3.2, the internal cell impedances are strongly dependent on the SoC. This is also visible in the measurements, as shown in figure 6.31 and figure 6.32 for respectively discharging and charging.

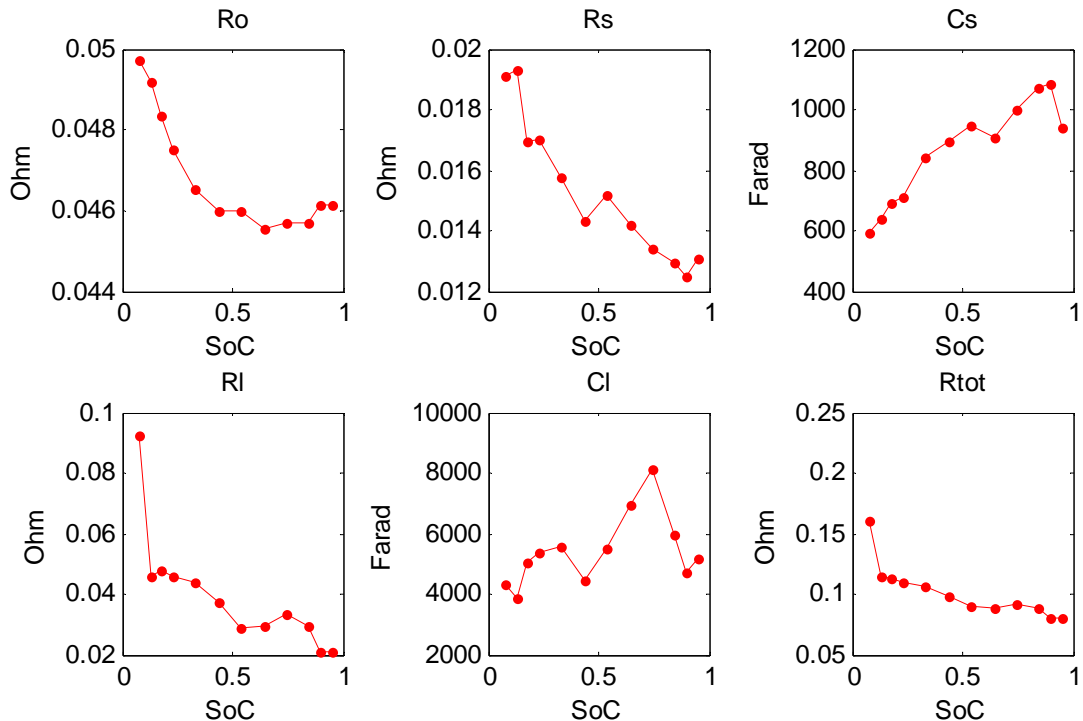


Figure 6.31: The internal cell impedance of reference Cell 13 for discharging.

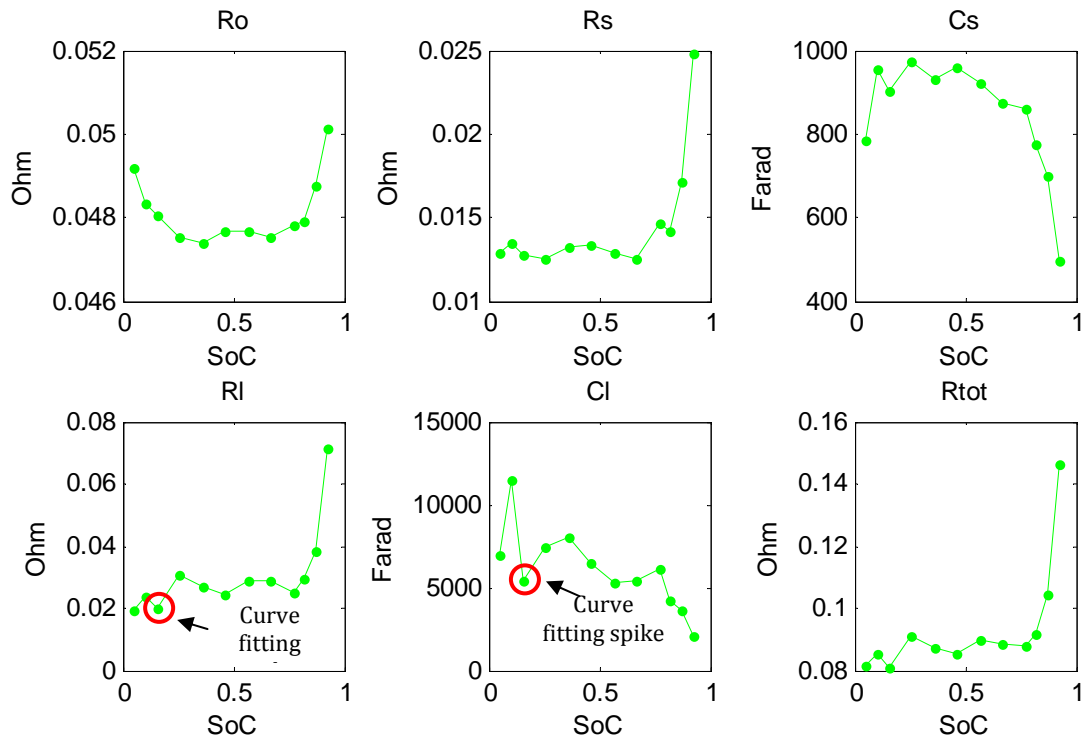


Figure 6.32: The internal cell impedance of reference Cell 13 for charging.

6 Empirical development of an improved practical circuit-based model

Since the internal impedance determination relies on curve fitting on an empirical equation of the OCV, unexpected spikes in the measurements can occur as shown in figure 6.32. These spikes occur in places where the OCV equation deviates from the measured OCV, which is where the OCV goes from the linear region into the exponential region. In the internal impedance analysis the spike data points will be omitted.

From both figure 6.31 and figure 6.32 it can be seen that the impedance elements vary severely over the SoC range; however, cells are designed to have a constant ohmic resistance over the entire SoC range. The ohmic resistance in the practical circuit-based model consists of the constant bulk resistance and SoC variable surface layer resistance, so R_o is not constant over the SoC range.

It can also be seen that the internal cell impedance for discharging is not the same as for charging. Only in the range between 70% and 40% SoC the discharge and charge impedance are somewhat equivalent. In an electric vehicle (EV), however, the SoC of the cell is expected to fluctuate over almost the entire SoC range and the internal cell impedance model cannot be assumed to be equivalent for charging and discharging.

Existing battery cell models only focus on modelling the discharge impedance, since most applications only discharge the cell during operation. During charging the application is not in operation, so the cell voltage behaviour is unimportant and the charging impedance is modelled the same way as for discharging. However, in EV applications this will lead to large inaccuracies. An EV recharges the battery cells constantly by regenerative braking, and thus operates in both discharge and charge mode of the battery cells. Therefore the internal cell impedance will be modelled with two sets of equations, one for discharge and one for charge.

Furthermore, in figure 6.31 and figure 6.32 the total cell resistance R_{tot} is shown in the bottom right graph for respectively discharging and charging. The behaviour of the internal cell resistance for discharging is like the mirrored behaviour for charging. Near a fully discharged/charged cell, the discharge/charge resistance rises exponentially. However, the charging resistance starts to rise exponentially around 80% SoC, while the discharge resistance exponential rise starts around 10% SoC. So from the internal cell impedance analysis it can be concluded that between 80% and 10% SoC the least energy is dissipated in the cells in EV applications.

The internal cell impedance has been determined for every cell at reference temperature, which is shown in figure 6.33 and figure 6.34 for respectively discharging and charging. The measured cell impedance for each cell is marked with a different colour. From the graphs it can clearly be seen that the SoC dependent behaviour of each internal impedance element is the same for every cell. The only difference is the magnitude of the impedance elements. The difference in R_o is caused by different contact resistances between the voltage measurement point and cell under test and manufacturing differences. The difference in the other impedance elements is caused by manufacturing and curve fitting offsets. This means that the internal cell impedance of every cell can be modelled with the same equations, with different parameters for each cell. The differences between the parameters of each cell except for R_o are, however, very small, so for a practical equivalent circuit-based model R_s , C_s , R_l and C_l can be modelled with the same equations and parameters for cells of the same manufacturer and type.

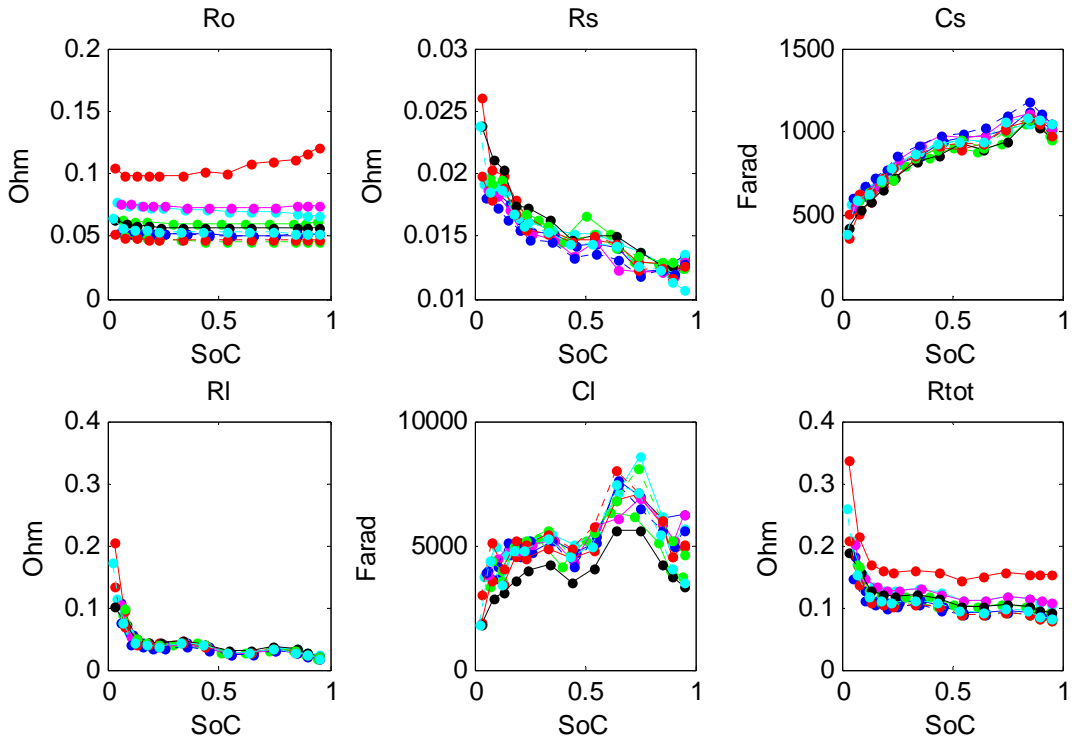


Figure 6.33: The internal cell impedance for discharging of different cells measured before the experiments.

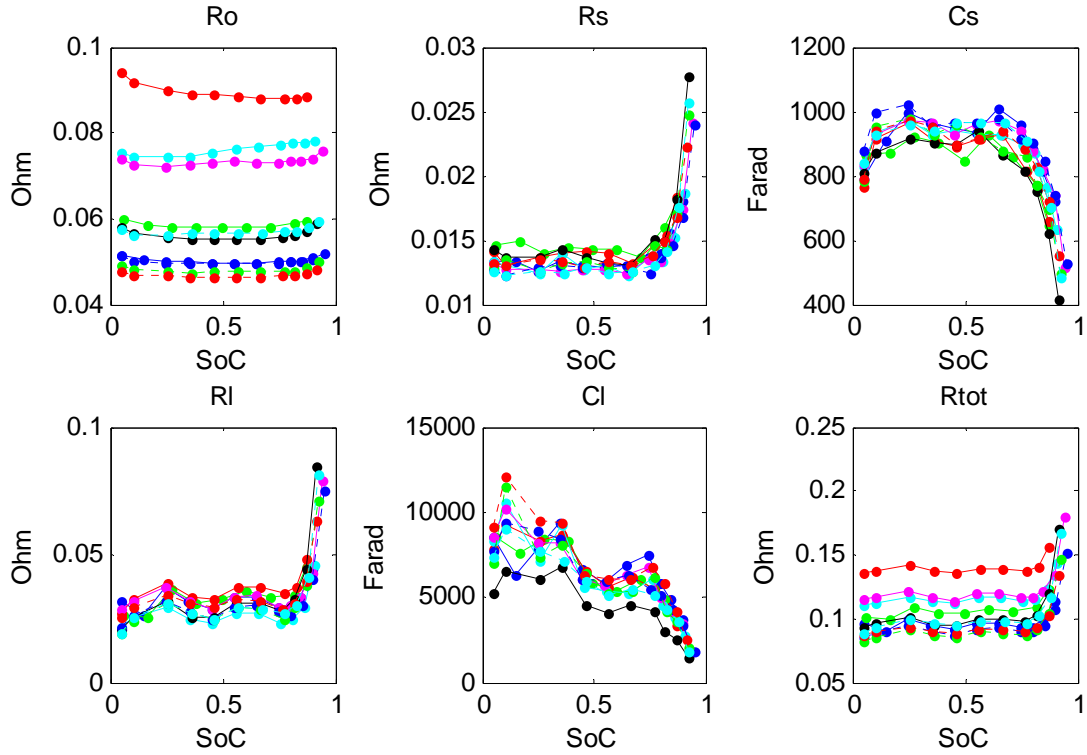


Figure 6.34: The internal cell impedance for charging of different cells measured before the experiments.

6.4.4.1 SoC dependence modelling

Modelling the SoC dependence of the internal cell impedance will be based on the polynomials and exponential functions as described in paragraph 5.3.2. For discharging in figure 6.33 R_o seems to be fairly constant, but in figure 6.31 it can be seen R_o rises for low and high SoC. To distinguish the impedance elements for discharging and charging, a subscript d will be added for

6 Empirical development of an improved practical circuit-based model

discharging impedance elements, and a subscript c for the charging elements. Using data from a fresh cell, the following empirical equations are obtained for discharging. R_{od} can be fitted with a 4th order polynomial:

$$R_{od} = b_{1d}SoC^4 + b_{2d}SoC^3 + b_{3d}SoC^2 + b_{4d}SoC + b_{5d} \quad (6.13)$$

with $b_{1d} = 1.298E-1$, $b_{2d} = -2.892E-1$, $b_{3d} = 2.273E-1$, $b_{4d} = -7.216E-2$ and $b_{5d} = 8.980E-2$. R_{sd} shows a linear dependent on the SoC with an exponential rise at low SoC, which is described by

$$R_{sd} = c_{1d}e^{-c_{2d}SoC} + c_{3d} + c_{4d}SoC \quad (6.14)$$

with $c_{1d} = 1.080E-2$, $c_{2d} = 11.03$, $c_{3d} = 1.827E-2$ and $c_{4d} = -6.462E-3$. C_s does not show an exponential behaviour, but can be accurately modelled by a third order polynomial:

$$C_{sd} = d_{1d}SoC^3 + d_{2d}SoC^2 + d_{3d}SoC + d_{4d} \quad (6.15)$$

with $d_{1d} = 1.697E2$, $d_{2d} = -1.007E3$, $d_{3d} = 1.408E3$ and $d_{4d} = 3.897E2$. At a very low SoC the exponential rise of R_{ld} is very strong as can be seen in figure 6.31, while the behaviour in the rest of the SoC range can be approximated by a linear function:

$$R_{ld} = g_{1d}e^{-g_{2d}SoC} + g_{3d} + g_{4d}SoC \quad (6.16)$$

with $g_{1d} = 2.950E-1$, $g_{2d} = 20.00$, $g_{3d} = 4.722E-2$ and $g_{4d} = -2.420E-2$. As can be seen from figure 6.31 C_{ld} cannot be modelled a simple exponential and linear equation. From the curve fitting analysis it was found that at least a 6th order polynomial was necessary for an acceptable fit, expressed by

$$C_{ld} = h_{1d}SoC^6 + h_{2d}SoC^5 + h_{3d}SoC^4 + h_{4d}SoC^3 + h_{5d}SoC^2 + h_{6d}SoC + h_{7d} \quad (6.17)$$

with $h_{1d} = 2.130E6$, $h_{2d} = -6.007E6$, $h_{3d} = 6.271E6$, $h_{4d} = -2.958E6$, $h_{5d} = 5.998E5$, $h_{6d} = -3.102E4$ and $h_{7d} = 2.232E3$. The fitted curves and corresponding data points of the internal impedance for discharge are given in figure 6.35.

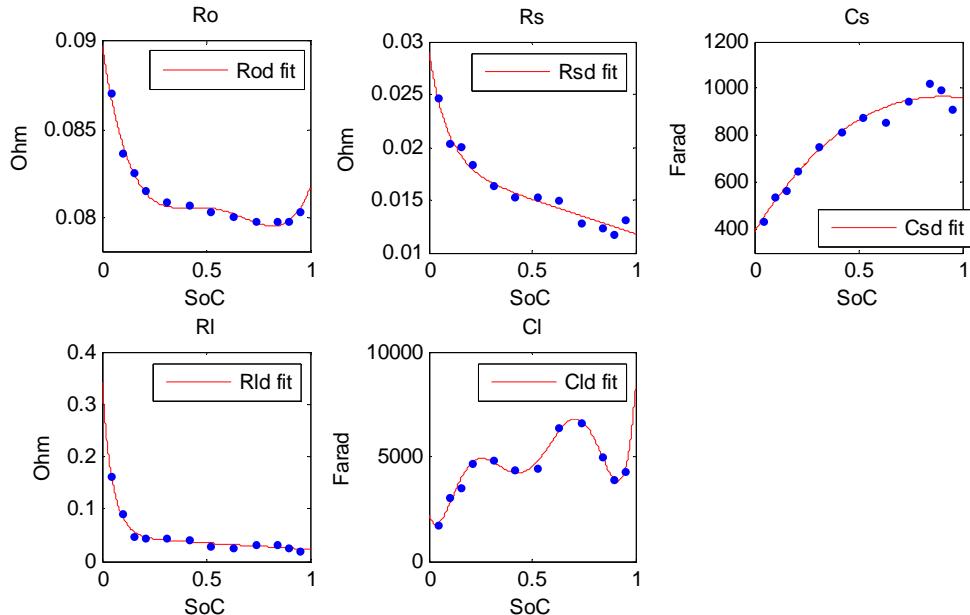


Figure 6.35: The data points and corresponding curve fits of the internal impedance for discharge.

To verify the accuracy of the empirical equations, a validation simulation is conducted in Simulink. The proposed circuit-based model in paragraph 5.2.5 has been implemented in Simulink with SoC dependent empirical equations for discharge. The simulation results were compared to the measured voltage as shown in figure 6.36.

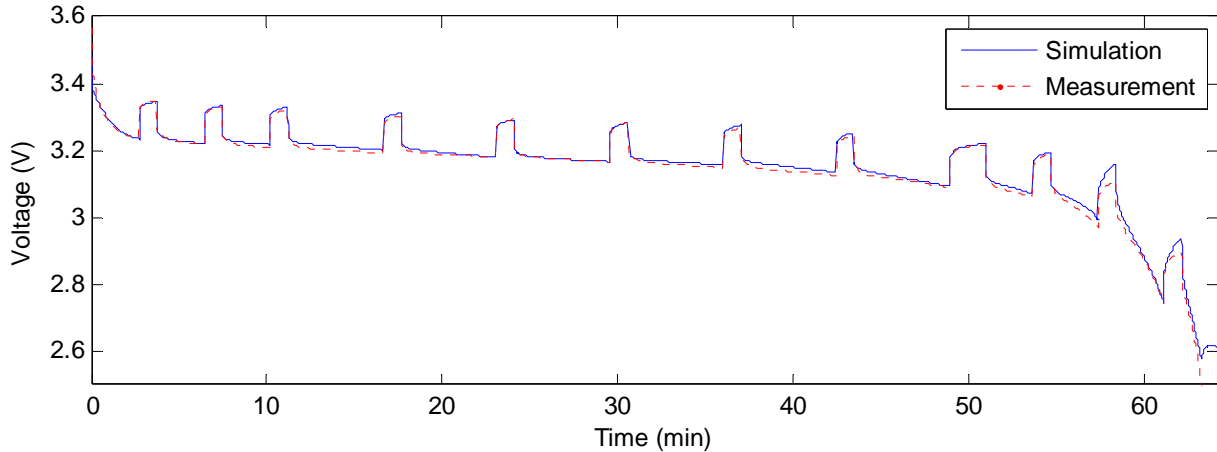


Figure 6.36: The modelled voltage behaviour for discharge compared to the measured voltage of a test cycle fully discharging the cell.

From figure 6.36 it can be seen that the empirical equations in the equivalent circuit-based model can accurately simulate the voltage behaviour of the cell. For discharging down to 10% SoC the simulation only has a maximum error of 11mV or 1% of the operating voltage range. Below 10% SoC the total cell impedance rises exponentially and the maximum error goes up to 10%. The inaccuracy is mainly due to the inaccurate fit of the long time transient parallel RC pair in the exponential region. A higher accuracy can be achieved if more parallel RC pairs are used in the model or if R_{ld} and C_{ld} are modelled with higher order polynomials; on the other hand, this would severely complicate the model while the inaccuracy in the linear region is very small. Furthermore, in EV applications battery cells will rarely operate in the region below 10% SoC, so the inaccuracy in this region is of very little importance.

The same analysis is used to model the internal impedance elements for charging. R_{oc} rises for high and low SoC as shown in figure 6.32. To obtain an accurate fit, a fourth order polynomial is used again:

$$R_{oc} = b_{1c}SoC^4 + b_{2c}SoC^3 + b_{3c}SoC^2 + b_{4c}SoC + b_{5c} \quad (6.18)$$

with $b_{1c} = 1.369E-1$, $b_{2c} = -2.518E-1$, $b_{3c} = 1.609E-1$, $b_{4c} = -4.100E-2$ and $b_{5c} = 8.210E-2$. From figure 6.32 it can be seen that R_{sc} is constant over the entire SoC range except at high SoC. Therefore only an exponential function is sufficient to model R_{sc} :

$$R_{sc} = c_{1c}e^{-c_{2c}SoC} + c_{3c} \quad (6.19)$$

with $c_{1c} = 5.896E-10$, $c_{2c} = -18.75$ and $c_{3c} = 1.388E-2$. The behaviour of C_{sc} is similar to R_{oc} , only C_{sc} falls instead of rising at high and low SoCs. So C_{sc} can also be modelled with a fourth order polynomial, resulting in

$$C_{sc} = d_{1c}SoC^4 + d_{2c}SoC^3 + d_{3c}SoC^2 + d_{4c}SoC + d_{5c} \quad (6.20)$$

6 Empirical development of an improved practical circuit-based model

with $d_{1c} = -1.026E4$, $d_{2c} = 1.723E4$, $d_{3c} = -1.013E4$, $d_{4c} = 2.340E3$ and $d_{5c} = 6.849E2$. R_{lc} shows an exponential rise at high SoC and a small rise leading to the exponential behaviour, which can be described by

$$R_{lc} = g_{1c}e^{-g_{2c}SoC} + g_{3c} + g_{4c}SoC \quad (6.21)$$

with $g_{1c} = 8.913E-15$, $g_{2c} = -32.23$, $g_{3c} = 3.100E-2$ and $g_{4c} = 7.473E-3$. Similar to C_{ld} , C_{lc} cannot be modelled with a simple exponential and linear equation. From the parameter analysis a fifth order polynomial was found to produce an acceptable fit, expressed by:

$$C_{lc} = h_{1c}SoC^5 + h_{2c}SoC^4 + h_{3c}SoC^3 + h_{4c}SoC^2 + h_{5c}SoC + h_{6c} \quad (6.22)$$

with $h_{1c} = -1.541E5$, $h_{2c} = 2.042E5$, $h_{3c} = -4.009E3$, $h_{4c} = -8.124E4$, $h_{5c} = 2.283E4$ and $h_{6c} = 7.144E3$. In figure 6.37 the data points and the corresponding curve fits are given. An additional data point has been added to C_{lc} at 100% SoC to prevent a value lower than 0 in the curve fit. As a result of curve fitting, C_{sc} and C_{lc} are negative near 100% SoC. The real value of C_{sc} and C_{lc} are not negative, but are expected to be low. By setting a minimum limit for C_{sc} and C_{lc} in the Simulink model, negative values are prevented.

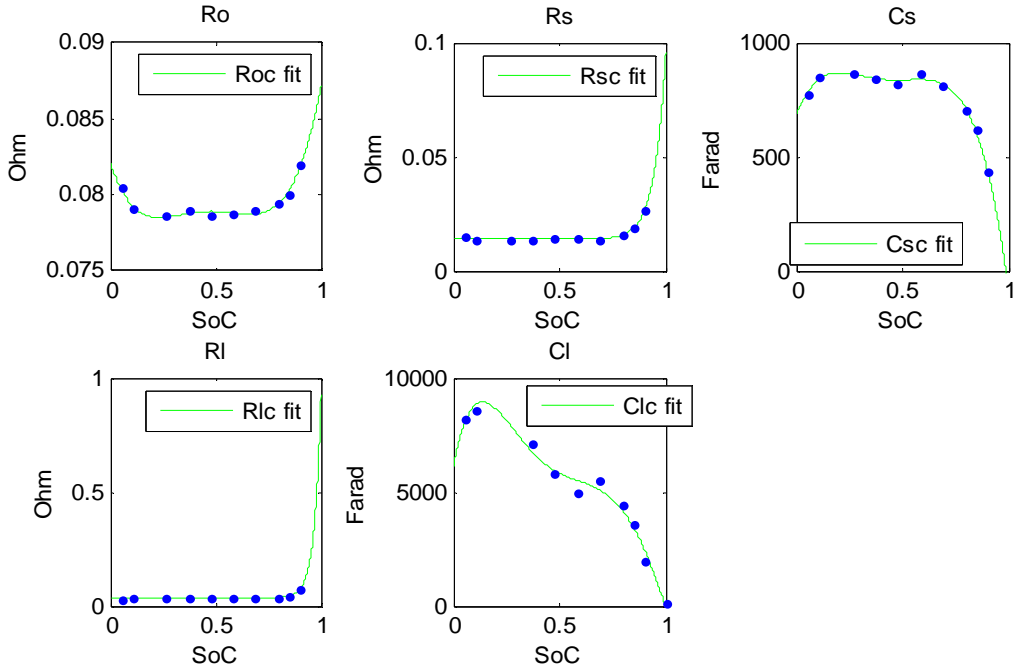


Figure 6.37: The data points and corresponding curve fits of the internal impedance for charge.

The empirical equations determined for internal impedance elements for charge have been incorporated in the proposed circuit-based model and simulated with Simulink as shown in figure 6.38. Just like the empirical equations modelling the internal impedance for discharging, the empirical equations for charging in the equivalent circuit-based model can also accurately simulate the voltage behaviour of the cell as shown in figure 6.38. Up to 90% SoC the maximum error is 12mV or 1.1% of the operating voltage range. Above 90% SoC the maximum error rises to 6%. For charging the inaccuracy is also mainly caused by the exponential curve fit of the long time transient parallel RC pair. The accuracy can be improved in the same way as for discharging; however, the accuracy gained is small compared to the increased complexity. To extend the life of battery cells, some battery management systems are programmed to charge the cells up to 90% SoC. As the life time of battery cells are a very important factor in EV applications, it is

expected that SoCs higher than 90% is prevented. Even if the cell is charged to 100%, the errors are acceptable small. Therefore the practical circuit-based model can sufficiently model the voltage behaviour in EV applications.

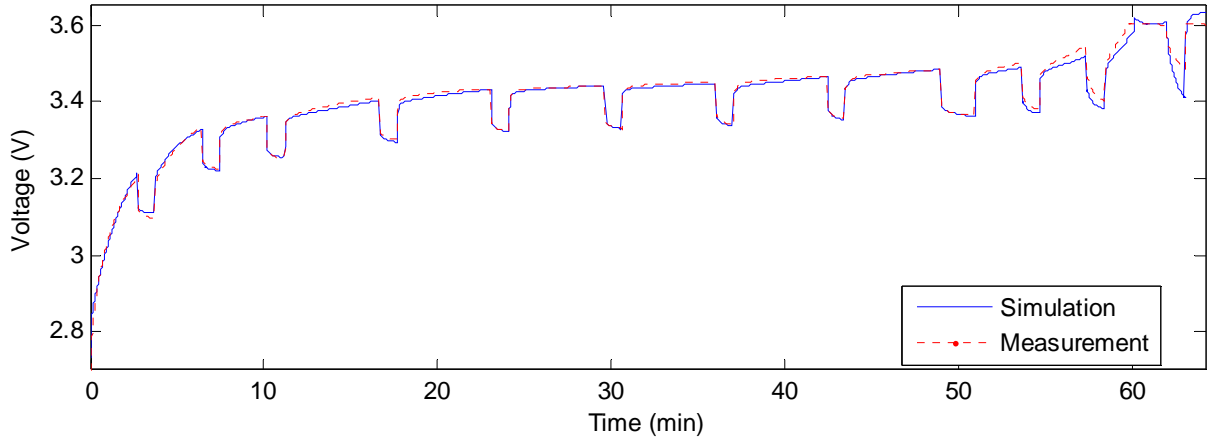


Figure 6.38: The modelled voltage behaviour for charge compared to the measured voltage of a test cycle fully charging the cell.

6.4.4.2 C-rate dependence modelling

In figure 6.36 and figure 6.38 a difference in voltage behaviour is shown in the decreasing current region. When the minimum/maximum voltage for discharging/charging is reached, the measured voltage is kept constant while the simulated voltage changes in value. This indicates that the internal cell impedance of the cell is dependent on the C-rate. To determine the C-rate dependence of the internal cell impedance, test cycles under different C-rates have been applied to several cells. A typical result for the internal impedance elements determined during discharge at different C-rates is shown in figure 6.39.

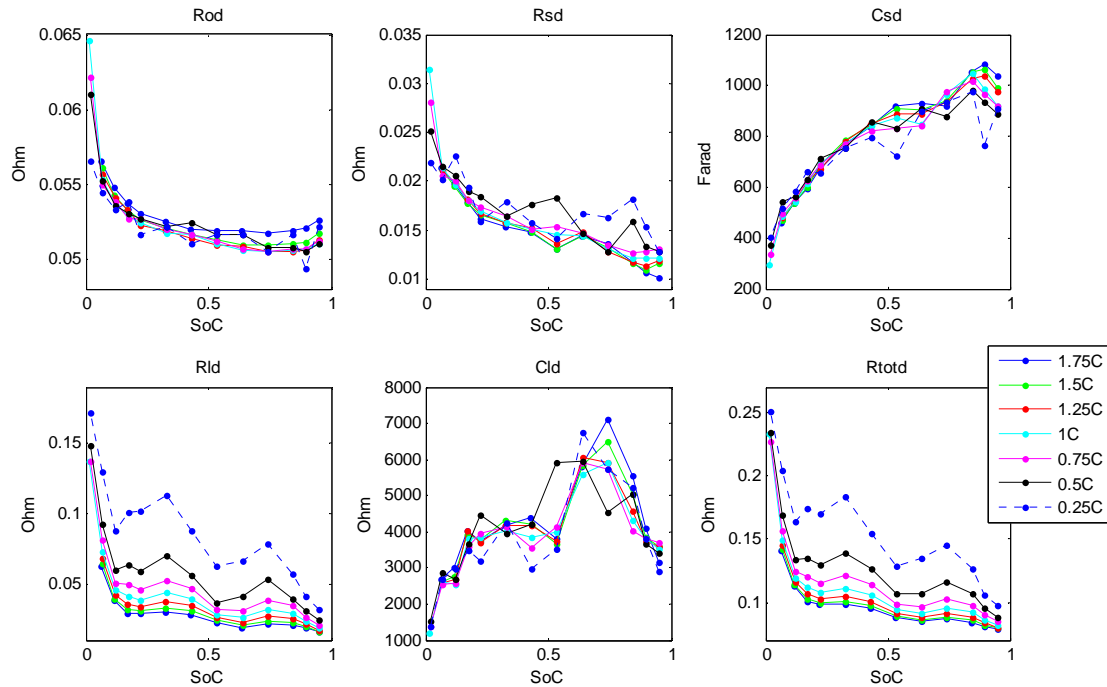


Figure 6.39: The internal cell impedance elements determined for different C-rates for discharge.

In Figure 6.39 the internal impedance elements seem to be fairly invariant with the C-rate except for R_{ld} . This is also reflected in the value of the total resistance R_{totd} , which C-rate dependent

6 Empirical development of an improved practical circuit-based model

variations correspond with R_{ld} . The fluctuations at low C-rates of the other impedance elements are caused by the curve fitting constraints for time constants, but do not have any effect on the actual C-rate influence. Therefore the C-rate dependency of the internal cell impedance for discharge is sufficiently modelled by only R_{ld} . In figure 6.40a the C-rate variations are shown as a ratio to R_{ld} at 1C. The C-rate variations are SoC dependent, but cannot be accurately modelled by a simple polynomial. Nevertheless, the C-rate dependency of R_{ld} is approximated as constant over the SoC range, changing equation 6.16 to:

$$R_{ld} = (g_{1d}e^{-g_{2d}SoC} + g_{3d} + g_{4d}SoC) \cdot f_d(I_{Crate}) \quad (6.23)$$

where I_{Crate} is the current in C-rates and f_d is a function dependent on the C-rate. The C-rate variations over the SoC range are averaged and the following C-rate dependency was found:

$$f_d(I_{Crate}) = g_{i1d}I_{Crate}^{g_{i2d}} + g_{i3d} \quad (6.24)$$

with $g_{i1d} = 6.994\text{E-}1$, $g_{i2d} = -6.920\text{E-}1$ and $g_{i3d} = 2.902\text{E-}1$. The curve fit is shown in figure 6.40b with the R_{ld} data points determined from measurements. In figure 6.40b the curve fit error appears to become larger as the C-rate drops. The voltage error resulting from R_{ld} is, however, a maximum of 9 mV for all C-rates or 0.8% of the voltage operation range, because a lower C-rate results in a smaller voltage error with the same resistance error. The voltage error is higher in the exponential region below 5% SoC, but since the expectation is that EVs will rarely operate in that region, the model is sufficient.

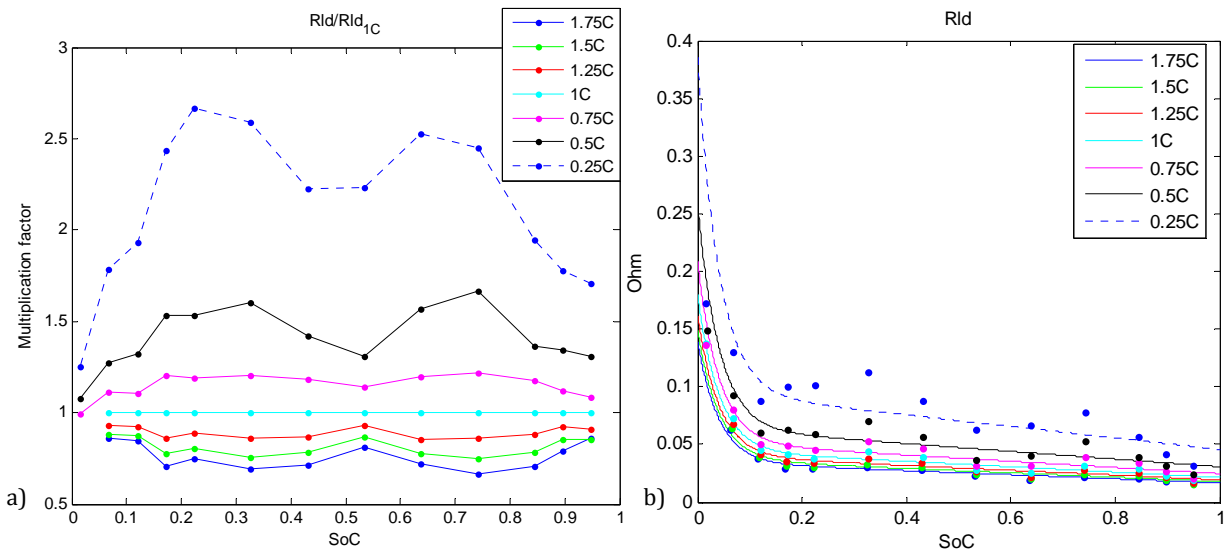


Figure 6.40: (a) The C-rate variations of R_{ld} vs. SoC as a ratio to R_{ld} determined at 1C and (b) the modelled R_{ld} for different C-rates with the measured data points.

A higher accuracy can be achieved by modelling f_d with at least a 6th order polynomial, but this will increase the complexity of the model significantly. Furthermore, each internal impedance element is not completely C-rate invariant. The accuracy of the model can be further improved by taking the C-rate dependency of all the other impedance elements into account as well. This will complicate the model even more while the variations are very small.

To verify the empirical equations modelling the C-rate dependency, equations 6.23 and 6.24 have been incorporated in proposed circuit-based model in Simulink. The simulation results are compared with the measurements as shown in figure 6.41.

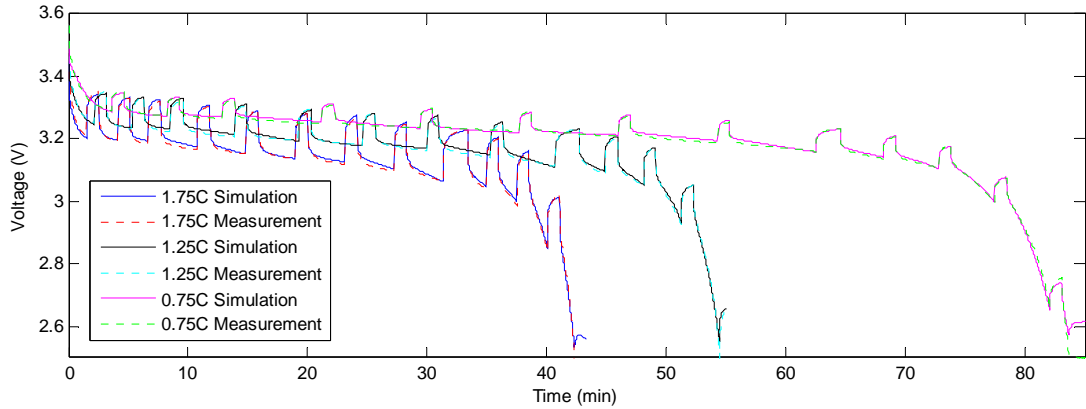


Figure 6.41: The modelled voltage behaviour for discharge at different C-rates compared to the measured voltage at the corresponding C-rates.

Simulations including C-rate dependency modelling in figure 6.41 show a maximum error of 14mV or 1.3% of the total voltage range for cells discharged with different C-rate in the SoC range of interest. In case the C-rate dependency is neglected, the maximum error is doubled and a constant error is present in the voltage response, which becomes more profound at low C-rates.

The C-rate dependency of the internal impedance elements has also been analysed for charging as shown in figure 6.42. The C-rate dependency for charging is similar to discharging. R_{lc} is the main cause of the C-rate dependent resistance variations, while the variations in the other elements are small as reflected in R_{totc} . Figure 6.42 shows strong variations of the impedance elements at low C-rates that do not follow the expected SoC behaviour. This is caused by small curve fitting errors which effects are enlarged by the low C-rate. The actual voltage error is very small.

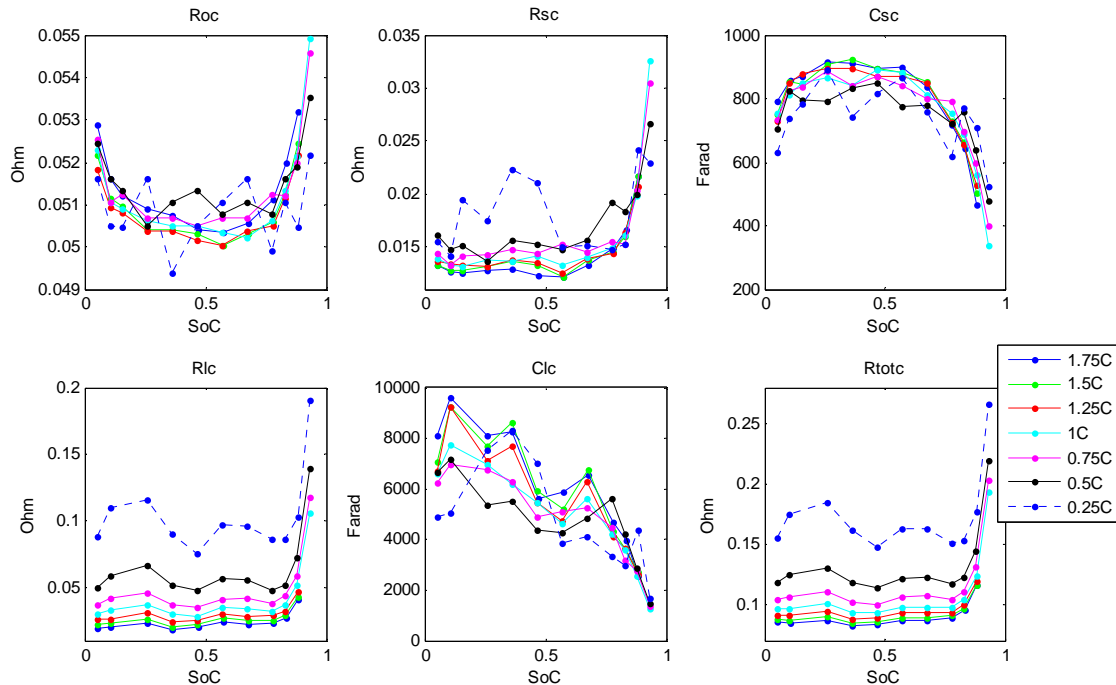


Figure 6.42: The internal cell impedance elements determined for different C-rates for charge.

In figure 6.43a the C-rate dependent variations of R_{lc} are plotted as a ratio of R_{lc} determined at 1C. The C-rate variations fluctuate over the SoC range, which cannot be modelled with a simple

6 Empirical development of an improved practical circuit-based model

equation. Nonetheless, a linear SoC dependency can be noticed from the C-rate variations. By incorporating the C-rate dependency in R_{lc} , equation 6.21 becomes:

$$R_{lc} = (g_{1c}e^{-g_{2c}SoC} + g_{3c} + g_{4c}SoC) \cdot f_c(I_{Crate}, SoC) \quad (6.25)$$

where the function f_c describes the C-rate variations. From the analysis of the C-rate variations the following equation was found to model the linear SoC dependency of the C-rate variations:

$$f_c(I_{Crate}, SoC) = g_{i1c}(I_{Crate}^{g_{i2c}} - 1)SoC + I_{Crate}^{g_{i3c}} \quad (6.26)$$

with $g_{i1c} = -4.124E-1$, $g_{i2c} = -1.082$ and $g_{i3c} = -8.730E-1$. The curve fit is shown in figure 6.43b with R_{lc} determined from the measured data. The curve fit error is larger for low C-rates just like R_{ld} , but the resulting voltage error is lower. For all the measured C-rates the voltage error of R_{lc} is a maximum of 6 mV or 0.6% of the voltage operation range. The voltage error is therefore acceptable small and equation 4.8 is sufficient to model the C-rate dependency.

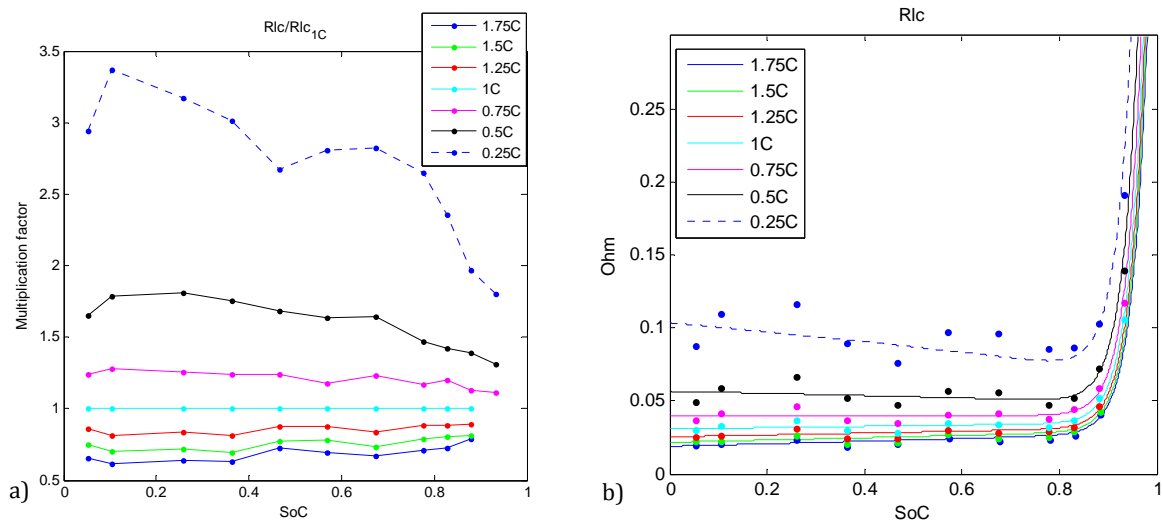


Figure 6.43: a) The C-rate variations of R_{lc} vs. SoC as a ratio of R_{lc} determined at 1C and b) the modelled R_{lc} for different C-rates with R_{lc} determined from measured data points.

The accuracy of the C-rate dependency modelling can be improved in the same way as for discharging. A higher accuracy can be achieved by including the SoC dependency in f_c with at least a 6th order polynomial. Furthermore, each impedance element is not completely C-rate invariant. The accuracy of the model can be approved by taking the C-rate variations for each impedance element into account. The gain in accuracy is, however, very small compared to the increase in complexity.

The empirical equations modelling the C-rate dependency have been verified as shown in figure 6.44. Equations 6.25 and 6.26 have been incorporated in proposed circuit-based model in Simulink. The maximum error found was equal to the maximum error found for discharge, i.e. a maximum error of 14mV or 1.3% of the total voltage range for cells charged with different C-rate in the SoC range of interest.

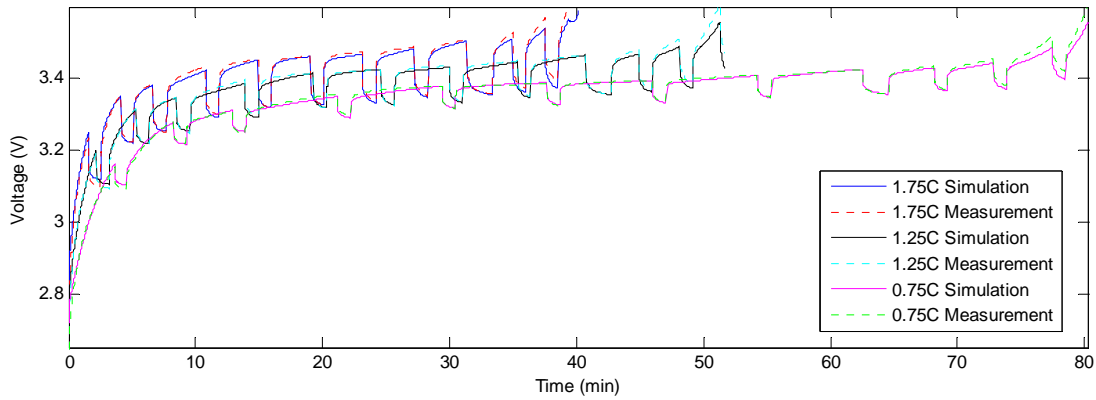


Figure 6.44: The modelled voltage behaviour for discharge at different C-rates compared to the measured voltage at the corresponding C-rates.

The C-rate dependency modelling of R_{ld} and R_{lc} has a limitation. Equations 6.23 and 6.25 are not valid when no current flows in the cell, so when the cell is at rest. R_{ld} and R_{lc} will then take on the values before the cell was in rest. Due to the switching time of the power electronics, the current is not directly cut-off but gradually reduces to zero. In that case R_{ld} and R_{lc} will be modelled with the current before the current switch-off occurred. In practical EV applications this will most likely not be a problem as the sampling times are larger than the converter switching times.

6.4.4.3 Temperature dependence modelling

The LiFePO₄ cells are also strongly affected by the temperature. To test the temperature dependence of the internal cell impedance elements, the temperature of one cell has been varied between 40 and -15°C. At each temperature the cell has been rested for at least 6 hours for it to reach a thermal equilibrium before a capacity and parameter test is conducted. The determined internal cell impedance elements are shown in figure 6.45 for discharging and in figure 6.46 for charging.

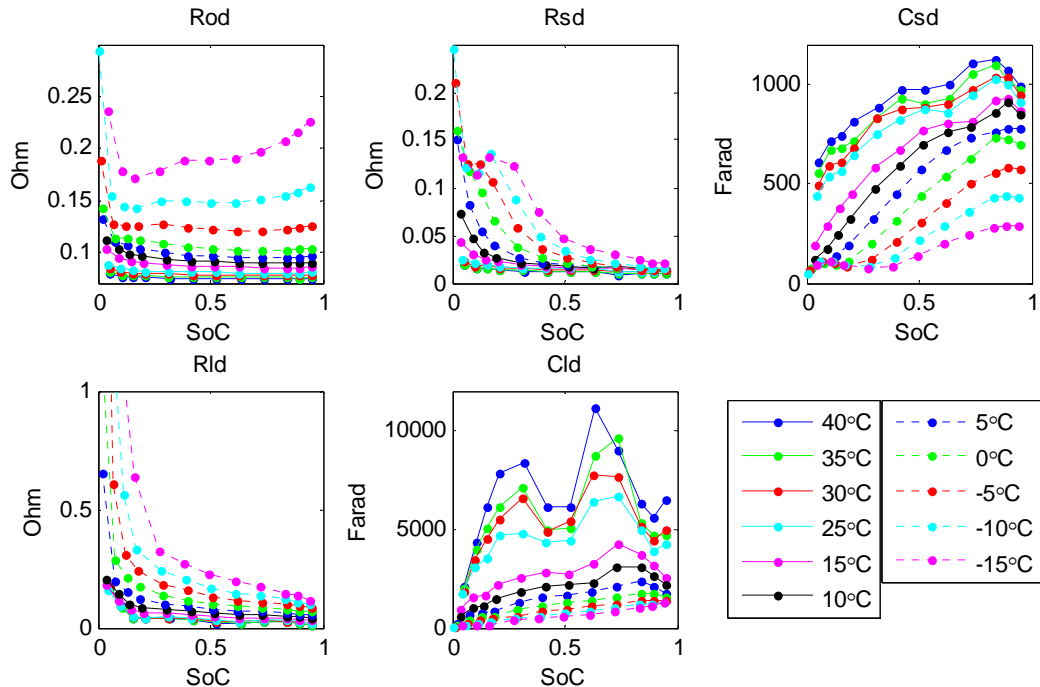


Figure 6.45: The impedance elements for discharging determined at different temperatures between 40°C and -15°C.

6 Empirical development of an improved practical circuit-based model

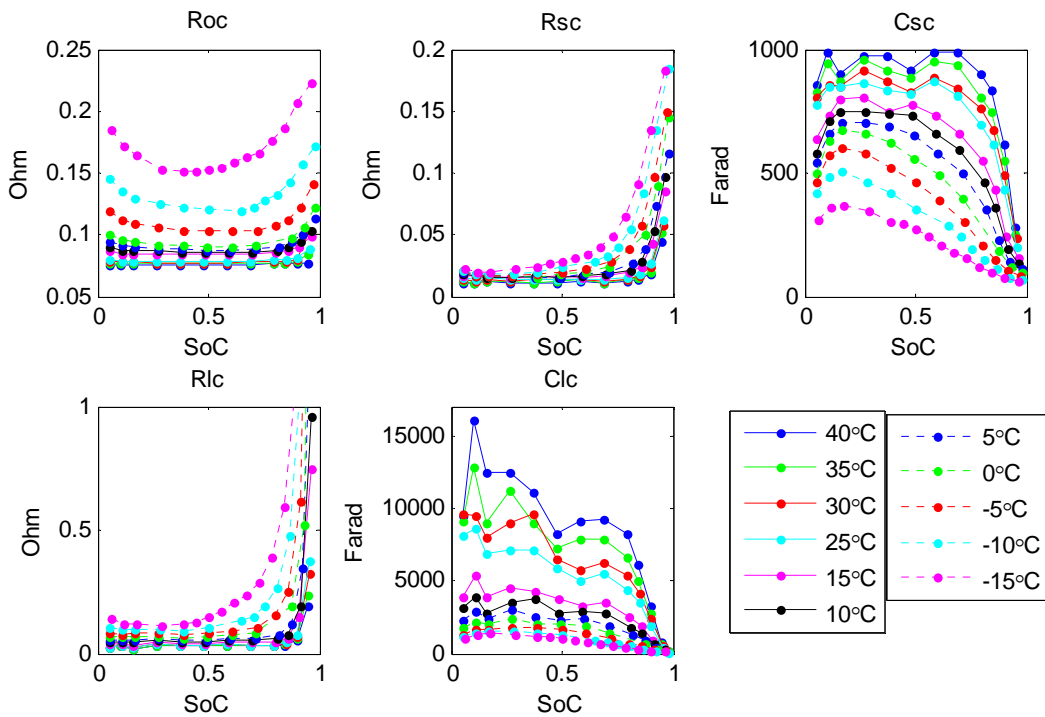


Figure 6.46: The impedance elements for discharging determined at different temperatures between 40°C and -15°C.

As can be seen from figure 6.45 and in figure 6.46 each impedance element is strongly dependent on the temperature. To be able to model the temperature dependence of the internal cell impedance, the each impedance element is analysed separately.

In the analysis two sets of equations are obtained for each impedance element. Different equations are used for high temperatures (20°C and above) and low temperatures (below 20°C) to limit the complexity of the equations. The split at 20°C is chosen because the behaviour of the impedance element changes between 25°C and 15°C. Due to practical reasons it was, however, not possible to determine the parameters at 20°C.

Since the impedance equations were obtained from curve fitting the voltage response, the impedance elements do not directly represent electrochemical processes in a cell, but can only be related to the processes. Consequently, equations describing the temperature dependence of the electrochemical processes cannot be used with the model and the temperature dependence has to be modelled with empirical equations as well. By observing the change with temperature of an impedance element, the empirical equations that model the temperature dependent behaviour of each impedance element is obtained. If a parameter changes from the value determined at 25°C in paragraph 6.4.4.1, a change in parameter will be mentioned or the parameter will contain a subscript *t*.

For high temperatures R_{od} was found to vary with a constant factor over the entire SoC range. This means that the high temperature dependence of R_{od} can be modelled with a temperature dependent factor over R_{od} at reference temperature. The VTF equation was found to model the R_{od} factor is accurately and equation 6.13 becomes:

$$R_{od,T_{high}}(SoC, T) = R_{od}(SoC) \cdot b_{t1d} e^{\frac{b_{t2d}}{T-b_{t3d}}} \quad (6.27)$$

with $b_{t1d} = 7.613E-1$, $b_{t2d} = 10.14$, $b_{t3d} = 2.608E2$ and T the temperature in Kelvin. At low temperatures R_{od} cannot be simply modelled by only a temperature dependent factor. The SoC behaviour changes and more complex equations will be necessary. From the parameter analysis it was concluded that the low temperature dependence of R_{od} could be modelled with several parameters, changing equation 6.13 to:

$$R_{od,T_{low}}(SoC, T) = (b_{t1d}T^3 + b_{t2d}T^2 + b_{t3d}T + b_{t4d})SoC^4 + b_{2d}SoC^3 + b_{3d}SoC^2 + b_{4d}SoC + b_{t5d}e^{\frac{b_{t6d}}{T-b_{t7d}}} \quad (6.28)$$

with $b_{t1d} = -5.930E-6$, $b_{t2d} = 5.011E-3$, $b_{t3d} = -1.411$, $b_{t4d} = 1.325E2$, $b_{t5d} = 6.297E-2$, $b_{t6d} = 24.37$ and $b_{t7d} = 2.363E2$. Furthermore, the SoC dependent parameters will also change into $b_{2d} = -2.819E-1$, $b_{3d} = 2.448E-1$ and $b_{4d} = -9.630E-2$. The value of R_{od} determined from measurements at different temperatures and the corresponding curve fits with respectively equation 6.27 and 6.28 are shown in figure 6.47a and b.

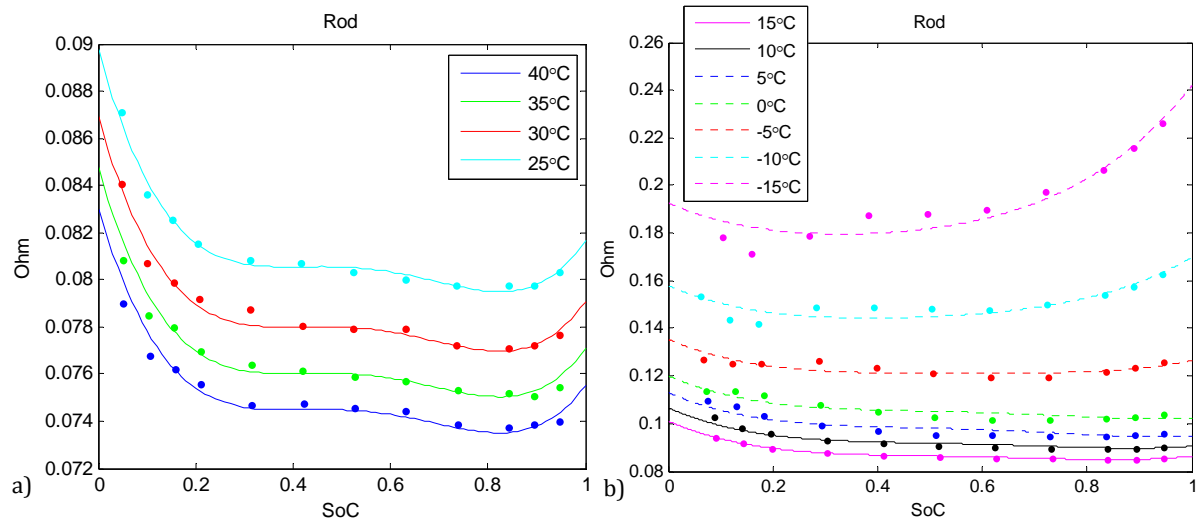


Figure 6.47: The measured values of R_{od} and corresponding curve fit for a) high and b) low temperatures.

In a similar way the modelling of R_{sd} is approached. By analysing the data of the temperature dependence of R_{sd} , for high temperatures equation 6.14 was found to change to

$$R_{sd,T_{high}}(SoC, T) = R_{sd}(SoC) + c_{t1d}\Delta T + c_{t2d}\Delta T \cdot SoC \quad (6.29)$$

with $c_{t1d} = -3.697E-4$ and $c_{t2d} = 2.225E-4$. Figure 6.45 shows that R_{sd} does not follow the expected trend in the decreasing current region at very low temperatures. This is possibly caused by either curve fitting errors or a C-rate dependence at very low temperatures. To be able to incorporate the low temperature dependence for all measurements conducted, the data points in the decreasing current region are omitted. Consequently, for low temperatures equation 6.14 becomes

$$R_{sd,T_{low}}(SoC, T) = (c_{t1d}T^2 + c_{t2d}T + c_{t3d})e^{-(c_{t4d}T^2 + c_{t5d}T + c_{t6d})SoC} + c_{3d} + c_{4d}SoC \quad (6.30)$$

with $c_{t1d} = 1.923E-4$, $c_{t2d} = -1.166E-1$, $c_{t3d} = 17.66$, $c_{t4d} = 1.098E-2$, $c_{t5d} = -5.644$ and $c_{t6d} = 7.299E2$. The obtained values for R_{sd} extracted from measurements at various temperatures and the corresponding curve fits are shown in figure 6.48.

6 Empirical development of an improved practical circuit-based model

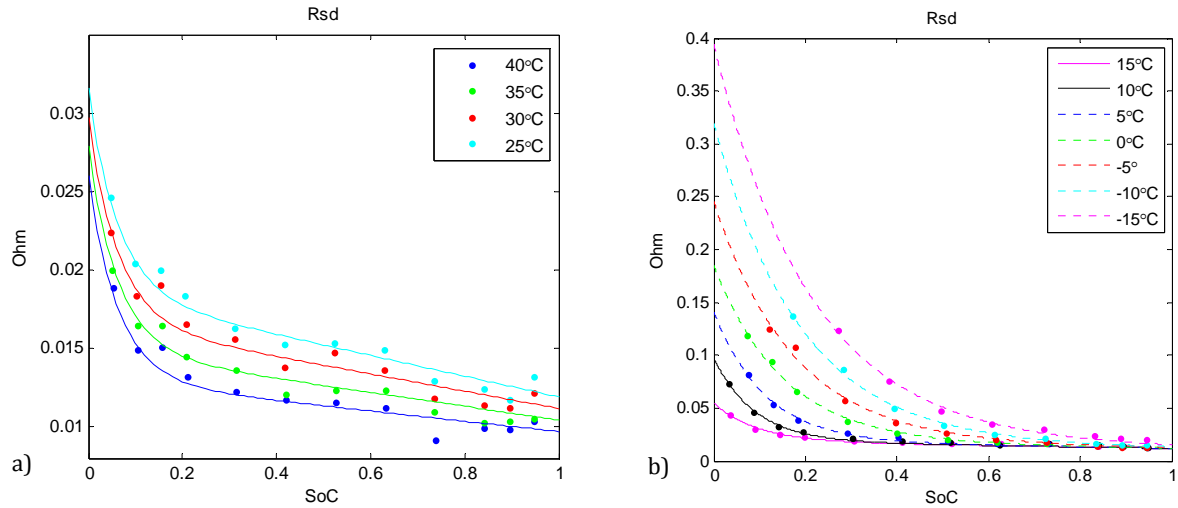


Figure 6.48: The measured values of R_{sd} and corresponding curve fit for a) high and b) low temperatures.

For high temperatures C_{sd} rises, but the SoC behaviour remains almost the same. Based on the measurement data at different temperatures, equation 6.15 changes to

$$C_{sd,T_{high}}(SoC, T) = C_{sd}(SoC) + d_{t1d}\Delta T \cdot SoC + d_{t2d}\Delta T \quad (6.31)$$

with $d_{t1d} = -6.580$ and $d_{t2d} = 12.11$. For low temperatures the SoC dependent curve of C_{sd} experiences a temperature dependent shift along SoC axis accompanied by a drop in value. These effects are incorporated in 6.15 by

$$C_{sd,T_{low}}(SoC, T) = d_{1d}(SoC + (d_{t1d}T - d_{t2d}))^3 + d_{2d}(SoC + (d_{t1d}T - d_{t2d}))^2 + d_{4d} + (d_{t3d}T^2 + d_{t4d}T + d_{t5d})(SoC + (d_{t1d}T - d_{t2d})) \quad (6.32)$$

with $d_{t1d} = 1.428E-2$, $d_{t2d} = 4.068$, $d_{t3d} = -6.807E-1$, $d_{t4d} = 4.002E2$ and $d_{t5d} = -5.769E4$. The other parameters also change, with $d_{1d} = -1.173E3$, $d_{2d} = 8.278E2$ and $d_{4d} = 1.005E2$. Modelling low temperatures will complicate the model, but for temperatures above 10°C C_{sd} can also be approximated by equation 6.31. The measured data points at different temperatures for C_{sd} is shown in figure 6.49 along with the curve fits of equations 6.31 and 6.32.

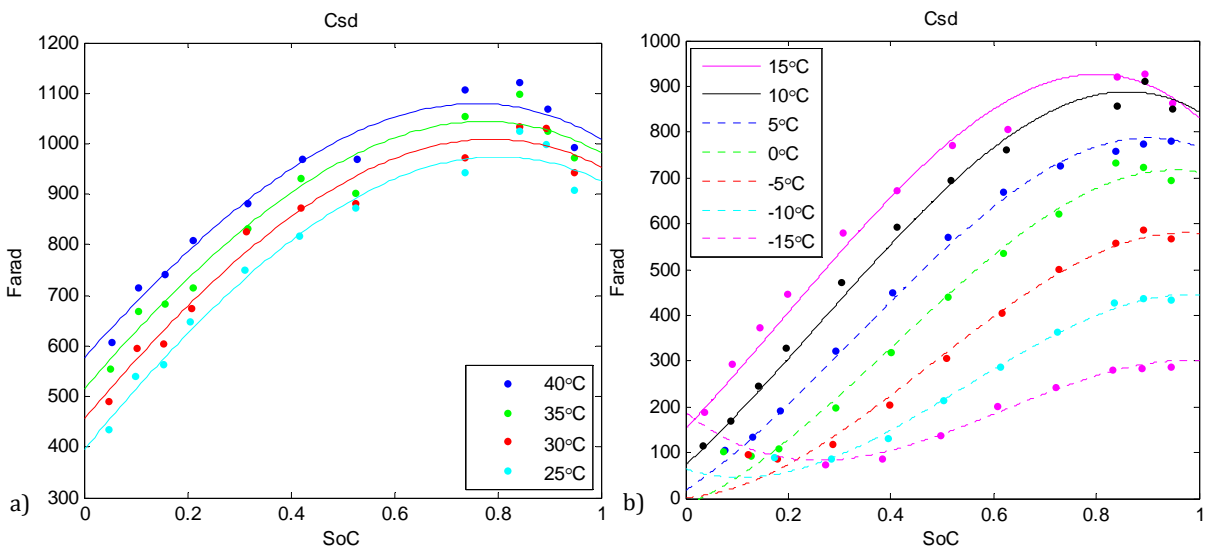


Figure 6.49: The measured values of C_{sd} and corresponding curve fit for a) high and b) low temperatures.

For high temperatures R_{ld} shows a constant drop in the linear region, while in the exponential region higher temperatures result in a slightly higher value. Consequently, based on the measurement data equation 6.16 becomes

$$R_{ld,T_{high}}(SoC, T) = R_{ld}(SoC) + (g_{t1d}\Delta T)e^{-g_{2d}SoC} + g_{t2d}\Delta T \quad (6.33)$$

with $g_{t1d} = 6.718\text{E-}3$, $g_{t2d} = -5.967\text{E-}4$. For low temperatures the SoC behaviour changes and every parameter except g_{2d} becomes dependent on the temperature, resulting in:

$$R_{ld,T_{low}}(SoC, T) = g_{t1d}e^{\left(\frac{g_{t2d}}{T-g_{t3d}}-g_{2d}SoC\right)} + g_{t4d}e^{\frac{g_{t5d}}{T}} + g_{t6d}e^{\frac{g_{t7d}}{T}}SoC \quad (6.34)$$

with $g_{t1d} = 8.238\text{E-}3$, $g_{t2d} = 1.805\text{E}2$, $g_{t3d} = 2.321\text{E}2$, $g_{t4d} = 1.589\text{E-}7$, $g_{t5d} = 3.779\text{E}3$, $g_{t6d} = -2.208\text{E-}8$ and $g_{t7d} = 4.202\text{E}3$. R_{ld} determined from measurements at different temperatures is shown in figure 6.50 with the corresponding curve fits of equation 6.33 and 6.34.

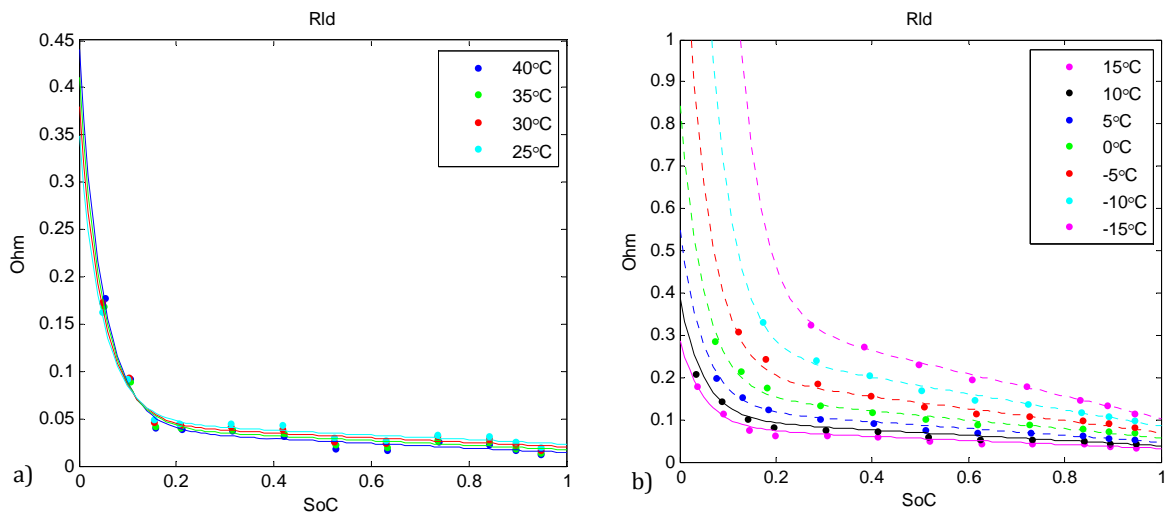


Figure 6.50: The measured values of R_{ld} and corresponding curve fit for a) high and b) low temperatures.

For high temperatures C_{ld} can be approximated by a multiplication factor with equation 6.17, leading to

$$C_{ld,T_{high}}(SoC, T) = C_{ld}(SoC) \cdot h_{t1d}e^{\frac{h_{t2d}}{T}} \quad (6.35)$$

with $h_{t1d} = 3.128\text{E}3$ and $h_{t2d} = -2.398\text{E}3$. According to the measurement for low temperatures variations were found to be less extreme data and can be therefore modelled with a 4th order polynomial. However, not every parameter has the same dependence on temperature, complicating the equation to

$$C_{ld,T_{low}}(SoC, T) = (h_{1d}SoC^4 + h_{2d}SoC^3 + h_{5d})e^{h_{t1d}T} + h_{3d}SoC^2e^{h_{t2d}T} + h_{4d}SoCe^{\frac{h_{t3d}}{T-h_{t4d}}} \quad (6.36)$$

with $h_{t1d} = 1.220\text{E-}1$, $h_{t2d} = 1.241\text{E-}1$, $h_{t3d} = -4.492\text{E}2$ and $h_{t4d} = 3.474\text{E}2$. Since a different order equation is used for C_{ld} , the SoC parameters change to $h_{1d} = -3.751\text{E-}11$, $h_{2d} = 6.764\text{E-}11$, $h_{3d} = -2.219\text{E-}11$, $h_{4d} = 10.75$ and $h_{5d} = 1.534\text{E-}13$. The measurement data of C_{ld} and the curve fits of equations 6.35 and 6.36 are shown in figure 6.51.

6 Empirical development of an improved practical circuit-based model

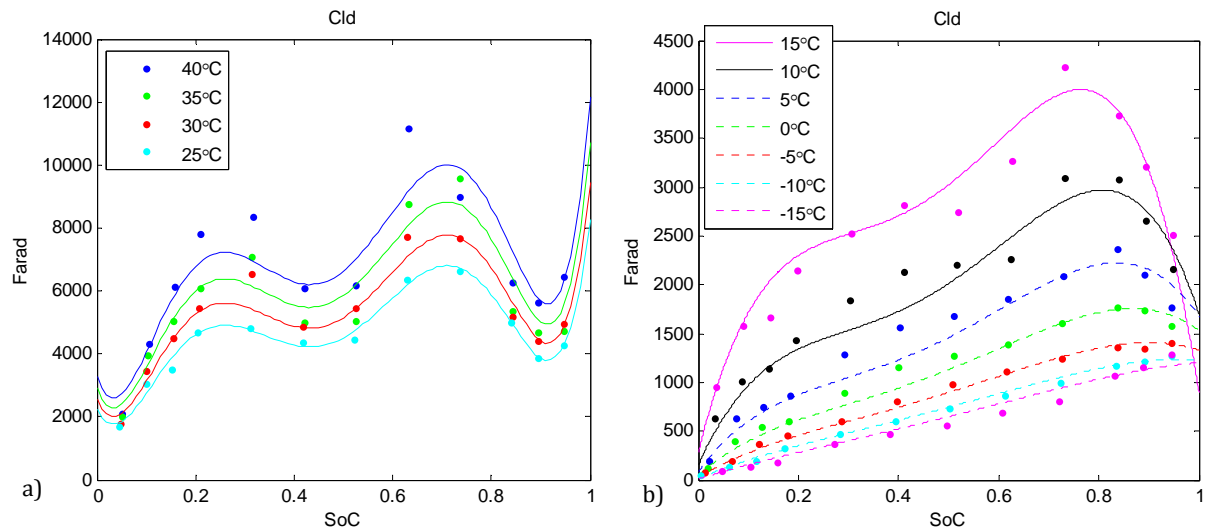


Figure 6.51: The measured values of C_{ld} and corresponding curve fit for a) high and b) low temperatures.

To validate the empirical equations describing the temperature dependence of the internal cell impedance for discharging, the equations are incorporated into the proposed circuit-based model in Simulink. In figure 6.52 comparisons between the simulation results and measurements are shown if only the equations for high temperatures are applied, since the high temperature equations are much less complex.

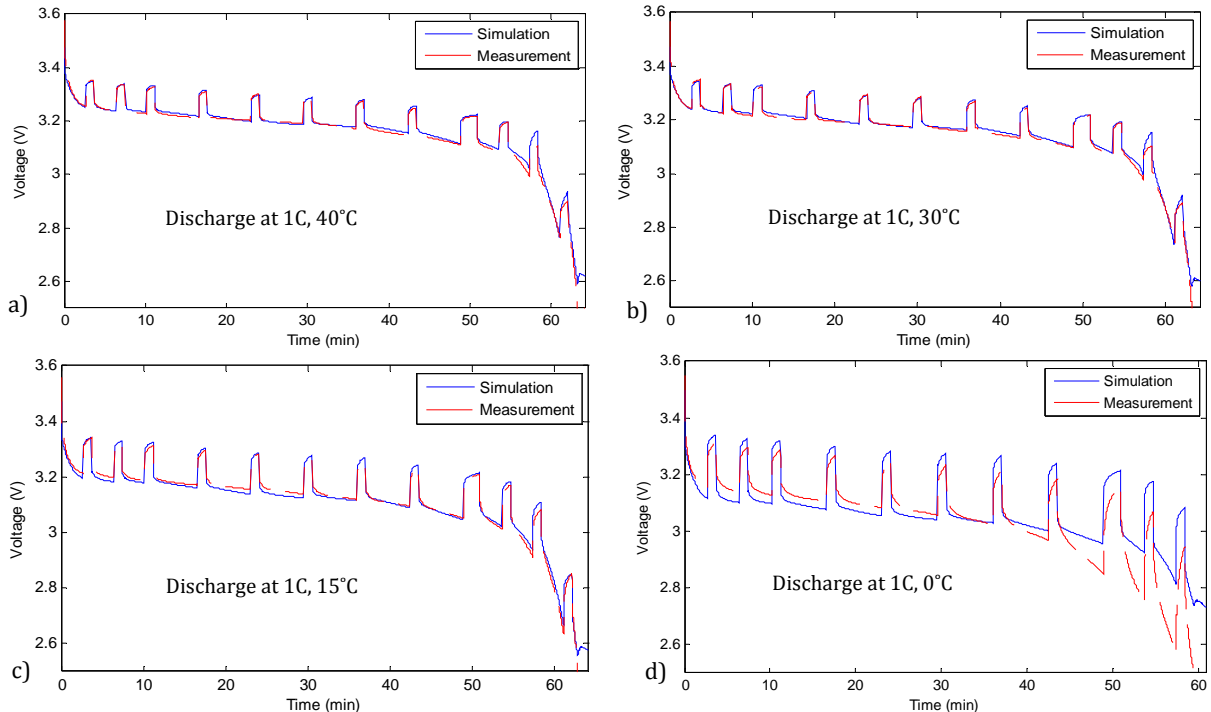


Figure 6.52: A comparison between simulation results and measurements for cells discharged at a) 40°C, b) 30°C, c) 15°C and d) 0°C if only the equations for high temperatures are applied.

Figure 6.52 shows that for high temperatures the model with high temperature equations is accurate with a maximum error of 11mV in the SoC range of interest. However, for low temperatures the model with high temperature equations starts to become inaccurate from 15°C, with a maximum error is 20mV in the linear voltage range, going up to 80mV in the nonlinear range. At low temperatures this error becomes very large as can be seen in figure 6.52d for 0°C.

By applying the low temperature equations a higher accuracy can be achieved as shown in figure 6.53. The maximum error at 15°C drops to 15mV in the SoC range of interest and can also accurately model voltage behaviour at very low temperatures. The disadvantage is, however, a large increase in equation complexity. So whether to use the low temperature equations or not depends on the required accuracy and operating conditions of the modelled cell.

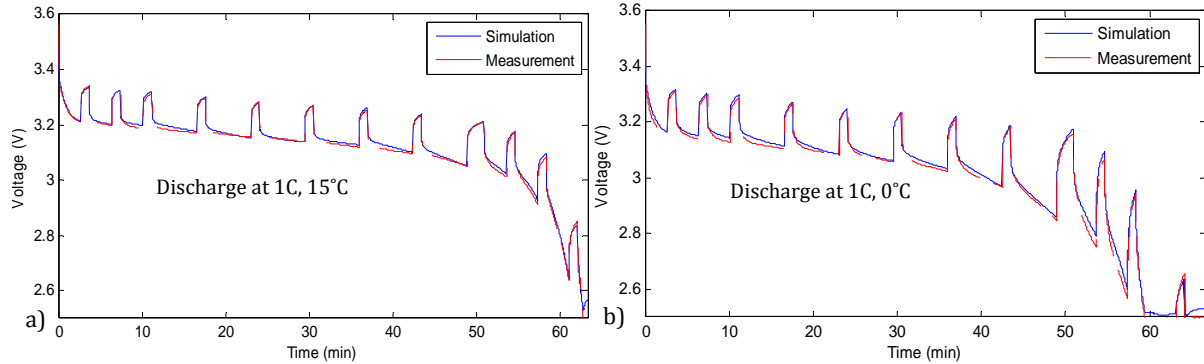


Figure 6.53: A comparison between simulation results and measurements for cells discharged at a) 15°C and b) 0°C with application of the low temperatures equations.

A similar analysis is conducted for the charging parameters. For charging the temperature dependence modelling is divided into high and low temperatures again. Temperatures of 20°C and above are considered high temperatures, while below 20°C is regarded as low temperature. By analysing the measurement data, the high temperature dependence of R_{oc} was found to be approximated by a constant factor over the SoC range with the VTF equation, changing equation 6.18 to

$$R_{oc,T_{high}}(SoC, T) = R_{oc}(SoC) \cdot b_{t1c} e^{\frac{b_{t2c}}{T-b_{t3c}}} \quad (6.37)$$

with $b_{t1c} = 7.192\text{E-}1$, $b_{t2c} = 33.91$ and $b_{t3c} = 1.999\text{E}2$. At low temperatures R_{oc} cannot be modelled with a constant factor and equation 6.18 becomes much more complex:

$$\begin{aligned} R_{oc,T_{low}}(SoC, T) = & (b_{t1c}SoC^4 + b_{t2c}SoC^3)(b_{t1c}T + b_{t2c}) + (b_{t3c}T^2 + b_{t4c}T + b_{t5c})SoC^2 + \\ & (b_{t6c}T^2 + b_{t7c}T + b_{t8c})SoC + b_{t9c}e^{\frac{b_{t10c}}{T-b_{t11c}}} \end{aligned} \quad (6.38)$$

with $b_{t1c} = -8.297\text{E-}2$, $b_{t2c} = 24.82$, $b_{t3c} = 2.136\text{E-}4$, $b_{t4c} = -1.422\text{E-}1$, $b_{t5c} = 23.48$, $b_{t6c} = -1.795\text{E-}4$, $b_{t7c} = 1.077\text{E-}1$, $b_{t8c} = -16.20$, $b_{t9c} = 4.968\text{E-}2$, $b_{t10c} = 28.78$ and $b_{t11c} = 2.376\text{E}2$. Furthermore, the SoC dependent parameters also change for low temperatures, resulting in $b_{t1c} = 2.192\text{E-}1$ and $b_{t2c} = -3.968\text{E-}1$. R_{oc} determined from measurements at different temperatures and the corresponding curve fits are shown in figure 6.54.

6 Empirical development of an improved practical circuit-based model

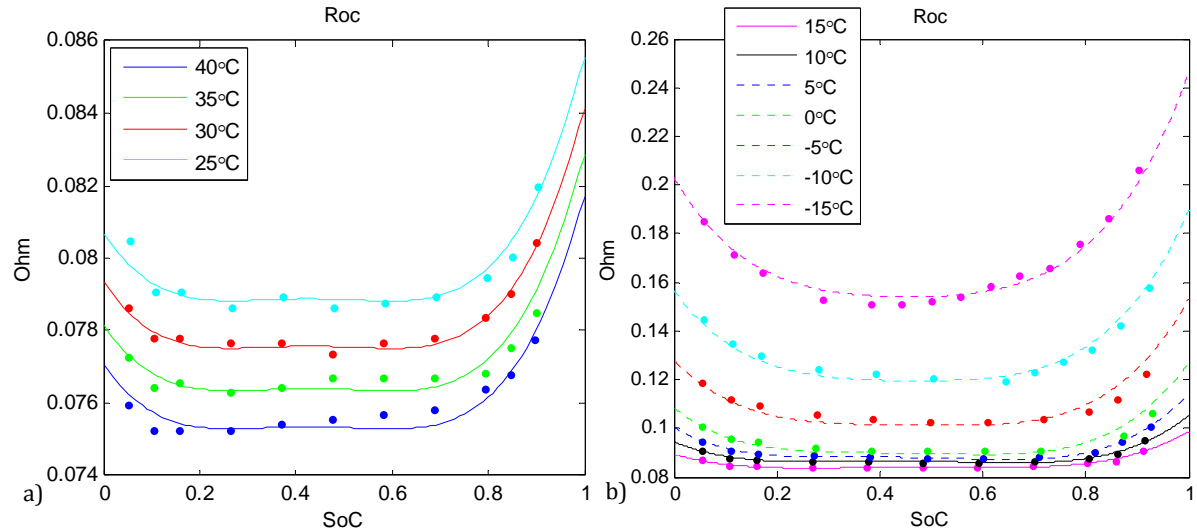


Figure 6.54: The measured values of R_{sc} and corresponding curve fit for a) high and b) low temperatures.

R_{sc} exhibits temperature dependent pattern along the measured temperatures. The slope of the exponential function slowly decreases with the temperature, while the exponential rise starts at lower SoC. Using equation 6.19 the temperature dependence for high temperatures found from the measurement data to be described by

$$R_{sc,T_{high}} = c_{t1c} e^{c_{t2c}T - (c_{t3c}T + c_{t4c})SoC} + c_{t5c}T + c_{t6c} \quad (6.39)$$

with $c_{t1c} = 9.867E8$, $c_{t2c} = -1.479E-1$, $c_{t3c} = -1.178E-1$, $c_{t4c} = 13.99$, $c_{t5c} = -1.897E-4$ and $c_{t6c} = 7.054E-2$. From analysis of the measurement data for low temperatures equation 6.19 becomes

$$R_{sc,T_{low}} = c_{t1c} e^{c_{t2c}T + (c_{t3c}T + c_{t4c})SoC} + c_{t5c}T^2 + c_{t6c}T + c_{t7c} \quad (6.40)$$

with $c_{t1c} = 7.008E29$, $c_{t2c} = -3.051E-1$, $c_{t3c} = 2.782E-1$, $c_{t4c} = -63.04$, $c_{t5c} = 2.840E-6$, $c_{t6c} = -1.733E-3$ and $c_{t7c} = 2.786E-1$. The measured data points of R_{sc} at different temperatures with the obtained curve fit equations are shown in figure 6.55.

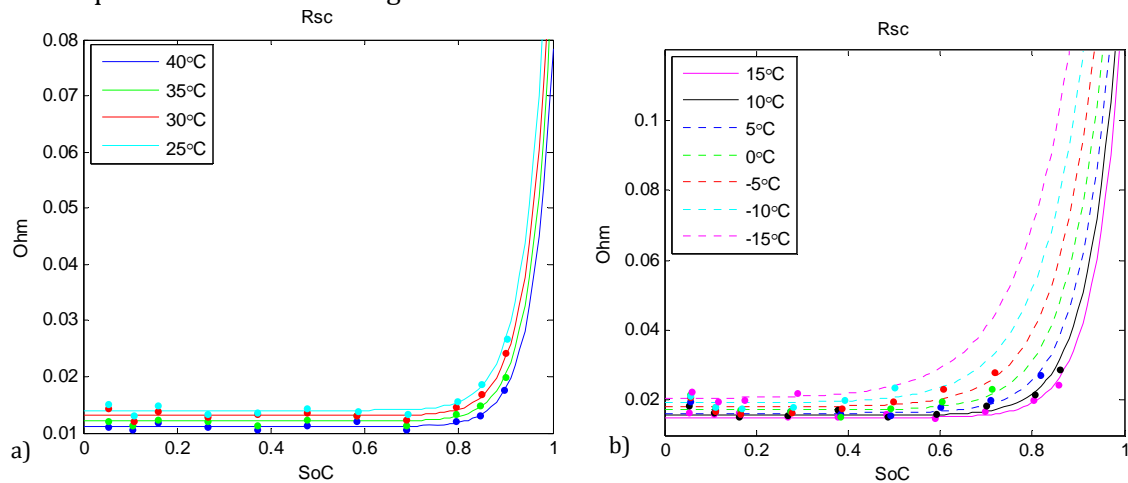


Figure 6.55: The measured values of R_{sc} and corresponding curve fit for a) high and b) low temperatures.

From the measurement data analysis temperature dependency of C_{sc} was found to be simply modelled adding a temperature dependent constant, changing equation 6.20 to

$$C_{sc,T_{high}}(SoC, T) = C_{sc}(SoC) + d_{t1c}\Delta T \quad (6.41)$$

with $d_{t1c} = 8.814$. For low temperatures every parameter was found to be temperature dependent, which severely complicates equation 6.20 to

$$\begin{aligned} C_{sc,T_{low}}(SoC, T) &= (d_{t1c}T^2 + d_{t2c}T + d_{t3c})SoC^4 + (d_{t4c}T^2 + d_{t5c}T + d_{t6c})SoC^3 \\ &+ d_{t7c}e^{d_{t8c}T}SoC^2 + (d_{t9c}T^2 + d_{t10c}T + d_{t11c})SoC + d_{t12c}T \\ &+ d_{t13c} \end{aligned} \quad (6.42)$$

with $d_{t1c} = -11.23$, $d_{t2c} = 5.941E3$, $d_{t3c} = -7.848E5$, $d_{t4c} = 16.18$, $d_{t5c} = -8.523E3$, $d_{t6c} = 1.123E6$, $d_{t7c} = -3.688E-2$, $d_{t8c} = 4.261E-2$, $d_{t9c} = -1.199$, $d_{t10c} = 7.103E2$, $d_{t11c} = -1.027E5$, $d_{t12c} = 8.493$ and $d_{t13c} = -1.902E3$. C_{sc} determined at different temperature and the corresponding curve fits are shown in figure 6.56.

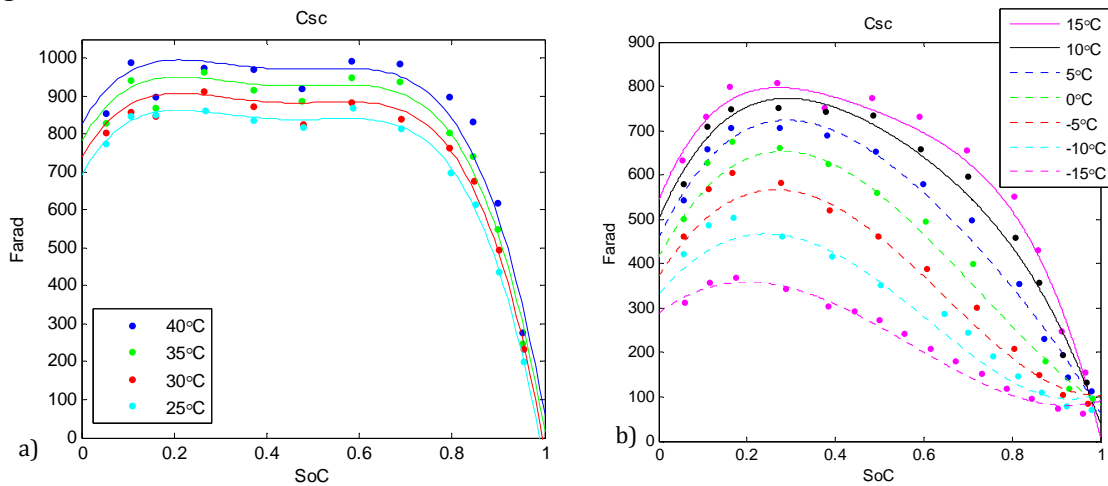


Figure 6.56: The measured values of C_{sc} and corresponding curve fit for a) high and b) low temperatures.

The modelling of R_{lc} poses a large problem, as in paragraph 6.4.4.2 it was shown that the C-rate has an influence on the value of R_{lc} . Therefore the data points determined at different C-rates cannot be taken into account, resulting in little available data points. Nonetheless, the development of R_{lc} can still be predicted as the SoC behaviour remains the same for different currents. Only the values of R_{lc} at the SoCs measured under a different current level will be different. For high temperatures this is of no concern, and equation 6.21 for R_{lc} was found to change to

$$R_{lc,T_{high}}(SoC, T) = R_{lc}(SoC) \cdot (g_{t1c}T + g_{t2c}) \quad (6.43)$$

with $g_{t1c} = -1.344E-2$ and $g_{t2c} = 5.011$. Since little data points at constant current are available for low temperatures, the data points at lower currents are used to estimate the SoC behaviour of R_{lc} . By considering the current dependency, for low temperatures equation 6.21 changes to

$$R_{lc,T_{low}}(SoC, T) = g_{t1c} \cdot e^{g_{t2c}T - g_{2c}SoC} + g_{t3c}T^2 + g_{t4c}T + g_{t5c} + g_{4c}SoC \quad (6.44)$$

with $g_{t1c} = 3.726E-8$, $g_{t2c} = -4.951E-2$, $g_{t3c} = 5.921E-5$, $g_{t4c} = -3.507E-2$ and $g_{t5c} = 5.225$. The SoC parameter g_{2c} does not change and remains -32.23, but g_{4c} changes to 1.571E-2. The data point of R_{lc} is shown in figure 6.57 along with the curve fit equations 6.43 and 6.44.

6 Empirical development of an improved practical circuit-based model

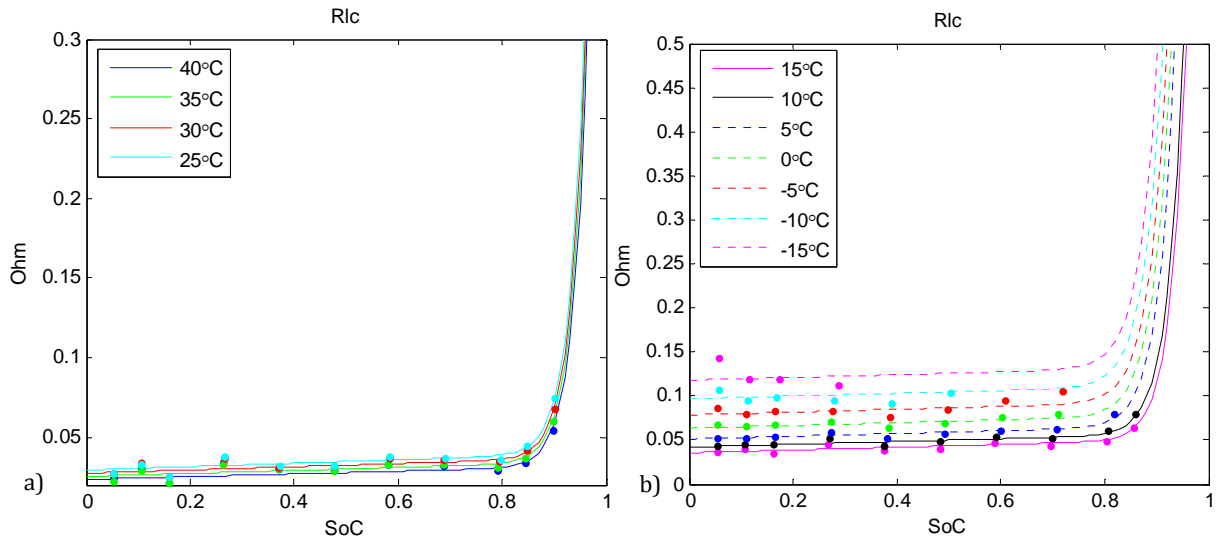


Figure 6.57: The measured values of R_{lc} and corresponding curve fit for a) high and b) low temperatures.

Since C_{lc} is not influenced by the C-rate, data points obtained with a current lower than 1C can also be used to estimate the temperature dependence. For high temperatures this will result in the following with equation 6.22:

$$C_{lc,T_{high}}(SoC, T) = C_{lc}(SoC) \cdot h_{t1c} e^{h_{t2c} T} \quad (6.45)$$

with $h_{t1c} = 2.611\text{E-}5$ and $h_{t2c} = 3.541\text{E-}2$. For low temperatures equation 6.22 becomes much more complex as with the other impedance elements:

$$C_{lc,T_{low}}(SoC, T) = (h_{t1c} SoC^5 + h_{t2c} SoC^4 + h_{t3c} SoC^3) e^{h_{t4c} T} + h_{t5c} e^{h_{t6c} T} SoC^2 + h_{t7c} e^{h_{t8c} SoC} + h_{t9c} \quad (6.46)$$

with $h_{t1c} = 6.343\text{E-}6$, $h_{t2c} = -1.817\text{E-}5$, $h_{t3c} = 1.887\text{E-}5$, $h_{t4c} = 8.551\text{E-}2$, $h_{t5c} = -1.414\text{E-}5$, $h_{t6c} = 8.381\text{E-}2$, $h_{t7c} = 1.057\text{E-}5$, $h_{t8c} = 7.897\text{E-}2$ and $h_{t9c} = 6.962\text{E-}2$. The measured values of C_{lc} at different temperatures and the corresponding curve fits are shown in figure 6.58.

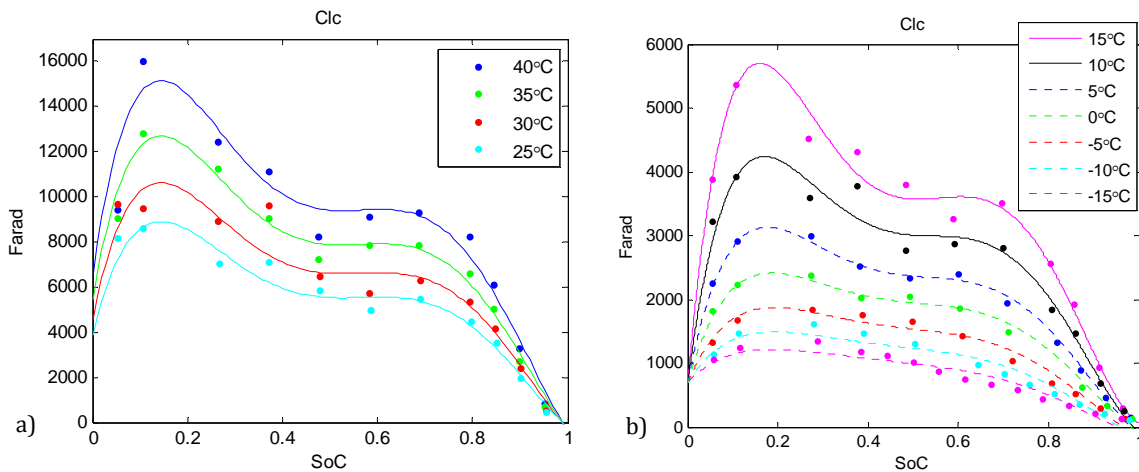


Figure 6.58: The measured values of C_{lc} and corresponding curve fit for a) high and b) low temperatures.

The empirical equations describing the temperature dependence of the impedance elements for charging are validated in the same way as for discharging. The newly obtained empirical equations are included in the proposed circuit-based model in Simulink and the simulation

results are compared with the measurements. In figure 6.59 the measurements at 40°C and 30°C are compared to simulations with high temperature equations, while the measurements at 15°C and 0°C are compared to simulations with low temperature equations. For the first three plots a high accuracy is achieved with a maximum error of 12mV in the SoC range of interest, while Figure 6.59d the maximum error goes up to 21mV in the SoC range of interest. The reason for the larger error is the difficulty to accurately model the low temperature behaviour with a limited complexity. Nevertheless, the obtained empirical equations of the impedance element for charging can accurately model the cell behaviour for changing temperatures.

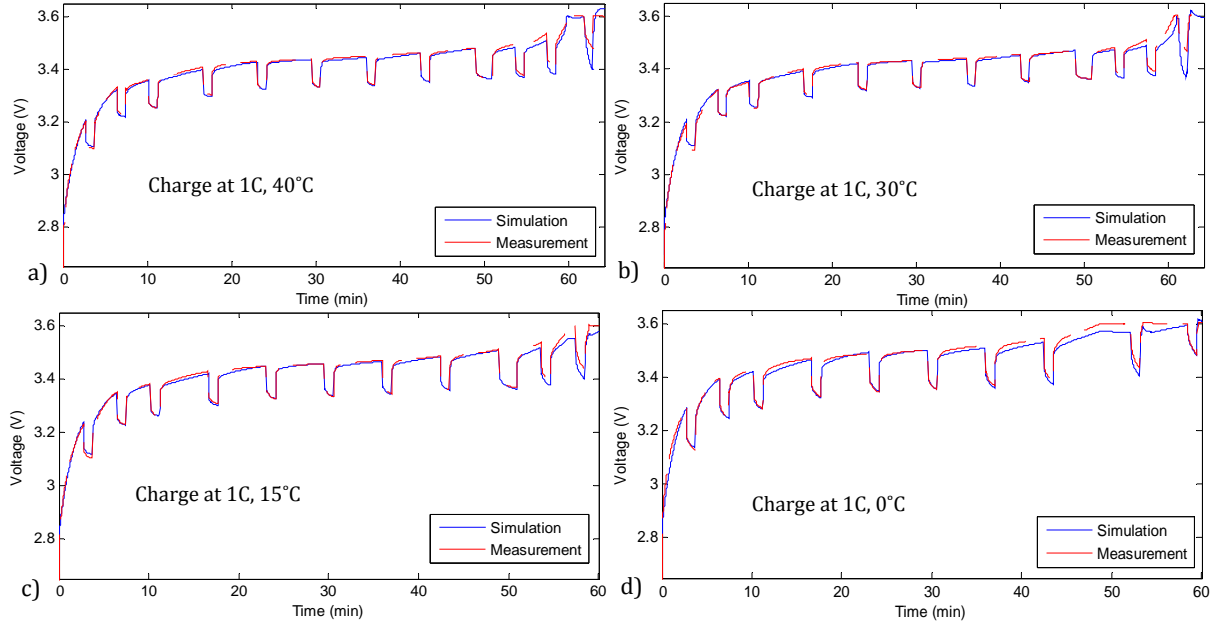


Figure 6.59: A comparison between simulation results and measurements for cells charged at a) 40°C and b) 30°C simulated with high temperature equations, and c) 15°C and d) 0°C simulated with low temperature equations.

6.4.4.4 Ageing of the internal cell impedance

In paragraph 5.3.2 several internal impedance elements were identified to change with the ageing of the cell. R_o and R_s were expected to grow with cycling of the cell whereas R_l was expected to be invariant of cycling. During the experiment the development of internal cell impedance was determined by each capacity and parameter test cycle as described in figure 6.6. In figure 6.60 the typical development of the internal cell impedance is given for a cell cycled with the current profile of figure 6.5. Each line represents the internal cell impedance determined at a different time over the course of the experiment.

In figure 6.60 it can be seen that only R_{od} shows a clear variation over the course of the experiment. This is also reflected in the total resistance R_{totd} , which variations are consistent with the variations of R_{od} . The variations of the impedance elements are better visible by plotting the incremental change per test cycle of the impedance elements in figure 6.61.

The incremental change for each impedance element except for R_{od} in figure 6.61 varies around zero over the SoC range; in addition, the variations are very small compared to ΔR_{od} as is reflected by ΔR_{totd} . It can therefore be concluded that the variations of the internal cell impedance due to cycling can be solely modelled by R_{od} . This is also consistent with literature, in which the resistance growth due to cycling mainly contributed to the growth of the SEI layer; the ohmic resistance consists of the surface layer resistance and bulk resistance of the cell.

6 Empirical development of an improved practical circuit-based model

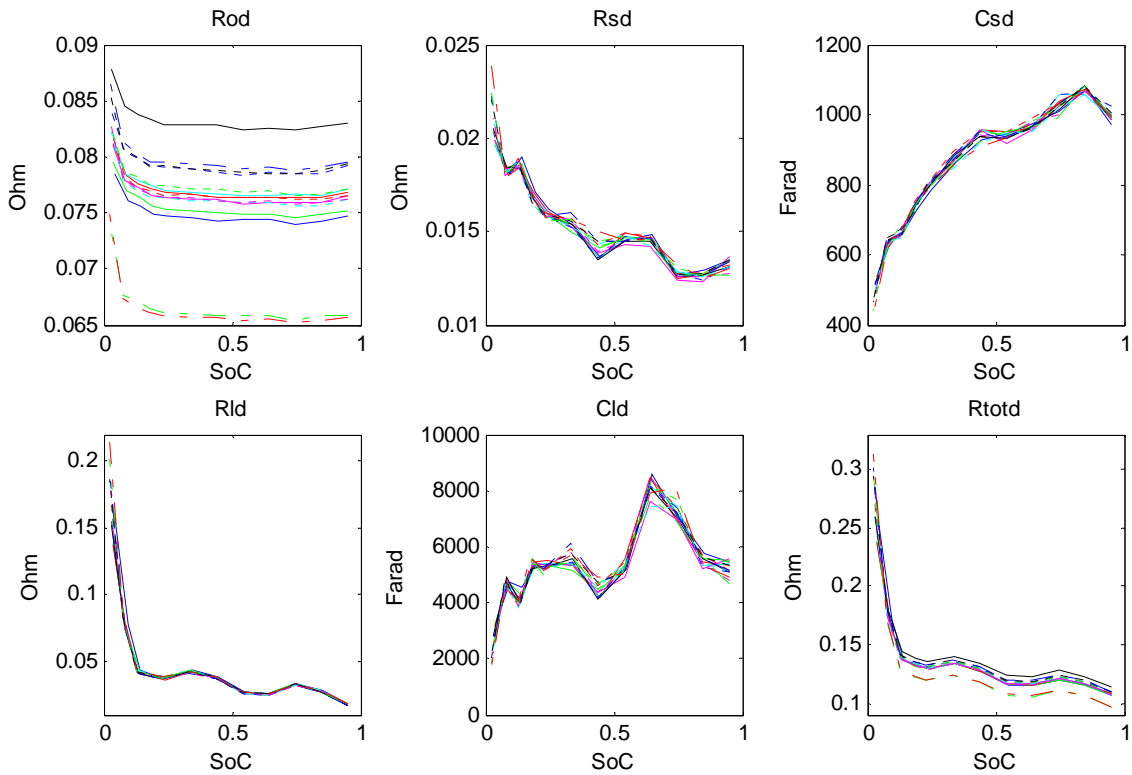


Figure 6.60: The internal cell impedance for discharge determined during the course of the cycling experiment with the proposed profile. Each line represents the internal cell impedance determined at a different time during the experiment.

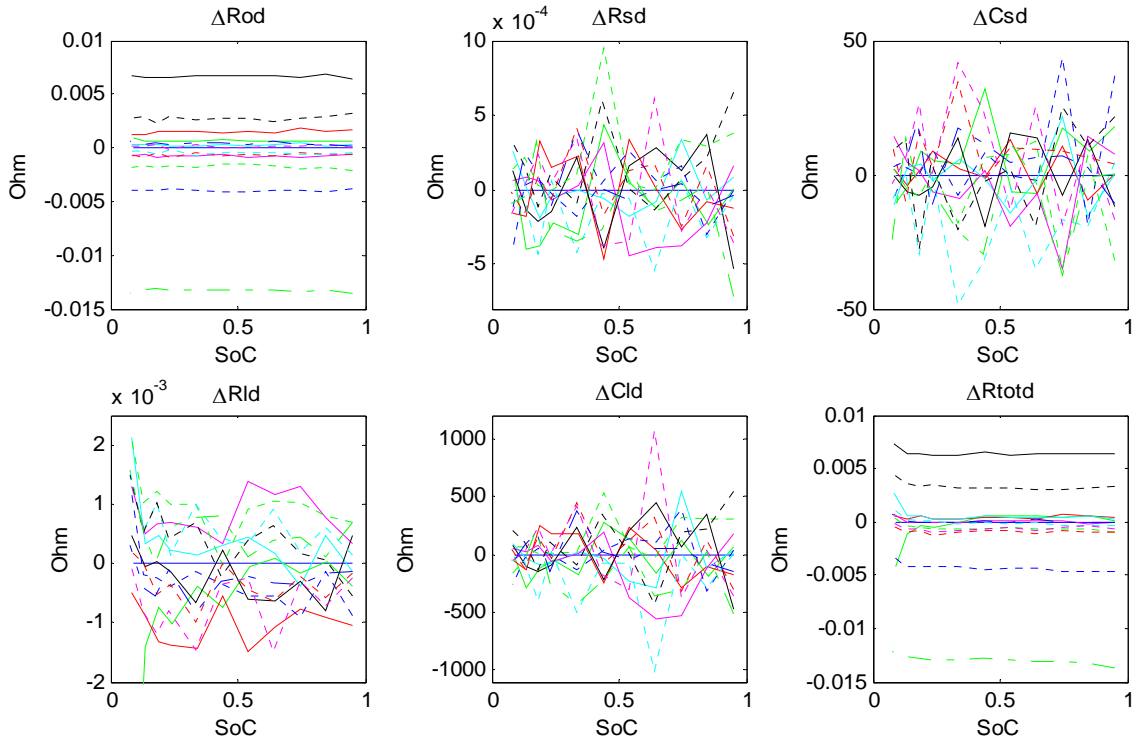


Figure 6.61: The incremental impedance per test cycle for discharge. Each line represents the incremental impedance determined at a different time during the experiment.

In figure 6.61 it can be seen that ΔR_{od} and ΔR_{totd} are fairly constant over the entire SoC range. The SoC dependent variations of ΔR_{totd} at low SoCs are caused by the fact that comparing the data points in the exponential range will lead to large errors even if the SoCs of the data points are

slightly apart. So the SoC variations of ΔR_{totd} be ignored. To determine the impedance variations in the course of the experiment, the mean value of the R_{od} and R_{totd} change are plotted against the charge processed in figure 6.62.

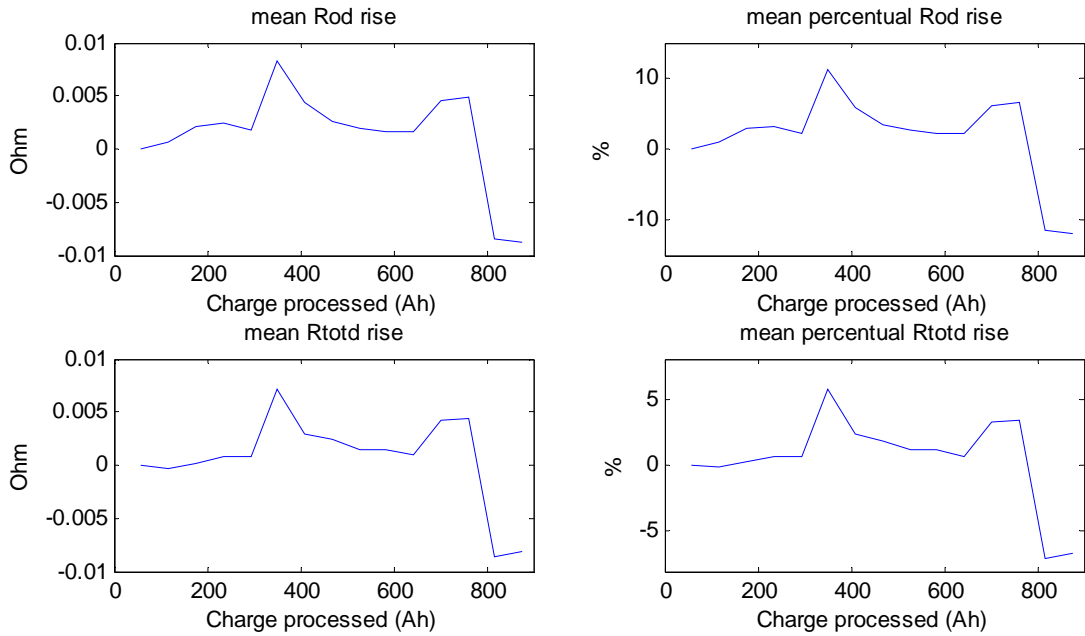


Figure 6.62: The typical development of R_{od} and R_{totd} vs. the charge processed in the cells cycled with the proposed profile in absolute value and percentage of the initial value.

Figure 6.62 shows that the development of R_{od} and R_{totd} is not in accordance to the findings in literature. R_{od} does not show any trend, whereas a rising trend is expected. These fluctuations are, however, not insignificantly small as seen in the top right graph. For this particular cell R_{od} can vary around 10% of the initial R_{od} , resulting in a variation of around 5% of the initial R_{totd} . All cells cycled with the current profile including regenerative braking exhibit the same behaviour. The development of the total cell resistance R_{totd} for each cell follows R_{od} , but the cells do not show a trend in the development of R_{od} . The difference between the tested cells is that the fluctuations of R_{od} do not occur at the same amount of charge processed or capacity faded and do not have a pattern. Furthermore, the fluctuations can go up to 50% of the initial measured R_{od} for some cells, whereas in other cells the fluctuations are negligible.

A possible explanation is that the cells have not been tested long enough for the impedance to show any trend. Another explanation is that the cells have not been stabilised yet before the cells were cycled with regenerative braking. The instability of the cell causes the resistance in the cell to fluctuate. In figure 6.63 the development of R_{od} and R_{totd} in Cell 3 is shown. Cell 3 was discharged under a constant current and did not experience any regenerative braking.

In contrast to the cells cycled with regenerative braking, Cell 3 does show a rising trend for R_{od} , which mainly also determines R_{totd} . The cell cycled with resting periods instead of regenerative braking (Cell 2) shows the same behaviour as in Figure 6.63. In a real life EV application regenerative braking will always occur, so the development of the internal cell impedance cannot be modelled with the results obtained from cells cycled without regenerative braking. The results for cells with regenerative braking are inconclusive and do not show a trend. In the practical circuit-based model the cell impedance for discharge will therefore be modelled as independent of the ageing.

6 Empirical development of an improved practical circuit-based model

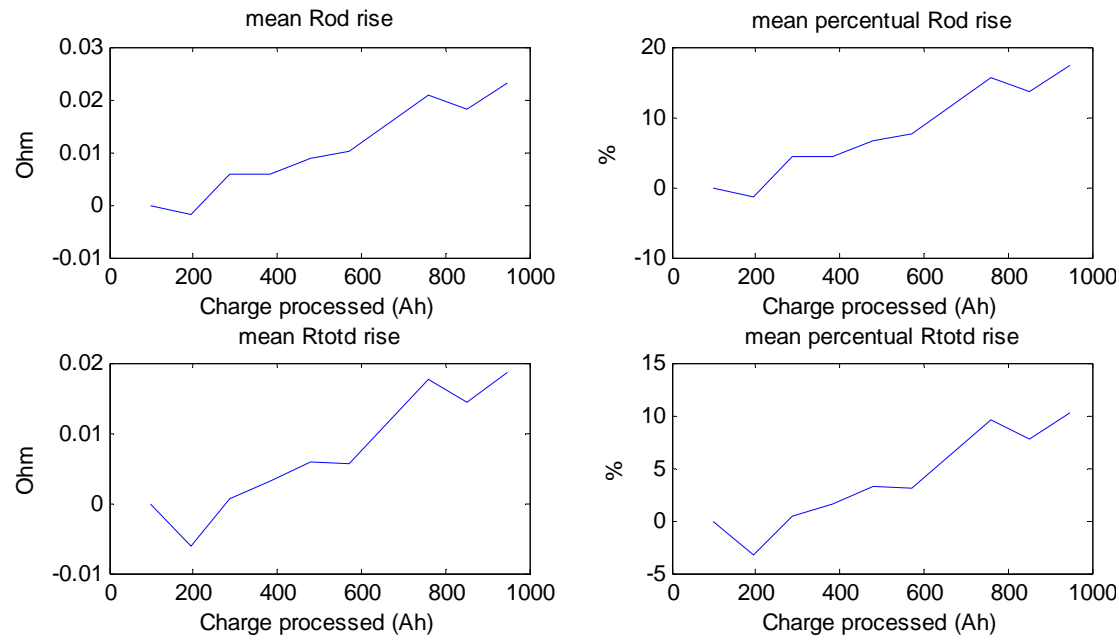


Figure 6.63: The development of R_{od} and R_{totd} vs. the charge processed in Cell 3 cycled under constant current in absolute value and percentage of the initial value.

The internal cell impedance for charging has been analysed the same way. In figure 6.64 the internal cell impedance elements for charge of a typical cell cycled with the proposed current profile is shown. The impedance elements of the same cell used for discharge in this paragraph are depicted. Each line represents the internal cell impedance determined over the course of the experiment.

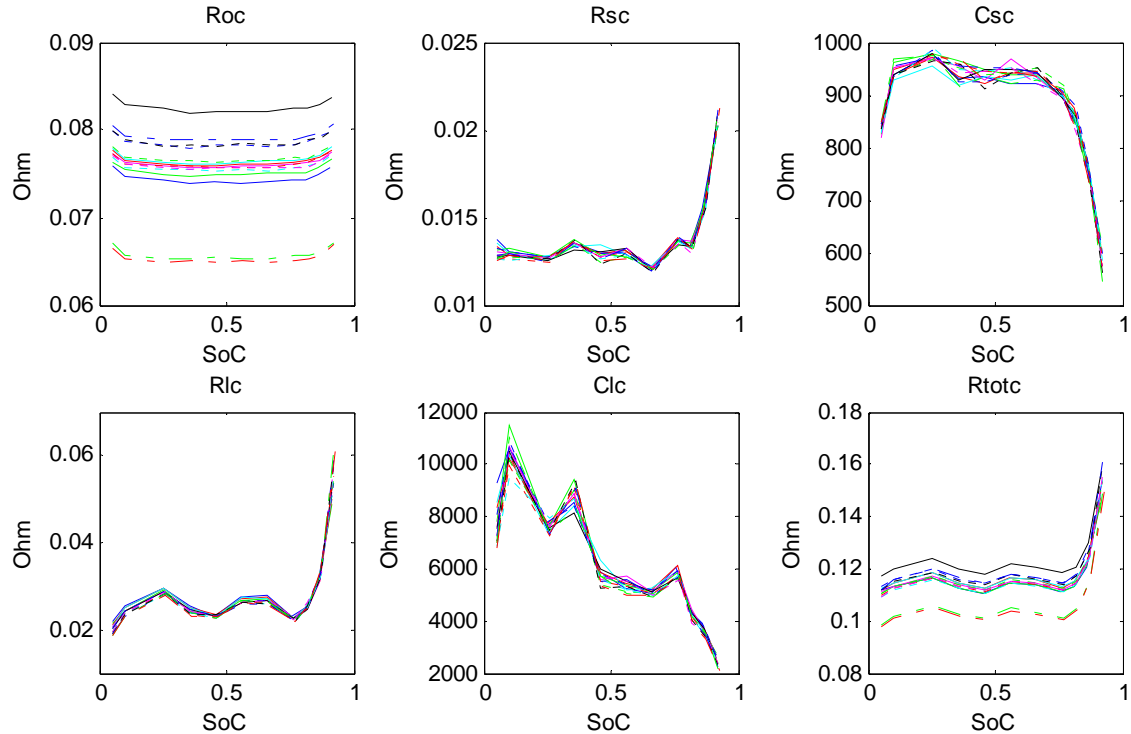


Figure 6.64: The internal cell impedance for charging determined during the course of the cycling experiment with the proposed profile. Each line represents the internal cell impedance determined at a different time during the experiment.

Every impedance element shows very little variation except for R_{oc} , which is also reflected in R_{totc} just like the impedance elements for discharging. The variations of R_{oc} over the entire SoC range are fairly constant, and by taking the mean variation of R_{oc} the development of R_{oc} can be plotted against the charge processed in figure 6.65.

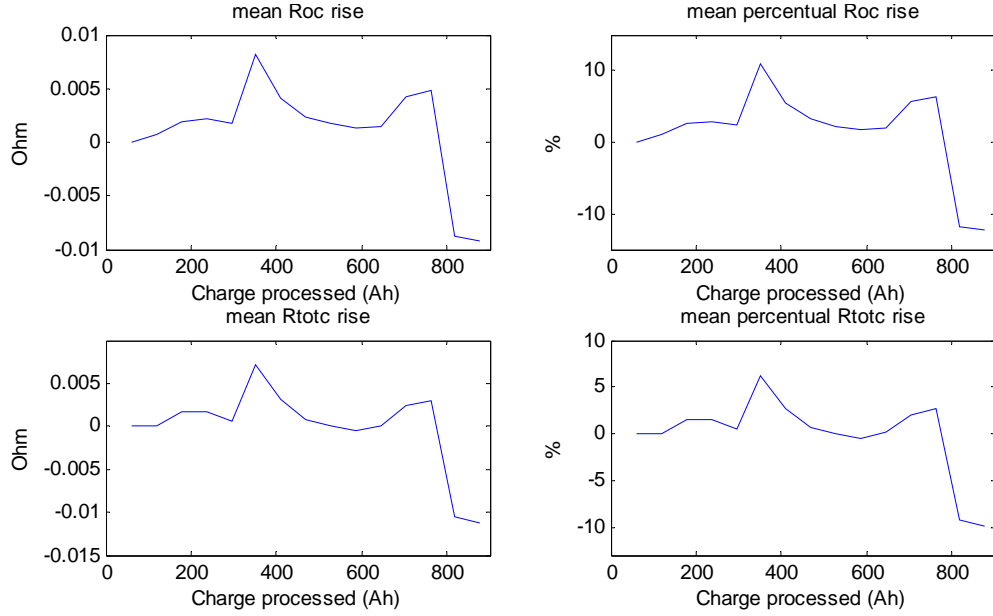


Figure 6.65: The typical development of R_{oc} and R_{totc} vs. the charge processed in the cells cycled with the proposed profile in absolute value and percentage of the initial value.

The development of R_{oc} is identical to the development of R_{od} . No trend in the development of R_{oc} is observed, but the values in the R_{oc} variations and behaviour are equal to R_{od} . Furthermore, the development of the total cell resistance for charging R_{totc} is almost equal to R_{oc} , and the ageing of the internal cell impedance for charging can be modelled by only R_{oc} . Also for charging the ageing behaviour of R_{oc} is different for each cell and do not show a trend. This indicates that the fluctuations for the charging impedance elements are also possible influenced by regenerative braking. In figure 6.66 the development of R_{oc} and R_{totc} of Cell 3 are given.

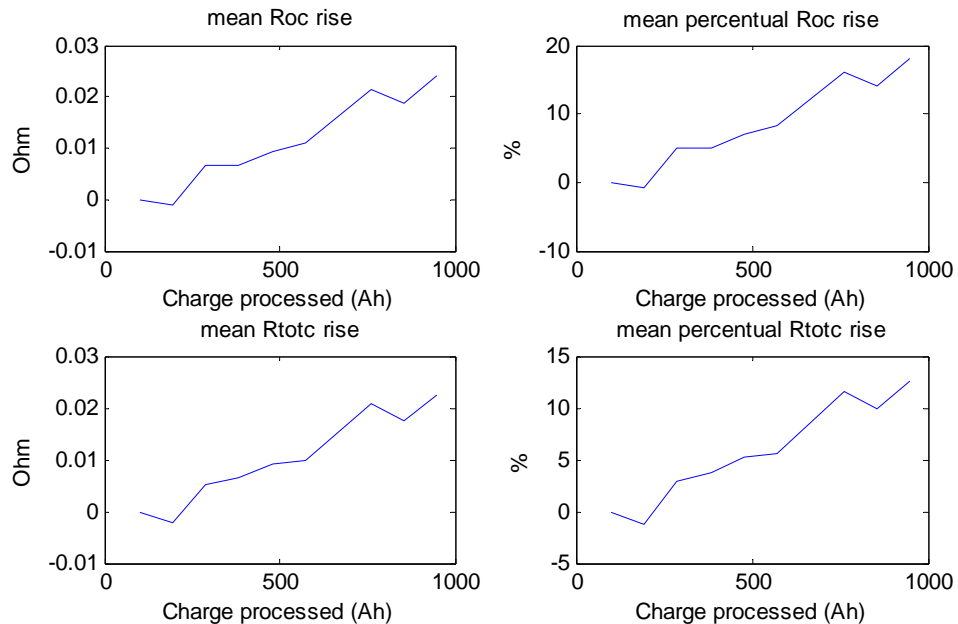


Figure 6.66: The development of R_{oc} and R_{totc} vs. the charge processed in Cell 3 cycled under constant current in absolute value and percentage of the initial value.

6 Empirical development of an improved practical circuit-based model

For charging the same conclusion can be drawn as for discharging concerning the ageing development of the internal cell impedance. The development of R_{oc} determined from the measurements of cells cycled with regenerative braking is inconclusive and does not show a trend. This may be caused by regenerative braking, as the cells cycled without regenerative braking do show a rising trend. Finally, it can be shown that the ageing development of R_{oc} is identical to R_{od} , leading to the conclusion that the ageing development of the internal cell impedance can be modelled with solely the ohmic resistance using the same equation for both discharging and charging.

6.4.5 Coulombic and energy efficiency

The efficiency in a battery cell can be measured as the round trip coulombic efficiency and the energy efficiency. The coulombic efficiency is the ratio between the Amp-hours discharged from and charged to the cell given by:

$$\eta_{Ah} = \frac{Ah_d}{Ah_c} \quad (6.47)$$

with η_{Ah} the coulombic efficiency, Ah_d the amount of Amp-hours discharged and Ah_c the amount of Amp-hours charged to the cell. Throughout the course of the experiment the coulombic efficiency has been determined for each cell during the test cycles. The coulombic efficiency for several cells is shown in figure 6.67. The other cells show similar results.

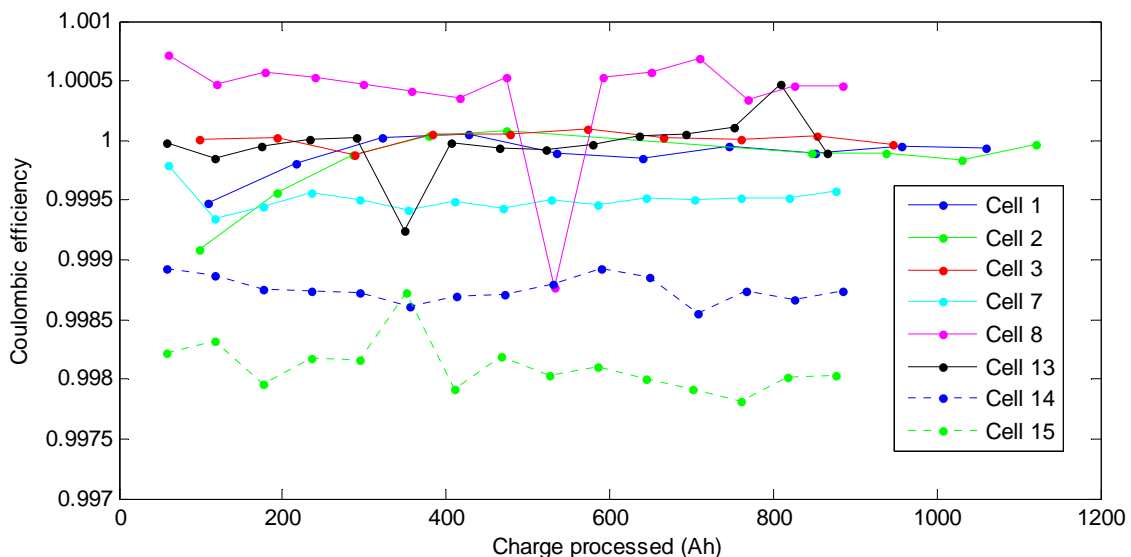


Figure 6.67: The round trip coulombic efficiency of several cells measured throughout the course of the experiment.

Figure 6.67 shows that the coulombic efficiency of each cell remains fairly constant over the course of the experiment. The coulombic efficiency varies between 100% and 99.8%, with some cells even showing a coulombic efficiency higher than 100%. The Amp-hours lost are consumed by the parasitic side reactions occurring in the cell [117]. Most coulombic efficiencies higher than 100% result from measurement errors. Cell 8, however, shows a constant coulomb efficiency higher than 100%. This is caused by the fact that the discharge resistance is lower than the charging resistance. Since the discharging and charging phase ends when the current is smaller than 0.01C, the cell resistance has a very small influence on the ending condition. The influence is however insignificantly small as seen in figure 6.67. Since the LiFePO₄ cells have a

high coulombic efficiency, coulomb counting is a good method to determine the state of charge (SoC) of a cell, under the condition that capacity fading is taken into account.

The round trip energy efficiency of the cell is the ratio between the energy discharged from and charged to the cell given by

$$\eta_{Wh} = \frac{Wh_d}{Wh_c} \quad (6.48)$$

with η_{Wh} the round trip energy efficiency, Wh_d the amount of Watt-hours discharged and Wh_c the amount of Watt-hours charged to the cell. The energy efficiency is determined by the internal impedance of the cell. This is also visible in figure 6.68. Energy lost in the cell is mainly dissipated into heat. In figure 6.68 the energy efficiency of the cell used in the impedance ageing analysis in paragraph 6.4.4.4 is used. The development of the energy efficiency is directly correlated to the development of the ohmic resistance as shown in figure 6.63 and figure 6.65, and therefore also the total resistance. Since it has been concluded in paragraph 6.4.4.4 that the development of the ohmic resistance does not show any trend, the development of the energy efficiency can also not be modelled.

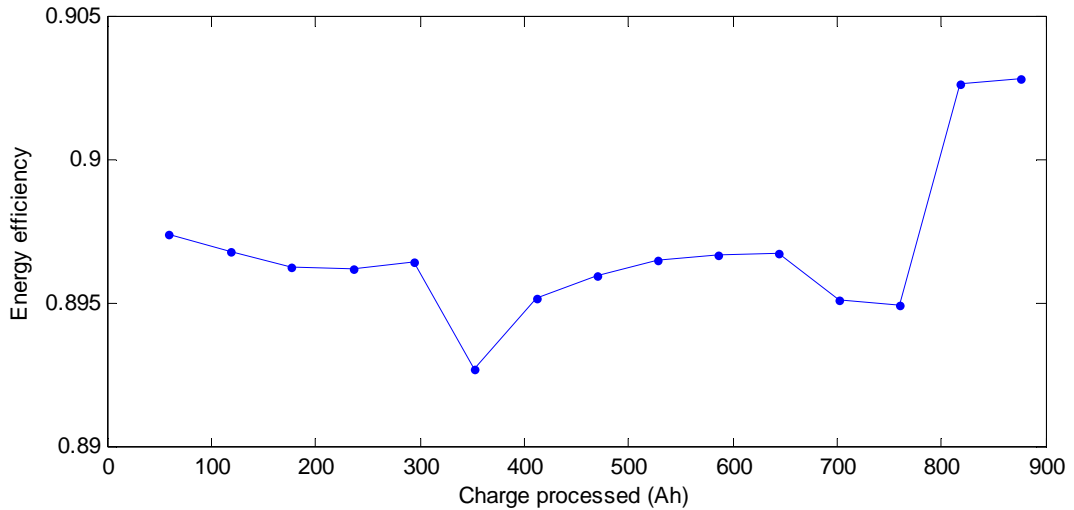


Figure 6.68: The round trip energy efficiency of the cell used in the impedance ageing analysis in paragraph 6.4.4.4.

6.5 The improved practical circuit-based model including ageing effects

In this chapter a practical circuit-based model based on empirical data has been developed. In the previous chapter a model based on literature has been developed, which comprised of models of different Li-ion cell types and the limited amount of measurement data available in literature. Many models in literature were determined with an Electrochemical Impedance Spectroscopy (EIS) measurement in the frequency domain, while model developed in this thesis is based practical considerations in the time domain. For these reasons the final proposed practical circuit-based model is not the same as the proposed practical equivalent circuit-based model developed based on literature in the previous chapter.

The final model and the literature based model are, however, not completely different. The equivalent circuit shown in figure 5.19 remains unchanged. The changes that did occur took place in the nonlinear equations of the circuit components.

6 Empirical development of an improved practical circuit-based model

In the energy balance circuit both the equations for the irreversible capacity fading and reversible capacity change have been modified. As mentioned in this thesis the capacity fading is modelled as a function of charge processed and not cycles. From the experiments the following conclusions are drawn for the cell capacity:

- The capacity fading rate was found to be equal for both cycling with regenerative braking and constant current cycling at room temperature for typical C-rate values in actual EVs, but is possibly influenced by resting times.
- The discharge C-rate level at room temperature did not influence the capacity fading rate directly for C-rate levels lower than the maximum rated C-rate. The accelerated capacity fading due to high C-rates found in literature resulted from the indirect influence on the capacity fading through cell temperature rise, as a result of increased ohmic heating.
- The C-rate for charging at low temperatures is a stress factor for capacity fading. Not enough measurements were, however, conducted to model the charging C-rate influence on the capacity fading rate.
- Temperature has a large influence on the capacity fading rate and is modelled by the Arrhenius equation. At low temperatures the Arrhenius equation is not sufficient, as another capacity fading mechanism is present due to regenerative braking. Unfortunately not enough measurements were conducted to model this effect.
- The average SoC and associated deviation from the average SoC greatly determines the capacity fading rate. A cell cycled with a large ΔDoD can have a lower capacity fading rate than a cell cycled with a lower ΔDoD , if the average SoC of the low ΔDoD cell is higher. The lower the average SoC and the smaller the deviation from the average SoC, the longer the lifetime of the cell is.
- The temperature dependent reversible capacity change is modelled with the VTF-equation. By combining the irreversible capacity fading and reversible capacity change the useable capacity is obtained.

The impedance elements obtained from measurements in the voltage response circuit differed significantly from the literature-based model. The following differences from the literature based model can be observed and the following conclusions can be drawn:

- The temperature dependence of the OCV is very small and is neglected in the model.
- For several impedance elements different equations than the literature-based model for the SoC dependence are obtained.
- Only the long time transient resistance is significantly influenced by changing C-rates.
- Since the impedance elements are determined empirically and represent multiple electrochemical processes in the cell, the temperature dependence cannot be modelled with the Arrhenius equation. The temperature dependence is modelled with empirical equations divided into high and low temperatures, in which the empirical equations for low temperatures are much more complex.
- Changes in the impedance elements as a result of ageing can be modelled by solely the ohmic resistance. The cells cycled with regenerative braking did not show a trend as a function of the charge processed or capacity faded. The ohmic resistance of cells cycled without regenerative braking, on the other hand, did show a rising trend. This led to the conclusion that regenerative braking possibly has an influence on the ageing dependence of the internal cell impedance. The internal cell impedance for both discharging and charging are therefore modelled as independent of ageing.

Furthermore, each capacity fading stress factor and impedance element influence has been determined separately and the correlation between these influences has not been investigated. It is possible that the different stress factors and influences are not independent of each other and cannot be simply combined in the model. In the capacity fading analysis it has also been determined that at low temperatures another capacity fading mechanism is present as a result of regenerative braking. The model is therefore inaccurate at temperatures below 0°C and will give an overoptimistic view of the capacity fading. Between 0°C and 25°C the model might be too optimistic, especially at lower temperatures, but will still give a good approximation of the capacity fading.

The empirical equations obtained for the internal cell impedance have similar issues. The parameters are determined under a unidirectional current. It has therefore not been determined what the dynamics between switching between discharging and charging will be. The assumption is made that the impedance element equations for discharging is directly switched to charging when the current direction changes.

Nonetheless the developed practical equivalent-circuit model will give a good indication of the short and long term behaviour of a LiFePO₄ in real-life EV applications. The useable capacity including capacity fading is modelled by

$$C_{use}(T, \xi) = (Q_{nom} - \xi) \cdot e^{k_1 \left(\frac{1}{T-k_2} - \frac{1}{T_{ref}-k_2} \right)} \quad (6.49)$$

$$\begin{aligned} \xi(T, SoC_{avg}, SoC_{dev}, Ah) \\ = \sum_i^E \left(k_{s1} SoC_{dev,i} \cdot e^{(k_{s2} \cdot SoC_{avg,i})} \right. \\ \left. + k_{s3} e^{k_{s4} SoC_{dev,i}} \right) e^{\left(-\frac{E_a}{R} \left(\frac{1}{T_i} - \frac{1}{T_{ref}} \right) \right)} Ah_i \end{aligned} \quad (6.50)$$

The possible hysteresis effect of the OCV is ignored in this model, making OCV independent of the current direction. By measuring the cte-OCV for discharging and charging the OCV is modelled with

$$V_{oc}(SoC) = a_1 e^{-a_2 SoC} + a_3 + a_4 SoC + a_5 e^{-\frac{a_6}{1-SoC}} \quad (6.51)$$

The behaviour of each impedance element in the model was found to be different for charging and discharging, which leads to two equations per impedance element. Furthermore, temperature had an influence on each impedance element. To prevent the equations becoming too complex, the temperature dependent equations were split into equations for high (20°C and above) and low (below 20°C). If the temperature dependence is taken into account, each impedance element will be described by four equations. For respectively high and low temperatures for discharging and charging the ohmic resistance R_o is described by

$$R_{od,T_{high}}(SoC, T) = (b_{1d} SoC^4 + b_{2d} SoC^3 + b_{3d} SoC^2 + b_{4d} SoC + b_{5d}) b_{t1d} e^{\frac{b_{t2d}}{T-b_{t3d}}} \quad (6.52)$$

6 Empirical development of an improved practical circuit-based model

$$\begin{aligned} R_{od,T_{low}}(SoC, T) &= (b_{t1d}T^3 + b_{t2d}T^2 + b_{t3d}T + b_{t4d})SoC^4 + b_{2d}SoC^3 + b_{3d}SoC^2 \\ &\quad + b_{4d}SoC + b_{t5d}e^{\frac{b_{t6d}}{T-b_{t7d}}} \end{aligned} \quad (6.53)$$

$$R_{oc,T_{high}}(SoC, T) = (b_{1c}SoC^4 + b_{2c}SoC^3 + b_{3c}SoC^2 + b_{4c}SoC + b_{5c})b_{t1c}e^{\frac{b_{t2c}}{T-b_{t3c}}} \quad (6.54)$$

$$\begin{aligned} R_{oc,T_{low}}(SoC, T) &= (b_{1c}SoC^4 + b_{2c}SoC^3)(b_{t1c}T + b_{t2c}) \\ &\quad + (b_{t3c}T^2 + b_{t4c}T + b_{t5c})SoC^2 + (b_{t6c}T^2 + b_{t7c}T + b_{t8c})SoC \\ &\quad + b_{t9c}e^{\frac{b_{t10c}}{T-b_{t1c}}} \end{aligned} \quad (6.55)$$

In a similar way the short time transient parallel RC pair is modelled. The high and low temperature dependence for discharging and charging for R_s and C_s are respectively modelled by

$$R_{sd,T_{high}}(SoC, T) = c_{1d}e^{-c_{2d}SoC} + c_{3d} + c_{t1d}\Delta T + (c_{4d} + c_{t2d}\Delta T)SoC \quad (6.56)$$

$$R_{sd,T_{low}}(SoC, T) = (c_{t1d}T^2 + c_{t2d}T + c_{t3d})e^{-(c_{t4d}T^2 + c_{t5d}T + c_{t6d})SoC} + c_{3d} + c_{4d}SoC \quad (6.57)$$

$$R_{sc,T_{high}}(SoC, T) = c_{t1c}e^{c_{t2c}T + (c_{t3c}T + c_{t4c})SoC} + c_{t5c}T + c_{t6c} \quad (6.58)$$

$$R_{sc,T_{low}}(SoC, T) = c_{t1c}e^{c_{t2c}T + (c_{t3c}T + c_{t4c})SoC} + c_{t5c}T^2 + c_{t6c}T + c_{t7c} \quad (6.59)$$

$$C_{sd,T_{high}}(SoC, T) = d_{1d}SoC^3 + d_{2d}SoC^2 + (d_{3d} + d_{t1d}\Delta T)SoC + d_{4d} + d_{t2d}\Delta T \quad (6.60)$$

$$\begin{aligned} C_{sd,T_{low}}(SoC, T) &= d_{1d}(SoC + (d_{t1d}T - d_{t2d}))^3 + d_{2d}(SoC + (d_{t1d}T - d_{t2d}))^2 \\ &\quad + d_{4d} + (d_{t3d}T^2 + d_{t4d}T + d_{t5d})(SoC + (d_{t1d}T - d_{t2d})) \end{aligned} \quad (6.61)$$

$$C_{sc,T_{high}}(SoC, T) = d_{1c}SoC^4 + d_{2c}SoC^3 + d_{3c}SoC^2 + d_{4c}SoC + d_{5c} + d_{t1c}\Delta T \quad (6.62)$$

$$\begin{aligned} C_{sc,T_{low}}(SoC, T) &= (d_{t1c}T^2 + d_{t2c}T + d_{t3c})SoC^4 + (d_{t4c}T^2 + d_{t5c}T + d_{t6c})SoC^3 \\ &\quad + d_{t7c}e^{d_{t8c}T}SoC^2 + (d_{t9c}T^2 + d_{t10c}T + d_{t11c})SoC + d_{t12c}T + d_{t13c} \end{aligned} \quad (6.63)$$

The modelling of the long time transient parallel RC pair produces similar equations. Unlike the other impedance elements, R_l was found to have a significant dependence on the C-rate, while the C-rate influence of C_l was not clearly visible. Combining the C-rate dependence with the temperature dependence, the long time transient parallel RC pair results in the following equations:

$$\begin{aligned} R_{ld,T_{high}}(SoC, T, I) &= ((g_{1d} + g_{t1d}\Delta T)e^{-g_{2d}SoC} + g_{3d} + g_{t2d}\Delta T + g_{4d}SoC) \\ &\quad \cdot (g_{i1d}I_{Crate}^{g_{i2d}} + g_{id3}) \end{aligned} \quad (6.64)$$

$$\begin{aligned} R_{ld,T_{low}}(SoC, T, I) &= \left(g_{t1d}e^{\left(\frac{g_{t2d}}{T-g_{t3d}}-g_{2d}SoC\right)} + g_{t4d}e^{\frac{g_{t5d}}{T}} + g_{t6d}e^{\frac{g_{t7d}}{T}}SoC \right) \\ &\quad \cdot (g_{i1d}I_{Crate}^{g_{i2d}} + g_{id3}) \end{aligned} \quad (6.65)$$

$$R_{lc,T_{high}}(SoC, T, I) = (g_{1c}e^{-g_{2c}SoC} + g_{3c} + g_{4c}SoC)(g_{t1c}T + g_{t2c}) \\ \cdot (g_{i1c}(I_{Crate}^{g_{i2c}} - 1)SoC + I_{Crate}^{g_{i3c}}) \quad (6.66)$$

$$R_{lc,T_{low}}(SoC, T, I) = (g_{t1c} \cdot e^{g_{t2c}T - g_{2c}SoC} + g_{t3c}T^2 + g_{t4c}T + g_{t5c} + g_{4c}SoC) \\ \cdot (g_{i1c}(I_{Crate}^{g_{i2c}} - 1)SoC + I_{Crate}^{g_{i3c}}) \quad (6.67)$$

$$C_{ld,T_{high}}(SoC, T) = (h_{1d}SoC^6 + h_{2d}SoC^5 + h_{3d}SoC^4 + h_{4d}SoC^3 + h_{5d}SoC^2 \\ + h_{6d}SoC + h_{7d})h_{t1d}e^{\frac{h_{t2d}}{T}} \quad (6.68)$$

$$C_{ld,T_{low}}(SoC, T) = (h_{1d}SoC^4 + h_{2d}SoC^3 + h_{5d})e^{h_{t1d}T} + h_{3d}SoC^2e^{h_{t2d}T} \\ + h_{4d}SoCe^{\frac{h_{t3d}}{T-h_{t4d}}} \quad (6.69)$$

$$C_{lc,T_{high}}(SoC, T) = (h_{1c}SoC^5 + h_{2c}SoC^4 + h_{3c}SoC^3 + h_{4c}SoC^2 + h_{5c}SoC \\ + h_{6c})h_{t1c}e^{h_{t2c}T} \quad (6.70)$$

$$C_{lc,T_{low}}(SoC, T) = (h_{t1c}SoC^5 + h_{t2c}SoC^4 + h_{t3c}SoC^3)e^{h_{t4c}T} + h_{t5c}e^{h_{t6c}T}SoC^2 \\ + h_{t7c}e^{h_{t8c}SoC} + h_{t9c} \quad (6.71)$$

By including the temperature and C-rate dependency in the practical circuit-based model, the equations for each impedance elements severely complicates. Since the temperature and C-rate dependence were determined independently, the correlation between the temperature dependency and C-rate dependency has to be investigated; the multiplication between the temperature and C-rate dependence as done in equations 6.64 to 6.67 are possibly inaccurate. An overview of the parameter values for the equations above is given in appendix B.

From the equations above it can be clearly seen that by including the low temperature dependency the model becomes much more complex. By only using the equations for high temperatures to simulate the low temperature dependency, the low temperature behaviour can be approximated. At very low temperatures, however, the error will become significant in the model. Nevertheless, equations 6.49 to 6.71 provide an EV system designer a tool to simulate the behaviour of a LiFePO₄ cell at various operating conditions. The choice lies with the system designer which operating conditions to include in the model with a trade-off between accuracy and complexity. A schematic overview of the proposed model is given in appendix A.2 and the corresponding model parameters in appendix B.

7 Lifetime optimisation of EV batteries – A case study

With the practical circuit-based model obtained from experiments in the previous chapter, a simple case study can be conducted on the lifetime optimisation of electric vehicle (EV) battery cells in reality. In this chapter a possible application of the model is demonstrated and several battery lifetime optimisation suggestions are made based on simulations.

The upscaling of a single low capacity cell to large multicell configurations introduces several complications in battery modelling. These complications will be first addressed. However, the large multicell problems are very complex and are beyond the scope of this work. Several simplifications and assumptions are made in regards to upscaling to an EV cell and the proposed Li-ion cell model is implemented in Simulink. Various driving profiles are simulated with the model, and through simulations the influence of various operating conditions on the state of health (SoH) is determined. Finally several suggestions are made to optimise the lifetime of EV batteries, which can be directly implemented with little modification to the current EV system.

7.1 Upscaling to an EV battery pack

In the previous chapter a practical circuit-based model including ageing effects was obtained from measurements on cylindrical laptop-sized cells. In EVs, however, mostly larger prismatic and possibly pouch cells are used. The larger prismatic cells will introduce additional issues in temperature distribution. Furthermore, only single cells have been characterised and validated in the previous chapter. However, not single cell configurations are used in EV, but multiple battery cells are placed in series and parallel to form an entire battery pack; in a battery pack additional problems have to be accounted for. These issues will be respectively described in this paragraph.

7.1.1 From small cylindrical to large prismatic cells

Prismatic cells can achieve a higher energy density compared to cylindrical cells. Less space is used because prismatic cells can be stacked without leaving spaces in between, while cylindrical cells have gaps between cells due to their cylindrical shape. Furthermore, prismatic cells offer a larger flexibility in shape and dimension, and both cell terminals are on the same side of the cell. Due to the flexibility prismatic cells on the market have a higher capacity than largest cylindrical cells. This means that fewer cells can be used to achieve the same amount of desired capacity for the EV. Consequently, fewer cells have to be monitored, which makes the control of the cells simpler for the battery management system (BMS).

The use of higher capacity cells result in a larger volume and mass per cell, which is associated with more heat generation and a larger heat capacity per cell. The heat generated in cell does not spread uniformly over the entire cell, resulting in temperature gradients in the cell. The temperature inside the cell is therefore higher than at the surface, and the difference becomes larger with a higher C-rate, i.e. a higher power dissipation rate [45]. For a small cylindrical cell the temperature over the entire cell surface is almost constant except at the positive terminal, which shows a higher temperature [45]. However, for prismatic cells the temperature distribution is not only nonuniform inside the cell, but the surface temperature at the bottom part of the cell is much lower than the top part of the cell [118]. The temperature nonuniformity increases with increasing C-rate. The temperature was found to be higher during discharging compared to charging, which corresponds to the findings of the internal resistance values in

chapter 6 and the entropy changes of the intercalation in the cell [16]. With various models the difference between the internal cell temperature and surface temperature [45], the nonuniform temperature distribution from the middle of the cell to the surface [119] and the surface temperature distribution [120] can be represented.

7.1.2 From battery cell to battery pack

Multicell configurations introduce additional difficulties in battery modelling, monitoring and management. For series connected cells battery modelling is straightforward; each model can be connected in series and the cell current is equal to the load current. On the other hand, modelling of parallel connected cells is much more challenging, as the state of each cell is not equal and variations between the cells result in an uneven load current distribution [121].

The capacity and the lifetime of the battery pack are determined by the weakest cell. To prevent overcharge and overdischarge, each cell has to be monitored individually. When the weakest cell reaches the minimum or maximum voltage in series connected cells, the current is cut off and each cell has reached a different state of charge (SoC). The different in SoC will result in a different ageing rate, which would cause the variations between the cells to become even larger. To use the entire battery pack capacity, the capacity of the individual cells needs to be equalised [122]. Different equalisation techniques have been presented in literature [123][124].

Parallel connected cells are forced to the same cell voltage, even though the individual state of charge (SoC) is rarely exactly equal. With a large SoC offset a high current may flow between the cells and damaging the cells. Additionally, in case of a short-circuit in one cell, the entire current will flow through that cell; the rest of the cells will be drained and the short-circuited cell will heat up, which may lead to a fire hazard.

In respect to thermal management, battery packs also introduce additional issues compared to single cells. When cylindrical cells are used, the gaps between the cells due to the cylindrical casing can be used for cooling. In prismatic cells, however, the cells are often placed close to each other to utilise the scarce space in the EV. Each cell will then be influenced by heating of the neighbouring cells and can only little surface area is available for cooling. The cells in the middle of the pack will experience more heating than the cells at the end. Since the performance and capacity of the cells are dependent on temperature, the temperature difference between cells will lead to offsets in the SoC and state of health of each cell. To minimise the differences between the cells in the pack, the BMS also has to conduct thermal management.

7.2 SoH simulation of real-life EV batteries

To simulate the development of the SoH of an EV battery cell under different driving conditions, the practical circuit-based model obtained in the previous chapter has been implemented in Simulink. The SoH has been simulated under different conditions with the New European Driving Cycle (NEDC) to illustrate the effect of different ways in treating an EV. However, the NEDC is a driving cycle under ideal circumstances on the road. In reality the speed variations are much more frequent and severe, which is represented by the United States Federal Test Procedure 75 (FTP-75) for an urban environment. Both the NEDC and FTP-75 are optimistic driving cycles, so the SoH development with a real driving profile, obtained from the EVs in the project, is evaluated as well.

7.2.1 EV cell Simulink model

The Simulink model is shown in figure 7.1. The model is split into the energy balance circuit, voltage response circuit and thermal circuit. The BMS in figure 7.1 only serves as an illustration and is not taken into account in the model. The Simulink model of the energy balance circuit and voltage response circuit are respectively shown in figure 7.2 and figure 7.3.

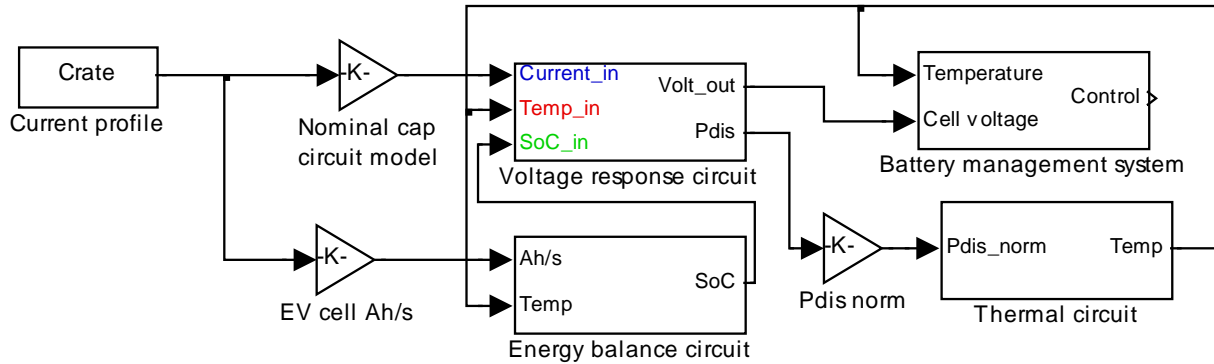


Figure 7.1: The Simulink model of the proposed model for an EV battery cell.

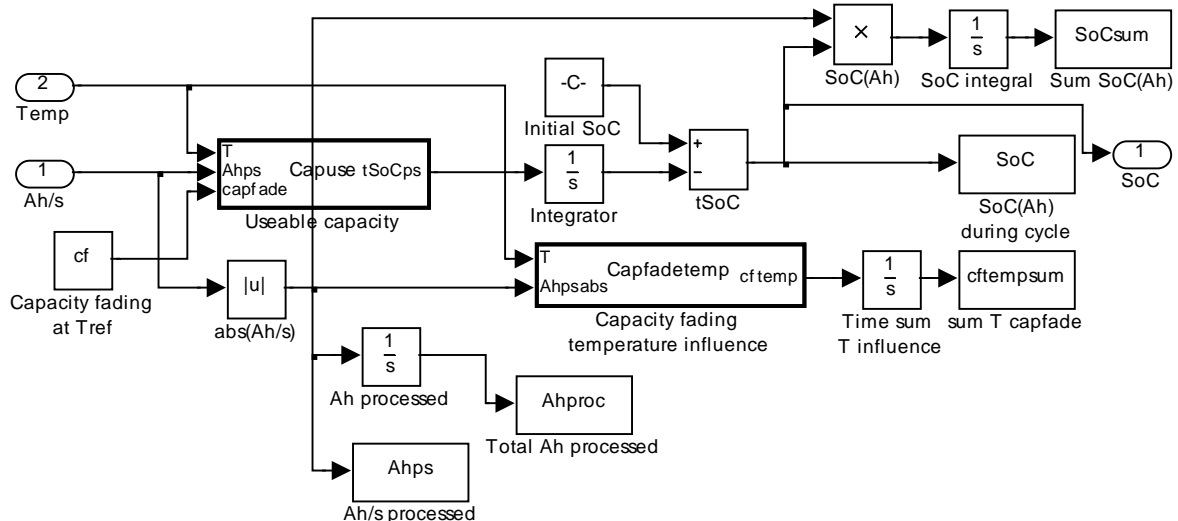


Figure 7.2: The Simulink model of the energy balance circuit.

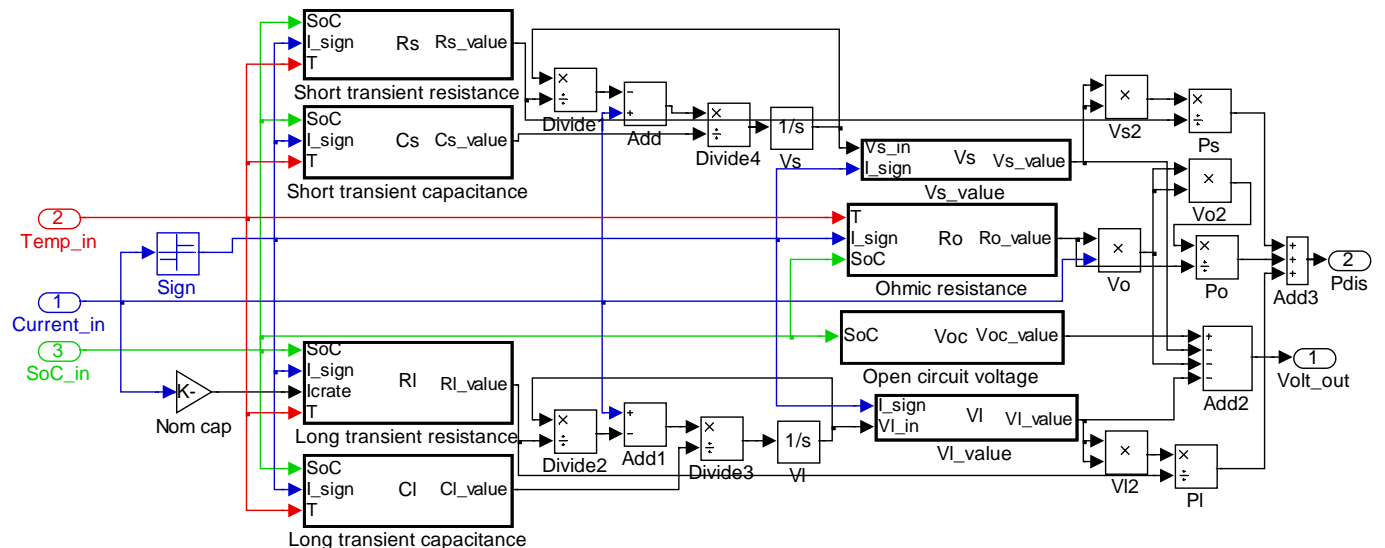


Figure 7.3: The Simulink model of the voltage response circuit.

Each circuit component is represented by an embedded Matlab function, which contains the equations and parameters determined in the previous chapter. In the energy balance circuit the charge processed dependent SoC is calculated by scaling the SoC development with time with the charge processed with time. Since the average SoC SoC_{avg} and the normalised standard deviation SoC_{dev} over one driving cycle is used to represent the initial SoC and ΔDoD , SoC_{avg} and SoC_{dev} are determined outside of the Simulink model in a Matlab script. In the voltage response circuit the total power dissipation of the cell is a summation of the power dissipation of the resistance elements, and scaled to the nominal capacity of the EV cell used in the project. The power dissipation is calculated with

$$P_{dis} = \frac{V_o^2}{R_o} + \frac{V_s^2}{R_s} + \frac{V_l^2}{R_l} \quad (7.1)$$

with P_{dis} the power dissipation, and V_o , V_s and V_l the voltage drop over respectively the ohmic resistance R_o , the short time transient resistance R_s and the long time transient resistance R_l . To model the temperature development of the EV cell due to ohmic heating of the cells, a simple lumped element thermal circuit is used. For the simplification of the thermal circuit model, the cell is seen as a plate. The side of the battery, the largest area, is taken as the surface area in the model. The heat is assumed to be generated uniformly in the middle of the cell, and travels to the surface area without a temperature gradient. The thermal circuit used in the simulation is shown in figure 7.4a. T is the cell temperature and T_{env} is the temperature of the environment, both in Kelvin. The temperature of the environment is assumed to be stable. The values for the thermal resistance R_{th} and thermal capacitance C_{th} are obtained from the manufacturer's website and literature [119]. The corresponding Simulink model is shown in figure 7.4b.

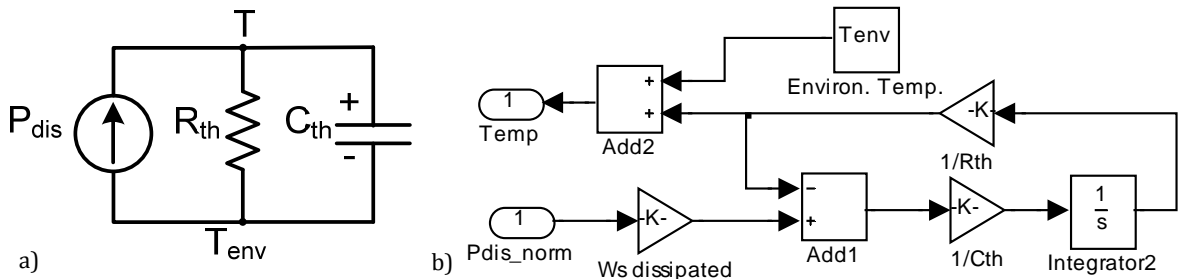


Figure 7.4: a) The lumped element thermal circuit used in the model and b) the corresponding Simulink model.

In the Simulink model several simplifications and assumptions are made. The issues encountered with upscaling a single small cylindrical cell to a large prismatic multicell configuration described in paragraph 7.1 have not been taken into account. Modelling of the temperature distribution and multicell configurations lies beyond the scope of this thesis. Entropy changes resulting in additional heating during discharge have also not been taken into account [16]. Furthermore, the influence of possible air or liquid cooling of the cells is neglected, and the heat generation of neighbouring cells is ignored as well. Additionally, the capacity over the period between two charges is assumed to be constant, and the amount of capacity fading is calculated at the end of a charge period. Finally, the BMS is not modelled either and the cell current is not controlled. To prevent overdischarge and overcharge, the simulated cell is therefore cycled between 90% and 10% SoC.

7.2.2 SoH simulation with the New European Driving Cycle

First the New European Driving Cycle (NEDC) is used to evaluate the SoH development of an EV cell. In this work the true capacity fading is taken as the SoH parameter, as described in paragraph 4.5. The NEDC is depicted in figure 7.5a. The NEDC consists of four urban driving profiles followed by one Extra Urban Driving Cycle (EUDC) profile. From the speed profile the power requirement P from the battery cell are calculated with the equations from [40]:

$$P = \frac{(ma + \frac{1}{2}\rho v^2 C_d A + C_{rr}mg)v + P_{ut}}{\eta_{bw}\eta_{bat}} \quad (7.2)$$

$$P = (ma + \frac{1}{2}\rho v^2 C_d A + C_{rr}mg)v\eta_{rb} + P_{ut} \quad (7.3)$$

g is the standard gravity and ρ the air density. The following assumptions were made for the parameters in equations 4.21 and 4.22. The drag coefficient C_d is assumed to be 0.28 and frontal area A 2.7 m² [40]. The rolling resistance coefficient C_{rr} is 0.01, battery-to-wheel efficiency η_{bw} 0.8, battery discharge efficiency η_{bat} 0.9 (square root of the battery round trip efficiency) and regenerative braking efficiency η_{rb} 0.5 was obtained from [125]. The mass m is the mass of the EV in the project, obtained from the dealer website, plus 80 kg for a person. A constant power load P_{ut} is taken as 500W for the power requirement of the electronics, radio and lights in the EV [126]. The EV did not have an air conditioner. The resulting power requirement from the battery is shown in figure 7.5b.

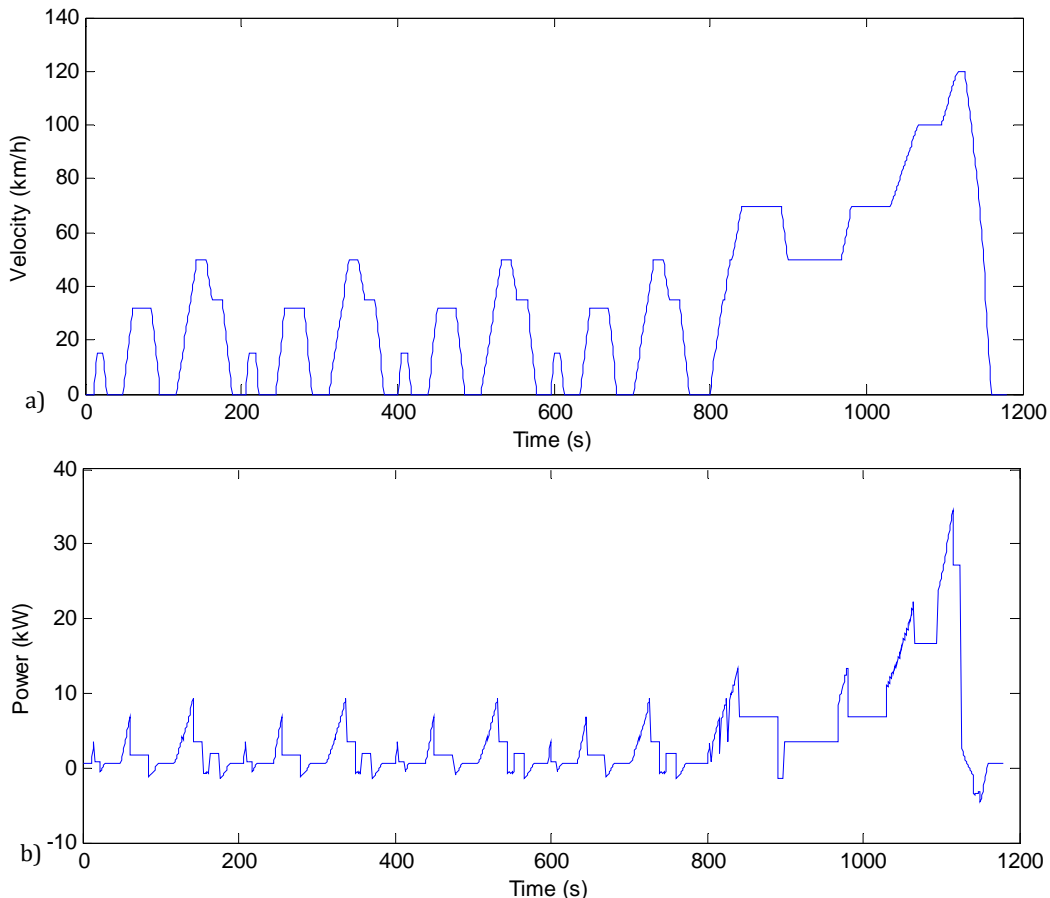


Figure 7.5: a) The NEDC used in the SoH simulation [127] and b) the corresponding estimated power requirement of the EV in the project.

With the power profile in figure 7.5b, the C-rate drawn from a single EV cell is calculated by assuming each cell delivers an equal amount of power. Since the voltage of a cell is not constant and the voltage constantly changes in response to the current, an iterative loop has to be employed to calculate the current profile corresponding to a given power profile. However, to prevent the excessive long simulation times caused by the iterative loop, the current profile is obtained by dividing the power profile of a single cell by the nominal voltage of the cell.

The NEDC is followed by a direct recharge to the initial SoC with a current of 0.1C for normal charging, found in the specifications of the EV. In figure 7.6a the current profile of one simulation cycle is depicted. With the thermal circuit in figure 7.4 the temperature development of the cell during one cycle is determined. The environment temperature, and thus the initial temperature of the cell, is taken as 25°C. The temperature development of a cell with 90% initial SoC is shown in figure 7.6b. The temperature development in figure 7.6b is an optimistic view of temperature in the cell, because the heating of the neighbouring cells is neglected. Nevertheless, the relative influence of the cell heating on the SoH is captured.

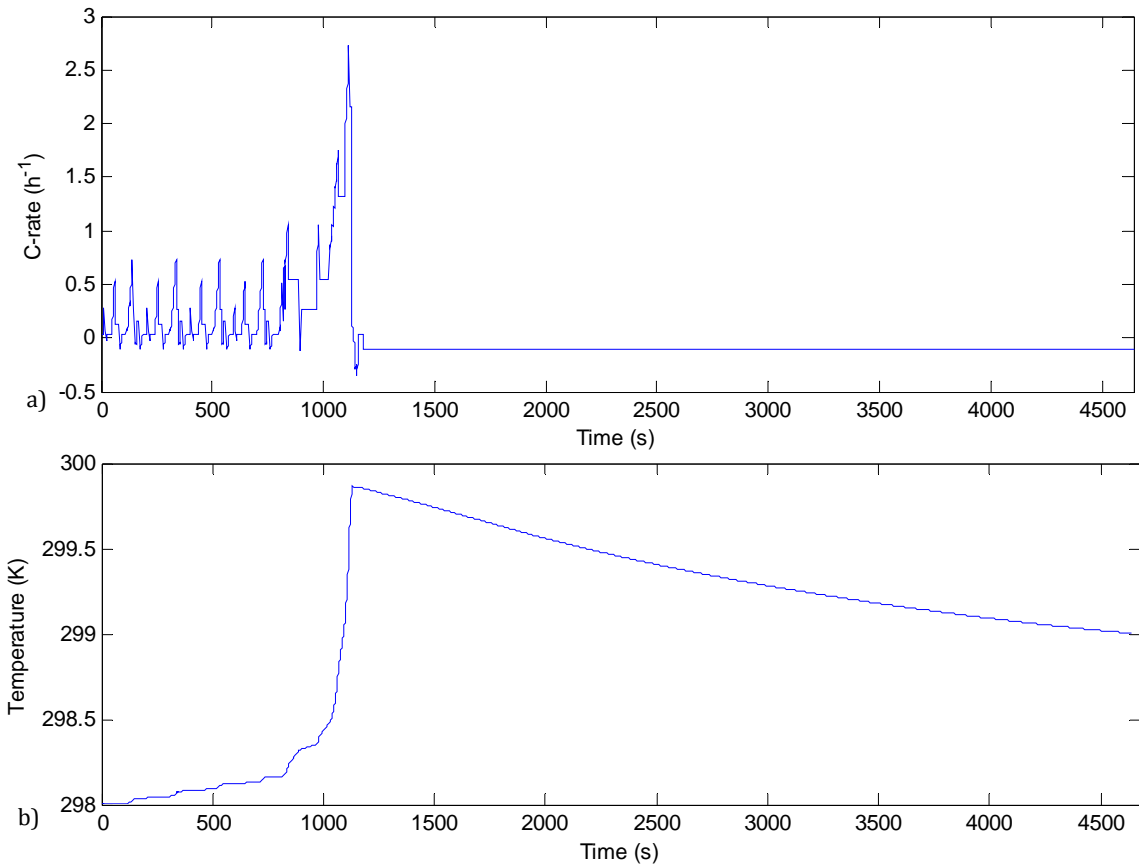


Figure 7.6: a) The current profile of one simulation cycle and b) the corresponding temperature development of the EV cell.

After one simulation cycle the capacity fading, dependent on the cell temperature, SoC_{avg} and SoC_{dev} , is determined. The total capacity faded is fed back into the Simulink model, which results in a slowly growing ΔDoD with the same current profile. However, the initial SoC stays the same during each cycle, leading to a slowly dropping SoC_{avg} associated with a growing SoC_{dev} . The dropping of SoC_{avg} will lead to less capacity fading, while growing SoC_{dev} accelerates the capacity fading. Consequently, the SoH development is not linear with a constant initial SoC and the same current profile.

7 Lifetime optimisation of EV batteries – A case study

The NEDC current profile corresponds to almost 10% ΔDoD of the EV cell. A low ΔDoD corresponds to a low capacity fading rate, and it takes at least 60000 driving cycles including recharge to reach 0% SoH for 90% initial SoC. 60000 driving cycles takes approximately 35 hours to simulate on an Intel Core2 Duo T9300 CPU 2.5GHz. Many simulations have to be conducted with different initial SoCs, different ΔDoD and different charging conditions, which will lead to excessively long simulation times. Since only the SoH relation between the different simulation conditions is of interest and not the absolute value of the SoH, the driving cycle is simulated for 1000 cycles and linearly extrapolated. The linearly extrapolated SoH was compared to a simulation cycled until 80% SoH, and the difference was found to be 0.6%. The linear extrapolation is therefore a good approximation.

In figure 7.7 the SoH of the simulated EV cell is determined for different initial SoC. It can clearly be seen that the lower the initial SoC, the longer the lifetime is. The round trip energy efficiency was found to be 95%, higher than the round trip energy efficiency found in paragraph 6.4.5. This is caused by two reasons: the high charging C-rate and constant voltage charging phase. The C-rate of the charging current in paragraph 6.4.5 was much higher, leading to a faster increase in polarisation voltage drop and decrease in energy efficiency. In the constant voltage charging phase the current slowly reduces, which is coupled to an increase in the long time transient resistance. The constant voltage charging phase is longer than the time constant associated with the long time transient impedance. Consequently, the maximum voltage drop occurs over the long time transient resistance, resulting in lower energy efficiency.

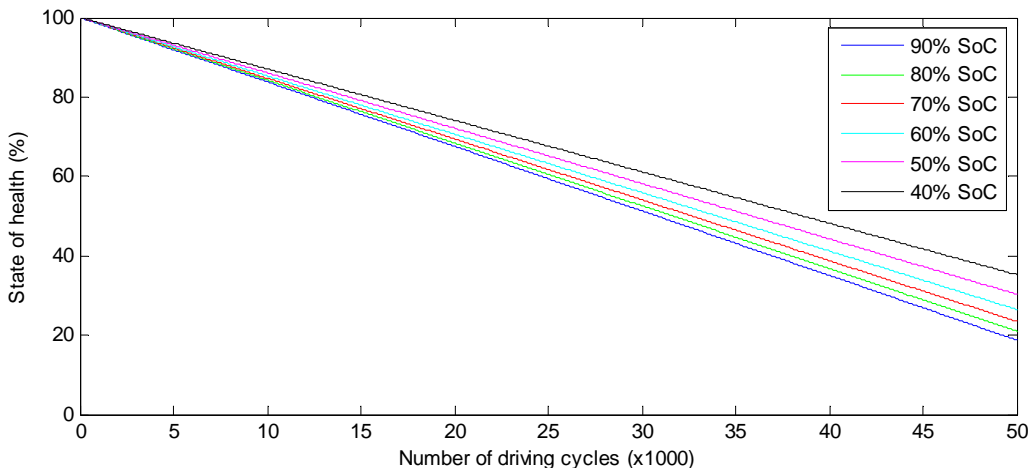


Figure 7.7: A comparison between the SoH developments for a simulated EV cell discharged with the NEDC profile from different initial SoCs.

To illustrate the effect of different ΔDoDs , the NEDC profile is repeated twice and four times before recharged. Before each NEDC repetition the cell is assumed to be rested and the temperature starts from the environment temperature. After the last NEDC profile the cell is directly recharged to the initial SoC. In a real-life situation this would correspond to a comparison between charging after every drive, only charging after a return trip and charging at home every 2 return trips. The NEDC profile is, however, not mirrored to represent the return trip and the NEDC profile is kept intact. The comparison for an initial SoC of 90%, 80%, 60% and 50% are respectively shown in figure 7.8a, b, c and d. To compare the different driving profiles, the SoH is plotted against the number of NEDCs instead of driving cycles.

From figure 7.8 the influence of a larger ΔDoD is clearly visible. At high SoC in figure 7.8a a large ΔDoD , corresponding to a large SoC_{dev} causes accelerated capacity fading. In figure 7.8b the profile the influence of a high SoC_{avg} is almost equal to the influence of a large SoC_{dev} . In figure 7.8c and d the cell cycled with a low ΔDoD actually shows the most SoH degradation, since the SoC_{avg} is higher than the cells cycled with a high ΔDoD . So at low SoCs the influence of SoC_{avg} becomes much larger than SoC_{dev} . This is under the assumption that the NEDC repetitions do not directly occur after one another.

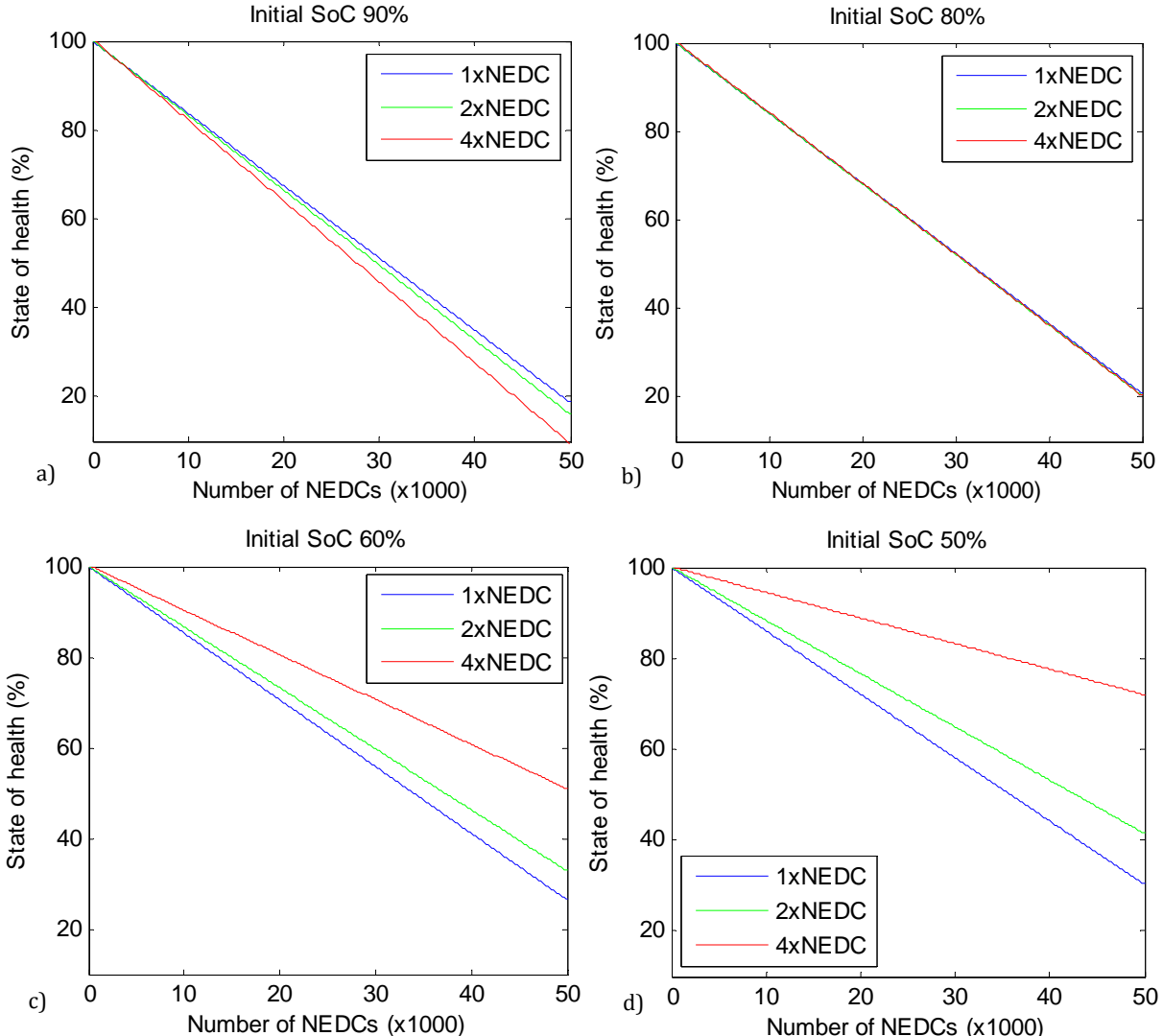


Figure 7.8: A comparison between the SoH developments for a simulated EV cell discharged with the 1 time, 2 times and 4 times the NEDC profile with sufficient rest between each NEDC repetition before a recharge to the initial SoC of a) 90%, b) 80%, c) 60% and d) 50%.

In the case that the NEDC repetitions are consecutive without resting time, the rising cell temperature will have a negative influence on the SoH of the cell as shown in figure 7.9a for an initial SoC of 90% and in figure 7.9b for an initial SoC of 60%. Figure 7.9b shows that even though the increase in temperature has a significant influence on the SoH of the cell, the SoC_{avg} is still has a stronger influence. This is caused by a simplistic and optimistic thermal model and driving profile, and in real-life situations the cell temperature will be much higher.

In the previous SoH simulations, the NEDC profile was directly followed by the charging phase. However, if the cells are rested until the temperature has sufficiently dropped, the lifetime of the

7 Lifetime optimisation of EV batteries – A case study

cells can be significantly increased. In figure 7.10 a comparison is shown between a cell charged with and without rest after driving. Furthermore, instead of normal charging, EV batteries also have the option for fast charging. For the EV in the project, the cells can be charged to 80% SoC from an empty state in less than an hour. However, fast charging will cause significant heating and SoH degradation as shown in figure 7.10. With sufficient resting time or cooling the increased SoH degradation due to fast charging can be reduced.

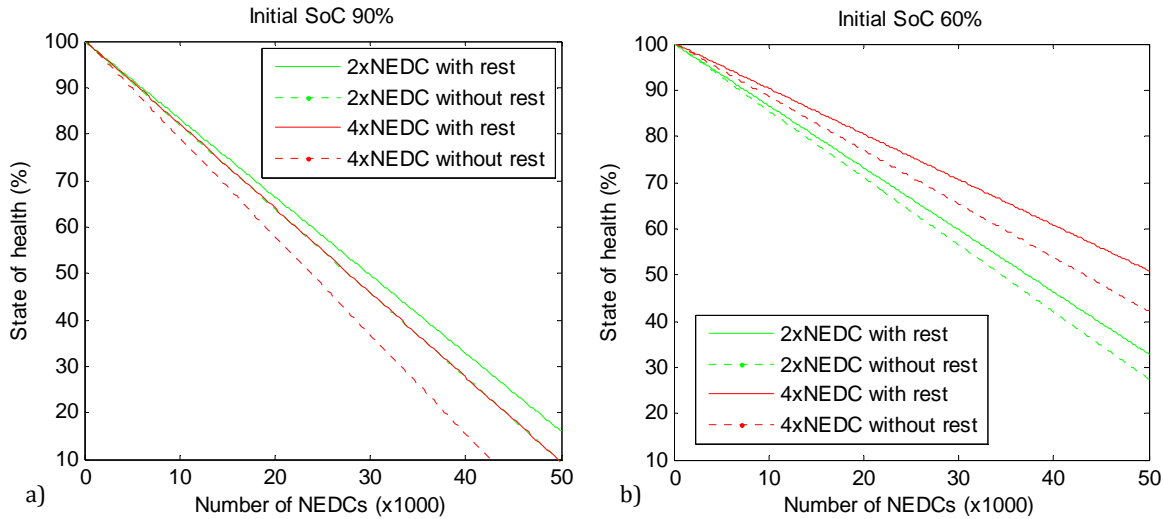


Figure 7.9: A comparison between the SoH development with and without resting periods between NEDC repetitions before a recharge for an initial SoC of a) 90% and b) 60%.

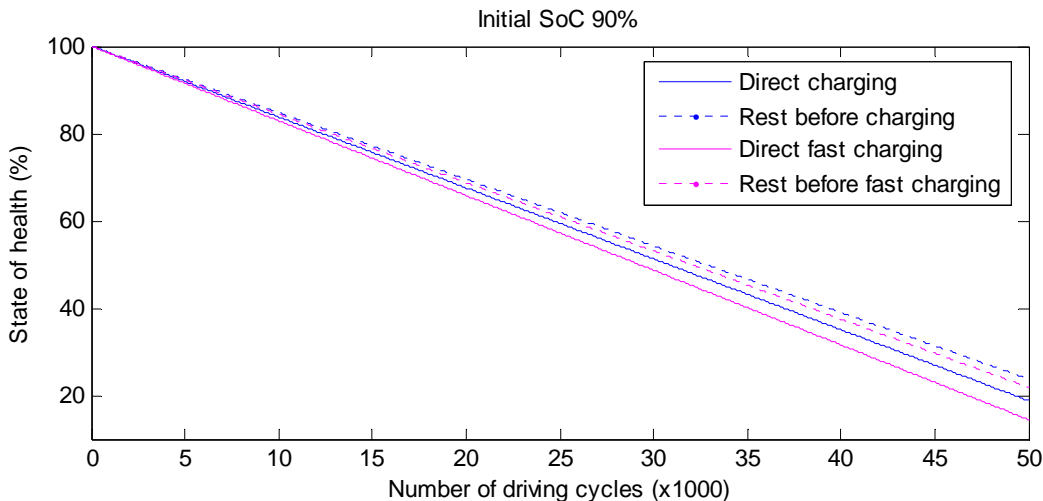


Figure 7.10: A comparison of the SoH development for a cell cycled with the NEDC rested before or directly followed by normal and fast charging.

Another method to extend the lifetime of the cells is to limit the maximum speed of the EV. A maximum speed limit of 90km/h can be simulated with the EUDC for low power vehicles instead of the normal EUDC as shown in figure 7.11. A maximum speed limit will reduce the required current, resulting in reduced heating of the cell. A comparison between the SoH development with and without a maximum speed limit is shown in figure 7.12a for 90% initial SoC and in figure 7.12b for 60% initial SoC. By limiting the speed of the EV the lifetime of the cells can be extended. Furthermore, by limiting the speed the mileage is improved from 110.64Wh/km for the NEDC to 101.14Wh/km for the NEDC with a 90km/h speed limit. However, the NEDC is a driving cycle under ideal circumstances a limited amount of speed variations, while in real-life situations the speed is constantly varying.

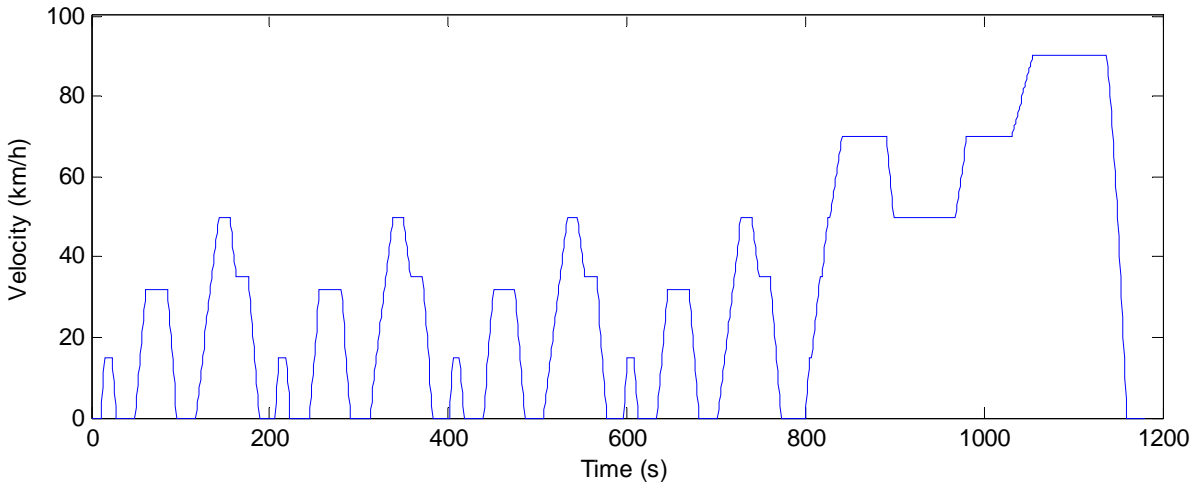


Figure 7.11: The NEDC for low power vehicles with a maximum speed limit of 90km/h [127].

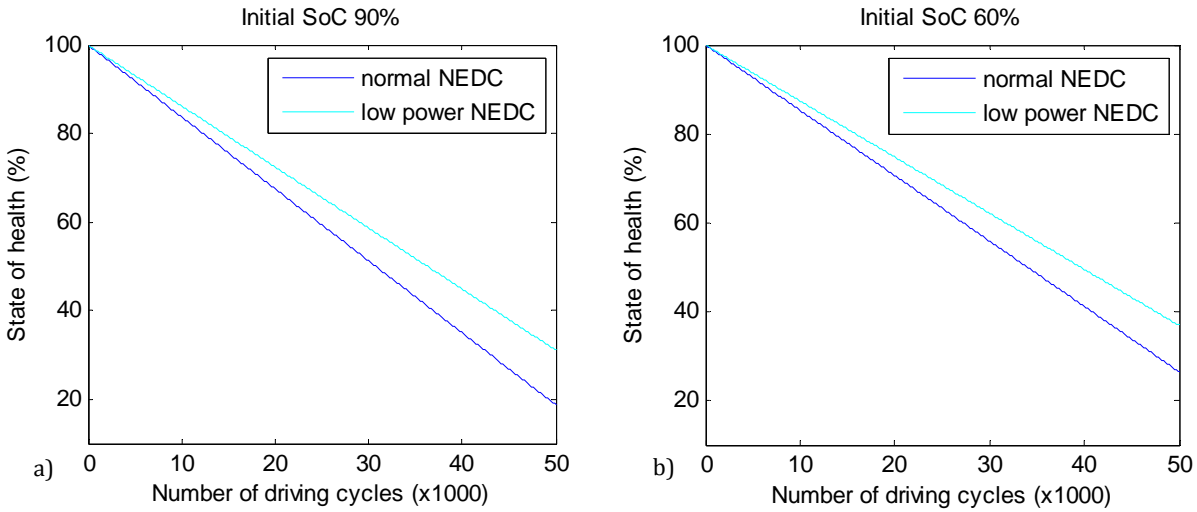


Figure 7.12: A comparison of the SoH development between cycling with the normal NEDC and the NEDC for low power vehicles with a maximum speed limit of 90km/h for a) a 90% and b) a 60% initial SoC.

7.2.3 SoH simulation with the United States Federal Test Procedure 75

The United States Federal Test Procedure (FTP-75) is a more realistic driving cycle compared to the NEDC. The FTP-75 is known as a transient driving cycle and represents a driving in an urban environment with frequent stops [127]. The FTP-75 is depicted in figure 7.13a. From the speed profile the associated C-rate profile for a single cell is calculated in the same way as in paragraph 7.2.2, which is shown in figure 7.13b. The coupled temperature profile of the FTP-75 for the cell in the simulation is given in figure 7.13c.

The main difference between the FTP-75 and NEDC is the amount of stops occurring in the driving cycle, accompanied by regenerative braking. Furthermore, the driven distance is also longer, with 11.007km compared to 17.77km. However, the FTP-75 shows a better mileage performance with 88.55Wh/km compared to 110.64Wh/km for the NEDC, and a lower temperature rise. This is caused by the fact that the FTP-75 does not include suburban driving and more regenerative braking occurs.

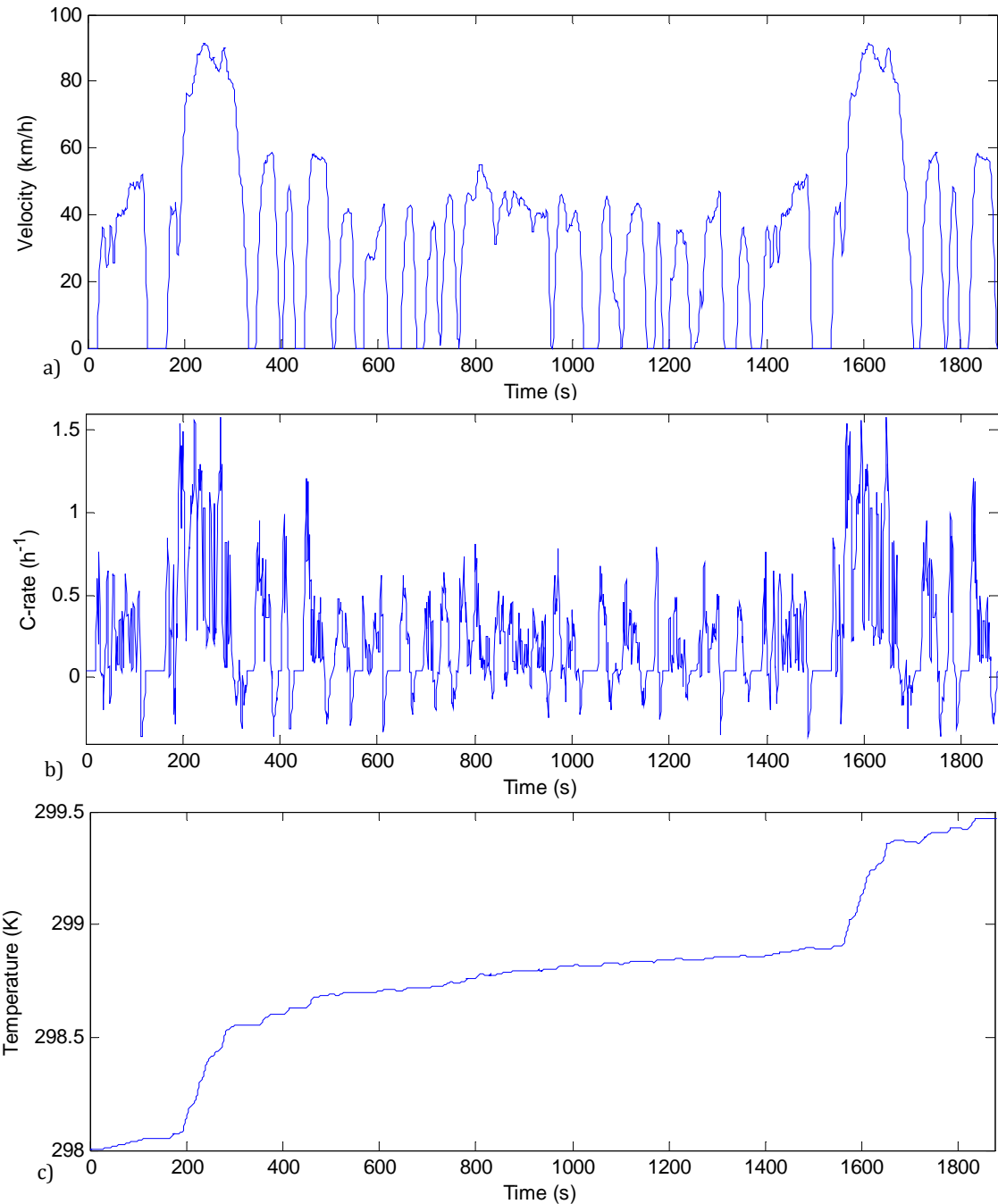


Figure 7.13: a) The FTP-75 profile [127] with b) the associated C-rate profile for the particular EV cell in the simulation and c) temperature profile determined from the thermal model in the simulation.

A similar analysis with the FTP-75 profile can be conducted as in the previous paragraph, which will result in similar results. In this paragraph only a comparison is made between different initial SoCs, as shown in figure 7.14. The FTP-75 profile shows a similar result as the NEDC profile. The only difference is the number of possible cycles before the SoH is 0%, because the FTP-75 profile consists of a longer driving distance i.e. more charge processed per cycle. The extra stops and regenerative braking does not introduce additional SoH degradation in the simulated model.

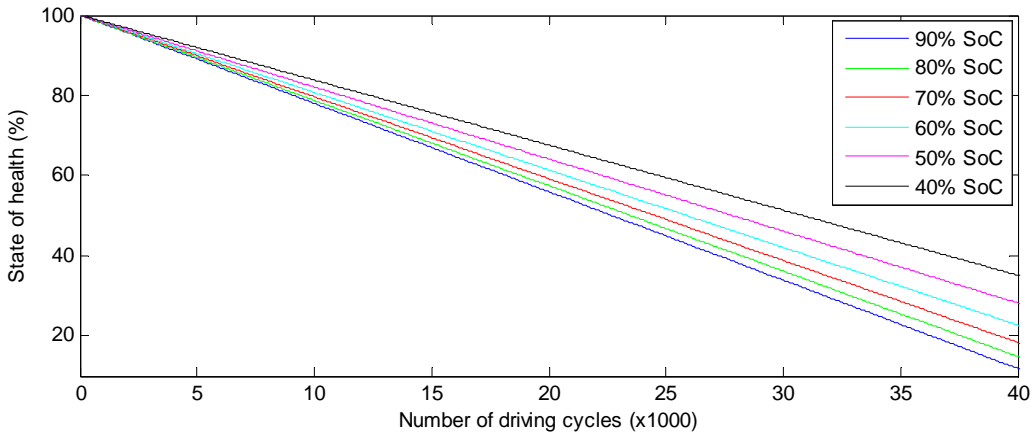


Figure 7.14: A comparison of the SoH development for a cell cycled with the FTP-75 profile from different initial SoCs.

7.2.4 SoH simulation with real driving data

Even though the FTP-75 is a more realistic driving cycle than the NEDC, the speed of the FTP-75 profile is low compared to real driving profile. To simulate a realistic driving profile, driving data obtained from the EVs in the project is used. Figure 7.15a shows a part of the C-rate profile of the EV. A noticeable difference is the higher discharge and regenerative braking current compared to the NEDC and FTP-75. This may be caused by the simplifications in calculating the C-rate requirement of the NEDC and FTP-75 or the fact that the NEDC and FTP-75 are not realistic. Furthermore, the fluctuations between discharging and regenerative braking are much more severe, which results in higher cell temperatures as shown in figure 7.15b.

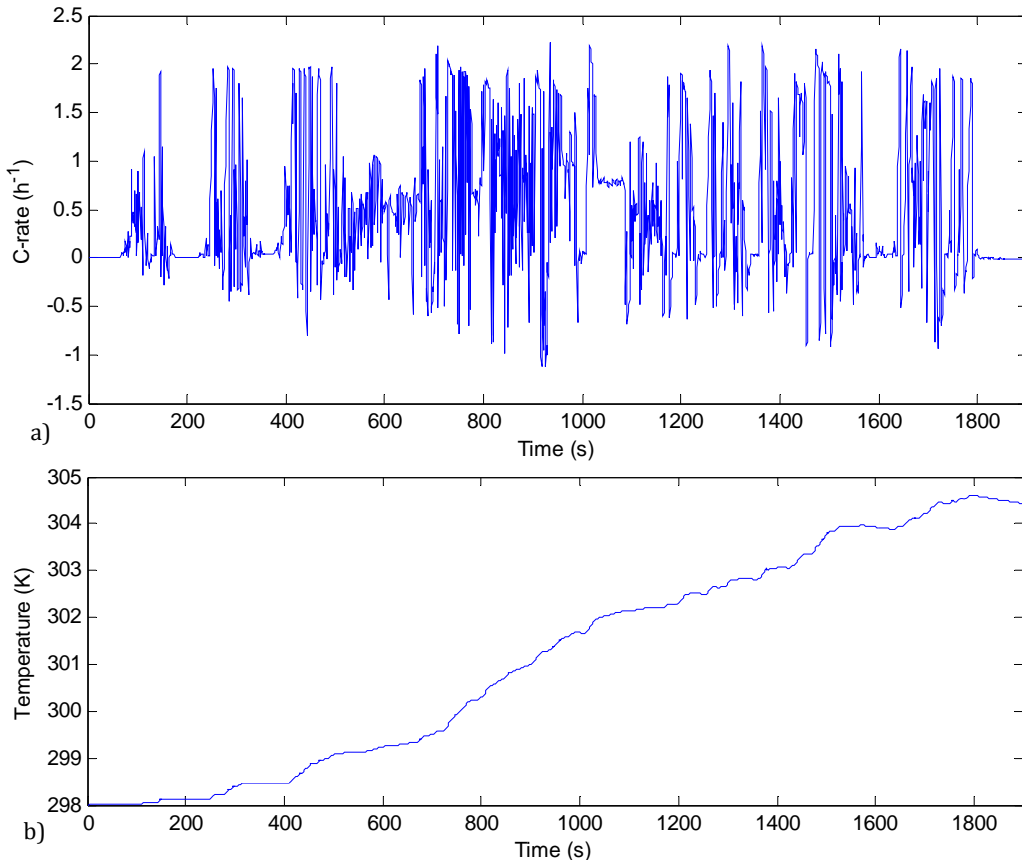


Figure 7.15: a) An example of a real C-rate profile obtained from the EV in the project and b) the coupled temperature profile obtained from the simulation with an initial SoC of 60%.

7 Lifetime optimisation of EV batteries – A case study

The ΔDoD is 26%, so the amount of Ah processed per cycle is also higher than with the other two profiles, resulting in a higher SoH degradation per driving cycle. The driven distance was, however, not registered, so a comparison between the mileage of a real driving profile and the modelled NEDC and FTP-75 cannot be made.

Heating of the cells will cause increased SoH degradation as simulated in paragraph 7.2.2. A way to reduce the heating is to implement a current limiter, which would be equivalent to an acceleration limiter. The C-rate profile in figure 7.15 is adjusted by limiting the current. To keep the total Ah processed equal, the limited current is extended in time. The SoH development with a current limitation of 2C and 1.5C is shown in figure 7.16a for 90% initial SoC and in figure 7.16b for 60% initial SoC. The coupled temperature profile per driving cycle is respectively given in figure 7.16c and figure 7.16d. A current limit of 2C does not show much different from a profile without current limit, since the C-rate rarely goes above 2C. On the other hand, a current limit of 1.5C shows a lower cell temperature, resulting in an improvement of lifetime. Lower current limits will result in an even greater lifetime, but will seriously undermine the driving experience.

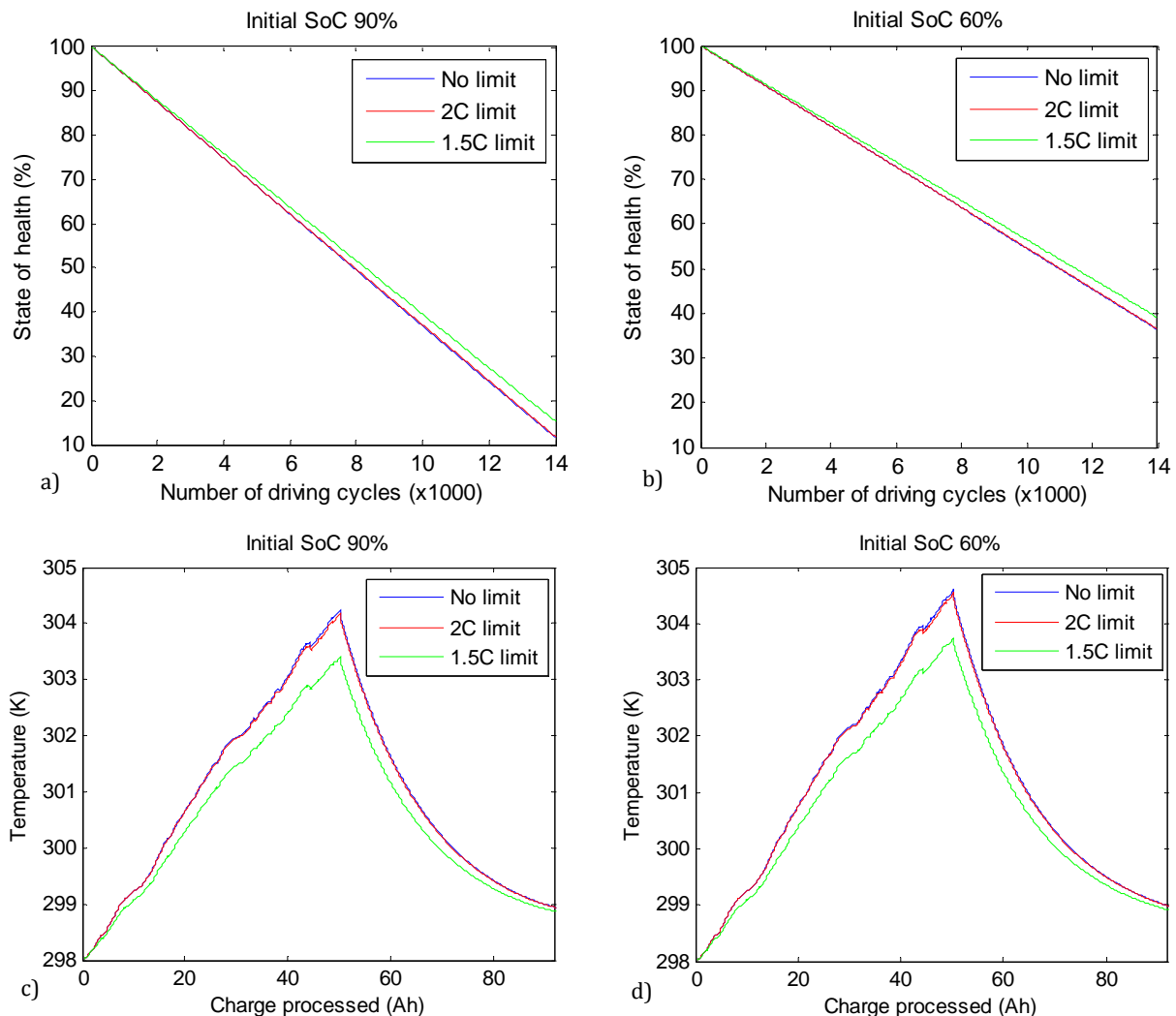


Figure 7.16: A comparison of the SoH development for a cell cycled with a real C-rate profile with different current limited for a) 90% initial SoC and b) 60% initial SoC, and the corresponding temperature profile over one driving cycle in respectively c) and d).

7.3 Recommendations

Several recommendations can be made based on the simulations with various driving profiles in regards to the lifetime optimisation of EV cells. The SoH of the cells are strongly affected by the SoC_{avg} and in a lesser degree by SoC_{dev} . This means the lower the initial SoC and the smaller the ΔDoD , the longer the lifetime of the cells will be. This is under the condition that overdischarge does not occur, so the lowest recommended SoC is 10%. Consequently, only charging the battery up to the necessary SoC to reach the destination optimises the battery lifetime.

The EV cell lifetime can be further optimised with proper thermal management of the cells. To properly quantify the effects of temperature on the cells, a sophisticated 3D-thermal model for an EV battery pack is required. With the thermal model the optimal placement and cooling of the EV battery pack can be determined.

Nevertheless, several simple solutions can also extend the lifetime of the cells by lowering the cell temperature during operation. Fast charging will rapidly heat the cells, so ideally fast charging must be avoided. Furthermore, by allowing the cells to rest before charging, the cell temperature will drop. By charging the cells at a lower temperature, the lifetime of the cells is improved. Limiting the acceleration or maximum speed will also reduce heating and nonuniform temperature distribution in the cells. This can be done by applying a less aggressive driving style or employing a current limiter.

In the previous chapter it was found at low temperatures additional SoH degradation is introduced. The low temperature SoH degradation will occur during charging, so the cells must not be rested for too long before recharged. Most recommendations mentioned above can be incorporated into a smart charger [128] and planning the required cell capacity for the upcoming trip.

In this chapter simulations showed an extreme high cycle life for the tested cells. However, the actual cycle life of the cells will be much lower. The SoH determination in this thesis only considers the true capacity fading, while the cell impedance growth has been neglected; the SoH determined with the apparent capacity will show a stronger degradation. Additionally, the nonuniform distribution of the temperature inside and on the surface of the cell has not been taken into account. Furthermore, additional issues at battery pack level will also have an impact on the lifetime of the cells. Finally, only SoH degradation due to cycling has been taken into account. However, most EVs are not driving around most of the time, so calendar SoH degradation will also have a significant influence on the battery lifetime. No conclusions can therefore be made on the actual lifetime of an EV battery pack.

The findings mentioned above are based on empirical results from LiFePO₄ cells and have not been verified for other chemistries. Furthermore, the SoH degradation equations were determined in accelerated experiments before the end of life condition had been reached. It is therefore unknown whether beyond the tested conditions and in real-life situations the cells will show similar results. Nevertheless, recommendations can be made for the lifetime optimisation of EV cells, as the factors influencing the SoH degradation will remain the same; only the degree in SoH degradation influence will change.

8 Conclusion

A practical circuit-based model for state of health (SoH) estimation of lithium ion (Li-ion) battery cells in electric vehicles (EVs) has been proposed in this thesis. From an extensive literature review it was concluded that existing models are not satisfactory for practical applications; models either require extensive background knowledge on electrochemistry and cannot be directly connected to a model of the rest of an EV system, or are too simple and cannot model all possible operating conditions in EVs. Many models for different types of Li-ion cells have been developed in literature testing various operating conditions, but it is not clear whether the models can be combined and used for other types of Li-ion cells. Furthermore, a lack of quantification of measurement results severely limits the integration of existing Li-ion cell models into the development of improved models. Therefore a model with empirical equations has been developed based on practical considerations, which can be directly connected to models of the rest of an EV system or other electrical and electronic systems.

The model consists of two parts: the energy balance circuit and the voltage response circuit. The energy balance circuit characterises the current independent useable capacity in the cell. In the model true capacity fading, the useable capacity fading at reference temperature, has been chosen as the SoH parameter. The energy balance circuit will therefore also model the SoH of the cell. Only cycling losses are modelled and calendar losses are neglected. Temperature, C-rate, the state of charge (SoC), depth of discharge (ΔDoD) and regenerative braking were found to be stress factors of the capacity fading from literature, but many stress factors have not been quantified or verified. Furthermore, cycle numbers were used to compare the capacity fading of cells discharged with different ΔDoDs , while the amount of charge or energy discharged is different for each ΔDoD . The capacity fading rate and coupled stress factors were therefore experimentally determined by testing numerous Li-ion cells of the type lithium iron phosphate (LiFePO_4), which is expected to be used in most EVs in the near future. The capacity fading rate was determined as a function of the charge processed by the cell instead of cycles, because using cycles leads to a wrong comparison between cells discharged with different ΔDoDs . From the experiments the following conclusions regarding to the capacity fading could be made:

- Capacity fading is not influenced by regenerative braking at room temperature with typical C-rates in EVs, but may be influenced by resting times.
- The discharge C-rate does not directly accelerate capacity fading, but only indirectly due to ohmic heating.
- At both high and low temperatures the capacity fading is accelerated and the cells have an optimal operating temperature range.
- At low temperatures high charging and regenerative braking C-rates increase the capacity fading.
- Both the initial SoC and the ΔDoD have an influence on the capacity fading rate. However, cells discharged from the same initial SoC with a larger ΔDoD may show less capacity fading, because the average SoC is lower. The average SoC over a predefined period was found to be a stronger influence on capacity fading than ΔDoD at low SoCs. So the lower the average SoC and the smaller the ΔDoD , the lower the capacity fading rate.
- The obtained capacity fading model is only valid for temperatures above 0°C and possibly too optimistic for temperatures between 0° and 25°C, since the capacity fading stress factors at low temperatures have not been quantified.

The findings mentioned above are obtained by assuming that the battery management system (BMS) prevents overcharge and overdischarge in the cell, and that the cell operates within its specifications. A complete overview of the energy balance circuit is given in appendix A.2 and the determined parameter values in appendix B.

Modelling of the voltage response circuit was conducted in the same way as the energy balance circuit. From literature the optimal circuit model was found to be a dependent voltage source representing the open-circuit voltage (OCV) and a resistance in series with two parallel RC pairs, describing the short and long time transient, as the internal cell impedance. Each circuit component consists of nonlinear equations dependent on the temperature, SoC, C-rate and ageing. Various equations of different complexities have been proposed in literature for different Li-ion cell types mainly describing the SoC dependence. Other influences on the voltage response circuit components have been neglected or wrongly been incorporated into the cell capacity model. Furthermore, most existing models can only model the discharge behaviour of the cell, and the charging behaviour is assumed to be modelled with the same equations. To investigate and model the various influences on the voltage response circuit components, empirical equations for the circuit components are extracted from the same LiFePO₄ cells used to obtain the energy balance circuit model. Based on the experiments, the following conclusions can be drawn for the voltage response circuit:

- The OCV is modelled as independent of hysteresis and the temperature has a negligible influence.
- The internal cell impedance has to be modelled with different equations for discharging and charging.
- Only the long time transient resistance is dependent on the C-rate and decreases with higher C-rates.
- Every internal cell impedance element is dependent on temperature and modelled with different equations for high and low temperature.
- Influence of ageing on the internal cell impedance can be modelled by solely the ohmic resistance, and the influence is the same for discharging and charging. However, the cycled cells did not show a trend and could therefore not be modelled. A possible cause is the influence of regenerative braking, as the cells cycled without regenerative braking did show a rising trend in the ohmic resistance.

An overview of the voltage response circuit is given in appendix A.2 and the parameter values in appendix B. The simulation results of the model have been compared to the measurements. At reference temperature 25°C and 1C the maximum error is 12mV in the range between 90% and 10% SoC. The expectation is that EVs will not be fully charged to 100% to extend the cell lifetime and prevent overcharge, or discharged lower than 10% SoC due to the fear of running out of energy. At different temperatures and C-rate the maximum error goes up to 14mV, which is 1.3% of the total operating voltage range. Higher accuracy can be obtained by modelling the voltage response circuit with more parallel RC pairs or additional empirical equations. This would, however, require additional data analysis or experiments and severely increase the complexity of the model. On the other hand, the model can be simplified by neglecting the C-rate or temperature effect. Hence, the model can be easily adjusted according to the desired accuracy and complexity. The choice lies with the EV system designer which influences to include as a trade-off between accuracy and complexity.

8 Conclusion

The proposed model is a generic model. LiFePO₄ cells of the same manufacturer will follow the modelled behaviour, but due to manufacturing differences the values of the circuit components in the model may vary slightly for cells from different batches. LiFePO₄ cells of other manufacturers are expected to follow a similar behaviour as described by the proposed empirical equations. However, the parameters of the empirical equations will be different, as materials with different impurities and different manufacturing processes are employed. With one test cycle, the parameters in the voltage response circuit can be extracted. The behaviour of the energy balance circuit including capacity fading is expected to be similar for all LiFePO₄ cells.

For other Li-ion types the OCV will be different and has to be determined experimentally. The internal cell impedance is expected to have a comparable behaviour as that of LiFePO₄ cells, but it may not be possible to model the internal impedance with the same empirical equations. With a test cycle, equations for the voltage response circuit can be extracted. The energy balance circuit may exhibit a different behaviour, as the capacity fading is strongly dependent on cathode and anode material. For certain types of anodes, at low temperatures the recharge C-rate will not accelerate capacity fading. Also the influence of the average SoC and SoC deviation will be different for different Li-ion types; some types may even show accelerated capacity fading if the average SoC is too low or the SoC deviation influence is much stronger than the average SoC. So only for LiFePO₄ cells it is confirmed that cycling with a low average SoC results in low capacity fading. With experiments similar to the ones in this work, the effect of the average SoC can be determined for other Li-ion cell types. The validity of the proposed model in this work can be confirmed for other Li-ion cell types.

8.1 Recommendations for EV battery cell life optimisation

With the proposed model simulations with the New European Driving Cycle, the Federal Test Procedure 75 and a driving profile obtained from an actual EV have been conducted. Based on the simulations it was found that a smart charger would significantly increase the lifetime of EV cells. By only charging the EV cells at the optimal temperature and limiting temperature rise in the cells, the lifetime of the cells can be extended. The lifetime can be further extended by keeping the SoC as low as possible and only charging enough capacity until the next charging point; the battery lifetime is optimised when the average SoC and ΔDoD are as low as possible. This is under the condition that overdischarge does not occur.

During operation several measures can also be taken to extend the cell lifetime. Regenerative braking at low temperatures will cause accelerated capacity fading. So until the battery has been heated to a certain temperature by usage, charging by regenerative braking should be avoided and the regenerative braking energy can be used to uniformly heat the cells. When the cells reach the optimal temperature, battery heating should be avoided by proper thermal management and cooling. By limiting the acceleration and speed of the vehicle, i.e. the discharge current, the temperature rise and nonuniform temperature distribution will be less severe and the lifetime of the EV battery cells is extended.

The proposed model provides more insight into the SoH development of EV batteries, so that EV lease companies do not have to be depreciated the EVs according to the worst case scenario; this will lead to a lower EV lease price. Based on the recommendations for battery lifetime optimisation, the lease price can be determined by logging the treatment of the battery. With the proposed model and an improved thermal model, the SoH development for different driving behaviours can be predicted while driving. Live feedback about the lease price with the current driving behaviour and suggestions to minimise the lease price can then be provided to the driver.

8.2 Future work

Battery modelling has only recently been in the spotlights again due to the rise of hybrid electric vehicles (HEVs) and battery electric vehicles (BEVs). Much is still unknown about the long term behaviour of EV batteries in real-life situations and a lot of possibilities for future work are present. Existing models are obtained from many experiments with small Li-ion cells, and validity of the models has to be confirmed for large automotive cells.

Improvements and expansion of the proposed model in this thesis can be made. The capacity fading model is not valid for temperatures below 0°C, because accelerated capacity fading was found to occur at low temperatures with due to the C-rate of regenerative braking and charging. This effect is dependent on the recharge C-rate and temperature; the lower the temperature, the more severe the capacity fading is due the charging C-rate. Furthermore, between 0°C and 25°C the model might be too optimistic, especially close to 0°C. Above 25°C the recharge C-rate was found to have no influence on capacity fading for typical EV C-rates. This means that between 0°C and 25°C an optimum temperature exist for minimum capacity fading with regenerative braking. Above this temperature the model in this thesis is accurate, and below this temperature somewhat optimistic. More experiments are necessary to model the charging C-rate effect at low temperatures and determine the optimum charging temperature.

The capacity fading rate was also found to be possibly related to the frequency and duration of resting periods, and more experiments are required to confirm this effect. Additionally, more cycle life experiments are needed with different initial SoCs and ΔDoDs improve the capacity fading model. The capacity fading results obtained were all based on usage of the cells, and calendar losses has not been considered. However, most of the time an EV is not being driven, and calendar losses cannot be simply ignored. More investigation is required on the correlation between calendar and cycling losses of the capacity.

The empirical equations of the internal cell impedance are determined with a unidirectional current; the validity of the equations has to be confirmed for changing current directions in a dynamic profile. The correlation between empirical equations modelling the temperature and C-rate dependence of the internal cell impedance has not been investigated either. Furthermore, the ohmic resistance was found to be varying with cycling of the cells. Unfortunately, the variations did not show a trend and the resistance rise could not be modelled. Additional experiments are required to investigate whether the variations are caused by regenerative braking and to model the ageing dependence of the ohmic resistance with various stress factors.

The parameters for the proposed model are obtained from laboratory experiments. Since the proposed model is based on voltage measurements in the time domain and practical considerations, the parameters of the model can also be extracted from measurement data in operating EVs by applying various algorithms which are still in development for EVs [106][129].

Finally, there are many research possibilities on pack level. Little research has been conducted on pack level for EVs, since testing such high power and high capacity battery packs require expensive testing equipment. Large EV battery packs introduce additional issues in the SoH modelling due to effects of cell imbalance. The SoH of an EV battery pack is also greatly influenced by the thermal management of the cells, and the thermal management can be improved with a sophisticated 3D-thermal model on pack level modelling the nonuniformity of the cell temperature and the heating influence of neighbouring cells. Hence, a lot of work is still required in battery modelling to characterise and accurately predict the SoH of EV batteries.

References

- [1] HSBC; N. Robins, C. Singh, R. Clover, Z. Knight, and J. Magness, "Sizing the climate economy," *HSBC Global Research*, Global climate change, September 2010.
- [2] PikeReserach, "Electric Vehicle Batteries", retrieved 22 July 2011.
<http://www.pikeresearch.com/research/electric-vehicle-batteries>
- [3] A. Millner, "Modeling Lithium Ion battery degradation in electric vehicles," *IEEE Conf. CITRES*, pp. 349-356, 2010.
- [4] V. Marano, S. Onori, Y. Guezennec, G. Rizzoni, and N. Madella, "Lithium-ion batteries life estimation for plug-in hybrid electric vehicles," *IEEE Conf. VPPC*, pp. 536-543, 2009.
- [5] M. Shnayerson, "The Car That Could. The Inside Story of GM's Revolutionary Electric Vehicle," Random House, chapter 2, 1996.
- [6] F.R. Kalhammer, B.M. Kopf, D.H. Swan, V.P. Roan, and M.P. Walsh, "Status and prospects for zero emissions vehicle technology," *Report of the ARB Independent Expert Panel*, 2007.
- [7] A. Vezzini, "Lithium Ion battery system and their application", *Pres. Fachtag energie Bern*, June 2009.
- [8] Electropaedia, "Cell chemistry comparison chart", retrieved 23 July 2011.
<http://www.mpoweruk.com/specifications/comparisons.pdf>
- [9] N. Kularatna, "Modern batteries and their management," *IECON 2010*, pp. 1-103, 2010.
- [10] G.A. Nazri and G. Pistaioie, "Li-Ion Batteries for EV, HEV and Other Industrial Applications," *Lithium Batteries, Science and Technology*, Kluwer Academic Publishers, chapter 21, 2004.
- [11] M. Dubarry, V. Svoboda, R. Hwu, and B.Y. Liaw, 'Capacity loss in rechargeable lithium cells during cycle life testing: The importance of determining state-of-charge,' *J. Power Sources*, vol. 174, no. 2, pp. 1121-1125, 2007.
- [12] Idaho National Laboratory, "Battery Test Manual for Plug-In Hybrid Electric Vehicles," September 2010.
- [13] L. Serrao, Z. Chehab, Y. Guezenne, and G. Rizzoni, "An aging model of Ni-MH batteries for hybrid electric vehicles," *IEEE Conf. VPPC*, pp. 78-85, 2005.
- [14] M. Dubarry and B.Y. Liaw, "Identify capacity fading mechanisms in a commercial LiFePO₄ cell," *J. Power Sources*, vol. 194, no. 1, pp. 541-549, 2009.
- [15] W. Tahil, "How much lithium does a LiIon EV battery really need?" Meridian International Research, March 2010.
- [16] V.V. Viswanathan, D. Choi, D. Wang, W. Xu, S. Towne, R.E. Williford, J.G. Zhang, J. Liu, and Z. Yang, "Effect of entropy change of lithium intercalation in cathodes and anodes on Li-ion battery thermal management," *J. Power Sources*, vol. 195, no. 11, pp. 3720-3729, 2010.
- [17] H.G. Schweiger, O. Obeidi, O. Komesker, A. Raschke, M. Schiemann, C. Zehner, M. Gehnen, M. Keller, and P. Birke, "Comparison of Several Methods for Determining the Internal Resistance of Lithium Ion Cells," *Sensors*, vol. 10, no. 6, pp. 5604-5625, 2010.

- [18] V. Pop, H.J. Bergveld, P.H.L. van Notten, and P.P.L. Regtien, "State-of-the-art of battery state-of-charge determination," *Meas. Science and Technology*, vol. 16, no. 12, pp. R93-R110, 2005.
- [19] W. Fang, O.J. Kwon, and C.Y. Wang. "Electrochemical-thermal modeling of automotive Li-ion batteries and experimental validation using a three-electrode cell", *Int. J. Energy Res.* vol. 34, pp. 107-115, 2010.
- [20] P. Arora and Z. Zhang, "Battery Separators", *Chem. Rev.*, vol. 104, pp. 4419-4468, 2004.
- [21] The Boston Consulting Group; A. Dinger, R. Martin, X. Mosquet, M. Rabl, D. Rizoulis, M. Russo, and G. Sticher, "Batteries for Electric Cars," January 2010.
- [22] Battery University, "Types of Lithium-ion", retrieved 23 July 2011.
http://batteryuniversity.com/learn/article/types_of_lithium_ion
- [23] Tesla Motors, "Roadster Innovations/Battery", retrieved 23 July 2011.
<http://www.teslamotors.com/roadster/technology/battery>
- [24] M. Wohlfahrt-Mehrens, P. Axmann, and Mario Wachtler, "Electrochemical energy storage systems for car applications," *Pres. HySA Systems Business Seminar*, November 2009.
- [25] Deutsche Bank; R. Lache, P. Nolan, D. Galves, G. Toulemonde, J. Gehrke, K. Sanger, V. ha, S. Rao, and J. Crane, "Electric Cars: Plugged In. Batteries must be included," June 2008.
- [26] J. McDowall, "Understanding lithium-ion technology," *Proc. of Battcon*, 2008 .
- [27] IT Times; J.H. Bang, "LG Chem's lithium polymer battery sweeps the EV market," retrieved 23 July 2011. <http://www.koreaittimes.com/story/7514/lg-chems-lithium-polymer-battery-sweeps-ev-market>
- [28] BMWBlog; H. Boeriu, "Lessons learned after 150,000 kilometers with the MINI E pilot," retrieved 20 August 2010. <http://www.bmwblog.com/2010/08/19/lessons-learned-after-150000-kilometers-with-the-mini-e-pilot/>
- [29] Next Green Car, "i-MiEV performs well in first UK trial," retrieved 20 June 2010.
<http://www.nextgreencar.com/news-item.php?iMiEV-performs-well-in-first-UK-trial>
- [30] R. Spotnitz, "Simulation of capacity fade in lithium-ion batteries," *J. Power Sources*, vol. 113, no. 1, pp. 72-80, 2003.
- [31] Q. Zhang and R.E. White. "Capacity fade analysis of a lithium ion cell", *J. Power Sources* vol. 179, no. 2, pp. 793-798, 2008.
- [32] Electropaedia, "Cell Chemistries", retrieved 29 January 2011.
<http://www.mpoweruk.com/chemistries.htm>
- [33] K. Edström, T. Gustafsson, and J.O. Thomas, 'The cathode-electrolyte interface in the Li-ion battery", *Electrochim. Acta*, vol. 50, no. 2-3, pp. 397-403, 2004.
- [34] X.H. Rui, Y. Jin. X.Y. Feng, L.C. Zhang, and C.H. Chen, "A comparative study on the low-temperature performance of LiFePO₄/C and Li₃V₂(PO₄)₃/C cathodes for lithium-ion batteries," *J. Power Sources*, vol. 196, no. 4, pp. 2109-2114, 2011.
- [35] D. Zane, M. Carewska, S. Scaccia, F. Cardellini, and P.P. Prosini, "Factor affecting rate performance of undoped LiFePO₄", *Electrochim. Acta*, vol. 49, no. 25, pp. 4259-4271, 2004.

References

- [36] K.F. Hsu, S.Y. Tsay and B.J. Hwang, "Synthesis and characterization of nano-sized LiFePO₄ cathode materials prepared by a citric acid-based sol-gel route", *J. Mater. Chem.*, no. 14, pp. 2690-2695, 2004.
- [37] P.P. Prosini, M. Carewska, S. Scaccia, P. Wisniewski, and M. Pasquali, "Long-term cyclability of nanostructured LiFePO₄," *Electrochim. Acta*, vol. 48, no. 28, pp. 4205-4211, 2003.
- [38] Y. Xia, M. Yoshio, and H. Noguchi, "Improved electrochemical performance of LiFePO₄ by increasing its specific surface area", *Electrochim. Acta*, vol. 52, no. 1, pp. 240-245, 2006.
- [39] W.J. Zhang, "Structure and performance of LiFePO₄ cathode materials: A review", *J. Power Sources*, vol. 196, no. 6, pp. 2962-2970, 2011.
- [40] S.B. Peterson, J. Apt, and J.F. Whitacre, "Lithium-ion battery cell degradation resulting from realistic vehicle and vehicle-to-grid utilization," *J. Power Sources*, vol. 195, no. 8, pp. 2385-2392, 2010.
- [41] Electropaedia, "Lithium Battery Failures," retrieved 2 February 2011.
http://www.mpoweruk.com/lithium_failures.htm
- [42] K. Anime, J. Liu, and I. Belharouak, "High-temperature storage and cycling of C-LiFePO₄/graphite Li-ion cells," *Electrochim. Com.*, vol. 7, no. 7, pp. 669-673, 2005.
- [43] J. Vetter, P. Novák, M.R. Wagner, C. Veit, K.C. Möller, J.O. Besenhard, M. Winter, M. Wohlfahrt-Mehrens, C. Vogler, and A. Hammouche, "Ageing mechanisms in lithium-ion batteries," *J. Power Sources*, vol. 147, no. 1-2, pp. 269-281, 2005.
- [44] J. Shim, R. Kostecki, T. Richardson, X. Song, and K.A. Striebel, "Electrochemical analysis for cycle performance and capacity fading of a lithium-ion battery cycled at elevated temperature", *J. Power Sources*, vol. 112, no. 1, pp. 222-230, 2002.
- [45] C. Forgez, D.V. Do, G. Friedrich, M. Morcrette, and C. Delacourt, "Thermal modeling of a cylindrical LiFePO₄/graphite lithium-ion battery", *J. Power Sources*, vol. 195, no. 9, pp. 2961-2968, 2010.
- [46] M.C. Smart, B.V. Ratnakumar, L. Whitcanack, K. Chin, M. Rodriguez, and S. Surampudi, "Performance Characteristics of Lithium Ion Cells at Low Temperatures", *IEEE Mag. AES*, vol. 17, no. 12, pp. 16-20, 2002.
- [47] T.D. Tran, J.H. Feikert, and R.W. Pekala, "Rate effect on lithium-ion graphite electrode performance", *J. Appl. Electrochem.* vol. 26, no. 11, pp. 1161-1167, 1996.
- [48] R. Rao, S. Vrudhula, and D. N. Rakhmatov, "Battery modeling for energy-aware system design," *Computer*, vol. 36, no. 12, pp. 77-87, Dec. 2003.
- [49] Thunder Sky (Winston Battery) datasheet TS-LFP160AHA.
- [50] S.S. Zhang, K. Xu, and T.R. Jow, "Study of the charging process of a LiCoO₂-based Li-ion battery," *J. Power Sources*, vol. 160, no. 2, pp. 1349-1354, 2006.
- [51] M. Broussely, "Aging mechanisms and calendar-life predictions in lithium-ion batteries," *Adv. in Li-ion batteries*, pp. 293-432, 2002.

- [52] S.S. Choi and H.S. Lim, "Factors that affect cycle-life and possible degradation mechanisms of a Li-ion cell based on LiCoO₂," *J. Power Sources*, vol. 111, no. 1, pp. 130-136, 2002.
- [53] P. Arora, R.E. White, and M. Doyle, "Capacity Fade Mechanisms and Side Reactions in Lithium-Ion Batteries," *J. Electrochem. Soc.*, vol. 145, no. 10, pp. 3647-3666, 1998.
- [54] H. Maleki and J.N. Howard, "Effects of Overdischarge on performance and thermal stability of a Li-ion cell," *J. Power Sources*, vol. 160, no. 2, pp. 1395-1402, 2006.
- [55] J.W. Braithwaite, A. Gonzales, G. Nagasubramanian, S.J. Lucero, D.E. Peebles, J.A. Ohlhausen, and W.R. Cieslak, "Corrosion of Lithium-Ion Battery Current Collectors," *J. Electrochem. Soc.*, vol. 146, no. 2, pp. 448-456, 1999.
- [56] C. Kishiyama, M. Nagata, T. Piao, J. Dodd, P. Lam, and H. Tsukamoto, "Improvement of Deep Discharge Capability for Lithium Ion Batteries," *Proc. Electrochem. Soc.*, vol. 28, pp. 252-259, 2004.
- [57] Electropaedia, "Battery Life (and Death)," retrieved 6 February 2011.
<http://www.mpoweruk.com/life.htm>
- [58] M. Broussely, Ph. Biensan, F. Bonhomme, Ph. Blanchard, S. Herreyre, K. Nechev, and R.J. Staniewicz, "Main aging mechanisms in Li ion batteries," *J. Power Sources*, vol. 146, no. 1-2, pp. 90-96, 2005.
- [59] Battery University; I. Buchmann, "How to store batteries," retrieved 1 February 2011.
<http://batteryuniversity.com/partone-19.htm>
- [60] P. Ramadass, B. Haran, R. White, and B.N. Popov, "Mathematical modelling of the capacity fade of Li-ion cells," *J. Power Sources*, vol. 123, no. 2, pp. 230-240, 2003.
- [61] H.J. Ploehn, P. Ramadass, and R.E. White, "Solvent diffusion model for aging of lithium-ion battery cells," *J. Electrochem. Soc.*, vol. 151, no. 3, pp. A456-A462, 2004.
- [62] I. Bloom, B.W. Cole, J.J. Sohn, S.A. Jones, E.G. Plozin, V.S. Battaglia, G.L. Henriksen, C. Motloch, R. Richardson, T. Unkelhaeuser, D. Ingersoll, and H.L. Case, "An accelerated calendar and cycle life study of Li-ion cells," *J. Power Sources*, vol. 101, no. 2, pp. 238-247, 2001.
- [63] B.Y. Liaw, E.P. Roth, R.G. Jungst, G. Nagasubramanian, H.L. Case, and D.H. Doughty, "Correlation of Arrhenius behaviours in power and capacity fades with cell impedance and heat generation in cylindrical lithium-ion cells," *J. Power Sources*, vol. 119-121, pp. 874-886, 2003.
- [64] P. Rong and M. Pedram, "An analytical model for predicting the remaining battery capacity of lithium-ion batteries," *Trans. IEEE VLSI*, vol. 14, no. 5, pp. 441-451, 2006.
- [65] Y. Zhang and C.Y. Wang, "Cycle-Life Characterization of Automotive Lithium-Ion Batteries with LiNiO₂ Cathode," *J. Electrochem. Soc.*, vol. 156, no. 7, pp. A527-A535, 2009.
- [66] T. Guena and P. Leblanc, "How Depth of Discharge Affects the Cycle Life of Lithium-Metal-Polymer Batteries," *IEEE INTELEC*, pp.1-8, 2006.
- [67] K. Smith, G.H. Kim, and A. Pesaran, "Modeling of nonuniform degradation in large-format Li-ion batteries," *Pres. Electrochem. Soc. Meeting*, May 2009.

References

- [68] D. Doerffel, "Testing and Characterisation of Large High-Energy Lithium-Ion Batteries for Electric and Hybrid Electric Vehicles," University of Southampton, Faculty of Engineering, Science and Mathematics, PhD thesis, 2007.
- [69] F.P. Tredeau and Z.M. Salameh, "Evaluation of Lithium iron phosphate batteries for electric vehicles application," *IEEE VPPC*, pp. 1266-1270, 2009.
- [70] S. Santhanagopalan, Q. Zhang, K. Kumaresan, and R.E. White, "Parameter estimation and life modelling of lithium-ion cells," *J. Electrochem. Soc.*, vol. 155, no. 4, pp. A345-A353, 2008.
- [71] L.H. Thaller and H.S. Lim, "A prediction model of the depth-of-discharge effect on the cycle life of a storage cell," *IECEC*, August 1987.
- [72] S. Drouilhet and B.L. Johnson, "A battery life prediction method for hybrid power applications," *Proc. AIAA*, 1997.
- [73] C. Rosenkranz, "Plug In Hybrid Batteries", *Pres EVS20*, p. 14, November 2003.
- [74] G. Ning and B.N. Popov, "Cycle life modeling of lithium-ion batteries," *J. Electrochem. Soc.*, vol. 151, no. 10, pp. A1584-A1591, 2004.
- [75] S.N. Zhurkov, "Kinetic concept of the strength of solids," *Int. J. Fracture*, vol. 26, pp. 295-307, 1984.
- [76] M. Safari, M. Morcrette, A. Teyssot, and C. Delacourt, "Life-prediction methods for lithium-ion batteries derived from a fatigue approach, I. Introduction: capacity-loss prediction based on damage accumulation," *J. Electrochem. Soc.*, vol. 157, no. 6, pp. A713-A720, 2010.
- [77] M. Safari, M. Morcrette, A. Teyssot, and C. Delacourt, "Life-prediction methods for lithium-ion batteries derived from a fatigue approach, II. capacity-loss prediction of batteries subjected to complex current profiles," *J. Electrochem. Soc.*, vol. 157, no. 7, pp. A892-A898, 2010.
- [78] M.T. Todinov, "Necessary and sufficient condition for additivity in the sense of the Palmgren-Miner rule," *Comp. Mater. Science*, vol. 21, no. 1, pp. 101-110, 2001.
- [79] E.V. Thomas, H.L. Case, D.H. Doughty, R.G. Jungst, G. Nagasubramanian, and E.P. Roth, "Accelerated power degradation of Li-ion cells," *J. Power Sources*, vol. 124, no. 1, pp. 254-260, 2003.
- [80] R.L. Hartmann II, "An aging model for lithium-ion cells," University of Akron, Phd thesis, 2008.
- [81] K. Li, J. Wu, Y. Jiang, Z. Hassan, Q. Lv, L. Shang, and D. Maksimovic, "Large-scale battery system modeling and analysis for emerging electric-drive vehicles," *ACM/IEEE ISLPED*, pp. 277-282, 2010.
- [82] P.L. Moss, "Study of capacity fade of lithium-ion polymer battery with continuous cycling & power performance modelling of energy storage devices," Florida State University, Department of Electrical and Computer Engineering, PhD thesis, 2008.
- [83] D.P. Abraham, E.M. Reynolds, P.L. Schultz, A.N. Jansen, and D.W. Dees, "Temperature dependence of capacity and impedance data from fresh and aged high-power lithium-ion cells," *J. Electrochem. Soc.*, vol. 153, no. 8, pp. A1610-A1616, 2006.

- [84] P. Suresh, A.K. Shukla, and N. Munichandraiah, "Temperature dependence studies of a.c. impedance of lithium-ion cells," *J. Appl. Electrochem.*, vol. 32, no. 3, pp. 267-273, 2002.
- [85] S.S. Zhang, K. Xu, and T.R. Jow, "The low temperature performance of Li-ion batteries," *J. Power Sources*, vol. 115, no. 1, pp. 139-140, 2003.
- [86] S.S. Zhang, K. Xu, and T.R. Jow, "Charge and discharge characteristics of a commercial LiCoO₂-based 18650 Li-ion battery," *J. Power Sources*, vol. 160, no. 2, pp. 1403-1409, 2006.
- [87] B.Y. Liaw, R.G. Jungst, G. Nagasubramanian, H.L. Case, and D.H. Doughty, "Modeling capacity fade in lithium-ion cells," *J. Power Sources*, vol. 140, no. 1, pp. 157-161, 2005.
- [88] D. Haifeng, W. Xuezhe, and S. Zechang, "A new SOH prediction concept for the power lithium-ion battery used on HEVs," *IEEE VPPC*, pp. 1649-1653, 2009.
- [89] Y. Hu, S. Yurkovich, Y. Guezennec, and B.J. Yurkovich, "Electro-thermal battery model identification for automotive applications," *J. Power Sources*, vol. 196, no. 1, pp. 449-457, 2011.
- [90] R. Benger, H. Wenzl, H.P. Beck, M. Jiang, D. Ohms, and G. Schaedlich, "Electrochemical and thermal modelling of lithium-ion cells for use in HEV or EV application," *J. World EV, EVS24*, vol. 3, pp. 1-10, 2009.
- [91] M. Chen and G.A. Rincón-Mora, "Accurate Electrical Battery Model Capable of Predicting Runtime and I-V Performance," *IEEE Trans. on Energy Conv.*, vol. 21, no. 2, pp. 504-511, 2006.
- [92] J. Zhang, S. Ci, H. Sharif, and M. Alahmad, "An Enhanced Circuit-Based Model for Single-Cell Battery," *APEC*, pp. 672-675, 2010.
- [93] D. Rakhmatov, S. Vrudhula, D.A. Wallach, "Battery lifetime prediction for energy-aware computing," *Proc. ISLPED*, pp. 154-159, 2002.
- [94] O. Erdinc, B. Vural, and M. Uzunoglu, "A dynamic lithium-ion battery model considering the effects of temperature and capacity fading," *Int. Conf. on Clean Electrical Power*, pp. 383-386, 2009.
- [95] L. Gao, S. Liu, and R.A. Dougal, "Dynamic lithium-ion battery model for system simulation," *Components and Packaging Technologies, IEEE Trans. on*, vol.25, no.3, pp. 495- 505, 2002.
- [96] H.L. Chan and D. Sutanto, "A new battery model for use with battery energy storage systems and electric vehicles power systems," *IEEE Power Eng. Soc. Winter Meeting*, vol.1, pp.470-475, 2000.
- [97] S. Mischie and D. Stoiciu, "A new and improved model of a lead acid battery" *J. FACTA UNIVERSITATIS*, vol. 20, no. 2, pp. 187-202, 2007.
- [98] R.C. Kroese and P.T. Krein, "Electrical battery model for use in dynamic electric vehicle simulations," *PESC*, pp.1336-1342, 2008.
- [99] S.S. Zhang, K. Xu, and T.R. Jow, "Electrochemical impedance study on the low temperature of Li-ion batteries," *Electrochim. Acta*, vol. 49, no. 7, pp. 1057-1061, 2004.

References

- [100] E. Kuhn, C. Forgez, and G. Friendrich, "Modeling diffusive phenomena using non integer derivatives," *European Phys. J. Appl. Phys.*, vol. 25, no. 3, pp. 183-190, 2004.
- [101] D.V. Do, C. Forgez, K. El Kadri Benkara, G. Friedrich, "Impedance Observer for a Li-Ion Battery Using Kalman Filter," *IEEE Trans. Veh. Tech.*, vol. 58, no. 8, pp. 3930-3937, 2009.
- [102] E. Kuhn, C. Forgez, P. Lagonotte, and G. Friedrich, "Modelling Ni-mH battery using Cauer and Foster structures," *J. Power Sources*, vol. 158, no. 2, pp. 1490-1497, 2006.
- [103] D.N. Rakhmatov and S.B.K. Vrudhula, "An analytical high-level battery model for use in energy management of portable electronic systems," *IEEE/ACM Proc. ICCAD*, pp. 488-493, 2001.
- [104] M. W. Verbrugge and R. S. Conell, "Electrochemical and Thermal Characterization of Battery Modules Commensurate with Electric Vehicle Integration," *J. Electrochem. Soc.*, vol. 149, no. 1, pp. A45-A53, 2002.
- [105] M.A. Roscher and D.U. Sauer, "Dynamic electric behavior and open-circuit-voltage modeling of LiFePO₄-based lithium ion secondary batteries", *J. Power Sources*, vol. 196, no. 1, pp. 331-336, 2011.
- [106] P. Kumar and P. Bauer, "Parameter Extraction of Battery Models Using Multiobjective Optimization Genetic Algorithms," *EPE/PEMC, 2010 14th International*, pp. T9-106-T9-110, 2010.
- [107] D. Saikia, A. Kumar, F. Singh, and D.K. Avasthi, "Study of Li³⁺ ion irradiation effects in P(VDF-HFP) based gel polymer electrolytes for application in Li-ion battery," *J. Phys. D: Appl. Phys.*, vol. 39, no. 19, pp. 4208-4214, 2006.
- [108] M. Takahashi, S. Tobishima, K. Takei, Y. Sakurai, "Reaction behaviour of LiFePO₄ as a cathode material for rechargeable lithium batteries," *Solid State Ionics*, vol. 148, no. 3-4, pp. 283-289, 2002.
- [109] A123 Systems Datasheet high power lithium ion APR18650m1.
- [110] M. Dubarry, V. Svoboda, R. Hwu, and B.Y. Liaw, "Capacity and power fading mechanisms identification from a commercial cell evaluation," *J. Power Sources*, vol. 165, no. 2, pp. 566-572, 2007.
- [111] S. Abu-Sharkh and D. Doerffel, "Rapid test and non-linear model characterisation of solid-state lithium-ion batteries", *J. Power Sources*, vol. 130, no. 1-2, pp. 266-274, 2004.
- [112] Koninklijk Nederlands Meteorologisch Instituut (KNMI), "Klimatologie," retrieved 3 February 2011. <http://www.knmi.nl/klimatologie/>
- [113] Y. Zhang, C.Y. Wang, and X. Tang, "Cycling degradation of an automotive LiFePO₄ lithium-ion battery," *J. Power Sources*, vol. 196, no. 3, pp. 1513-1520, 2011.
- [114] SwitchEV, "North East drivers switched on by EV trials," retrieved 28 November 2010. <http://www.switchev.co.uk/news/2010/05/north-east-drivers-switched-on-by-ev-trials.aspx>
- [115] B. Schweighofer, K.M. Raab, and G. Brasseur, "Modeling of high power automotive batteries by the use of an automated test system," *IEEE Trans.Instrum. Meas.*, vol. 52, no. 4, pp. 1087-1091, 2003.

- [116] G. Ning, R.E. White, and B.N. Popov, "A generalized cycle life model of rechargeable Li-ion batteries," *Electrochim. Acta*, vol. 51, no. 10, pp. 2012-2022, 2006.
- [117] A.J. Smith, J.C. Burns, and J.R. Dahn, "A high precision study of the coulombic efficiency of Li-ion batteries," *Electrochem. & Solid-State Letters*, vol. 13, no. 12, pp. A177-A179, 2010.
- [118] K. Yang, J.J. An, and S. Chen, "Temperature characterization analysis of LiFePO₄/C power battery during charging and discharging," *J. Thermal Analysis and Calorimetry*, vol. 99, no. 2, pp. 515-521, 2010.
- [119] M. Canova, Y. Guezennec, and G. Rizzoni, "A reduced-order model for the thermal dynamics of Li-ion battery cells," *IFAC*, pp. 192-197, 2010.
- [120] U.S. Kim, C.B. Shin, and C.S. Kim, "Modeling for the scale-up a lithium-ion polymer battery," *J. Power Sources*, vol. 189, no. 1, pp. 841-846, 2009.
- [121] J. Zhang, S. Ci, H. Sharif, and M. Alahmad, "Modeling Discharge Behavior of Multicell Battery," *IEEE Trans. Energy Conversion*, vol. 25, no. 4, pp. 1133-1141, 2010.
- [122] A. Affanni, A. Bellini, G. Franceschini, P. Guglielmi, and C. Tassoni, "Battery choice and management for new-generation electric vehicles," *IEEE Trans. Industrial Electronics*, vol. 52, no. 5, pp. 1343-1349, 2005.
- [123] S.W. Moore and P.J. Schneider, "A review of cell equalization methods for lithium ion and lithium polymer battery systems," *SAE World Congress*, pp. 959-564, March 2001.
- [124] Y.S. Lee and G.T. Cheng, "Quasi-Resonant Zero-Current-Switching Bidirectional Converter for Battery Equalization Applications," *IEEE Trans. Power Electronics*, vol. 21, no. 5, pp. 1213-1224, 2006.
- [125] N. Demirdöven and J. Deutch, "Hybrid cars now, fuel cell cars later," *Science*, vol. 305, pp. 974-976, 2004.
- [126] R. Farrington and J. Rugh, "Impact of vehicle air-conditioning on fuel economy, tailpipe emissions, and electric vehicle range," *Earth Technologies Forum*, October 2000.
- [127] DieselNet, "Emission Test Cycles," retrieved 2 August 2011.
<http://www.dieselnet.com/standards/cycles/>
- [128] Y. Wang, J. Li, J. Jiang, and L. Niu, "Management information system of charging station for electric vehicle (EV)," *Conf. Proc. ICEMS*, vol. 1, pp. 857-860, 2005.
- [129] Y. Hu, S. Yurkovich, Y. Guezennec, and B. J. Yurkovich, "A technique for dynamic battery model identification in automotive applications using linear parameter varying structures," *Control Eng. Practice*, vol. 17, no. 10, pp. 1190-1201, 2009.

Appendix A.1: Literature-based model

The internal cell impedance equations shown here are only for discharge obtained from literature. Charging will be modelled a similar set of equation with different parameters. So the equations shown here are only half of the required equations for the practical circuit-based model

Ohmic resistance
 R_o *Dependent on T, SoC, C-rate current direction, Ah processed.*

$$R_o(SoC, T, I, Ah) = (R_o(SoC, I) + R_{o,n}(Ah, T, I)) \cdot e^{\left(\frac{E_{a,o}}{R} \left(\frac{1}{T} - \frac{1}{T_{ref}}\right)\right)}$$

$$R_o(SoC, I) = (b_1 + b_4 I + b_5 I^2) e^{-b_2 SoC} + b_3 + b_6 I + b_7 I^2$$

$$R_{o,n}(Ah, T, I) = \sum_{i=1}^E \left((b_{n1} + b_{n2} I_i + b_{n3} I_i^2) \cdot b_n \Delta Ah_i \cdot e^{\left(\frac{E_{a,on}}{R} \left(\frac{1}{T_i} - \frac{1}{T_{ref}}\right)\right)} \right)$$

Capacity of the cell
 C_{use} *Dependent on T, C-rate, Ah processed.*

$$C_{use}(\xi, T) = (Q_{nom} - \xi) \cdot e^{\left(\frac{E_{a,q}}{R} \left(\frac{1}{T} - \frac{1}{T_{ref}}\right)\right)}$$

$$\xi(T, I, Ah) = \sum_i^E \left(\frac{1}{2} k_{\sigma,i}(T, I) \Delta Ah_i^2 + \Delta Ah_i \sqrt{k_1^2 + 2k_{\sigma,i}(T, I) \xi_{i-1}} \right)$$

$$k_{\sigma,i} = k_2 (k_3 + k_4 I + k_5 I^2) e^{\left(\frac{E_a}{R} \left(\frac{1}{T_i} - \frac{1}{T_{ref}}\right)\right)}$$

Open circuit voltage
 V_{oc} *Dependent on SoC.*

$$V_{oc}(SoC) = a_1 e^{-a_2 SoC} + a_3 + a_4 SoC + a_5 e^{-\frac{a_6}{1-SoC}}$$

Short time transient capacitance
 C_s *Dependent on T, SoC, C-rate, current direction, Ah processed.*

$$C_s(SoC, T, I, Ah) = (C_s(SoC, I) + C_{s,n}(Ah, T)) \cdot T e^{\left(\frac{E_{a,cs}}{R} \left(\frac{1}{T} - \frac{1}{T_{ref}}\right)\right)}$$

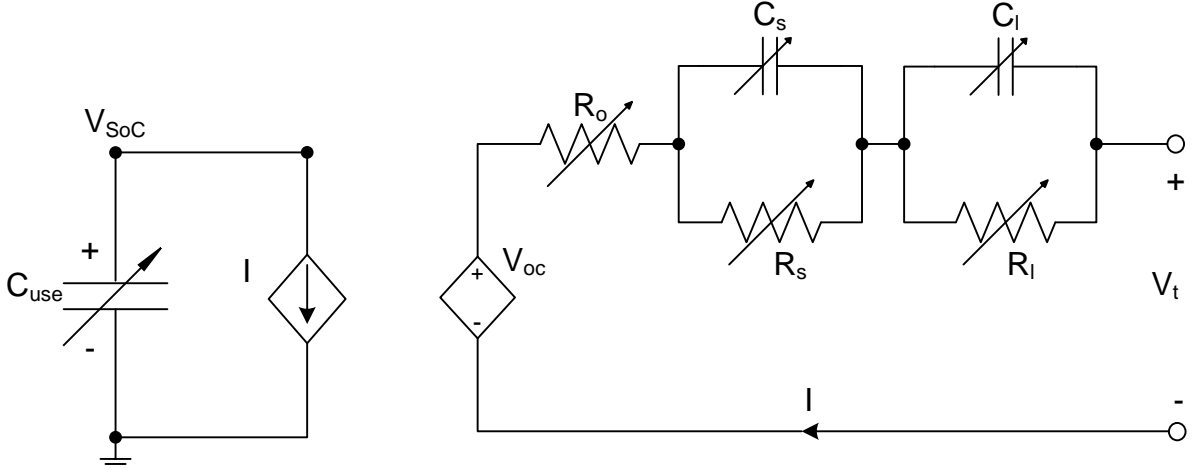
$$C_s(SoC, I) = (d_1 + d_5 I + d_6 I^2) e^{-d_2 SoC} + (d_3 + d_7 I + d_8 I^2) + d_4 SoC$$

$$C_{s,n}(Ah, T) = \sum_{i=1}^E \left(\sqrt{C_{s,ni}^2 + \left(d_{n0} e^{\left(-\frac{E_{a,csn}}{R} \left(\frac{1}{T_i} - \frac{1}{T_{ref}}\right)\right)} \right)^2} \Delta Ah_i - C_{s,ni} \right)$$

Long time transient capacitance
 C_l *Dependent on T, SoC, C-rate, current direction.*

$$C_l(SoC, I, T) = C_l(SoC, I) \cdot e^{\left(\frac{E_{a,cl}}{R} \left(\frac{1}{T} - \frac{1}{T_{ref}}\right)\right)}$$

$$C_l(SoC, I) = h_1 SoC^6 + h_2 SoC^5 + h_3 SoC^4 + h_4 SoC^3 + h_5 SoC^2 + h_6 SoC + h_7 + h_8 I + h_9 I^2$$



Short time transient resistance
 R_s *Dependent on T, SoC, C-rate, current direction, Ah processed.*

$$R_s(SoC, T, I, Ah) = (R_s(SoC, I) + R_{s,n}(Ah, T)) \cdot T e^{\left(\frac{E_{a,rs}}{R} \left(\frac{1}{T} - \frac{1}{T_{ref}}\right)\right)}$$

$$R_s(SoC, I) = (c_1 + c_5 I + c_6 I^2) e^{-c_2 SoC} + (c_3 + c_7 I + c_8 I^2) + c_4 SoC$$

$$R_{s,n}(Ah, T) = \sum_{i=1}^E \left(\sqrt{R_{s,ni}^2 + \left(c_{n0} e^{\left(-\frac{E_{a,rsn}}{R} \left(\frac{1}{T_i} - \frac{1}{T_{ref}}\right)\right)} \right)^2} \Delta Ah_i - R_{s,ni} \right)$$

Long time transient resistance
 R_l *Dependent on T, SoC, C-rate, current direction.*

$$R_l(SoC, I, T) = R_l(SoC, I) \cdot e^{\left(\frac{E_{a,rl}}{R} \left(\frac{1}{T} - \frac{1}{T_{ref}}\right)\right)}$$

$$R_l(SoC, I) = (g_1 + g_4 I + g_5 I^2) e^{-g_2 SoC} + g_3 + g_6 I + g_7 I^2$$

Appendix A.2: Proposed model

Series resistance

R_o Dependent on T , SoC, current direction, Ah processed.

$$R_{od,T_{high}}(SoC, T) = (b_{1d}SoC^4 + b_{2d}SoC^3 + b_{3d}SoC^2 + b_{4d}SoC + b_{5d})b_{t1d}e^{\frac{b_{t2d}}{T-b_{t3d}}}$$

$$R_{oc,T_{high}}(SoC, T) = (b_{1c}SoC^4 + b_{2c}SoC^3 + b_{3c}SoC^2 + b_{4c}SoC + b_{5c})b_{t1c}e^{\frac{b_{t2c}}{T-b_{t3c}}}$$

$$R_{od,T_{low}}(SoC, T) = (b_{t1d}T^3 + b_{t2d}T^2 + b_{t3d}T + b_{t4d})SoC^4 + b_{2d}SoC^3 + b_{3d}SoC^2 + b_{4d}SoC + b_{5d}e^{\frac{b_{t6d}}{T-b_{t7d}}}$$

$$R_{oc,T_{low}}(SoC, T) = (b_{1c}SoC^4 + b_{2c}SoC^3)(b_{t1c}T + b_{t2c}) + (b_{t3c}T^2 + b_{t4c}T + b_{t5c})SoC^2 + (b_{t6c}T^2 + b_{t7c}T + b_{t8c})SoC + b_{9c}e^{\frac{b_{t10c}}{T-b_{t11c}}}$$

Ageing of R_o , cycled with regenerative braking, varied with Ah processed, but did not show a trend.

Capacity of the cell

C_{use} Dependent on T , recharge C-rate, SoC_{avg}, SoC_{dev}, Ah processed.

$$C_{use}(T, \xi) = (Q_{nom} - \xi) \cdot e^{k_1(\frac{1}{T-k_2} - \frac{1}{T_{ref}-k_2})}$$

$$\xi(T, SoC_{avg}, SoC_{dev}, Ah) =$$

$$\sum_i^E \left((k_{s1}SoC_{dev,i} \cdot e^{(k_{s2} \cdot SoC_{avg,i})} + k_{s3}e^{k_{s4}SoC_{dev,i}}) e^{-\frac{E_a(1-T_i)}{R(T_i-T_{ref})}} \right) Ah_i$$

$$SoC_{avg} = \frac{1}{\Delta Ah_m} \int_{Ah_{m-1}}^{Ah_m} SoC(Ah) dAh$$

$$SoC_{dev} = \sqrt{\frac{3}{\Delta Ah_m} \int_{Ah_{m-1}}^{Ah_m} (SoC(Ah) - SoC_{avg})^2 dAh}$$

Not enough data was available to model the influence of recharge C-rate at low temperatures.

Open circuit voltage

Dependent on SoC.

$$V_{oc}(SoC) = a_1e^{-a_2SoC} + a_3 + a_4SoC + a_5 e^{\frac{a_6}{1-SoC}}$$

Short time transient capacitance

Dependent on T , SoC, current direction.

C_s

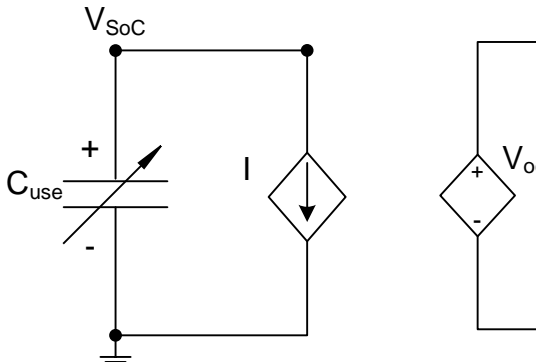
$$C_{sd,T_{high}}(SoC, T) = d_{1d}SoC^3 + d_{2d}SoC^2 + (d_{3d} + d_{t1d}\Delta T)SoC + d_{4d} + d_{t2d}\Delta T$$

$$C_{sc,T_{high}}(SoC, T) = d_{1c}SoC^4 + d_{2c}SoC^3 + d_{3c}SoC^2 + d_{4c}SoC + d_{5c} + d_{t1c}\Delta T$$

$$C_{sd,T_{low}}(SoC, T) = d_{1d}(SoC + (d_{t1d}T - d_{t2d}))^3 + d_{2d}(SoC + (d_{t1d}T - d_{t2d}))^2 + d_{4d} + (d_{t3d}T^2 + d_{t4d}T + d_{t5d})(SoC + (d_{t1d}T - d_{t2d}))$$

$$C_{sc,T_{low}}(SoC, T) = (d_{t1c}T^2 + d_{t2c}T + d_{t3c})SoC^4 + (d_{t4c}T^2 + d_{t5c}T + d_{t6c})SoC^3 + d_{7c}e^{d_{t8c}T}SoC^2 + (d_{t9c}T^2 + d_{t10c}T + d_{t11c})SoC + d_{t12c}T + d_{t13c}$$

ΔT is the temperature deviation from reference temperature 25°C



Short time transient resistance

Dependent on T , SoC, current direction

$$R_{sd,T_{high}}(SoC, T) = c_{1d}e^{-c_{2d}SoC} + c_{3d} + c_{t1d}\Delta T + (c_{4d} + c_{t2d}\Delta T)SoC$$

$$R_{sc,T_{high}}(SoC, T) = c_{1c}e^{c_{t2c}T + (c_{t3c}T + c_{t4c})SoC} + c_{t5c}T + c_{t6c}$$

$$R_{sd,T_{low}}(SoC, T) = (c_{t1d}T^2 + c_{t2d}T + c_{t3d})e^{-(c_{t4d}T^2 + c_{t5d}T + c_{t6d})SoC} + c_{3d} + c_{4d}SoC$$

$$R_{sc,T_{low}}(SoC, T) = c_{1c}e^{c_{t2c}T + (c_{t3c}T + c_{t4c})SoC} + c_{t5c}T^2 + c_{t6c}T + c_{t7c}$$

Long time transient capacitance

Dependent on T , SoC, current direction.

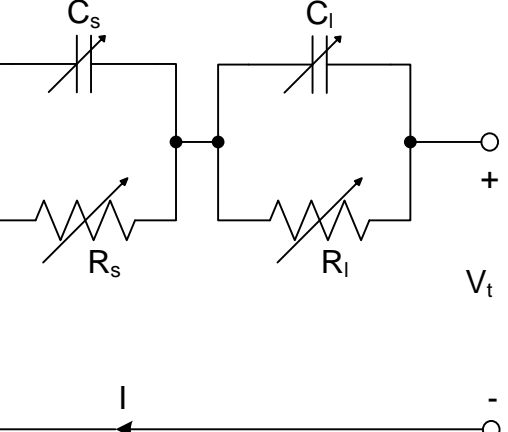
C_l

$$C_{ld,T_{high}}(SoC, T) = (h_{1d}SoC^6 + h_{2d}SoC^5 + h_{3d}SoC^4 + h_{4d}SoC^3 + h_{5d}SoC^2 + h_{6d}SoC + h_{7d})h_{t1d}e^{\frac{h_{t2d}}{T}}$$

$$C_{lc,T_{high}}(SoC, T) = (h_{1c}SoC^5 + h_{2c}SoC^4 + h_{3c}SoC^3 + h_{4c}SoC^2 + h_{5c}SoC + h_{6c})h_{t1c}e^{h_{t2c}T}$$

$$C_{ld,T_{low}}(SoC, T) = (h_{1d}SoC^4 + h_{2d}SoC^3 + h_{5d})e^{h_{t1d}T} + h_{3d}SoC^2e^{h_{t2d}T} + h_{4d}SoCe^{\frac{h_{t3d}}{T-h_{t4d}}}$$

$$C_{lc,T_{low}}(SoC, T) = (h_{1c}SoC^5 + h_{2c}SoC^4 + h_{3c}SoC^3)e^{h_{t4c}T} + h_{5c}e^{h_{t6c}T}SoC^2 + h_{7c}e^{h_{t8c}T}SoC + h_{9c}$$



Long time transient resistance

Dependent on T , C-rate, SoC, current direction.

R_l

$$R_{ld,T_{high}}(SoC, T, I) = ((g_{1d} + g_{t1d}\Delta T)e^{-g_{2d}SoC} + g_{3d} + g_{t2d}\Delta T + g_{4d}SoC) \cdot (g_{i1d}I_{Crage}^{g_{i2d}} + g_{id3})$$

$$R_{lc,T_{high}}(SoC, T, I) = (g_{1c}e^{-g_{2c}SoC} + g_{3c} + g_{4c}SoC)(g_{t1c}T + g_{t2c}) \cdot (g_{i1c}(I_{Crage}^{g_{i2c}} - 1)SoC + I_{Crage}^{g_{i3c}})$$

$$R_{ld,T_{low}}(SoC, T, I) = \left(g_{t1d}e^{\frac{g_{t2d}}{T-g_{t3d}}-g_{2d}SoC} + g_{t4d}e^{\frac{g_{t5d}}{T}-T} + g_{t6d}e^{\frac{g_{t7d}}{T}}SoC \right) \cdot (g_{i1d}I_{Crage}^{g_{i2d}} + g_{id3})$$

$$R_{lc,T_{low}}(SoC, T, I) = (g_{t1c} \cdot e^{g_{t2c}T-g_{2c}SoC} + g_{t3c}T^2 + g_{t4c}T + g_{t5c} + g_{4c}SoC) \cdot (g_{i1c}(I_{Crage}^{g_{i2c}} - 1)SoC + I_{Crage}^{g_{i3c}})$$

Appendix B: Model parameters

k_1	-5.738	k_{s2}	-2.1665
k_2	2.099E2	k_{s3}	1.408E-5
k_{s1}	-2.046E-4	k_{s4}	3.065

Table B.1: The parameter values of the cell capacity C_{use} .

a_1	-5.863E-1	a_4	1.102E-1
a_2	21.90	a_5	-1.718E-1
a_3	3.414	a_6	8.000E-3

Table B.2: The parameter values of the OCV V_{oc} .

b_{1d}	1.298E-1	c_{2d}	11.03	d_{4d}	3.897E2	h_{2d}	-6.007E6
b_{2d}	-2.892E-1	c_{3d}	1.827E-2	g_{1d}	2.950E-1	h_{3d}	6.271E6
b_{3d}	2.273E-1	c_{4d}	-6.462E-3	g_{2d}	20.00	h_{4d}	-2.958E6
b_{4d}	-7.216E-2	d_{1d}	1.697E2	g_{3d}	4.722E-2	h_{5d}	5.998E5
b_{5d}	8.980E-2	d_{2d}	-1.007E3	g_{4d}	-2.420E-2	h_{6d}	-3.102E4
c_{1d}	1.080E-2	d_{3d}	1.408E3	h_{1d}	2.130E6	h_{7d}	2.232E3

Table B.3: The parameter values of the SoC dependency of internal cell impedance for discharging.

b_{1c}	1.369E-1	c_{2c}	-18.75	d_{5c}	6.849E2	h_{2c}	2.042E5
b_{2c}	-2.518E-1	c_{3c}	1.388E-2	g_{1c}	8.913E-15	h_{3c}	-4.009E3
b_{3c}	1.609E-1	d_{1c}	-1.026E4	g_{2c}	-32.23	h_{4c}	-8.124E4
b_{4c}	-4.100E-2	d_{2c}	1.723E4	g_{3c}	3.100E-2	h_{5c}	2.283E4
b_{5c}	8.210E-2	d_{3c}	-1.013E4	g_{4c}	7.473E-3	h_{6c}	7.144E3
c_{1c}	5.896E-10	d_{4c}	2.340E3	h_{1c}	-1.541E5		

Table B.4: The parameter values of the SoC dependency of internal cell impedance for charging.

g_{i1d}	6.993E-1	g_{i1c}	-4.124E-1
g_{i2d}	-6.919E-1	g_{i2c}	-1.082
g_{i3d}	2.902E-1	g_{i3c}	-8.730E-1

Table B.5: The parameter values of the C-rate dependency of internal cell impedance for both discharging and charging.

b_{t1d}	7.613E-1	c_{t1d}	-3.697E-4	d_{t2d}	12.11	h_{t1d}	3.128E3
b_{t2d}	10.14	c_{t2d}	2.225E-4	g_{t1d}	6.718E-3	h_{t2d}	-2.398E3
b_{t3d}	2.608E2	d_{t1d}	-6.580	g_{t2d}	-5.967E-4		

Table B.6: The parameter values of the high temperature dependency of internal cell impedance for discharging.

b_{t1c}	7.192E-1	c_{t2c}	-1.479E-1	c_{t6c}	7.054E-2	h_{t1c}	2.611E-5
b_{t2c}	33.91	c_{t3c}	-1.178E-1	d_{t1c}	8.814	h_{t2c}	3.541E-2
b_{t3c}	1.999E2	c_{t4c}	13.99	g_{t1c}	-1.344E-2		
c_{t1c}	9.869E8	c_{t5c}	-1.897E-4	g_{t2c}	5.011		

Table B.7: The parameter values of the high temperature dependency of internal cell impedance for charging.

b_{2d}	-2.819E-1	c_{4d}	-6.462E-3	d_{t2d}	4.068	g_{t7d}	4.202E3
b_{3d}	2.448E-1	c_{t1d}	1.923E-4	d_{t3d}	-6.807E-1	h_{1d}	-3.751E-11
b_{4d}	-9.630E-2	c_{t2d}	-1.166E-1	d_{t4d}	4.002E2	h_{2d}	6.764E-11
b_{t1d}	-5.930E-6	c_{t3d}	17.66	d_{t5d}	-5.769E4	h_{3d}	-2.219E-11
b_{t2d}	5.011E-3	c_{t4d}	1.098E-2	g_{2d}	20.00	h_{4d}	10.75
b_{t3d}	-1.411	c_{t5d}	-5.644	g_{t1d}	8.238E-3	h_{5d}	1.534E-13
b_{t4d}	1.325E2	c_{t6d}	7.299E2	g_{t2d}	1.805E2	h_{t1d}	1.220E-1
b_{t5d}	6.297E-2	d_{1d}	-1.173E3	g_{t3d}	2.321E2	h_{t2d}	1.241E-1
b_{t6d}	24.37	d_{2d}	8.278E2	g_{t4d}	1.589E-7	h_{t3d}	-4.492E2
b_{t7d}	2.363E2	d_{4d}	1.005E2	g_{t5d}	3.779E3	h_{t4d}	3.474E2
c_{3d}	1.827E-2	d_{t1d}	1.428E-2	g_{t6d}	-2.208E-8		

Table B.8: The parameter values of the low temperature dependency of internal cell impedance for discharging.

b_{1c}	2.192E-1	c_{t1c}	7.008E29	d_{t7c}	-3.688E-2	g_{t5c}	5.225
b_{2c}	-3.968E-1	c_{t2c}	-3.051E-1	d_{t8c}	4.261E-2	h_{t1c}	6.343E-6
b_{t1c}	-8.297E-2	c_{t3c}	2.782E-1	d_{t9c}	-1.199	h_{t2c}	-1.817E-5
b_{t2c}	24.82	c_{t4c}	-63.04	d_{t10c}	7.103E2	h_{t3c}	1.887E-5
b_{t3c}	2.136E-4	c_{t5c}	2.840E-6	d_{t11c}	-1.027E5	h_{t4c}	8.551E-2
b_{t4c}	-1.422E-1	c_{t6c}	-1.733E-3	d_{t12c}	8.493	h_{t5c}	-1.414E-5
b_{t5c}	23.48	c_{t7c}	2.786E-1	d_{t13c}	-1.902E3	h_{t6c}	8.381E-2
b_{t6c}	-1.795E-4	d_{t1c}	-11.23	g_{2c}	-32.23	h_{t7c}	1.057E-5
b_{t7c}	1.077E-1	d_{t2c}	5.941E3	g_{4c}	1.571E-2	h_{t8c}	7.897E-2
b_{t8c}	-16.20	d_{t3c}	-7.848E5	g_{t1c}	3.726E-8	h_{t9c}	6.962E2
b_{t9c}	4.968E-2	d_{t4c}	16.18	g_{t2c}	-4.951E-2		
b_{t10c}	28.78	d_{t5c}	-8.523E3	g_{t3c}	5.921E-5		
b_{t11c}	2.376E2	d_{t6c}	1.123E6	g_{t4c}	-3.507E-2		

Table B.9: The parameter values of the low temperature dependency of internal cell impedance for charging.

Appendix C

Paper title: A Practical Circuit-based Model for Li-ion Battery Cells in Electric Vehicle Applications.

Authors: Long Lam, Pavol Bauer, and Erik Kelder.

Conference: *33rd International Telecommunications Energy Conference (INTELEC), 9-13 October 2011, Amsterdam, the Netherlands.*

A Practical Circuit-based Model for Li-ion Battery Cells in Electric Vehicle Applications

Long Lam, Pavol Bauer

Department of Electrical Sustainable Energy
Delft University of Technology
Delft, the Netherlands
P.Bauer@tudelft.nl

Erik Kelder

Department of Chemical Engineering
Delft University of Technology
Delft, the Netherlands
E.M.Kelder@tudelft.nl

Abstract—This paper proposes a practical circuit-based model for Li-ion cells, which can be directly connected to a model of a complete electric vehicle (EV) system. The goal of this paper is to provide EV system designers with a tool in simulation programs such as Matlab/Simulink to model the behaviour of Li-ion cells under various operating conditions in EV or other applications. The current direction, state of charge (SoC), temperature and C-rate dependency are represented by empirical equations obtained from measurements on LiFePO₄ cells. Tradeoffs between model complexity and accuracy have been made based on practical considerations in EV applications. Depending on the required accuracy and operating conditions, the EV system designer can choose the influences to be included in the system simulation.

Keywords: LiFePO₄, battery model, regenerative braking, electric vehicle, practical circuit model.

I. INTRODUCTION

Batteries, instead of the engine, have become the heart of the car in the transition from internal combustion engine (ICE) vehicles to electric vehicles (EVs). In designing EVs it is therefore important to be able to simulate the behaviour of the battery system, in particular the battery pack. Hence, a battery model that can be directly connected to a model of the rest of the electronic system is required.

In the field of battery modelling many different battery models have been proposed in literature [1]. The battery models can be divided into analytical, electrochemical and electrical circuit models or a combination of the model types. Analytical models [2] do not give a good view of the electrochemical processes occurring in the cell. Electrochemical models [3][4] require a large amount of computational power to solve the time-varying spatial partial differential equations and cannot be directly connected to the rest of the system. Combined analytical and electrochemical models [5][6] also suffer from high complexity and poor system modelling compatibility. On the other hand, electrical circuit models can easily be connected to the rest of the electronic systems, but suffer from lower accuracy [7][8]. Nevertheless, to model the general behaviour of the battery in an EV system electrical circuit models are sufficient.

Most electrical circuit models can be classified as impedance-based [9][10] or Thevenin-based [11][12] models. Impedance-based models require Electrochemical Impedance

Spectroscopy (EIS) to determine the circuit components; the circuit components are related to electrochemical processes in the cell. In Thevenin-based models the circuit component values are extracted from the measured voltage response. The advantage of Thevenin-based models is that using various algorithms [13][14] the circuit components can be extracted from voltage measurements of an operating EV battery without any additional equipment in the EV.

The equivalent circuit-based model developed by Chen & Rincón-Mora [15] is capable of modelling the runtime, DC, AC and transient response of a single cell. Other works have attempted to include the C-rate effect [16], temperature effect and capacity fading [17] in the capacity of the cell using the model in [15]. However, only the discharge phase of the cell has been modelled and regenerative braking has not been considered. Chan & Sutanto [18] recognised the need to model the charging phase of the cell in EV applications, and introduced separate circuit components for discharging and charging. The model was expanded with additional circuit components for modelling in circuit simulation programs, but suffered from incapability to model fast transitions between discharging and charging states [19]. In Matlab/Simulink the model can, however, be implemented by nonlinear equations for each circuit components [20], removing the need for separate circuit components for discharging and charging.

In this paper a practical electrical circuit model based on [15] for EVs will be proposed. The model consists of empirical equations extracted from measurements on LiFePO₄ cells. With adjustments to the equations and parameters other battery chemistries can also be modelled. The goal of the model is to provide EV system designers with a tool to simulate the behaviour of LiFePO₄ cells under possible operating conditions in simulation programs such as Matlab/Simulink, and not to validate the characteristics of the cells. The focus of this paper will lie on the short term behaviour of the cell, but the long term behaviour will be touched upon. Empirical equations are presented to model the influence of different temperatures and C-rates on the discharging and charging behaviour of the cells. In contrast to previous works of other authors, an attempt will be made to relate the different influences on the electrochemical processes to the correct circuit components instead of the cell capacity. This utilises EV system designers to simulate the energy efficiency of a cell as well.

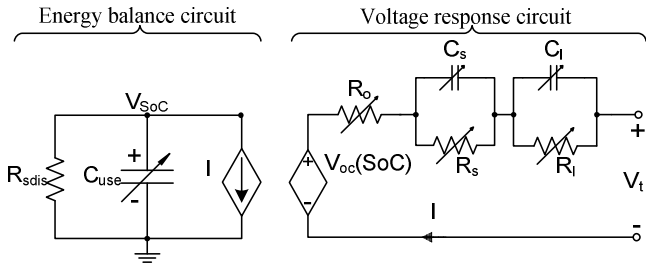


Fig. 1. The proposed model based on [15].

This paper is organised as follows. Section II presents the proposed model. The extraction of the empirical equations and parameters for the proposed model is described in section III. In section IV the proposed model is validated by comparing the simulation results with the measurements. Section V concludes this paper.

II. PROPOSED MODEL

Fig. 1 shows the battery cell model proposed in this work. The circuit is divided into an energy balance and voltage response circuit. Each circuit component is made variable, since they depend on various factors such as temperature, C-rate (capacity normalised current) and state of charge (SoC). The energy balance circuit models the cell capacity with C_{use} and the self-discharge with R_{sdis} . V_{SoC} is circuit representation of SoC and the value is equal to SoC. Therefore only SoC will be used in this paper. The voltage response circuit consists of the open-circuit voltage (OCV) V_{oc} , the ohmic resistance R_o , the short time transient parallel RC pair R_s and C_s , and the long time transient parallel RC pair R_l and C_l . With the OCV and the internal cell impedance the voltage response of the cell is modelled under different operating conditions.

In the model the useable capacity C_{use} is the current independent capacity of the cell; this is the theoretically possible amount of charge that can be discharged from a fully charged cell with an infinitely small current for a given minimum cell voltage, so that the voltage drop over the internal resistance becomes close to zero. Furthermore, the SoC used in the model is thermodynamic-SoC (t-SoC) in contrast to the often used engineering-SoC (e-SoC) [21]. The e-SoC is the state of the cell capacity apparent to the user and is current dependent. The t-SoC is the SoC defined by the thermodynamic properties in the cell and is directly related to the OCV of the cell, i.e. the state of the useable capacity. Since the current effect on the capacity is already taken into account by the internal impedance, it would be duplication to model the energy balance circuit with the apparent capacity and e-SoC.

In the practical equivalent circuit-based model it is not important if every influence on the cell has been taken into account, but whether the different influences have a noticeable effect on the behaviour of the cell. Each impedance element in the voltage response circuit can be related to electrochemical processes in the cell by comparing the circuit with an impedance-based model. Impedance-based models characterise the internal cell impedance obtained from EIS measurements with a 2nd order Randles circuit shown in Fig. 2. R_b is the bulk resistance of the cell, accounting for the electric conductivity of the electrolyte, separator and electrodes. R_{SEI} and C_{SEI} represent the resistance and capacitance of the surface film layer on the

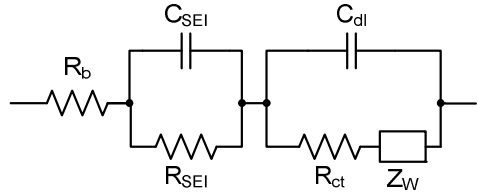


Fig. 2. A typical 2nd order Randles circuit used in impedance-based models.

electrodes e.g. the solid electrolyte interface (SEI) layer and corresponds to the high frequency impedances [9]. The charge transfer resistance R_{ct} and double layer capacitance C_{dl} characterise the activation polarisation voltage drop and the Warburg impedance Z_W represents the diffusion of the lithium ions in the cell. In real-life EV applications the data sample rate is limited and can be as low as 1 Hz, causing the high frequency impedance R_{SEI} and C_{SEI} to be indiscernible from R_b . Furthermore, Z_W can be approximated by a number of parallel RC pairs in series with the rest of the circuit [22] to represent the diffusion phenomena in the cell. Consequently, the electrochemical processes modelled in the impedance-based model are related to the proposed model as following: the ohmic resistance R_o consists of the bulk resistance and surface layer impedance, the activation polarisation is modelled by R_s and C_s , and the concentration polarisation as a result of low diffusion rate is represented R_l and C_l .

In the practical equivalent circuit-based model R_{sdis} is considered to be infinite, since LiFePO₄ cells have a very low self-discharge [23]. The OCV has been reported to exhibit a hysteresis effect [11][24] and temperature dependency [20]. Temperature and C-rate dependence have also been reported for the impedance elements [25], although the Li-ion chemistry was not LiFePO₄. Equations of various complexities have been proposed to describe the circuit components in literature [15][20]. From measurements it has to be determined which level of complexity is required to reach sufficient accuracy and which influences have to be taken into account in the practical equivalent circuit-based model for LiFePO₄ cells.

III. EMPIRICAL MODELLING

Numerous experiments have been conducted on LiFePO₄ cells to determine various influences on the circuit components in the proposed model. Empirical equations describing the influences were then extracted from the measurements.

A. Experimental setup

A123 Systems' APR18650m1 LiFePO₄ cells of 1.1Ah nominal capacity obtained from a third party vendor have been used in the experiment with a Maccor Series 2000 Automated Battery tester. The battery tester has 16 independent channels with a maximum rating of 10V and 2A. The data was logged on the internal memory of the battery tester and occasionally written to the PC. The cells were placed in closed temperature regulated chambers and initially the surface temperature change of each cell was monitored. However, the temperature change was very small during testing and the cell temperature was assumed to be equal to the temperature of the chamber.

B. Measurement method

The values for the circuit components in the proposed model were extracted with a similar method as described in

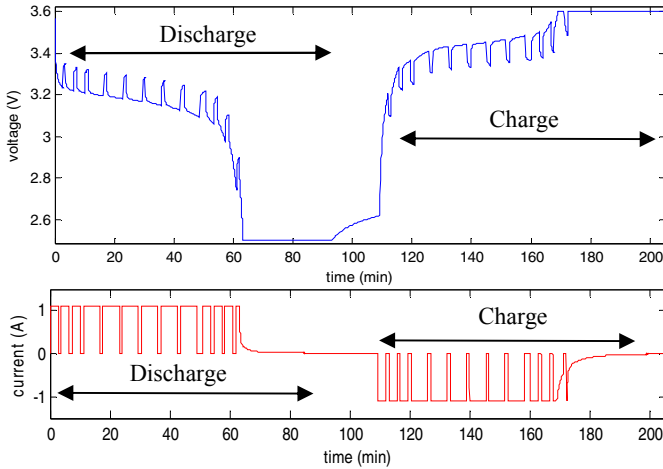


Fig. 3. The test cycle for determining the capacity and parameter of the equivalent circuit components of a cell under test.

[26]. Each cell was charged with the constant current constant voltage (CCCV) method. The cells were charged with the recommended current up to 3.6V, and then charged at constant voltage until the current was lower than 0.01C. The cells were then rested for at least an hour before experiments were conducted. Cells for modelling the temperature influence on the circuit components were rested for at least 6 hours at the test temperature for the cells to reach thermal equilibrium.

The values of the circuit components have been determined by the test cycle shown in Fig. 3. In the nonlinear voltage region cells were discharged with 1C in steps of 0.05Ah and rested for 1 minute. In the linear voltage region cells were discharged with 1C in 0.1Ah steps before rested for 1 minute until the cell had been fully discharged. To approximate the useable capacity of the cell, cells were both charged and discharged with the CCCV method. The minimum cell voltage was set to 2.5V to prevent overdischarge. After a resting period of 15 minutes, the same sequence was repeated for charging. From experiments with different resting times it has been determined the designated resting times were sufficient to have a negligible influence on the practical model.

C. Useable capacity modelling

Changes in the useable capacity C_{use} can be either a result of irreversible capacity loss or reversible capacity change. The irreversible capacity loss is known as capacity fading and is a result of cell ageing due to cycling or storage. Capacity fading depends on many stress factors such as temperature, C-rate, SoC and depth of discharge. The reversible capacity change is only dependent on temperature and is generally modelled with the Arrhenius equation. By plotting the natural logarithm of the capacity against $1000/T$ in Fig. 4a it was, however, found that the capacity development did not satisfy the Arrhenius equation. The natural logarithm of the capacity changed with a curve, which suggested that the Vogel-Tamman-Fulcher (VTF) equation could model the reversible capacity change as shown in Fig. 4b. With the VTF equation the equation for the useable cell capacity was found to be

$$C_{use} = (Q_{nom} - \xi) \cdot e^{k_1 \left(\frac{1}{T - k_2} - \frac{1}{T_{ref} - k_2} \right)}, \quad (1)$$

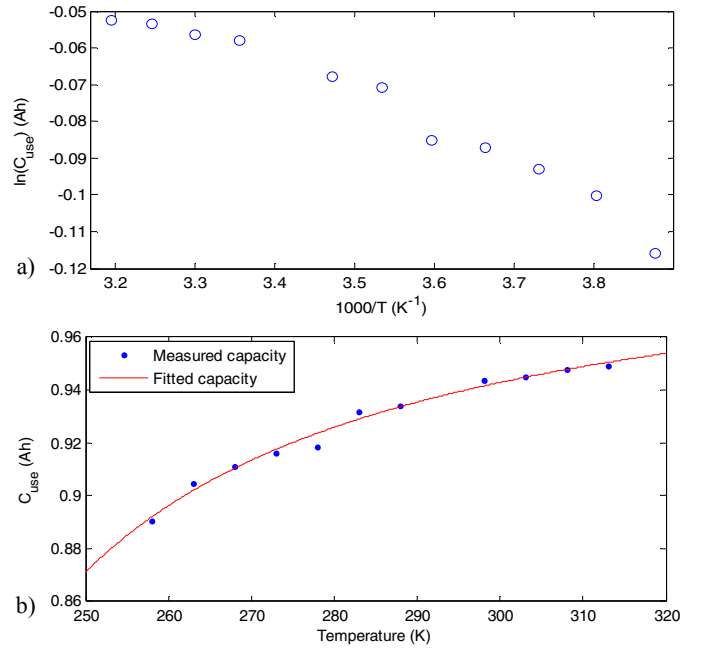


Fig. 4. a) The natural logarithm of the capacity vs. $1000/T$ and (b) the measured temperature dependency of the capacity with the corresponding curve fit according to the VTF equation.

where Q_{nom} is the initial capacity in Ah and ξ the amount of capacity faded in Ah, both determined at reference temperature T_{ref} . The measured temperature T and T_{ref} are in Kelvin. The parameters k_1 and k_2 are given in Table I.

D. Open-circuit voltage modelling

The OCV was determined with the same test procedure as in Fig. 3, but with two hours rest instead of one min to measure the close-to-equilibrium open-circuit voltage (cte-OCV) for discharging and charging. Furthermore, each resting period occurred after every 5% SoC instead of every 0.05Ah or 0.1Ah. The cte-OCV for discharging and charging were averaged to obtain the OCV as shown in Fig. 5. Possible hysteresis of the OCV was neglected, as this is modelled by the internal cell impedance. The OCV was strongly dependent on the SoC and by curve fitting the data in Fig. 5 an equation modelling the OCV was obtained as

$$V_{oc}(SoC) = a_1 e^{-a_2 SoC} + a_3 + a_4 SoC + a_5 e^{-\frac{a_6}{1-SoC}}. \quad (2)$$

The values for the parameters a_1 to a_6 are given in Table I. OCV measurements have been conducted at temperatures from -20°C to 40°C to determine the temperature dependence of the OCV. The deviations from reference temperature were found to be less than 2mV at most temperatures, going up to 8mV at -20°C. Since the temperature fluctuations were insignificantly small, the OCV is considered temperature independent.

TABLE I. PARAMETER VALUES FOR C_{use} AND V_{oc}

k_1	-5.738	a_3	3.414
k_2	2.099E2	a_4	1.102E-1
a_1	-5.863E-1	a_5	-1.718E-1
a_2	21.90	a_6	8.000E-3

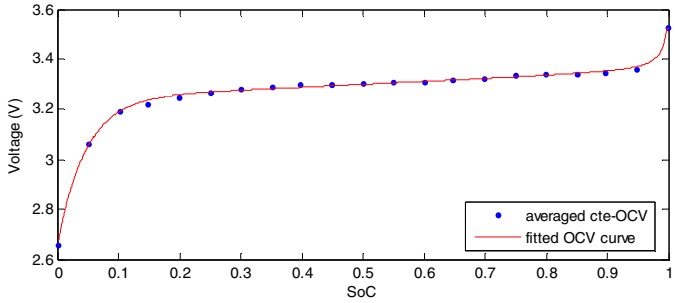


Fig. 5. The averaged cte-OCV measurement and the corresponding OCV model.

E. Internal impedance modelling

The internal impedance elements were determined from the voltage response during the rest period as described in [27]. In the practical equivalent circuit-based model the voltage drop within one second is considered to be the instantaneous voltage drop U_o . The short-time and long-time transient parallel RC pairs are determined by curve fitting the rest of the voltage response to the following equations:

$$V_{trans} = V_s \left(1 - e^{-\frac{t}{\tau_s}} \right) + V_l \left(1 - e^{-\frac{t}{\tau_l}} \right) \quad (3)$$

$$V_s = R_s I \quad (4)$$

$$V_l = R_l I = \left(\frac{(V_{oc} - V_i)}{I} - R_s \right) I \quad (5)$$

$$\tau_s = R_s C_s \quad \tau_l = R_l C_l. \quad (6)$$

V_{trans} is the voltage response minus V_o , V_s and V_l respectively the short and long time transient voltage drop with the time constants τ_s and τ_l , V_{oc} the OCV at the measured SoC and V_i the voltage after the instantaneous voltage drop as shown in Fig. 6. I is the current in Amps before the rest interval, positive for discharging and negative for charging. The resistances and time constants are determined by curve fitting with the nonlinear least squares method in Matlab. The short time transient time constant is determined to be several seconds, and the rest of the voltage response until the OCV is contributed by the long time transient voltage drop.

From the measurements it was determined that the impedance elements for discharging were not equal to charging, resulting in two sets of equations per impedance element. It was found that only between 70% and 40% SoC the voltage response can be approximated with the same equations for discharge and charge. In Fig. 7 and Fig. 8 the values of the impedance elements determined for respectively discharging and charging at 1C are shown to be dependent on the SoC. Using empirical equations consisting of exponential functions and polynomials, the SoC dependence was modelled with the tradeoff between accuracy and complexity of the equations in mind. For discharging the equations of the impedance elements are given by

$$R_{od}(SoC) = b_{1d} SoC^4 + b_{2d} SoC^3 + b_{3d} SoC^2 + b_{4d} SoC + b_{5d} \quad (7)$$

$$R_{sd}(SoC) = c_{1d} e^{-c_{2d} SoC} + c_{3d} + c_{4d} SoC \quad (8)$$

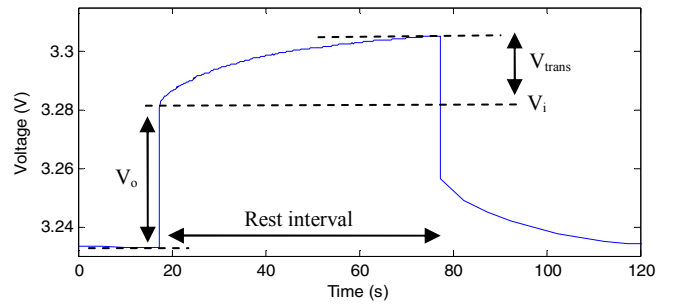


Fig. 6. An example of the voltage response during a rest interval of a discharge test cycle.

$$C_{sd}(SoC) = d_{1d} SoC^3 + d_{2d} SoC^2 + d_{3d} SoC + d_4 \quad (9)$$

$$R_{ld}(SoC) = g_{1d} e^{-g_{2d} SoC} + g_{3d} + g_{4d} SoC \quad (10)$$

$$C_{ld}(SoC) = h_{1d} SoC^6 + h_{2d} SoC^5 + h_{3d} SoC^4 + h_{4d} SoC^3 + h_{5d} SoC^2 + h_{6d} SoC + h_{7d}. \quad (11)$$

The values of the discharge parameters are given in Table II. The subscript d represents the discharging impedance and parameters of the impedance elements. The equations of the impedance elements for charging are labelled with a subscript c and are given by

$$R_{oc}(SoC) = b_{1c} SoC^4 + b_{2c} SoC^3 + b_{3c} SoC^2 + b_{4c} SoC + b_{5c} \quad (12)$$

$$R_{sc}(SoC) = c_{1c} e^{-c_{2c} SoC} + c_{3c} \quad (13)$$

$$C_{sc}(SoC) = d_{1c} SoC^4 + d_{2c} SoC^3 + d_{3c} SoC^2 + d_{4c} SoC + d_{5c} \quad (14)$$

$$R_{lc}(SoC) = g_{1c} e^{-g_{2c} SoC} + g_{3c} + g_{4c} SoC \quad (15)$$

$$C_{lc}(SoC) = h_{1c} SoC^5 + h_{2c} SoC^4 + h_{3c} SoC^3 + h_{4c} SoC^2 + h_{5c} SoC + h_{6c}. \quad (16)$$

In Table III the values of the charge parameters are given. The equations for discharging and charging are depicted in respectively Fig. 7 and Fig. 8. As a result of curve fitting, C_{sc} and C_{lc} are negative near 100% SoC. The negative value is prevented by implementing a minimum value in the simulation for C_{sc} and C_{lc} . The validity of the equations has been confirmed by determining the SoC dependence of numerous cells of the same type and manufacturer. Each cell shows the same SoC dependence modelled by equations 7 to 16.

TABLE II. IMPEDANCE PARAMETERS FOR DISCHARGING

b _{1d}	1.298E-1	c _{4d}	-6.462E-3	g _{4d}	-2.420E-2
b _{2d}	-2.892E-1	d _{1d}	1.697E2	h _{1d}	2.130E6
b _{3d}	2.273E-1	d _{2d}	-1.007E3	h _{2d}	-6.007E6
b _{4d}	-7.216E-2	d _{3d}	1.408E3	h _{3d}	6.271E6
b _{5d}	8.980E-2	d _{4d}	3.897E2	h _{4d}	-2.958E6
c _{1d}	1.080E-2	g _{1d}	2.950E-1	h _{5d}	5.998E5
c _{2d}	11.03	g _{2d}	20.00	h _{6d}	-3.102E4
c _{3d}	1.827E-2	g _{3d}	4.722E-2	h _{7d}	2.232E3

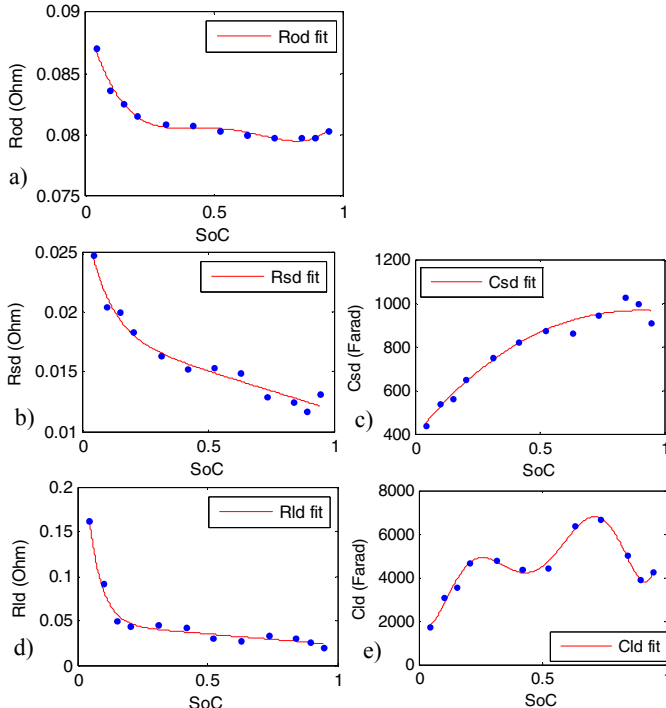


Fig. 7. The data points and corresponding curve fits of a) R_{od} , b) R_{sd} , c) C_{sd} , d) R_{ld} and e) C_{ld} for discharge.

To test the temperature dependence of the impedance elements, the temperature of one cell was varied from 40°C to -15°C in steps of 5°C. At each temperature the impedance elements were determined at 1C as shown in Fig. 9 for discharging. The impedance elements for charging showed a similar behaviour. It can clearly be seen that the SoC behaviour of the impedance elements changes with temperature and can therefore not be regarded as temperature independent. Furthermore, the SoC behaviour changes between 25°C and 15°C. To limit the complexity of the equations, the temperature dependence modelling is split into equations for 20°C and above (high temperatures) and below 20°C (low temperatures). Since the impedance equations were obtained from curve fitting the voltage response, the impedance elements do not directly represent electrochemical processes in a cell, but can only be related to the processes. Consequently, equations describing the temperature dependence of the electrochemical processes cannot be used with the model and the temperature dependence has to be modelled with empirical equations as well. For high temperatures equations 7 to 11 then become

$$R_{od,T_{high}}(SoC, T) = R_{od}(SoC) \cdot b_{t1d} e^{\frac{b_{t2d}}{T-b_{t3d}}} \quad (17)$$

$$R_{sd,T_{high}}(SoC, T) = R_{sd}(SoC) + c_{t1d} \Delta T + c_{t2d} \Delta T \cdot SoC \quad (18)$$

$$C_{sd,T_{high}}(SoC, T) = C_{sd}(SoC) + d_{t1d} \Delta T \cdot SoC + d_{t2d} \Delta T \quad (19)$$

$$R_{ld,T_{high}}(SoC, T) = R_{ld}(SoC) + (g_{t1d} \Delta T) e^{-g_{2d} SoC} + g_{t2d} \Delta T \quad (20)$$

$$C_{ld,T_{high}}(SoC, T) = C_{ld}(SoC) \cdot h_{t1d} e^{\frac{h_{t2d}}{T}}, \quad (21)$$

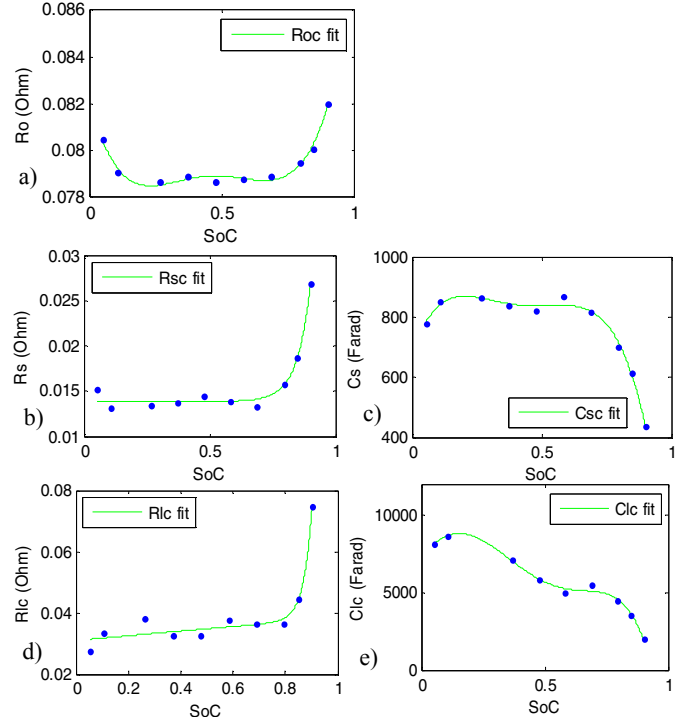


Fig. 8. The data points and corresponding curve fits of a) R_{oc} , b) R_{sc} , c) C_{sc} , d) R_{lc} and e) C_{lc} for charge.

TABLE III. IMPEDANCE PARAMETERS FOR CHARGING

b_{1c}	1.369E-1	d_{1c}	-1.026E4	g_{4c}	7.473E-3
b_{2c}	-2.518E-1	d_{2c}	1.723E4	h_{1c}	-1.541E5
b_{3c}	1.609E-1	d_{3c}	-1.013E4	h_{2c}	2.042E5
b_{4c}	-4.100E-2	d_{4c}	2.340E3	h_{3c}	-4.009E3
b_{5c}	8.210E-2	d_{5c}	6.849E2	h_{4c}	-8.124E4
c_{1c}	5.896E-10	g_{1c}	8.913E-15	h_{5c}	2.283E4
c_{2c}	-18.75	g_{2c}	-32.23	h_{6c}	7.144E3
c_{3c}	1.388E-2	g_{3c}	3.100E-2		

where T is the temperature in Kelvin and ΔT the temperature deviation from the reference temperature. The parameters with a subscript t are additional parameters introduced to model the temperature dependence and are given in Table IV. For high temperatures the impedance model for charging modelled with equations 12 to 16 change to:

$$R_{oc,T_{high}}(SoC, T) = R_{oc}(SoC) \cdot b_{t1c} e^{\frac{b_{t2c}}{T-b_{t3c}}} \quad (22)$$

$$R_{sc,T_{high}}(SoC, T) = c_{t1c} e^{c_{t2c} T - (c_{t3c} T + c_{t4c}) SoC} + c_{t5c} T + c_{t6c} \quad (23)$$

$$C_{sc,T_{high}}(SoC, T) = C_{sc}(SoC) + d_{t1c} \Delta T \quad (24)$$

$$R_{lc,T_{high}}(SoC, T) = R_{lc}(SoC) \cdot (g_{t1c} T + g_{t2c}) \quad (25)$$

$$C_{lc,T_{high}}(SoC, T) = C_{lc}(SoC) \cdot h_{t1c} e^{h_{t2c} T}. \quad (26)$$

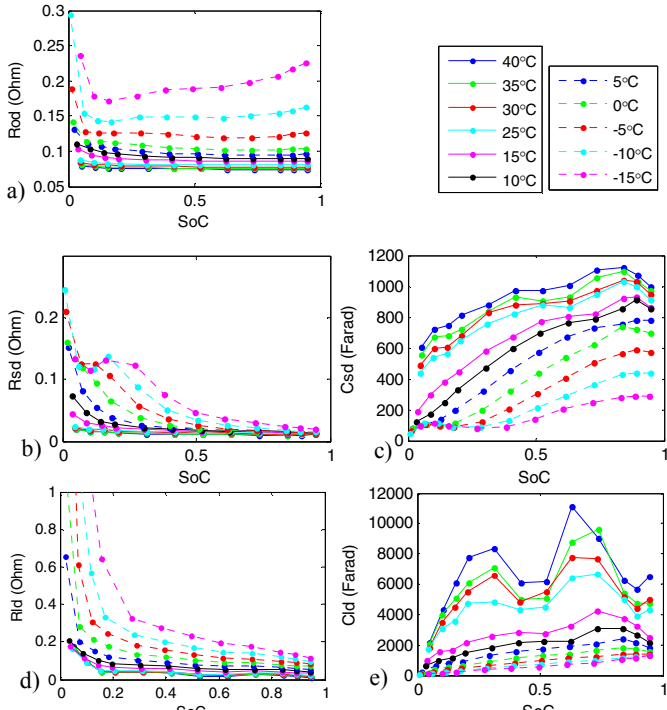


Fig. 9. a) R_{od} , b) R_{sd} , c) C_{sd} , d) R_{ld} and e) C_{ld} determined at different temperatures between 40°C and -15°C for discharge.

Only the equation of R_{sc} is completely changed to model the temperature dependence for high temperatures. The parameters for the temperature dependence are given in Table V. For low temperatures the equations in the impedance model become much more complex as the SoC behaviour changes dramatically. The impedance element equations for low temperatures are given in the Appendix.

The C-rate dependence of the impedance elements was determined by conducting the test cycle at different C-rates between 1.75C and 0.25C with steps of 0.25 at reference temperature. For both discharging and charging the impedance elements were almost invariant with the C-rate except for R_l . This is also reflected in the value of the total resistance R_{tot} for both discharge and charge, which C-rate dependent variations correspond with R_l as shown in Fig. 10. By including the C-rate dependency equations 20 and 25 will respectively become

$$R_{ld,T_{high}}(SoC, T, I) = R_{ld,T_{high}}(SoC, T) \cdot (g_{i1d} I_{Crate}^{g_{i2d}} + g_{i3d}) \quad (27)$$

$$R_{lc,T_{high}}(SoC, T, I) = R_{lc,T_{high}}(SoC, T) \cdot (g_{i1c} (I_{Crate}^{g_{i2c}} - 1) SoC + I_{Crate}^{g_{i3c}}), \quad (28)$$

where I_{Crate} is the current of the cell in C-rates. The parameters with a subscript i model the C-rate dependency and are given in Table VI. For low temperatures the C-rate dependence can be modelled in the same way.

The C-rate dependence has only been validated for reference temperature and the correlation with the temperature dependence needs further investigation. Additionally, the C-rate dependency modelling of R_{ld} and R_{lc} has a limitation. Equations 27 and 28 are not valid when no current flows in the

TABLE IV. IMPEDANCE PARAMETERS FOR DISCHARGING AT HIGH TEMPERATURES

b_{t1d}	7.613E-1	c_{t2d}	2.225E-4	g_{t2d}	-5.967E-4
b_{t2d}	10.14	d_{t1d}	-6.580	h_{t1d}	3.128E3
b_{t3d}	2.608E2	d_{t2d}	12.11	h_{t2d}	-2.398E3
c_{t1d}	-3.697E-4	g_{t1d}	6.718E-3		

TABLE V. IMPEDANCE PARAMETERS FOR CHARGING AT HIGH TEMPERATURES

b_{t1c}	7.192E-1	c_{t3c}	-1.178E-1	g_{t1c}	-1.344E-2
b_{t2c}	33.91	c_{t4c}	13.99	g_{t2c}	5.011
b_{t3c}	1.999E2	c_{t5c}	-1.897E-4	h_{t1c}	2.611E-5
c_{t1c}	9.869E8	c_{t6c}	7.054E-2	h_{t2c}	3.541E-2
c_{t2c}	-1.479E-1	d_{t1c}	8.814		

cell, so when the cell is at rest, R_{ld} and R_{lc} will then take on the values before the cell was in rest. However, due to the switching time of the power electronics, the current is not directly cut-off, but gradually reduces to zero. In that case R_{ld} and R_{lc} will be modelled with the current before the current switch-off occurred. In practical EV applications this will most likely not be a problem as the sampling times are larger than the converter switching times. So to model and predict the general short term behaviour of a cell under possible operating conditions, the proposed practical equivalent circuit-based model is sufficient.

Finally, the long term behaviour of the internal cell impedance has also been investigated. Over the course of an extensive cycling experiment for capacity fading determination, the change in the internal cell impedance has also been measured. The results of the capacity fading experiment will be described in another paper. Only R_o was found to vary during cycling. Furthermore, the change in R_o was constant over the entire SoC region and equal in magnitude for discharging and charging. Consequently, the resistance rise due to ageing can be modelled by solely R_o with the same equation for discharging and charging. However, no pattern was observed in the R_o development during the cycling experiment. A possible explanation is that the runtime of the cycling experiment was insufficient to observe any change. Another possibility is the influence of the current profile used for cycling. The cells in the capacity fading experiment were continuously cycled with a current profile containing regenerative braking and only resting times at the end and beginning of each cycle. Under this cycling profile the resistance growth in the cell may not have been stable, leading to fluctuations in R_o . On the other hand, cells cycled without regenerative braking did show a rising trend of R_o . The ageing results of the internal cell impedance are therefore inconclusive.

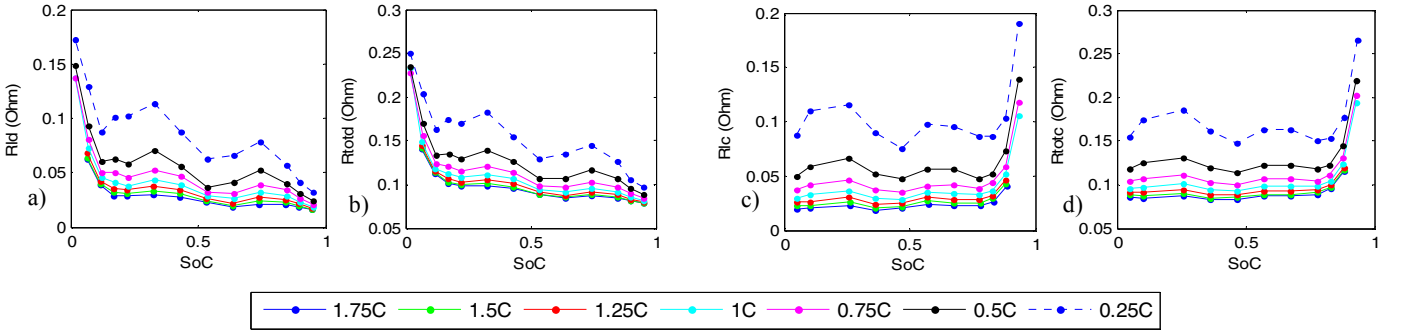


Fig. 1. a) R_{id} , b) R_{totd} , c) R_{lc} and d) R_{totc} determined at different C-rates between 1.75C and 0.25C.

TABLE VI. IMPEDANCE PARAMETERS FOR C-RATE DEPENDENCY

g_{i1d}	6.993E-1	g_{i1c}	-4.124E-1
g_{i2d}	-6.919E-1	g_{i2c}	-1.082
g_{i3d}	2.902E-1	g_{i3c}	-8.730E-1

IV. SIMULATION

To validate the proposed practical equivalent circuit-based model, the voltage response resulting from the model simulation is compared to the measured voltage. The model is implemented in Simulink and can be directly connected the rest of an EV system model. In Fig. 11 the simulation results of the practical equivalent circuit-based model for discharging and charging at reference temperature is shown.

The voltage behaviour of the cell in Fig. 11 for both discharging and charging is accurately modelled. For discharging down to 10% SoC the simulation only has a maximum error of 11mV or 1% of the operating voltage range. But below 10% SoC the total cell impedance rises exponentially and the maximum error goes up to 10%. The inaccuracy is mainly due to the inaccurate fit of the long time transient parallel RC pair in the exponential region. A higher accuracy can be achieved if more parallel RC pairs are used in the model or if R_{ld} and C_{ld} are modelled with higher order polynomials; on the other hand, this would severely complicate the model while the inaccuracy in the linear region is very small. Furthermore, in EV applications battery cells will rarely operate in the region below 10% SoC, so the inaccuracy in this region is of very little importance.

For charging the same accuracy is observed. Up to 90% SoC the maximum error is 12mV or 1.1% of the operating voltage range. Above 90% SoC the maximum error rises to 6%. For charging the inaccuracy is also mainly caused by the exponential curve fit of the long time transient parallel RC pair. The accuracy can be improved in the same way as for discharging; however, the accuracy gained is small compared to the increased complexity. To extend the life of battery cells, some battery management systems are programmed to charge the cells up to 90% SoC. As the life time of battery cells are a very important factor in EV applications, it is expected that SoCs higher than 90% is prevented. Even if the cell is charged to 100%, the errors are acceptable small. Therefore the equivalent circuit-based model can sufficiently model the voltage behaviour in EV applications.

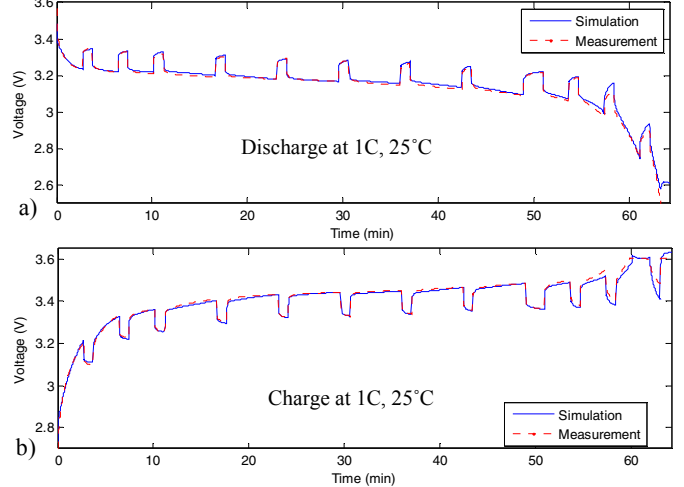


Fig. 11. Comparison between simulation and measurement for a) discharging and b) charging.

Modelling of the temperature and C-rate dependency is also validated in Fig. 12. For high temperatures the maximum voltage error for both discharging and charging is similar to the error found at reference temperature. However, at low temperatures the error becomes significantly large as shown in Fig. 12c and d for 0°C. The error has been determined to grow from 15°C. Using the equations for high temperature, at 15°C the maximum error is 20mV in the linear voltage range, going up to 80mV in the nonlinear range. Using the equations for low temperatures in the Appendix the low temperature behaviour of the cell can be modelled more accurately.

Simulations including C-rate dependency modelling show a maximum error of 14mV or 1.3% of the total voltage range for cells discharged with different C-rate. But if the C-rate dependency is neglected, the maximum error is doubled and a constant error is present in the voltage response, which becomes more profound at low C-rates. So depending on the required accuracy and operating conditions the temperature and C-rate dependency can be chosen to be taken into account.

The parameters are determined under a unidirectional current. It has therefore not been determined what the dynamics between switching between discharging and charging will be. The assumption is made that the impedance element equations for discharging is directly switched to charging when the current direction changes. Future works can include an investigation on the switching dynamics of the current from discharge to charge.

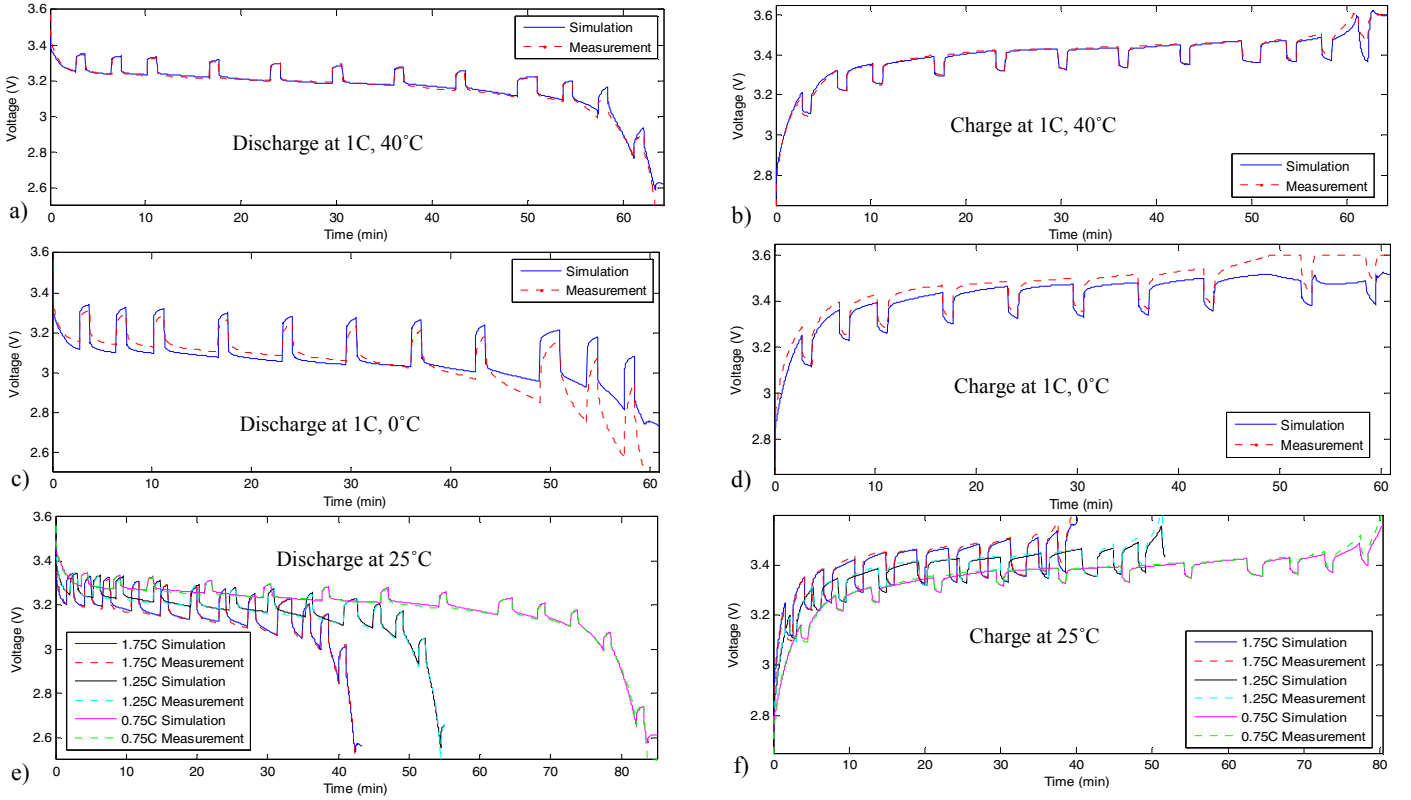


Fig. 2. Comparison between simulation and measurement for a) discharge at 40°C 1C, b) charge. at 40°C 1C, c) discharge at 0°C 1C with high temperature model, d) charge at 0°C 1C with high temperature model, e) discharge at 25°C with different C-rates and f) charge at 25°C with different C-rates.

V. CONCLUSION

A practical equivalent circuit-based model for EV applications is presented in this paper, which is capable of accurately modelling the behaviour of a LiFePO₄ cell under various operating conditions. Tradeoffs between complexity and accuracy of the model have been made based on practical situations in EV applications. The goal of the proposed model is to provide EV system designer with a tool to accurately simulate the behaviour of LiFePO₄ cells under possible operating conditions and optimise the battery operating range. From experiments equations have been extracted to describe the short term behaviour of the useable capacity and voltage response of the cell.

Between 90% and 10% SoC the model accurately represents the voltage response, with a maximum error of 12mV or 1.1% of the operating voltage range at reference temperature and 1C. However, at different temperatures and C-rates the maximum error triples compared to the reference conditions. To reduce the error empirical equations modelling the temperature and C-rate dependency of the cell have been proposed, which have a maximum error to 14mV. Ageing effects on the internal cell impedance have also been investigated, but were inconclusive. Depending on the required accuracy of the model and operating conditions of the cells, an EV system designer can choose the influences to be included in a system simulation.

ACKNOWLEDGMENT

This work was supported by High Tech Automotive Systems (HTAS) under project Databox.

APPENDIX

The empirical equations modelling the low temperature dependence of LiFePO₄ cells for discharge and charge are as follows with the parameters given in respectively Table VII and VIII.

$$R_{od,T_{low}}(SoC, T) = (b_{t1d}T^3 + b_{t2d}T^2 + b_{t3d}T + b_{t4d})SoC^4 + b_{2d}SoC^3 + b_{3d}SoC^2 + b_{4d}SoC + \frac{b_{t6d}}{b_{t5d}e^{\frac{T}{T-b_{t7d}}}} \quad (A1)$$

$$R_{sd,T_{low}}(SoC, T) = (c_{t1d}T^2 + c_{t2d}T + c_{t3d}) \cdot e^{-(c_{t4d}T^2 + c_{t5d}T + c_{t6d})SoC} + c_{3d} + c_{4d}SoC \quad (A2)$$

$$C_{sd,T_{low}}(SoC, T) = d_{1d}(SoC + (d_{t1d}T - d_{t2d}))^3 + d_{2d}(SoC + (d_{t1d}T - d_{t2d}))^2 + d_{4d} + (d_{t3d}T^2 + d_{t4d}T + d_{t5d})(SoC + (d_{t1d}T - d_{t2d})) \quad (A3)$$

$$R_{ld,T_{low}}(SoC, T, I) = g_{t1d}e^{\frac{(g_{t2d}-g_{2d})SoC}{T-g_{t3d}}} + g_{t4d}e^{\frac{g_{t5d}}{T}} + g_{t6d}e^{\frac{g_{t7d}}{T}}SoC \quad (A4)$$

$$C_{ld,T_{low}}(SoC, T) = (h_{1d}SoC^4 + h_{2d}SoC^3 + h_{5d})e^{h_{t1d}T} + h_{3d}SoC^2e^{h_{t2d}T} + h_{4d}SoCe^{\frac{h_{t3d}}{T-h_{t4d}}}. \quad (A5)$$

$$R_{oc,T_{low}}(SoC, T) = (b_{1c}SoC^4 + b_{2c}SoC^3)(b_{t1c}T + b_{t2c}) + (b_{t3c}T^2 + b_{t4c}T + b_{t5c})SoC^2 + (b_{t6c}T^2 + b_{t7c}T + b_{t8c})SoC + b_{t9c}e^{\frac{b_{t10c}}{T-b_{t11c}}} \quad (A6)$$

$$R_{sc,T_{low}}(SoC, T) = c_{t1c} e^{ct2cT + (ct3cT + ct4c)SoC} + c_{t5c} T^2 + c_{t6c} T + c_{t7c} \quad (A7)$$

$$C_{sc,T_{low}}(SoC, T) = (d_{t1c} T^2 + d_{t2c} T + d_{t3c}) SoC^4 + (d_{t4c} T^2 + d_{t5c} T + d_{t6c}) SoC^3 + d_{t7c} e^{dt8cT} SoC^2 + (d_{t9c} T^2 + d_{t10c} T + d_{t11c}) SoC + d_{t12c} T + d_{t13c} \quad (A8)$$

$$R_{lc,T_{low}}(SoC, T) = g_{t1c} \cdot e^{gt2cT - g_{2c} SoC} + g_{t3c} T^2 + g_{t4c} T + g_{t5c} + g_{4c} SoC \quad (A9)$$

$$C_{lc,T_{low}}(SoC, T) = (h_{t1c} SoC^5 + h_{t2c} SoC^4 + h_{t3c} SoC^3) \cdot e^{ht4cT} + h_{t5c} e^{ht6cT} SoC^2 + h_{t7c} e^{ht8c} SoC + h_{t9c} \quad (A10)$$

TABLE VII. LOW TEMPERATURE IMPEDANCE PARAMETERS DISCHARGE

b _{2d}	-2.819E-1	c _{4d}	-6.462E-3	d _{2d}	4.068	g _{7d}	4.202E3
b _{3d}	2.448E-1	c _{1d}	1.923E-4	d _{3d}	-6.807E-1	h _{1d}	-3.751E-11
b _{4d}	-9.630E-2	c _{2d}	-1.166E-1	d _{4d}	4.002E2	h _{2d}	6.764E-11
b _{11d}	-5.930E-6	c _{3d}	17.66	d _{5d}	-5.769E4	h _{3d}	-2.219E-11
b _{2d}	5.011E-3	c _{4d}	1.098E-2	g _{2d}	20.00	h _{4d}	10.75
b _{5d}	-1.411	c _{5d}	-5.644	g _{1d}	8.238E-3	h _{5d}	1.534E-13
b _{14d}	1.325E2	c _{6d}	7.299E2	g _{2d}	1.805E2	h _{1d}	1.220E-1
b _{15d}	6.297E-2	d _{1d}	-1.173E3	g _{3d}	2.321E2	h _{2d}	1.241E-1
b _{6d}	24.37	d _{2d}	8.278E2	g _{4d}	1.589E-7	h _{3d}	-4.492E2
b _{7d}	2.363E2	d _{4d}	1.005E2	g _{5d}	3.779E3	h _{4d}	3.474E2
c _{3d}	1.827E-2	d _{1d}	1.428E-2	g _{6d}	-2.208E-8		

TABLE VIII. LOW TEMPERATURE IMPEDANCE PARAMETERS CHARGE

b _{1c}	2.192E-1	c _{11c}	7.008E29	d _{7c}	-3.688E-2	g _{9c}	5.225
b _{2c}	-3.968E-1	c _{12c}	-3.051E-1	d _{8c}	4.261E-2	h _{1c}	6.343E-6
b _{11c}	-8.297E-2	c _{3c}	2.782E-1	d _{9c}	-1.199	h _{2c}	-1.817E-5
b _{2c}	24.82	c _{4c}	-63.04	d _{10c}	7.103E2	h _{3c}	1.887E-5
b _{3c}	2.136E-4	c _{5c}	2.840E-6	d _{11c}	-1.027E5	h _{4c}	8.551E-2
b _{4c}	-1.422E-1	c _{6c}	-1.733E-3	d _{12c}	8.493	h _{5c}	-1.414E-5
b _{5c}	23.48	c _{7c}	2.786E-1	d _{13c}	-1.902E3	h _{6c}	8.381E-2
b _{6c}	-1.795E-4	d _{1c}	-11.23	g _{2c}	-32.23	h _{7c}	1.057E-5
b _{7c}	1.077E-1	d _{2c}	5.941E3	g _{4c}	1.571E-2	h _{8c}	7.897E-2
b _{8c}	-16.20	d _{3c}	-7.848E5	g _{1c}	3.726E-8	h _{9c}	6.962E2
b _{9c}	4.968E-2	d _{4c}	16.18	g _{2c}	-4.951E-2		
b _{10c}	28.78	d _{5c}	-8.523E3	g _{7c}	5.921E-5		
b _{11c}	2.376E2	d _{6c}	1.123E6	g _{8c}	-3.507E-2		

REFERENCES

- R. Rao, S. Vrudhula, and D. N. Rakhmatov, "Battery modeling for energy-aware system design," *Computer*, vol. 36, no. 12, pp. 77-87, Dec. 2003.
- D. Rakhmatov, "Battery Voltage Modeling for Portable Systems," *ACM Trans. on Design Automation of Electronic Systems*, vol. 14, no. 2, 2009.
- M. Safari, M. Morcrette, A. Teyssot, and C. Delacourt, "Multimodal Physics-Based Aging Model for Life Prediction of Li-Ion Batteries," *J. Electrochem. Soc.*, vol. 156, no. 3, pp. A145-A153, 2009.
- W. B. Gu and C. Y. Wang, "Thermal and electrochemical coupled modeling of a lithium-ion cell in lithium batteries," in *Proc. ECS*, 2000, pp.748-762.
- P. Rong and M. Pedram, "An analytical model for predicting the remaining battery capacity of lithium-ion batteries," *IEEE Trans. VLSI Systems*, vol. 14, no. 5, pp. 441-451, May 2006.
- S. Santhanagopalan, Q. Zhang, K. Kumaresan, and R. E. White, "Parameter Estimation and Life Modeling of Lithium-Ion Cells," *J. Electrochem. Soc.*, vol. 155, no. 4, pp. A345-A353, 2008.
- M. W. Verbrugge and R. S. Conell, "Electrochemical and Thermal Characterization of Battery Modules Commensurate with Electric Vehicle Integration," *J. Electrochem. Soc.*, Vol. 149, no. 1, pp. A45-A53, 2002.
- B. Y. Liaw, G. Nagasubramanian, R. G. Jungst, and D. H. Doughty, "Modeling of lithium ion cells—A simple equivalent-circuit model approach," *Solid State Ionics*, vol. 175, no. 1-4, pp. 835-839, 2004.
- S. S. Zhang, K. Xu, and T. R. Jow, "Electrochemical impedance study on the low temperature of Li-ion batteries," *Electrochim. Acta*, vol. 49, no. 7, pp. 1057-1061, 2004.
- P. Suresh, A. K. Shukla, and N. Munichandraiah, "Temperature dependence studies of a.c. impedance of lithium-ion cells," *J. Applied Electrochem.*, vol. 32, no. 3, pp. 267-273, 2002.
- Y. Hu, S. Yurkovich, Y. Guezennec, and B.J. Yurkovich, "Electro-thermal battery model identification for automotive applications," *J. Power Sources*, vol. 196, no. 1, pp. 449-457, 2011.
- L. Gao, S. Liu, and R. A. Dougal, "Dynamic lithium-ion battery model for system simulation," *Components and Packaging Technologies, IEEE Trans. on*, vol. 25, no. 3, pp. 495- 505, 2002.
- P. Kumar and P. Bauer, "Parameter Extraction of Battery Models Using Multiobjective Optimization Genetic Algorithms," *EPE/PEMC, 2010 14th International*, pp. T9-106-T9-110, 2010.
- Y. Hu, S. Yurkovich, Y. Guezennec, and B. J. Yurkovich, "A technique for dynamic battery model identification in automotive applications using linear parameter varying structures," *Control Eng. Practice*, vol. 17, no. 10, pp. 1190-1201, 2009.
- M. Chen and G.A. Rincón-Mora, "Accurate Electrical Battery Model Capable of Predicting Runtime and I-V Performance," *IEEE Trans. on Energy Conv.*, vol. 21, no. 2, pp. 504-511, 2006.
- J. Zhang, S. Ci, H. Sharif, and M. Alahmad, "An Enhanced Circuit-Based Model for Single-Cell Battery," *APEC*, pp. 672-675, 2010.
- O. Erdinc, B. Vural, and M. Uzunoglu, "A dynamic lithium-ion battery model considering the effects of temperature and capacity fading," *Int. Conf. on Clean Electrical Power*, pp.383-386, 2009.
- H. L. Chan and D. Sutanto, "A new battery model for use with battery energy storage systems and electric vehicles power systems," *IEEE Power Eng. Soc. Winter Meeting*, vol.1, pp.470-475, 2000.
- S. Mischie and D. Stoiciu, "A new and improved model of a lead acid battery" *J. FACTA UNIVERSITATIS*, vol. 20, no. 2, pp. 187-202, 2007.
- R.C. Kroese and P.T. Krein, "Electrical battery model for use in dynamic electric vehicle simulations," *PESC*, pp.1336-1342, 2008.
- M. Dubarry, V. Svoboda, R. Hwu, and B. Y. Liaw, "Capacity loss in rechargeable lithium cells during cycle life testing: The importance of determining state-of-charge," *J. Power Sources*, vol. 174, no. 2, pp. 1121-1125, 2007.
- E. Kuhn, C. Forgez, P. Lagonotte and G. Friedrich, "Modelling Ni-mH battery using Cauer and Foster structures", *J. Power Sources*, vol.158, no. 2, pp. 1490-1497, 2006.
- L. Alexander, S. Mani, and D. Carmen, "Development of battery packs for space applications," *NASA Aerospace Battery workshop*, 2007.
- M. A. Roscher and D. U. Sauer, "Dynamic electric behavior and open-circuit-voltage modeling of LiFePO4-based lithium ion secondary batteries", *J. Power Sources*, vol. 196, no. 1, pp. 331-336, 2011.
- F. Baronti, G. Fantechi, E. Leonardi, R. Roncella, and R. Saletti, "Enhanced model for Lithium-Polymer cells including temperature effects," *IECON 2010*, pp. 2329-2333, 2010.
- S. Abu-Sharkh and D. Doerffel, "Rapid test and non-linear model characterisation of solid-state lithium-ion batteries", *J. Power Sources*, vol. 130, no. 1-2, pp. 266-274, 2004.
- B. Schweighofer, K. M. Raab, and G. Brasseur, "Modeling of high power automotive batteries by the use of an automated test system," *IEEE Trans.Instrum. Meas.*, vol. 52, no. 4, pp. 1087-1091, 2003.